Gravitational wave sources from massive binary and triple stellar systems

by

Andras (Andris) Dorozsmai

A thesis submitted to the University of Birmingham for the degree of
DOCTOR OF PHILOSOPHY

Institute for Gravitational Wave Astronomy

School of Physics and Astronomy

College of Engineering and Physical Sciences

University of Birmingham

15/09/2023

UNIVERSITYOF
BIRMINGHAM

University of Birmingham Research Archive

e-theses repository

Thesis summary

In this thesis, I investigate the formation paths of merging stellar mass binary black holes originating from massive binary and massive triple systems.

Massive stars are short-lived objects and extremely rare, making up less than 1 percent of the total population of stars. Despite their rarity, they dominate and drive the evolution of galaxies due to their enormous energy output and are progenitors to some of the most energetic astrophysical phenomena in the Universe. Understanding their evolution is crucial for almost all branches of astronomy. However, due to their scarcity, it is remarkably difficult to directly study them. Therefore, we need to consider every possible indirect observational clues to constrain their evolution.

Gravitational wave (GW) astronomy offers a unique way to study massive stars. Most GW signals detected to date were emitted by merging binary black holes. The large number of such detections make it possible to infer the demographics of these objects. Since massive stars are progenitors of stellar mass black holes, the demographics of stellar mass black hole binaries are heavily influenced by currently poorly understood processes related to massive stars and their interactions, such as various mixing mechanisms in stellar interiors, mass transfer episodes and three-body dynamics. Therefore, in principle, observations of GW sources can help us to better understand several aspects of massive star evolution. We have to understand how the properties of merging binary compact objects depend on uncertain stellar physics. This can help us to identify certain features in the demographics of GW sources that help us to learn about the poorly known evolutionary processes massive stars experience.

This is in practice, however, an extremely difficult task. Due to the large number highly uncertain evolutionary stages that massive stars undergo to become GW sources, at the present time, we cannot create completely robust methods to directly infer stellar physics from GW observations. However, it is still crucial to understand how different assumptions of poorly constrained physics change our pre-

dictions about the demographics of merging binary black holes. Such studies can guide us in understanding which are the most critical aspects of stellar evolutionary models that needs urgent attention for improvement. Furthermore, it can also help us determining the best way to combine GW data with other, electromagnetic observations of immediate evolutionary stages of massive stars to obtain the most robust tests for our evolutionary models.

In this thesis, I use a population synthesis approach. I sample a large number of systems composed of zero-age main sequence stars from distributions that are in agreement with recent observations of young, massive stars. Using stellar evolutionary codes, I evolve these systems and I predict the properties of their remnants and eventual GW sources they might form, by making different assumptions about the physics of key processes that define their evolution.

In Chapter 2, I study the the so-called classical isolated binary evolution channel. This formation channel is considered to be one of the most promising source of merging binary black holes. In the first part of Chapter 2, I explore how uncertainties related to the first phase of mass transfer can affect the properties of GW sources. Among many results, I show that models with different assumptions about the highly uncertain angular momentum loss during the first phase of mass transfer yield very similar binary black hole observables (in terms of merger rate, mass and mass ratio distributions), however, the dominant formation channel is entirely different. This highlights why inferring stellar physics alone from GW data should be done with extreme caution given our current uncertainties.

In the second part of Chapter 2, I investigate the impact of uncertainties of stellar winds on the sources from the isolated binary formation channel. It is well known that the mass-loss rates of line-driven winds are by uncertain about a factor of three, and this can have a significant effect on the mass spectrum of black holes formed from single star evolution. I show that the impact of lowered mass loss rates on the masses of merging binary black holes, however, significantly depends

on the assumption of other, seemingly unrelated binary physics. This demonstrates that inferring mass loss rates based on the masses of merging binary black holes can be misleading, unless the implications of other, uncertain binary physics is well explored.

In the final part of Chapter 2, I show that a large fraction of GW sources, formed via two subsequent stable phases of mass transfer, never cross the Humphreys-Davidson limit during their evolution. Therefore, these systems are likely not affected by any related uncertainties. As we show, the predicted merger rate of this channel can be comparable to the inferred merger rate from GW observations. This implies that even, if the most massive stars never cross the Humpreys-Davidson limit (and therefore do not experience significant radial expansion), currently inferred merger rates are still compatible with the classical isolated binary channel.

In Chapter 3, I study the evolution of hierarchical triples, in which the stars in the inner binary experience chemically homogeneous evolution. My primary aim is to understand the implications of this evolutionary channel in the context of GW astronomy.

I show that in a large fraction of these sources, the tertiary eventually fills its Roche-lobe. This is unique to triples with chemically homogeneously evolving stars and occurs very rarely in classically evolving triples. More importantly, in about 30 per cent of the cases, this tertiary mass transfer occurs towards a short period binary black hole (of which a large fraction eventually forms GW sources). The impact of the tertiary mass transfer on the inner binary black hole can be significant, as the inner orbit can shrink, leading to shorter delay times associated with GW mergers.

I also show that three-body dynamics plays a significant role in the evolution of the inner binary in an appreciable fraction of these triples. In some case, von Zeipel-Lidov-Kozai oscillations can prompt double helium star mergers in the inner binary. Such a scenario would be extremely rare among massive stars.

Although, chemically homogeneous evolution is predicted to be rather unevent-

ful, if it occurs with an isolated binary (stars remain fully detached and might form merging binary black holes), if these systems are part of a hierarchical triple, then the tertiary star can influence their evolution in various ways, leading to a number of different possible sub-channels with qualitatively different evolution, possibly accompanied by the formation of various electromagnetic transients.

In the final Chapter 4, I briefly summarise the main findings of this thesis, and discuss recommended future work.

Dedication

To Anyu, Srija, Nepu and Csimpi.

Acknowledgements

First and foremost, I would like to thank my PhD supervisor, Silvia Toonen. Thank you for offering me to opportunity to work on this amazing project, for introducing me to the exciting world of stellar triples, for your guidance, for all the interesting science discussions, for always making sure that you have time to help me and for creating a wonderful, welcoming group at Amsterdam. But perhaps, above all, I would like to thank you for your endless patience. I know I have not been the easiest PhD student to deal with, but I really appreciate you never giving up on me, even during the most challenging times.

I would like to thank to Alejandro for all the amazing help he provided for Chapter 2. I learnt a lot from you. I would lie, if I said it was always easy to keep up with your many, many (great) suggestions for improving the writing and structure of our paper. In the end, however, it is clear you were right, as your persistence has definitely paid off. Besides being a great scientist, you are a very good supervisor too, so I have no doubt in my mind that one day you'll be an excellent professor!

I am really grateful to my group members in Amsterdam: Floris, Tomer, Caspar, Yan, Sancho, Jan, Freek, Adam, Steven, Maitrey, Gabriel. You are some of the most helpful and friendliest people I have met during my PhD. I feel very lucky that I had the chance to have you as my colleagues.

I would like to thank Alex de Koter for taking the time to have meetings with me (despite of never being officially affiliated with University of Amsterdam), offering very good advice and help for my projects.

I would like to thank Selma de Mink for all the very helpful advice she gave for Chapter 2, and for providing me an opportunity to visit MPA Garching. It was great to meet her wonderful group.

I would like to thank my fellow PhD students at University of Birmingham. I couldn't spend as much time with you guys as I expected at the beginning of my PhD, but I am still very grateful for being so helpful all the time. Thank you Eliot,

Matt, Lucy.

I would like to thank Alberto Vecchio for leading the Gravitational Astronomy group at University of Birmingham. I would like to thank David Stops, Jo Cox for the amazing assistance they provide for the PhD students in Birmingham.

I would also like to thank my Mom, my Father, without their continuous support and faith in me, it would have been impossibly for me to finish my PhD. I'm also really grateful to Maa, Baba, my two brothers Gergo, Viki, Kasia, Syd, and also Csimpi and Nepu! You've all provided me an amazing support throughout these difficult years. Last, but not least, I would like to express my gratitude to my amazing wife, Srija. Thank you!

Contents

Chapter 1

Introduction

In this chapter, we discuss the most important aspects and related uncertainties of massive star evolution theory. We start by considering single stellar evolution in section 1.1,. We summarise the evolution of non-interacting massive stars from the onset of core-hydrogen burning until black hole (BH) formation. In section 1.2, we discuss stellar interactions in multiple systems. In these two sections, we introduce the necessary ingredients to determine detailed, interacting stellar evolutionary models. We note that the results presented in this thesis were determined by using rapid population synthesis codes, which are not detailed stellar models, but rather use fitting formulae to earlier detailed simulations [276, 138, 139]. Yet, understanding the foundations behind stellar evolution modelling provides important context for the results presented in the upcoming chapters. Finally, in section 1.3, we briefly discuss the basics of gravitational wave (GW) astronomy, the properties of the detected binary BH mergers, and the proposed formation channels.

1.1 Physics of massive stars

1.1.1 Role of massive stars in astrophysics

Massive stars can be defined as those stars that experience core-collapse by the end of their lives, thereby evading the formation of white dwarfs. Following this definition, massive stars have initial masses (i.e. mass at zero-age main sequence) that are equal or larger than $\sim$8-9 $M_\odot$ [though this is somewhat metallicity dependent, see 273].

Massive stars are rare and short lived objects. Only about 6 out of every 1000 newly formed stars is expected to be a massive star[1]. Their lifetime is only few to few tens of million years, which is several orders of magnitude shorter than that of the Sun (which is about $\sim 10^{10}$ years). Their low formation rate and their short lifespan makes massive stars rare and perhaps one would consider them exotic astronomical objects. However, they play a major role in almost every branch of astrophysics [see e.g. 187]. They are progenitors of a number of high-energy astrophysics transients, such as supernova (SN) explosions, gamma-ray bursts. They drive the evolution of star clusters and provide energetic and chemical feedback to the interstellar medium, affecting the subsequent star formation epochs and thereby ultimately driving the evolution of galaxies [see e.g. 187]. Last but not least, they also form neutron stars and stellar mass BHs and are progenitors to GW sources.

In Fig. 1.1, we show the stellar tracks of massive stars with various initial masses in the Hertzsprung-Russel diagram. As it can be seen, these objects can be up to a million times more luminous than the Sun. Consequently, they dominate the light of star-forming galaxies due to their enormous energy output, despite being

---

[1]Assuming massive stars have an initial mass at zero-age main sequence $M_{\mathrm{ZAMS}} \geq 8\,M_\odot$ and a universal initial mass function (IMF) of [176].

extremely rare [372]. Given their high effective temperatures (i.e. $T_{\text{eff}} \geq 10\text{kK}$ for the majority of their lifetime), most of their light is emitted in the UV range [see e.g. 306]. The intense radiation of massive stars in this wavelength range allows the emitted high energy photons to transfer their momentum to the stellar matter via line scattering efficiently and drive strong stellar winds. As we discuss in section 1.1.3, these so-called line driven winds can result in significant mass loss, with large terminal speeds [up to $v_{\infty} \sim 1000\,\text{kms}^{-1}$, see e.g. 113, 282, 62]. Such a supersonic outflow shock-heats the surrounding gas to $T \sim 10^6\,K$ and creates a bubble and introduces turbulent motions in the interstellar medium [50, 378]. The total energy deposited by stellar winds by a massive star throughout its lifetime is significant and comparable to the energy introduced by supernova explosions [$\sim 10^{50}$ergs, see e.g. 382].

Another consequence of the strong UV radiation from massive stars is that they efficiently ionise the surrounding gas [267]. As the energy and the amount of ionising photons emitted sensitively depends on the effective temperature of the star, this process is influenced by mass exchange that can result in envelope stripping and a formation of a hot naked helium star [e.g. 332, 111, 307] and stellar rotation [e.g. 341]. Furthermore, some binary configurations can evolve into X-ray binaries, which contribute to an even more energetical ionising radiation [e.g. 317, 310]. Massive stars are also thought to have played a pivotal role in the reionisation epoch of the early universe [e.g. 114, 112].

Massive stars experience core collapse, when all the nuclear fuel is exhausted in their interiors. As we discuss in section 1.1.5, this process is often followed by a violent supernova (SN) explosion. Similarly to stellar winds, SN also has a profound effect on the environment of these stars. A large amount of energy ($\sim 10^{51}$ergs) and mass is fed back to the interstellar medium, leading to turbulent motions and to the formation of bubbles and destruction of molecular clouds, influencing subsequent

star formation epochs. Supernova explosions can also trigger galactic winds and outflows.

We finally note that massive stars are also crucial for nucleosynthesis. In Fig. 1.2, we show the predicted origin and abundance of each chemical element in the universe [169]. As it can be seen, many elements, including the oxygen, is primarily produced by massive stars.

1.1.2 Physics of massive stars

The structure of stars and their evolution can be described by 5 equations, which describe 5 fundamental concepts: i) conservation of mass, ii) balance of forces, iii) energy generation, iv) energy transport, v) changes in composition. These equations, in the same order, are [e.g 162]:

$$\frac{\partial r}{\partial m} = \frac{1}{4\pi r^2 \rho}, \tag{1.1}$$

$$\frac{\partial P}{\partial m} = -\frac{Gm}{4\pi r^4} - \frac{1}{4\pi r^2}\frac{\partial^2 r}{\partial t}, \tag{1.2}$$

$$\frac{\partial l}{\partial m} = \epsilon_{\mathrm{nuc}} - \epsilon_\nu - T\frac{\partial s}{\partial t}, \tag{1.3}$$
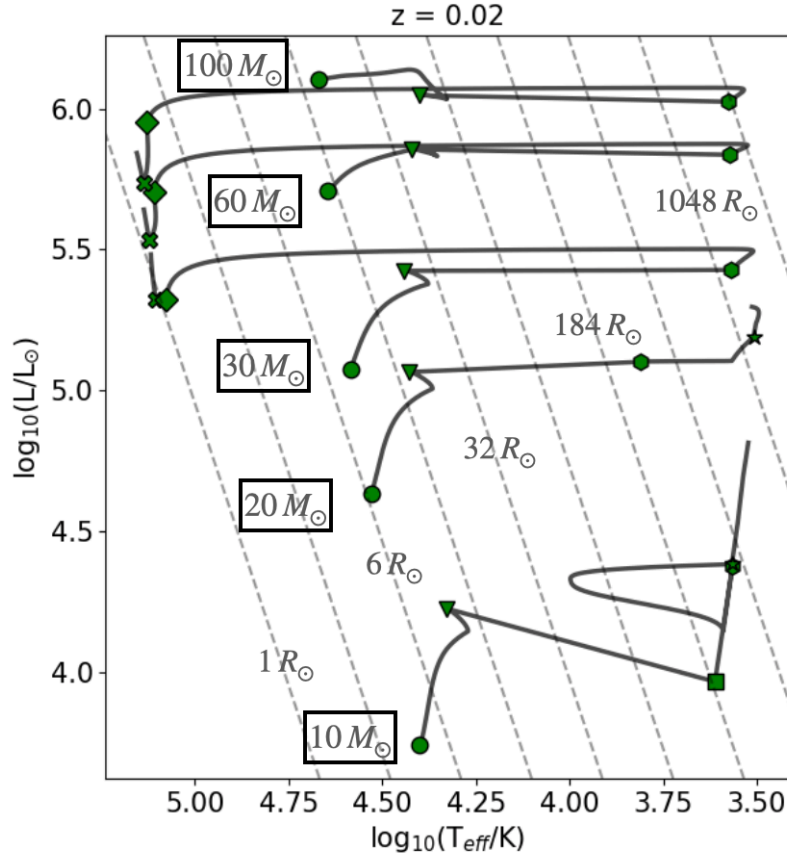
Figure 1.1: Stellar tracks for massive stars in the Hertzsprung-Russel diagram at Z = 0.02. We determined the stellar tracks by using the fitting formula of [138]. The initial mass of each star is shown left to the each track. The green markers indicate the beginning of a particular stellar evolutionary phase; circle: main sequence (MS), inverted triangle: end of MS (or "Hertzsprung gap phase"), square: subgiant phase, hexagone: core-helium burning phase, star: asymptotic giant branch, diamond: helium star, cross: helium giant. We also show isoradius curves with dashed gray lines. These lines have been linearly spaced in logarithmic space between 1 $R_\odot$ and 2500 $R_\odot$.
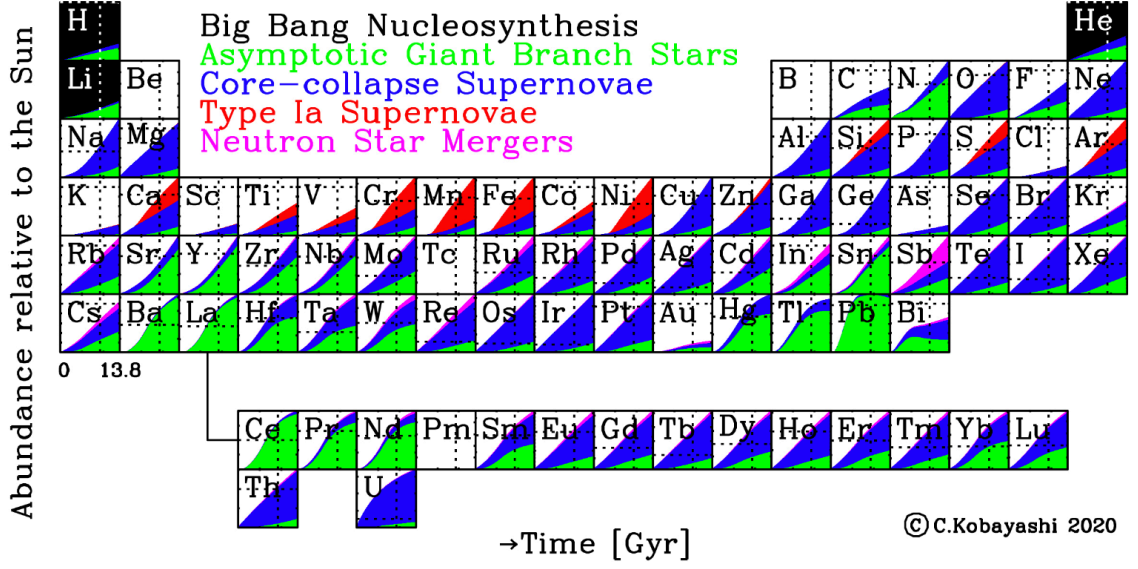
Figure 1.2: The origin of each element as predicted by the chemo-dynamical simulations of [169]. For each chemical element the predicted relative fraction is shown as a function of time. Different production channels are shown in different colours. The dashed lines indicate the solar abundance for each element. Figure adopted [169].

$$\frac{\partial T}{\partial m} = -\frac{Gm}{4\pi r^4}\frac{T}{P}\nabla, \tag{1.4}$$

$$\frac{\partial X_i}{\partial t} = \frac{A_i m_u}{\rho}\left(-\sum_j (1+\delta_{ij})r_{ij} + \sum_{k,i} r_{kl,i}\right) + \frac{\partial}{\partial m}\left[(4\pi\rho r^2)D_{\text{mixing}}\frac{\partial X_i}{m}\right]. \tag{1.5}$$

These equations are valid, if spherical symmetry is maintained. Parameters r and m are the radial and mass coordinates, respectively. The equations above are expressed in terms of the mass coordinate (i.e. using a Langrangian coordinate system).

Equation 1.1 relates the mass distribution of the star to its density profile, $\rho(r)$, and can be derived from the principle of mass conservation. Equation 1.2 expresses

the pressure gradient and follows from the Navier-Stokes equation. In case of hydrostatic equilibrium (which is a valid assumption for most of a star's lifespan), the last term on the right hand becomes zero. Equations 1.1 and 1.2 describe the mechanical structure of the star.

Equation 1.3 is related to the energy generation in the stellar interior, and can be derived considering energy conversation on a local scale (i.e. first law of thermodynamics). Here, l is the local luminosity, ϵ_{nuc} is the nuclear energy production rate per unit mass and ϵ_ν is the energy carried away by neutrinos per unit mass. The term $T\partial s/\partial t$ expresses the net change of heat in a given mass shell[2]. If $T\partial s/\partial t < 0$, then energy is released by the shell, this occurs in case of contraction, if $T\partial s/\partial t > 0$, then energy is absorbed by the shell, which happens during expansion, and if $T\partial s/\partial t = 0$, then the mass shell is in thermal equilibrium. Massive stars are in thermal equilibrium for most of their lifetime, one notable exception occurs when they cross the Hertzsprung gap (hydrogen-shell burning but before the ignition of helium, see Fig. 1.1). Equation 1.4 describes the energy transport in the stellar interior and expresses a relation for the necessary temperature gradient $(\partial T/\partial m)$ that is required to carry the entire luminosity of the star. This relation is only valid in case of hydrostatic equilibrium. Here, $\nabla = d\log\mathrm{T}/d\mathrm{P}$, and in case radiation is responsible for the energy transport and there is (local) thermal equilibrium, $\nabla_{\mathrm{rad}} = 3\kappa l P/16\pi a c G m T^4$, where κ is the (Rosseland mean) opacity and $a = 8\pi^5 k^4/15h^3c^3$, is the radiation constant. If convection also contributes significantly to the transport of the energy, then $\nabla = \nabla_{\mathrm{ad}} + \Delta$, where ∇_{ad} is the adiabatically stratified temperature gradient (i.e. $[d\log\mathrm{T}/d\mathrm{P}]_{\mathrm{ad}}$) and Δ expresses the degree of superadiabacity. The latter is computed based on the theory that is adopted to model convection [e.g. mixing length theory, see 37]. Equation 1.3 and 1.4 describe the thermal structure of the star.

---

[2]since according to the first law of thermodynamics: $T\partial s/\partial t = \partial u/\partial t - (P/\rho^2)\partial\rho/\partial t = \partial q/\partial t$, where u and q are the specific internal energy and the specific heat content of the mass shell

Finally, equation 1.5, describes the rate of change in the mass fraction of the ith chemical species in a given mass shell. The first term on the right-hand side is the change in composition due to nuclear reactions. Here A_i is the atomic mass number, m_u is the atomic mass unit. The first term is the sum of all reactions that destroys the given chemical species. The term r_{ij} is the reaction rate between chemical species i and j and δ_{ij} is the Kronecker delta, which is required, since if there exists a reaction that requires two of the same chemical species, then two nuclei will be destroyed. The term $r_{kl,i}$ denotes all the reactions between chemical species k and l that produces i. The second term in the right-hand side on equation 1.5 expresses the composition change in a given mass shell due to mixing. D_{mixing} is the diffusion coefficient, which is typically a sum of individual diffusion coefficients from various processes, such as mixing due to convection, semiconvection, convective overshoot and various rotational mixing processes [see e.g. 125]. In case of hydrostatic and thermal equlilibrium, equation 1.5 is the only one that depends on time and this expresses the primary process that drives the evolution (i.e. the change in structure) of the star.

If the star is composed of N different chemical species, then there are 4+N equations that fully describes its structure. This can be in principle solved, if one knows:

1. Equation of state [see e.g. 298, 309, 348, 281]: $P = P(\rho, TX_i)$,

2. Opacity [see e.g. 143, 144]: $\kappa = \kappa(\rho, T, X_i)$,

3. A nuclear network, which provides the rates of nuclear reactions and the corresponding energy input and neutrino energy losses [see e.g. 15, 51]: $r_{ij} = r_{ij}(\rho, TX_i)$, $\epsilon_{nuc} = \epsilon_{nuc}(\rho, TX_i)$, $\epsilon_\nu = \epsilon_\mu(\rho, TX_i)$

4. Boundary conditions: i) for the centre (m = 0): r = 0, l = 0, ii) for the surface

(m = M) $P = 2GM/3\kappa_{\mathrm{ph}}R^2$, L = $4\pi R^2 \sigma T^4$. Here κ_{ph} is the average value of the opacity over the atmosphere.

The boundary condition for $P(m = M)$ follows from identifying the photosphere with the radial coordinate, at which the optical depth equals to 2/3 (that is $\tau_{\mathrm{ph}} = \int_R^\infty \kappa \rho dr = \kappa_{\mathrm{ph}} \int_R^\infty \rho dr = 2/3$). Strictly speaking, this is not correct because at such an optical depth the radiative diffusion approximation breaks down. A more accurate solution could be found by fitting a detailed stellar atmosphere model to an interior to an interior shell, where $\tau > 2/3$.

For massive stars a detailed stellar atmosphere is especially important, because intense stellar winds are developed near the atmosphere, which lead to significant mass loss rates and this strongly influences its evolution (see section 1.1.3). However, for most applications, it is sufficient to apply the boundary conditions presented in 4) and calculate the mass-loss rates from stellar wind prescriptions derived from observations or detailed stellar atmosphere models (see section 1.1.3).

Solving equations 1.1 - 1.5 provide values of r, P, l and X_i for each mass shell and time. This set of solution is typically referred to as a 1D *detailed stellar evolutionary model*. As these equations are coupled and highly non-linear, it is typically not possible to find analytical solutions, especially if one uses realistic equation of states, opacities etc. Nevertheless, using a numerical method [e.g. Henyey's method 127], it is in principle straight forward to determine the evolution of a star. Yet, it is notoriously difficult to compute reliable evolutionary models of massive stars. This is mostly due to the huge uncertainties regarding many important processes. These uncertainties also constitute a major obstacle in determining the origin of GW sources detected by LIGO/Virgo [see e.g. 30]. Below, the most significant and important uncertainties for single massive star evolution are summarised [see also 81, 187]:

1. **Convection**: Convection is a type of dynamical instability that commonly occurs inside stars. If a parcel of gas is displaced due to random thermal motions, e.g upwards, then the ambient pressure in the new environment is lower than that of the parcel. To regain pressure equilibrium, the parcel expands adiabatically. While the pressure balance is restored, the density of the parcel (ρ_{parcel}) and its environment (ρ_{env}) generally will be different, and if $\rho_{\mathrm{parcel}} < \rho_{\mathrm{env}}$, then the gas parcel will keep moving upwards due to the buoyancy force. This is called convection [3]. There are a number of reasons why convection is challenging to model in stellar evolutionary codes. First, it is an inherently three dimensional phenomenon, with complex, random and turbulent movements of the gas cells, which cannot be accounted for in 1D stellar models. Secondly, convection remains difficult to model even in complex 3D hydrodynamical simulations, as there are various physical processes with very different timescales, which renders the computation time prohibitive [see e.g. 155]. In 1D stellar models, mixing length theory is the most commonly used approximation, in which it is assumed that convective cells in a given mass shell travel strictly vertically a given distance, which is expressed in terms of the local pressure scale height, called mixing length [e.g 37, 155]. Furthermore, instantaneous mixing is assumed in the convective regions. The mixing length is parameterised with α_{MLT}, that is the mixing length is $\alpha_{\mathrm{MLT}} \cdot H_p$, where H_p is the pressure scale height. In most stellar evolutionary studies, α_{MLT} is considered as a free parameter, and is assumed to be independent of radial coordinate and of the parameters of the stars. Calibration of α_{MLT} for massive stars remains

---

[3]This can be translated to two commonly used criteria; convection occurs, if $\nabla_{\mathrm{rad}} > \nabla_{\mathrm{ad}}$ (Schwarzschild criterion) or $\nabla_{\mathrm{rad}} > \nabla_{\mathrm{ad}} - \chi_\mu/\chi_T \nabla_\mu$, where μ is the mean molecular weight, $\chi_\mu = \mu/P(\partial P/\partial \mu)_{\rho,X_i}$, $\chi_T = T/P(\partial P/\partial T)_{\rho,X_i}$, and $\nabla_\mu = d\log\mu/d\log P$, which is the chemical gradient. The main difference is that the Ledoux criterion also takes into account that chemical species with larger μ are more likely to be found in the deeper layers (as that is where nuclear reactions take place). In that case an upward moving cell also has a higher μ and therefore a larger density than its environment, in which case the cell might move downwards due to the buoyancy force, despite being hotter than its surrounding. Therefore the chemical gradient has a stabilising effects against convection.

challenging. For massive stars, convection plays an important role in i) the core on the MS and ii) in the envelope of a star that has reached an evolved giant stage and has relatively cool effective temperature. In the former case, energy transport due to convection is expected to be very efficient due to the typical high densities (since the convective flux is proportional to density), and a negligible superadiabacity (Δ) is required to carry the flux. Consequently, the temperature gradient is adiabatic by a very good approximation, and the choice of α_{MLT} is not expected to significantly influence the predicted evolution of massive stars [e.g. 155]. In the latter, however, convection is less efficient, and therefore the flux is carried by both radiation and convection, and superadiabacity is important. In this case, the adopted α_{MLT} has a strong influence on the predicted structure and the size of the envelope of an evolved massive star that has developed a deep convective envelope.

2. **Convective overshoot**: Near the boundary of convective regions, parcels of gas within the convective region, that gained sufficient acceleration, might penetrate into radiatively stable regions. This is called convective overshoot and this provides mixing and additional energy transport to non-convective regions. This is a highly-non linear process, as the overshot parcels carry away heat and effectively decrease the temperature and composition gradient near the boundary, which in turn increases the acceleration of the parcels that could be potentially overshot, thereby gradually increasing the size of the region that is affected. In the context of massive stars, convective overshoot is perhaps the most important around the convective boundary regions of hydrogen burning cores of MS stars. The poorly constrained efficiency of convective overshoot significantly affects the size of the helium core at the end of the MS . This also determines the size and the luminosity of a massive star at the end of core-hydrogen burning [e.g 128, 108], and the extent of the subsequent rapid radial expansion, when the star is crossing the Hertzsprung gap [see e.g. Fig. 4 in

219]. As the mass of the BHs is sensitively dependent on the mass of the helium core of the progenitor star (this is especially true for mass exchanging binaries, where envelope stripping in unavoidable), convective overshooting also plays an essential role in shaping the BH mass spectrum. In detailed massive star evolutionary models, convective overshoot is typically modelled by assuming that the extent of the affected region is $\alpha_{\mathrm{OV}} H_p$, where α_{OV} referred to as the convective overshooting parameter. Similarly to α_{MLT}, α_{OV} is also assumed to be independent of the parameters of massive stars [which is probably incorrect, see e.g. 289, 58]. For studies involving massive star evolution, an $\alpha_{\mathrm{OV}} = 0.335$ is typically assumed, which is based on the calibration of [46] to the observations of the VLT-FLAMES survey of massive stars [86].

3. **Semiconvection**: Semiconvection occurs in regions, which are stable to convection according to the Ledoux criterion, but not according to the Schwarzschild criterion [see e.g. 157, 190]. In these regions, a vibrational instability develops that triggers mixing, which occurs on a timescale that is slower than thermal timescale, but faster than than nuclear timescale of the star. Consequently, the effect of semiconvection is most important for stars that have already evolved off MS [187]. Semiconvection is typically modelled as a time-dependent diffusive process, in which the efficiency of the mixing is (α_{SC}) is treated as a free parameter [189]. This parameter is poorly constrained, and it sensitively affects the structure of evolved massive stars. In particular, more efficient semiconvective mixing (that is higher α_{SC}) leads to more blue supergiants and less red supergiants. Therefore accurate models of semiconvection could be indispensable for solving the red supergiant problem [e.g. 188, 128, 64, 173, 108]. Recent observational studies suggest a rather high semiconvective mixing efficiency for the massive stars found in the Small Magellanic Cloud [$\alpha_{\mathrm{SC}} \approx 100$, see 313], though how this parameter depends on stellar parameters, evolutionary stage and metallicity remains inconclusive.

4. **Rotation and angular momentum transport**: A sizeable fraction of massive stars are rapid rotators [284]. Rotation alters the structure and the evolution of massive stars in several ways. Firstly, stars become deformed and oblate due to rotation. As a result, the assumption of spherical symmetry assumed in equation 1.1-1.5 become invalid. In 1D stellar modelling, it is common to include only the spherical symmetrical terms of the centrifugal force, which is a good approximation for rotation far below the critical rotational rate [343, 208]. However, nearly critically rotating stars are common among accretors in binary systems [e.g. 404]. Furthermore, a rare subset of massive binaries, composed of extremely rapidly rotating stars could be important for the formation of GW sources (i.e. the so-called chemically homogeneous evolution channel, see and Chapter 2). Therefore, it is important to understand the evolution of stars that are deformed due to rapid rotation. Secondly, rotation leads to gravity darkening, which means that the flux is reduced near the equator and enhanced near the poles. This is a direct consequence of the von-Zeipel theorem [412]. Finally, rotation causes a number of different processes and instabilities that causes angular momentum transport and mixing in the stellar interior [e.g. 187]. Most 1D stellar models, assume shelluar rotation (shells are defined by isobars rotate with a given rotational velocity) and treat the mixing process as a diffusion process [see second term on the right hand side of equation 1.5, and also see 84, 271, 125]. Since several different mechanism are responsible for rotational mixing, the diffusion of each process has to be calibrated separately based on observations, which constitutes a major challenge and therefore rotational mixing and its effect on stellar evolution remains an important uncertainty for massive star evolution.

Stellar winds are also commonly noted as one of the biggest uncertainties in modelling massive star evolution. We discuss this in in the next section.

1.1.3 Stellar winds

Stellar wind is a continuous outflow from the outer regions of a star. Typical associated mass loss rates of (hot) massive stars are in the order of $\dot{M}_{\mathrm{wind}} \approx 10^{-6}$-$10^{-5}\ M_{\odot}\mathrm{yr}^{-1}$ or even possibly higher. These are several orders of magnitude higher than for hot low- and intermediate-mass stars (e.g. mass loss rate of Sun is about $\approx 10^{-14}\ M_{\odot}\mathrm{yr}^{-1}$). Stellar winds of massive stars can therefore lead to severe mass losses already on the MS and they need to be taken into account for accurate evolutionary models.

Stellar winds of massive stars are powered by radiation. The high energy photons leaving the photosphere transfer their momentum to the stellar matter via line-scattering, which is then accelerated beyond the escape velocity of the star. These so-called line-driven stellar winds are unique to massive stars, while winds of low- and intermediate mass stars are typically either thermal- or dust-driven. The reason why line-driven stellar winds are only relevant for massive stars is because of the extremely high luminosities and hot effective temperatures that these objects exhibit (see again Fig. 1.1). Firstly, the typical momenta of photons emerging from the photosphere of a massive star (given by L/c) is significant, as opposed to those of low- and intermediate-mass stars. Secondly, the high momenta of these photons can be transferred very efficiently to the ions in the stellar atmosphere via line-scattering of metals due to the typical frequencies of these photons. For example, the opacity of a resonance line of C IV at 1550 Å is about a factor 10^6 stronger than the opacity of electron scattering. The majority of the scattering lines are found in the UV range in which bulk of the radiation of massive stars are emitted.

The most efficient stellar wind drivers are C, N, O, Ne, Si or Fe. H and He are typically completely ionised in the atmosphere of massive stars and furthermore these elements do not posses strong lines at frequencies that correspond to the

photons emitted by massive stars. Consequently, mass-loss rates of line-driven winds are a strong function of metallicity. For O stars a scaling-factor of $\dot{M} \propto Z^{0.69}$ is predicted [376], while for Wolf-Rayet stars the same is $\dot{M} \propto Z^{0.86}$ [374]. Although, the actual relations are considered highly uncertain, [e.g. compare with 182, 33, 373].

Outflow with significant mass loss will only develop, if the momentum that is transferred from the photons to the metal ions is shared with all the other constituents in the stellar atmosphere. This occurs, if the ions are slowed down efficiently by the plasma as a result of Coulomb interactions. Such a condition is always met for O/B stars.

A very important feature of line-driven stellar winds is that once a steady-state has been reached, the stellar atmosphere is dynamic, that is, it has a non-zero velocity gradient. Consequently, from the comoving frame of the atmosphere, the photons that emerge from the photosphere are redshifted due to Doppler effect. This means that a much larger, continuous range of photons can interact with the stellar matter via line-scattering. This feature makes line-driven winds particularly efficient and without this effect, the photons that can interact via line scattering would be already saturated in the lower regions of the stellar atmosphere and high intensity outflows could never develop.

There are two major ways to obtain models that predict mass loss rates of a massive star: (i) deriving empirical formulaes based on observations [e.g. 285, 248, 363, 115] and (ii) determining mass-loss recipes theoretically via semi-analytical or computational methods using (detailed) stellar atmosphere models. Both methods are riddled with uncertainties. In case of observations, the derived mass loss rates are sensitively dependent on the inhomogeneities in the stellar winds (i.e. clumping), which are very difficult to determine [98]. We explain the difficulties in the computational method below.

Mass loss rates can be determined by finding a solution for the following two equations below:

$$v\frac{dv}{dr} = -\frac{GM_*}{r^2} - \frac{1}{\rho}\frac{dp}{dr} + g_L + g_{es}, \qquad (1.6)$$

$$\dot{M} = 4\pi r^2 v(r)\rho(r). \qquad (1.7)$$

Equation 1.6 is the momentum equation for a dynamical atmosphere, where v is the velocity of the outflowing gas and it is dependent on the radial coordinate r, M_* is the mass of the star, g_L and g_{es} are the radiative acceleration due to line scattering and electron scattering, respectively. Equation 1.7 follows from mass conservation and it relates the mass-loss rate to the velocity profile. If one finds $v(r)$ by integrating equation 1.6, then the mass-loss rate can be determined via 1.7.

However, this task is computationally very challenging. Firstly, a major complication arises due to the dynamical stellar atmosphere. The radiative acceleration due to line-scattering (g_L) is dependent on the velocity profile. This is because the velocity profile determines by how much photons are redshifted in the frame of the outflow at a given radial distance and therefore it also determines the rate of photons that interact with a given scattering line associated with a certain frequency. This complexity introduces a non-linearity in equation 1.6; the radiative acceleration determines the velocity field, but at the same time the velocity field has a profound effect on the radiative acceleration as well. Therefore, solutions typically can only be found iteratively.

Secondly, scattering lines typically have a broadened profile due to random thermal and turbulent motions. This means that there is a range of radial coordinates at

which interaction between a photon with a given energy and a scattering line with a given frequency is possible, typically called *interaction region*. The implication is that in order to determine the optical depth at a given radial coordinate, *only* due to one specific scattering line and photons with a specific particular rest-frame frequency will already involve solving a spatial integral that requires the knowledge of the ionisation, density and velocity structure over the entire interaction length. Consequently, it is computationally a very expensive task to determine the optical depth to all line scattering and considering all the photons that emerge from the photosphere.

If the velocity gradient is very steep or the absorption profile is very narrow, then the interaction region becomes very short. In such cases, it is valid to approximate the absorption profile with a delta function, in which case the interaction region reduces to a point, and therefore the optical depth can be determined solely based on local quantities. This is called the Sobolev's approximation [327].

Finally, in order to know the ionization states of each chemical species at a given radial coordinate, a detailed model of the stellar atmosphere is required. However, assumption of local thermodynamic equilibrium, that is usually assumed in the interior of stars is no longer valid due to low densities, intense radiation and supersonic velocity fields. Determining the radiative transfer in such environments poses significant challenges.

One of the first successful attempts to find mass loss rates of line-driven winds using semi-analytical methods was from [49], commonly referred to as *CAK solution*. In this study a number of simplifying assumptions were made: i) local thermodynamic equilibrium was assumed, ii) Sobolev approximation was used to calculate the optical depth, iii) the flux-weighted number distribution of scattering line was assumed to follow a power law in the line opacity, iv) the star (i.e. source of the

photons) is modelled as a point source, v) only a limited number of scattering lines were taken into account, and vi) it was assumed that a photon can only be scattered once. The CAK predicted supersonic velocities and mass-loss rates that are dependent on stellar mass, luminosity and Eddington factor, with values that were broadly in agreement with the observations (though the predicted rates somewhat underestimated the observations). It also showed that there exists a one-to-one relationship between the modified wind momentum (i.e. $D_{\mathrm{mom}} = 1/2\dot{M}v_\infty R^{1/2}$) and the luminosity. This relation helped to derive an empirical mass-loss metallicity relation based on observations in the Small and Large Magellanic Clouds [237].

An alternative approach involves Monte Carlo simulations of photons emitted from the photoshphere and following their scattering history the stellar atmosphere [1]. The mass-loss rate then can be obtained from global energy conversation, that is $1/2\dot{M}(v_\infty^2 + v_{\mathrm{esc}}^2) = \Delta(L)$, where $\Delta(L)$ is to total amount of energy that is transferred from the photons to the scattering ions per unit time, and it can be directly obtained from the Monte Carlo simulations. This method therefore requires to assume a velocity profile beforehand (and therefore does not provide a self-consistent solution to equations 1.6 and 1.7).

Perhaps, one of the most commonly used mass-loss recipe of hot massive stars were determined this way [e.g. 375, 376]. The predicted mass loss rates roughly have the following scaling:

$$\dot{M} \sim L^{2.2} M_*^{-1.2} T_{\mathrm{eff}} \left(\frac{v_\infty}{v_{\mathrm{esc}}} \right)^{-1.3}, \tag{1.8}$$

where L is the luminosity of the star, T_{eff} is the effective temperature and v_{esc} is the escape and v_∞ is the terminal velocity of the outflowing gass. The predicted mass-loss rates from this prescription are in a better agreement than that of [49], which demonstrated that multiple scattering is important and needs to be taken into

account. An important feature of the mass-loss recipe of [376] was the prediction of the so-called bi-stability jump. While mass-loss rates typically decrease, as the star is evolving to cooler effective temperatures, roughly a factor of five increase is predicted near $T_{\mathrm{eff}} \approx 30kK$. This is due to the recombination of Fe III, which provides strong scattering lines.

Recent measurements of stellar winds have demonstrated that clumping is significant and ignoring it can overestimate the derived mass-loss rates [see e.g. 98]. Furthermore, in the last few years, improved theoretical calculations of mass-loss rates, which self-consistently solve the momentum equation and do not use the Sobolev approximaton, determined mass loss rates that are about a factor of three lower than predicted by [376].

1.1.4 Evolution of massive stars

In this section, we describe how single massive stars evolve from zero-age main sequence until the onset of core-collapse. We mostly follow the evolutionary predictions from [276, 138, 162].

In Fig. 1.1, we show the stellar tracks in HR diagram of a few massive stars at Z = 0.02. The starting point of these tracks is the onset of core hydrogen burning, i.e. the zero-age main sequence, shown by a green circle in Fig. 1.1. At this point, the stars are nearly homogeneous in composition.

The dominant energy production of massive stars on MS is via the CNO cycle. The energy production rate for this reaction is extremely sensitive on the temperature, i.e. $\epsilon_{\mathrm{nuc}} \sim T^{18}$. Consequently, the the radial distribution of ϵ_{nuc} in the core is centrally peaked, which results in a very steep temperature gradient ∇, leading to

convection in the core of massive stars. On the other hand, the envelopes of massive stars are radiative, as opposed to those of stars with $M_{\mathrm{ZAMS}} \lesssim 1.2\,M_\odot$. This is because temperatures in the envelopes of massive stars are significantly higher compared to those of low mass stars, and consequently the opacities are lower as well, which has a stabilising effect against convection [e.g. 162].

During the MS phase, which for massive stars lasts for a few Myrs, the luminosity of the star gradually increases. This latter property is generally true for all stars, and can be understood by considering that i) the mean atomic weight increases as hydrogen is burnt into helium and that ii) homology relations of stars imply $L \sim \mu^4 M^3$ [e.g. 162]. Additionally, Fig. 1.1 shows that the increase in luminosity on MS becomes more modest with increasing M_{ZAMS} for massive stars. This is because mass loss rates due to stellar winds increase with increasing mass. In particular for $M_{\mathrm{ZAMS}} \gtrsim 30\,M_\odot$, the mass loss rates on MS become so severe, that the temperatures drop in the centre of the star, leading to a smaller core, in which hydrogen fusion takes place. Therefore there are two opposing effects for the evolution of luminosity of massive stars on the MS; the increase in mean molecular weight, which increases and the mass loss which decreases luminosity [e.g. 162].

Massive stars experience a relatively significant expansion in radius on MS (i.e. about a factor of five) when compared to lower mass stars which is about a factor of two, at most. When the core becomes depleted of hydrogen, energy generation halts, which results in contraction of the star (see the hook feature near before the inverse triangle in Fig. 1.1). The contraction stops, when the temperature near the core sufficiently increases such that hydrogen ignites in a shell around the helium core (shown by the inverted triangle in Fig. 1.1). As the helium core is above the Schonberg-Chandrasekhar limit, the star cannot be in thermal equilibrium and it will rapidly expand in radius, with approximately constant luminosity until the onset of core-helium burning (shown by the hexagone in Fig. 1.1). This phase is

very short (10^4 years) and therefore, it is extremely difficult to observe such stars. Because of this, the area in the HR diagram which is between the terminal-age main sequence stars and red (super)giant stars is called Hertzsprung gap. In this thesis, these thermally unstable, hydrogen shell burning massive stars will be refereed to as *stars crossing the Hertzsprung gap* or simply as *Hertzspring gap stars* [e.g. 162].

Helium ignites in a non-degenerate core via the triple-α process, when the core temperature reaches $T_c \sim 10^8\, K$. Massive stars with $M_{\mathrm{ZAMS}} \lesssim 10\text{-}12\, M_\odot$ exhibit the blue loop during their core-helium burning phase. Stars more massive than that, on the other hand, monotonically expand in this phase, unless they lose their hydrogen-rich envelopes due to stellar winds. In this thesis, we are interested in such stars, as we study BH progenitors (e.g. stars with $M_{\mathrm{ZAMS}} \gtrsim 20\, M_\odot$). When massive stars reach sufficiently low effective temperatures [$\log T_{\mathrm{eff}} \approx 3.73\, K$ or lower, see 167], they might develop deep convective envelopes, since the opacities in the outer layers become sufficiently high. Whether this occurs at all for the most massive stars and how it depends on metallicity remains uncertain [e.g. 167].

At Z = 0.02, stars with $M_{\mathrm{ZAMS}} \gtrsim 30\, M_\odot$ lose their hydrogen envelope due to stellar winds after the onset of core-helium burning. In the stellar models shown in Fig. 1.1, this occurs due to LBV winds [137, 325], if $M_{\mathrm{ZAMS}} \gtrsim 40\, M_\odot$ (since these stars cross the Humphreys-Davidson limit) and due to dust-driven winds, if $M_{\mathrm{ZAMS}} \lesssim 40\, M_\odot$.

When the core temperature reaches $T_c \sim 5 \cdot 10^8\, K$, carbon is ignited non-degenerately. From this stage, energy losses from neutrinos become increasingly important. After carbon ignition, stars undergo several subsequent and gradually shorter nuclear fusion phases (i.e. O, Ne, Si burning), until a Fe-Ni core is developed. When this state is reached, no more energy can be generated and the core will collapse and a BH or a neutron star will be formed, depending on the mass of

Table 1.1: A summary of different nucelar fusion processes in the core of a 25 $M_\odot$ star. Table adopted from [386]

Nucler fuel	T_c (K)	ρ_c (g/cm^3)	$t_{burning}$
H	$3.8 \cdot 10^7$	3.8	6.7 Myr
He	$2.0 \cdot 10^8$	$0.8 \cdot 10^3$	0.8 Myr
C	$8.4 \cdot 10^8$	$1.3 \cdot 10^5$	0.5 kyr
Ne	$1.6 \cdot 10^9$	$3.9 \cdot 10^6$	0.9 yr
O	$2.1 \cdot 10^9$	$3.6 \cdot 10^6$	0.4 yr
Si	$3.4 \cdot 10^9$	$3.0 \cdot 10^7$	0.7 d

the collapsing CO core. The numerous core and shell burning phases lead to the formation of an "onion structure" in the core of a massive star. This is shown in Fig. 1.3. The core comprises concentric shells, which consist of heavier nuclei as one moves from the envelope towards the centre [e.g. 162].

We finally note that metallicity significantly affects the evolution of massive stars [e.g. 187, 168]. Generally, at lower metallicities, stars are more compact and hotter (this is partially because of the lower mass fraction of C,N,O but also due to the lower opacities). Mass loss rates are also lower, which leads to more massive He core and more massive remnants [e.g. 376]. Finally, the ignition of helium in the core generally occurs at a higher effective temperature, which is then followed by a more significant expansion in stellar radius [see e.g. 219].

1.1.5 Death of massive stars

Core-collapse occurs when the iron core reaches a critical mass (due to Si shell burning) above which it can no longer support its own weight. During the core collapse, the density rapidly increases, which sets in two important instabilities: electron capture and photo-disintegration. In the former, free electrons are captured by heavy, β-unstable nuclei which produces a neutron rich nuclei and more importantly re-
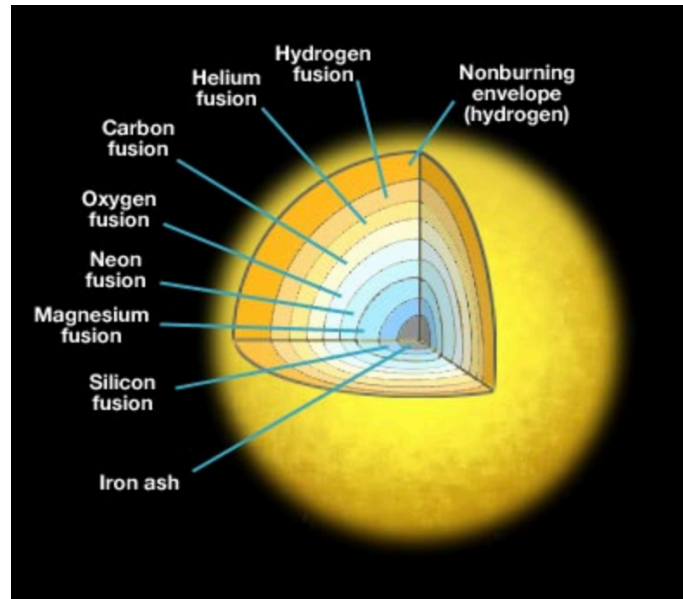
Figure 1.3: A typical onion structure of massive stars near the onset of core-collapse. This schematic drawing contains simplifications, as in reality different shells can have more complex structures and abundance profiles due to mixing due to convection and off-centre burning. Credit: Penn State Astronomy & Astrophysics, `https://www.e-education.psu.edu/astro801/content/l6_p5.html`

moves electron pressure. Photodisintegration sets in at temperatures $T \sim 10^{10}\,K$. In this case, photons become energetic to break up heavy nuclei (such as iron) into lighter ones. This process absorbs energy and therefore reduces the thermal energy of the core. Due to these two instabilities, core-collapse is significantly accelerated and practically proceeds as free-fall. In about one second, the radius of the core decreases from that of a white dwarf (comparable to size of Earth) to just ~ 50 km [e.g. 162].

Two important events occur during this dramatic collapse. First, when densities reach $\rho \approx 10^{12}$g/cm^3, neutrinos produced by electron capture and β-decays become trapped. Second, when $\rho \approx 8 \cdot 10^{14}$g/cm^3, the densities become comparable with that of an atomic nucleus and the strong interactions between nucleons becomes repulsive and additionally neutron degeneracy pressure sets in. This halts the collapse and the nuclear matter bounces back and triggers a shockwave travelling outwards. This shock is, however, not sufficient enough to power the SN explosion, as it stalls

before it could reach the surface of the star. This is because the energy of the shock is lost as a result its interaction with the infalling outer core due to two processes. First, photodisintegration of iron occurs in the infalling outer core as it is heated up by the shockwave. Second, after the change in the composition due to the photodisintegration, electron capture processes create energetic neutrinos behind the shockwave, which carry away a large fraction of the energy from the core-collapse (especially in relatively low density outer regions, i.e. $\rho \lesssim 10^{12} \mathrm{g/cm^3}$, where these neutrinos can easily escape without any interaction). Yet, SN explosions caused by the core-collapse of massive stars are regularly observed (of which the closest and perhaps the most well studied was the SN1987A in the Large Magellanic Cloud). What is the exact process that revives the shock that makes SN explosions possible is still a matter of debate [162].

The dominant theory is that the shock is revived via the neutrinos [see e.g 154]. This could be plausible, because a significant portion of the core reaches densities of $\rho \gtrsim 10^{12} \mathrm{g/cm^3}$, at which the mean free path of neutrinos becomes smaller than the characteristic size of the core and can only escape after numerous scattering events. Therefore, at such high densities, neutrinos can transfer energy to the core and could possibly play an essential role in reviving the shock.

However, complex hydrodynamical simulations suggest, that various instabilities in the core (e.g. convective, Rayleigh–Taylor, standing accretion shock or magnetohydrodynamic instabilities) could be required to sufficiently boost the neutrino luminosity for a successful shock revival for stars more massive than $M_{\mathrm{ZAMS}} \approx 9\,M_{\odot}$. Many of these instabilities are asymmetric and lead to asymmetric explosions, which is supported by the observed, high velocities of radio pulsars [see e.g. 131, 365, 145]. Asymmetry also means that modelling these processes require 2D or 3D hydrodynamical simulations. 3D hydrodynamical simulations that include all the relevant physics for a supernova explosions (e.g. general relativity, neutrino energy transport

etc.) are computationally extremely expensive, therefore most studies need to make numerous simplifying assumptions. Consequently, understanding the process behind shock revival is still an active area research. Without understanding how the core collapse occurs in detail, a number of very important questions remain unanswered [e.g. 154]:

1. How the remnant mass of compact object depends on the initial mass (M_{ZAMS})?

2. What is the minimum M_{ZAMS} for BH progenitors?

3. Which stars explode as SN and which stars collapse directly?

4. What is the natal kick velocity distribution of neutron stars, BHs and how does the natal kick depend on the core mass?

In binary evolutionary codes, the core-collapse prescription of [97] is commonly used. These prescriptions predict the remnant mass and the ejected mass as a function of CO core mass and metallicity. In this study, two different supernova engines were adopted, all based on convection-enhanced neutrino-driven paradigm, but with a difference in how much time after the core bounce the revival explosion occurs in the convective region. In the *Rapid model*, the shock reviving explosion occurs 250 ms after the core bounce, while in the *Delayed model* this occurs much later and it is more consistent with the scenario where standing accretion shock instability revives the shock. The initial mass - remnant mass relation based on these two SN engines is shown in Fig. 1.4. Note that the results shown in this figure are also dependent on the stellar wind models adopted. The Rapid model produces a mass gap of BHs between 2-5 $M_{\odot}$ (consistent with studies of BH distribution in the galaxy [89], but most likely not consistent with recent GW detections [9]), while the Delayed model yields a continuous BH mass distribution. Stars with $M_{\mathrm{ZAMS}} \gtrsim$ 18-20 $M_{\odot}$ form BHs. stars with $M_{\mathrm{ZAMS}} \gtrsim 40\,M_{\odot}$ form BH with direct collapse (therefore no SN explosion
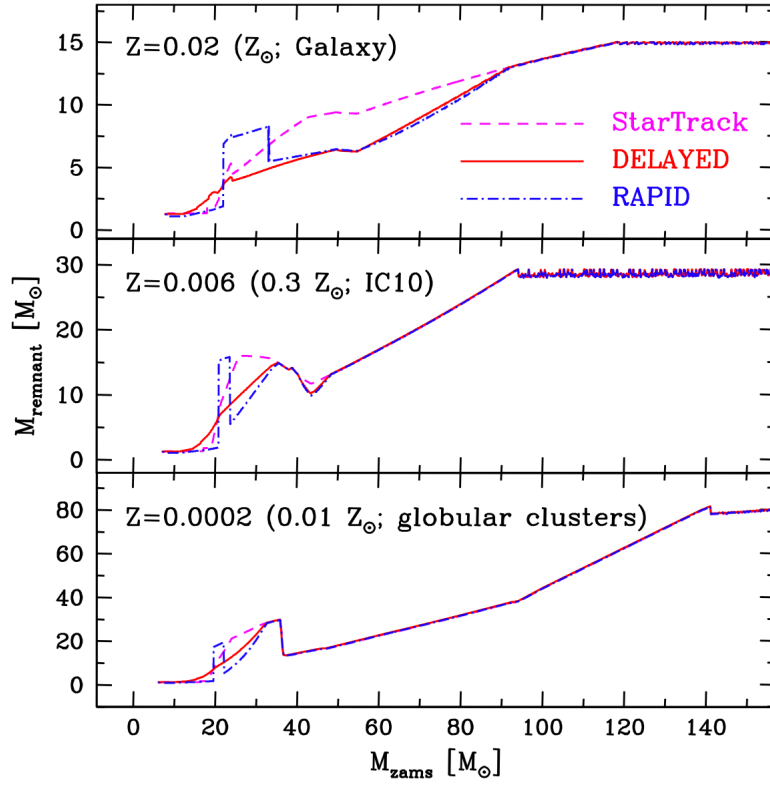
Figure 1.4: The zero-age main sequence - remnant mass relation as predicted by the supernova model of [97]. Note that the remnant masses, especially at higher metallicities are also affected by stellar winds. Figure adopted [97].

occurs), while for stars with $20\,M_\odot \lesssim M_{\rm ZAMS} \lesssim 40\,M_\odot$, some fraction of the mass is decelerated after the shock revival and falls back and gets accreted by the newly formed BH. This fallback fraction increases with increasing $M_{\rm ZAMS}$.

Predictions for remnant mass spectra, minimum $M_{\rm zams}$ for BHs and for the fraction successfully ejected mass can be significantly different, based on how the SN is modelled. In particular [212] based on the semi-analytical models of [241] predicts probabilistic recipes due to the intrinsic stochasticity of stellar evolution (e.g. due to rotation), i.e. there is a range of $M_{\rm ZAMS}$ at which both NS and BH could be formed.

1.2   Multiple systems among massive stars

Interactions in multiple system can significantly alter the evolution of stars. For sufficiently short period binaries, this can occur, for example via mass exchange, tidal interactions or via GWs. In hierarchical triples, three-body dynamics might facilitate mass transfer episodes, stellar mergers via von Zeipel-Lidov-Kozai oscillations (ZLK oscillations) or by triggering transitions to dynamically unstable configurations [354]. As explained in the following sections, these processes play a key role in the formation of several very important astrophysical phenomena (including the main topic of this thesis; GW sources). Therefore, it is extremely important to understand how common multiple systems are, what their birth properties are and how often stellar interactions take place in such systems. Thus, we need observational surveys that infer the primordial demographics of multiple systems, such as multiplicity fractions, distributions of period, eccentricity, mass and mass ratio. In the last decade, spectroscopic and long baseline interferometric observations of young, open star cluster and associations have unveiled these properties [e.g. 170, 171, 76, 303, 305]. In the following, we summarise the results of these observational campaigns, though we will mostly focus on [303], as this study have provided the most complete results in terms of orbital solutions of close massive binaries. The observational results of [170, 171, 76] are consistent with that of [303].

About half of the stars are found in binaries or higher order hierarchies [74]. However, the multiplicity fraction and generally the birth properties of multiple system sensitively depend on the mass of the primary star [235]. This is illustrated in the upper panel of Fig. 1.5, which is from [235], based on the compilation of different observational studies. While single star systems dominate among solar-type stars, this is clearly not the case for massive stars. About 90 per cent of the BH progenitors ($M_{\rm ZAMS} \gtrsim 20\,M_\odot$) are found in multiple stellar systems according

to [235]. The majority of O/B stars (i.e. massive stars) are in found in hierarchical triples or higher order hierarchies. [303] finds a binary fraction of $f_{\text{binary}} = 0.69 \pm 0.09$ for O stars[4] The inferred period distribution reveals that high mass stars tend to be in short-period binaries:

$$f_p(\log p) \propto (\log p)^\pi, \qquad \text{for } \log p \in [0.15, 5.5], \tag{1.9}$$

where p is the period of the binary system, f_p is the period distribution and $\pi = -0.55$ [for comparison: the period distribution of lower mass stars is more consistent with Opik's law, that is $\pi = 0$, see 253]. This is a remarkable result, which implies that about 70 per cent of massive binaries are predicted to engage in a mass transfer phase at some point in their evolution (see lower panel of Fig. 1.5). Clearly, it is not possible to understand the evolution of massive stars without understanding mass transfer episodes.

[303] finds a mass ratio distribution that is nearly uniform: $f_q(q) \sim q^\kappa$, where $q = M_2/M_1$ on an interval of [0.1,1] and $\kappa = -0.1 \pm 0.6$, an eccentricity distribution with $f_e(e) \sim e^\eta$ on an interval of [0,0.9] with $\eta = -0.42 \pm 0.17$, and a primary mass distribution that is consistent with the observations of [176].

Unfortunately, similar reliable predictions do not exist yet for the demographics of the outer binaries of hierarchical triples. Therefore, it is currently challenging to determine what fraction of triples are affected by three-body dynamics. However, in the context of solar-type stars, [351, 350] showed, that the distributions of the inner and outer binary in hierarchical triples tend to be the same. If similar principles hold for massive triples, then we should expect that three-body dynamics lead to an increased rate of interactions in the inner binary [see e.g 184].

---

[4][303] does not investigate whether these binary systems are a part of a higher-order hierarchical system. Therefore, this binary fraction could be interpreted as a multiplicity fraction (i.e. fraction of non-single systems).
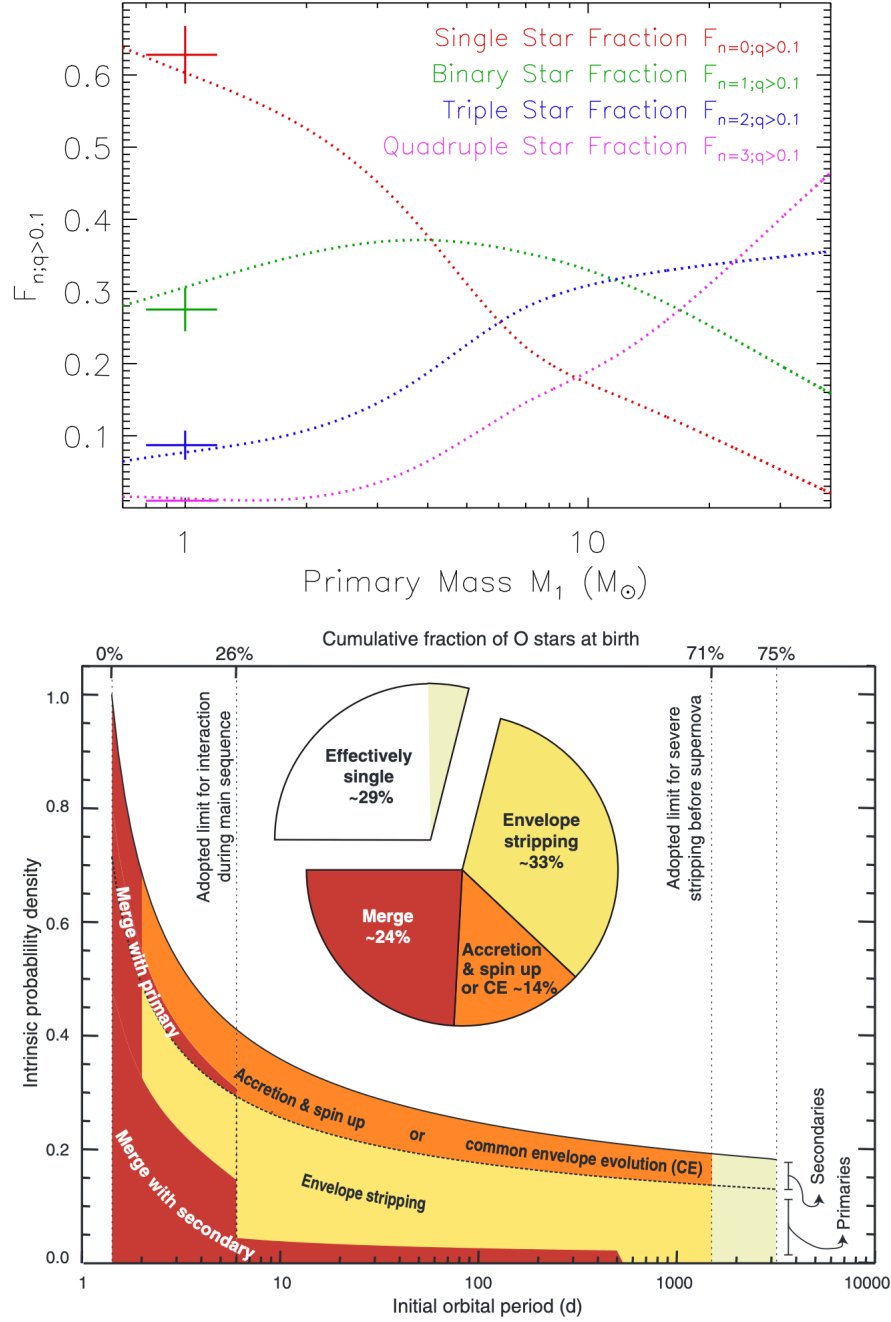
Figure 1.5: Upper panel (from [235]): multiplicity fractions as a function of the primary mass in the stellar system . Lower panel (from [303]): The initial period distribution and the corresponding predicted evolutionary outcome for massive stars.

1.2.1   Physics of binary interactions: Roche pontential

Since we are interested in the long-term evolution of massive binaries and possible binary interactions, we do not need to consider the instantaneous positions of the stars in the binary system. Instead, we need to determine the orbital evolution in terms of semimajor axis and eccentricity. We use these two parameters (along with parameters of the stars) to assess when binary interactions will take place.

In order to achieve this, it is convenient to adopt the use of the Roche-potential, which is the effective gravitational potential of a binary system derived under three assumptions. First, the components of the binaries are treated as point masses. Second, the orbital frequency of the binary is assumed to be synchronised with the rotational frequencies of the stars. Third, the orbit is assumed to be circular. In this case the potential can be given as [see e.g. 79]:

$$\Phi = -\frac{GM_1}{[x^2 + y^2 + z^2]^{1/2}} - \frac{GM_2}{[(x-a)^2 + y^2 + z^2]^{1/2}} - \frac{1}{2}\Omega_{\rm orb}^2 \left[(x - \mu a)^2 + y^2\right] \quad (1.10)$$

This is defined in a coordinate system, which is co-rotating with the binary. The origin of the coordinate system is placed at centre of the primary star, a is the binary separation, $\mu = M_2/(M_1 + M_2)$ and $\Omega_{\rm orb}$ is the rotational angular frequency of the binary and G is the gravitational constant.

A useful fitting formula for the volume equivalent Roche-lobe radius is found by [78]

$$R_{\rm L1} \approx \frac{0.49 q^{2/3} a}{0.6 q^{2/3} + \ln(1 + q^{1/3})} \approx 0.44 a \frac{q^{0.33}}{(1 + q)^{0.2}} \quad (1.11)$$

where the mass ratio $q = m_1/m_2$. In the last equation the first relation is accurate within 1%. The second relation only holds for $0.1 \le q \le 10$. This means that we
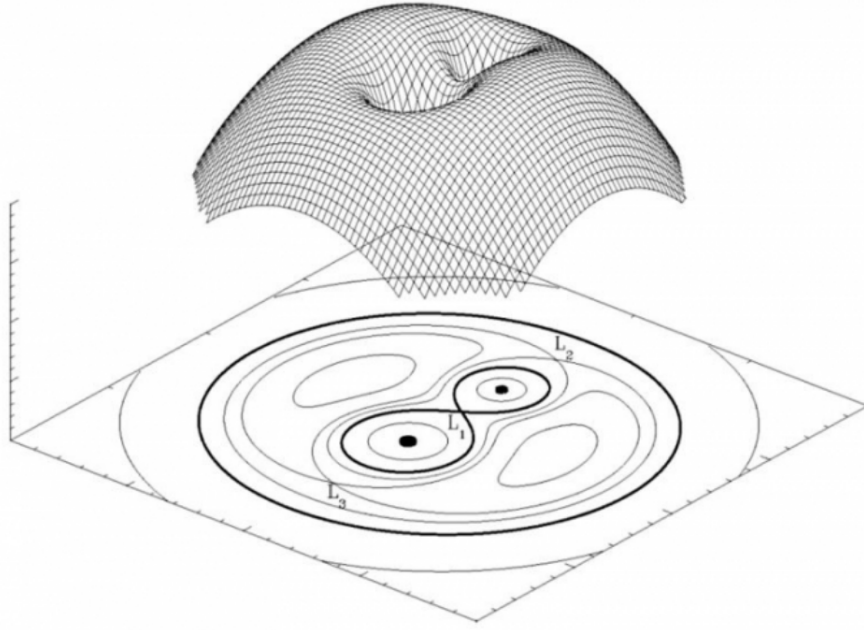
Figure 1.6: A schematic depiction of the the Roche potential for a binary system $q = M_1/M_2 = 2$. Figure adopted [280]

assume Roche-lobe overflow (i.e. onset of mass transfer phase) when the star radius becomes larger than R_{L1}.

1.2.2   Mass transfer in binaries

Stars in binaries may lose mass via stellar winds or via Roche-lobe overflow. Both cases change the total angular momentum of the binary (even if the mass transfer phase is fully conservative) and therefore these processes also change the period of the binary. In particular, mass transfer episode plays a key role for the formation of many well-known astrophysical systems, such as cataclysmic variable stars, Type Ia supernova, Algol binaries, X-ray binaries, Be stars, Wolf-Rayet - O/B binaries, milisecond pulsars etc. Mass transfer episodes are also essential for the formation of compact binary mergers from isolated systems and for gamma ray bursts [see e.g. 187, 252].

In the following subsections, we summarise the formalism that is typically used in (detailed and rapid) binary evolution codes to model mass transfer episodes. In subsection 1.2.8, we describe how the the semimajor axis changes due to a unit of mass transferred to the accretor. This results in a differential equation for a, which is parameterised in terms of mass transfer efficiency β and a parameter expressing the angular momentum carried away from the expelled matter, in case of non-conservative mass transfer episodes, γ. In subsection 1.2.4, we discuss the uncertainties regarding β and γ. In order to determine the long-term orbital evolution of the binary, one also needs to know the radial response of the donor star due to mass loss (which determines the stability of the mass transfer phase). We discuss this in subsection 2.3.3. The final ingredient needed to model mass transfer events is the mass transfer rate. We summarise common mass transfer schemes used in binary evolution codes (including the ones used in this thesis) in subsection 1.2.6. We discuss the orbital evolution due to dynamically unstable mass transfers and wind mass loss in seperate sections, 1.1.3 and 1.2.7, respectively.

1.2.3 How the orbital separation changes due to mass loss from the donor star

In the following subsection, we closely follow the formalism presented in [326] and [252]. The total angular momentum of a binary is:

$$J^2 = G \frac{M_{\text{donor}}^2 M_{\text{accretor}}^2}{M_{\text{donor}} + M_{\text{accretor}}} a(1 - e^2), \tag{1.12}$$

where M_{donor} is mass of the donor (or mass-losing) star, M_{accretor} is the mass of the accretor star, a is the semimajor axis and e is the eccentricity. Differentiating equation 1.12, one can describe how the semimajor axis changes due to mass loss

from one of the stars in the binary. For this, we only consider circular orbits, and introduce mass transfer efficiency, which is the fraction of mass accreted by the accretor star (i.e. $\beta = -\dot{M}_{\mathrm{accretor}}/\dot{M}_{\mathrm{donor}}$). Additionally, we also define the parameter γ:

$$\gamma = \left[\frac{J}{M_a + M_d}\right] \left[\frac{\dot{J}}{\dot{M}_a + \dot{M}_d}\right]^{-1}, \tag{1.13}$$

which is ratio of the specific angular momentum lost from the system and the specific angular momentum of the entire binary. In this case, the change in the semimajor axis can be given as:

$$\frac{\dot{a}}{a} = -2\frac{\dot{M}_{\mathrm{donor}}}{M_{\mathrm{donor}}}\left[1 - \beta\frac{M_{\mathrm{donor}}}{M_{\mathrm{accretor}}} - (1 - \beta)\left(\gamma + \frac{1}{2}\right)\frac{M_{\mathrm{donor}}}{M_{\mathrm{donor}} + M_{\mathrm{accretor}}}\right]. \tag{1.14}$$

Equation 1.14 then can be applied for various scenarios. For example, the change in the orbital separation due to a mass transfer episode, if γ can be assumed to be constant:

$$\frac{a}{a_i} = \left(\frac{M_{\mathrm{donor}}}{M_{\mathrm{donor,i}}}\frac{M_{\mathrm{accretor}}}{M_{\mathrm{accretor,i}}}\right)^{-2}\left(\frac{M_{\mathrm{tot}}}{M_{\mathrm{tot,i}}}\right)^{2\gamma+1}, \tag{1.15}$$

where the subscript 'i' refers to the initial state, that is the parameter at the onset of the mass transfer episode. M_{tot} is the total mass of the binary. A special case is a fully conservative mass transfer mode (i.e. $\beta = 1$ and $\gamma = 0$). In this case, equation 1.14 becomes $\dot{a}/a = 2\dot{M}_{\mathrm{donor}}/M_{\mathrm{donor}}(M_{\mathrm{donor}}/M_{\mathrm{accretor}}-1)$. Since $\dot{M}_{\mathrm{donor}} < 1$, then the orbit will shrink as long as $M_{\mathrm{donor}} > M_{\mathrm{accretor}}$ and will widen when $M_{\mathrm{donor}} < M_{\mathrm{accretor}}$.

Perhaps a more realistic scenario is to assume that the matter is ejected from near the accretor and therefore the specific angular momentum loss is that of the accretor, which implies $\gamma = M_{\mathrm{donor}}/M_{\mathrm{accretor}}$. This provides a reasonably realistic scenario for when an accretion disc is formed, but the accretor cannot accrete a

fraction of the matter, which is then removed from the binary system, carrying away a specific angular momentum that is equal to that of the accretor object. In this case:

$$\frac{a}{a_i} = \left(\frac{M_\mathrm{donor}}{M_\mathrm{donor,i}} \left[\frac{M_\mathrm{accretor}}{M_{\mathrm{accretor},i}} \right]^{1/\beta} \right)^{-2} \left(\frac{M_\mathrm{tot,i}}{M_\mathrm{tot}} \right) \tag{1.16}$$

A special case of the previous mass transfer mode is the so-called isotropical reemission. In this case, it is assumed that a negligible amount is accreted, i.e. $\beta \approx 0$. In this case, equation 1.14 becomes [e.g. 326, 410]:

$$\frac{a}{a_i} = \frac{M_\mathrm{tot,i}}{M_\mathrm{tot}} \left(\frac{M_\mathrm{donor,i}}{M_\mathrm{donor}} \right)^2 \exp \left(2 \frac{M_\mathrm{donor} - M_\mathrm{donor,i}}{M_\mathrm{accretor}} \right), \tag{1.17}$$

which shows that for sufficiently high mass ratio, a stable phase of mass transfer can significantly shrink the orbit in case of isotropical reemission. This can be used to model a stable mass transfer episode with BH accretor, in case of Eddington-limited accretion. If the mass transfer rate is high (e.g. proceeds on thermal timescale of the donor), then only a negligible amount of mass can be accreted by the BH, and the rest is expelled near from the accretor in a form of a jet [410]. In Chapter 2, we show this plays an important role for one of the predicted dominant formation channels of merging binary BHs.

1.2.4 Angular momentum loss and mass transfer efficiency

The mass transfer efficiency (β) and angular momentum loss (γ) for a stable mass transfer episode is highly uncertain [see e.g 187]. These two parameters are probably dependent on the parameters of the binary and evolve as the mass exchange proceeds. The stream from the donor star that hits the accretor transfers angular momentum

to the accretor. From this point of view, it is important whether an accretion disc is formed during the mass transfer process or if accretion occurs in a ballistic fashion. Based on the models of [201, 362], a fitting formula can be found, which states that an accretion disk is formed, if:

$$R_{\text{accretor}} \leq 0.0425a \left(\frac{M_{\text{accretor}}}{M_{\text{donor}}} + \frac{M_{\text{accretor}}^2}{M_{\text{donor}}^2} \right)^{1/4}, \tag{1.18}$$

where R_{accretor} is the radius of the accretor, and the term on the right-hand side of the inequality is R_{min}, which is the the closest approach of the incoming stream. The angular momentum of the stream reaching the accretor star is $\sqrt{GMR_{\text{accretor}}}$, if an accretion disc is formed, and $\sqrt{1.7GMR_{\text{min}}}$ if accretion occurs on a ballistic fashion [201].

[254] showed that during a mass transfer phase, an accretor spins up to critical rotation soon after the onset of the mass transfer phase, only after gaining a few percentage of its original mass. Whether accretion is possible above critical rotation is debated [277]. [187, 191] assumed that accretion ceases once the accretor star reaches critical rotation and any further transferred matter becomes expelled from the system (with a specific angular momentum that of the accretor). Under these assumptions, it was shown that the average β for an entire mass transfer episode is very low (typically ∼10 per cent), if the pre-mass-transfer orbit is relatively wide. This implies that the mass transfer phase is highly non-conservative, if donor star fills its Roche-lobe when crossing the Hertzsprung gap (so-called Case B mass transfer) or during core-helium burning (we refer to this type of mass transfer as Case C). For binaries with shorter orbit, where the donor star is still on MS (Case A), tides are sufficiently strong to counteract the spinning up, which leads to a more conservative mass transfer phases [see also 316]. These results are broadly consistent with the observed properties of WR systems and WR-O/B binaries [e.g 268, 258], however not with the Be X-ray binaries [e.g 370]. The radial response of the accretor star

could also affect the mass transfer efficiency. In particular, if the mass transfer rate is higher than the thermal timescale of the accretor star, then the mass gainer star is not able to regain thermal equilibrium during the mass transfer phase and swells up and might not be able to accrete further [see e.g. 275, 139, 293].

The angular momentum that is carried away also remains uncertain. It is commonly assumed that if the matter is expelled near from the accretor than it carries away a specific angular momentum of the accretor (corresponding to $\gamma = M_{\mathrm{donor}}/M_{\mathrm{accretor}}$). However, matter could also be expelled from any of the outer Langrange points and the corresponding mass loss rates could be significant, if the accretor star swells up or if the donor star overfills its Roche-lobe. The angular momentum loss associated with the outer Langrange point overflow is highly uncertain and could be significantly higher than $\gamma = M_{\mathrm{donor}}/M_{\mathrm{accretor}}$. It is not clear by how much tidal effects can modify the angular momentum of the matter leaving through the outer Langrange points and whether the matter can completely leave the binary system or will form a circumbinary disk, in which case it can exert a torque on the binary and further affect its orbital evolution [e.g. 321, 326, 262, 263, 219].

1.2.5 Donor star response and mass transfer stability

Mass transfer stability is typically assessed in terms of comparing the so-called mass-radius exponents [see e.g. 326, 358]:

$$\zeta_L = \frac{d\log R_L}{d\log M_{\mathrm{donor}}} \qquad \zeta_{\mathrm{ad}} = \left(\frac{d\log R_{\mathrm{donor}}}{d\log M_{\mathrm{donor}}}\right)_{\mathrm{ad}} \qquad \zeta_{\mathrm{th}} = \left(\frac{d\log R_{\mathrm{donor}}}{d\log M_{\mathrm{donor}}}\right)_{\mathrm{th}}, \quad (1.19)$$

where R_L is the Roche-lobe and it is given by equation 1.11 and R_{donor} is the radius of the donor. Therefore ζ_L describes how the Roche-lobe of the donor star changes with mass loss, while ζ_{ad} and ζ_{th} describe how the radius of the donor star changes

with mass loss on a dynamical and thermal timescale, respectively. When mass is removed from a star as a result of Roche-lobe overflow, the star needs to readjust its structure to regain its hydrostatic and thermal equilibrium. This occurs on a dynamical and thermal timescale, respectively. The mass-radius exponents ζ_{ad} and ζ_{th} then express the stellar radial response due to the readjustment on these two different timescales. If the radius of the donor decreases at a slower rate than the Roche-lobe is receding, then the mass transfer phase is unstable. Based on this rationale, we can distinguish three different mass transfer modes:

1. Stable mass transfer proceeding on nuclear timescale ($\zeta_L \leq \min(\zeta_{ad}, \zeta_{th})$). This typically occurs, if the mass of the donor star is lower than the accretor star, since in that case, the semimajor axis widens due to the mass transfer episode, and therefore typically $\zeta_L < 0$ (since the Roche-lobe is getting further away from the edge of the donor star). Stable mass transfer on nuclear timescale is typical for Algol binaries and low mass X-ray binaries.

2. Stable mass transfer proceeding on thermal timescale ($\zeta_{ad} \geq \zeta_L \geq \zeta_{th}$). The donor star is dynamically stable, but thermally unstable. In this mass transfer mode, the donor star will be within its Roche-lobe after it regains hydrostatic equilibrium, but will refill its Roche-lobe after it regains thermal equilibrium

3. Dynamically unstable mass transfer ($\zeta_L > \max(\zeta_{ad}, \zeta_{th})$). The mass transfer rate keeps increasing in an runaway fashion, and it leads to common envelope evolution (see section 1.2.7).

The adiabatic mass-radius exponent (ζ_{ad}) can be determined from detailed stellar models [see e.g 101, 260, 219]. Stars with deep convective envelopes are thought to have very low ζ_{ad} due to their entropy profiles as opposed to stars with radiatve envelopes. In some cases, giants with deep convective envelopes expand upon mass

loss, which implies that they have a negative ζ_{ad} [130], but see [383]. This means that such stars easily instigate dynamically unstable mass transfers.

1.2.6 Mass transfer rate

In order to solve the orbital evolution due to a mass transfer episode using equation 1.14, one needs to know the stellar structure response (previous subsection) and the mass transfer rate for each timestep. In principle, this is a very complicated process that would ideally require a 3D hydrodynamical simulation to obtain self-consistent results derived from first principles. This, however, remains computationally prohibitive, as the long-term orbital evolution during mass exchange is also governed by the stellar structure response of the donor and accretor star, which means that a large range of timescales are required for accurate modelling. Because of these challenges, most binary evolutionary codes, combine 1D stellar modelling with semi-analytical mass transfer schemes [see e.g. 174, 256, 101, 259, 219, 52]. In this subsection, we discuss how the mass transfer rate can be determined based on such simplified models.

The mass transfer-rate through the L1 point is: [294]:

$$\dot{M}_{L1} = \int \rho v dA, \tag{1.20}$$

where dA is a surface element of the plane perpendicular to the orbital radius vector, containing L1, v is the velocity at the L1 point.

Then equation 1.20 is solved with two important assumptions made, motivated by the results of a simplified hydrodynamical model of mass transfer of [201]: i) the flow is in a steady state and ii) the flow becomes sonic at the cross-section coinciding

with the L1 point. The first assumption means that Bernoulli's theorem applies:

$$\frac{1}{2}v_f^2 + \int_i^f \frac{dP}{\rho} + \Phi_f = \frac{1}{2}v_i^2 + \Phi_i \tag{1.21}$$

Furthermore, a distinction is typically made between optically thin and optically thick mass transfer episodes. The former occurs, when the photosphere of the star is still within its Roche-lobe, but some low density layers above the photosphere are not. This results in a isothermal flow. Then in equation 1.21, the starting point is chosen at the photosphere, where $v_i = 0$ and $\Phi_i = \Phi_{\mathrm{ph}}$ and at the final point, where $v_f = k_b T_{\mathrm{eff}}/\mu m_h$ (i.e. the thermal sound speed and k_b is the Boltzmann constant) and Φ_{L1}. Then the mass transfer rate becomes [294]:

$$\dot{M}_{\mathrm{L1}}^{\mathrm{thin}} = \frac{\rho_{\mathrm{ph}}}{e^{1/2}} \left(\frac{k_b T_{\mathrm{eff}}}{\mu m_h} \right)^{3/2} \left(\frac{dA}{d\Phi} \right)_{\mathrm{L1}} \exp\left(\frac{\Phi_{\mathrm{ph}} - \Phi_{\mathrm{L1}}}{k_b T_{\mathrm{eff}}/\mu m_h} \right) = \dot{M}_{\mathrm{L1,0}}^{\mathrm{thin}} \cdot \exp\left(\frac{\Phi_{\mathrm{ph}} - \Phi_{\mathrm{L1}}}{k_b T_{\mathrm{eff}}/\mu m_h} \right), \tag{1.22}$$

where ρ_{ph} and T_{eff}, i.e. density at photosphere and effective temperature, follows from the stellar model of the donor star, $(dA/d\Phi)_{\mathrm{L1}}$ and $\Phi_{\mathrm{ph}} - \Phi_{\mathrm{L1}}$ are essentially geometrical terms for the Roche potential and approximative solutions can be found in [e.g 153, 219].

Optically thin mass transfer episodes are unlikely to contribute significantly to the overall mass transfer rate in mass exchange episodes of massive stars. Nevertheless, in binary evolutionary codes, they are still important to provide a smooth increase of mass transfer rate at the onset of the Roche-lobe overflow to avoid numerical issues associated with large jumps in $\dot{M}_{\mathrm{L1}}$ [219].

In case of the optically thick mass transfer episode, the photosphere is above the L1 point and the flow is assumed to be adiabatic [e.g. 174, 256, 101, 259, 219] and

therefore, the equation of state of the flow and the corresponding sound speed is $P = k\rho^{\Gamma}$, $c_s = (\Gamma P/\rho)^{1/2}$, respectively (where Γ is the adiabatic exponent and k is the adiabatic constant and can be expressed in terms of a reference point such that $k = P_i/\rho_i^{\Gamma}$). Then choosing an initial point, for which negligible velocity and hydrostatic equilibrium can be assumed, density at L1 point can be calculated via Bernoulli's law (ie. equation 1.21): $\rho = \rho_i(2/(\Gamma+2))^{1/(\Gamma-1)}$. Then the mass transfer rate becomes [174]:

$$\dot{M}_{\mathrm{L1}}^{\mathrm{thck}} = \dot{M}_{\mathrm{L1,0}}^{\mathrm{thin}} + \int_{\Phi_{L1}}^{\Phi_{\mathrm{ph}}} \left(\frac{\rho_i}{P_i}\right) \Gamma^{1/2} \left(\frac{2}{\Gamma+1}\right)^{\frac{\Gamma+1)}{2(\Gamma-1)}} \frac{dA}{d\Phi} \rho_i d\Phi. \tag{1.23}$$

[174] considered only ideal gas and therefore in the integrand ρ_i/P_i was replaced with $k_b T_i/\mu m_h$. However, [219] recently showed that for mass exchanging massive binaries, the radiation pressure also plays an important role and this should be taken into account in equation 1.23.

Rapid population synthesis codes often adopt an even simpler scheme (and this is what we do in the subsequent chapters as well). First, the approximate timescale of the mass transfer phase is estimated with the help of the mass-radius exponents (equation 1.19), then assume a mass transfer rate:

$$\dot{M}_{\mathrm{L1}} = M_{\mathrm{donor}}/\tau_{\mathrm{nuc}} \qquad \text{or} \qquad \dot{M}_{\mathrm{L1}} = M_{\mathrm{donor}}/\tau_{\mathrm{th}}, \tag{1.24}$$

if the mass transfer episodes proceeds on a nuclear or thermal timescale, respectively. Alternatively, a few other codes assume $\dot{M}_{\mathrm{L1}} = (7.5 \cdot 10^{-5}/M_{\odot})\ln(\mathrm{R}_1/\mathrm{R}_{\mathrm{L1}})^3$ for nuclear timescale mass transfer mass transfer rate instead [e.g. 139].

1.2.7 Common envelope evolution

If stars in a binary system are engulfed by a single, shared envelope, the system is said to experience common envelope evolution [CEE, see e.g. 255, 409, 152]. This could be triggered by a dynamically unstable mass transfer phase, in which the common envelope originates from the donor star. The common envelope loses co-rotation and therefore exerts friction on the binary, which leads to a significant orbital decay and heating of the envelope, resulting in either a merger or envelope ejection. Even in the latter case, the orbit could shrink by orders of magnitude.

Perhaps the most important aspect of CEE in the context of binary evolution is that it can potentially lead to a dramatic decrease in the period of a binary. Many observed compact binaries have extremely small orbits, which are orders of magnitude smaller than the typical sizes of their progenitors [see e.g. 181]. CEE offers the most natural explanation for the formation of such short period compact binaries and could therefore play a key role to understand the origin of these objects and their associated astrophysical phenomena, such as type Ia SN, X-ray binaries, and cataclysmic variables.

Hydrodynamical simulations of CEE from first principles is extremely challenging and computationally expensive, as there is a huge range of time- and length scales involved in this process. While such studies have provided invaluable insights about the conditions of successful envelope ejection, they cannot explore an extensive parameter space of binaries undergoing CEE, and often only follow the early phase of common evolution [e.g. 291, 257, 242, 149, 204, 59, 94]. Because of these challenges, typically a much simpler formalism is adopted in binary population synthesis studies, in which it is assumed that the energy to eject the envelope originates from the orbital energy dissipation [see e.g. 255, 409, 379]. The change in orbital

energy due to orbital decay is:

$$\Delta E_{\mathrm{orb}} = -\frac{GM_{\mathrm{core}}M_{\mathrm{accretor}}}{2a_i} + \frac{GM_{\mathrm{core}}M_{\mathrm{accretor}}}{2a_f}, \qquad (1.25)$$

where M_{core} is the mass of the helium core of the donor star, M_{accretor} is the mass of the accretor star, a_i is the initial orbital separation (i.e. at the onset of the CEE) and a_f is the final orbital separation (at the time of envelope ejection). Generally, only a fraction of ΔE_{orb} is used to unbind the envelope. This fraction is called the common envelope efficiency [i.e. α_{CEE}, see 198]. Then $\alpha_{\mathrm{CEE}}\Delta E_{\mathrm{orb}}$ must be compared with the binding energy of the common envelope around the binary to determine whether envelope ejection is possible and the final orbit (i.e. $E_{\mathrm{bind}} = \alpha_{\mathrm{CEE}}\Delta E_{\mathrm{orb}}$, where E_{bind} is the binding energy of the common envelope). Binding energy is typically parameterised as [e.g. 397]:

$$E_{\mathrm{bind}} = \frac{GM_{\mathrm{donor}}M_{\mathrm{donor,env}}}{\lambda R_{\mathrm{donor}}}, \qquad (1.26)$$

where $M_{\mathrm{donor,env}}$ is the envelope of the donor star, R_{donor} is the radius of the donor star at the onset of the CEE and λ is a free-parameter that needs to be calibrated depending on the envelope structure. A major assumption is that the binding energy of the common envelope around the binary is the same as the binding energy of the envelope of the donor star, before the CEE [e.g 397, 67]. Determining λ is not straightforward, mostly due to two reasons. First, identifying the boundary between the core and the envelope is not obvious and the value of λ is sensitively dependent on where exactly this boundary lies [e.g. 67]. Various methods have been proposed to identify the boundary of the core, including using the energy generation rate [344, 65], the hydrogen fraction [e.g. 388], or where the maximum compression occurs in the interior, i.e. where P/ρ has a maximum [e.g. 148, 168] or by artificially removing mass layers of detailed stellar models and determining the readjusted stellar strucutre until the star detaches from its Roche-lobe [e.g. 219, 66].

The second complication stems from the ambiguity of what terms should be included in E_{bind}. In particular, it is not clear whether only gravitational binding energy plays a role in the envelope ejection process or if the thermal internal energy and recombination energy also contributes to the binding energy of the common envelope. Most commonly λ is determined by applying the following relation to detailed stellar evolutionary models [e.g. 122]:

$$E_{\text{bind}} = \int_{M_{\text{core}}}^{M_{\text{donor,i}}} \left(-\frac{Gm}{r} + \alpha_{\text{th}} u \right) dm, \tag{1.27}$$

where u is the specific internal energy of the envelope, including thermal and recombination energy and α_{th} is the efficiency with which the internal energy contributes to the binding energy [122].

Combining equations 1.25 and 1.26, the change in the orbital separation, in case of successful envelope ejection can be determined from the following equation:

$$\frac{GM_d(M_d - M_{d,\text{core}})}{\lambda R_d} = \alpha_{\text{CEE}} \left(\frac{GM_a M_{d,\text{core}}}{2a_f} - \frac{GM_d M_a}{2a_i} \right), \tag{1.28}$$

where M_d is the donor mass, $M_{d,\text{core}}$ is the mass of the helium core of the donor star and M_a is the mass of the accretor star.

The common envelope efficiency parameter remains perhaps the biggest uncertain parameter in the energy budget formalism. In population synthesis studies, this is often assumed to be a constant, although there is no reason to believe that α_{CEE} is independent of binary and stellar parameters. In earlier studies, α_{CEE} is often combined with λ and a single value is assumed for $\alpha_{\text{CEE}}\lambda$. By comparing population synthesis simulations to observed short-period binaries containing white dwarfs, [352] and [47] finds $\alpha_{\text{CEE}}\lambda \approx 0.25$. Hydrodynamical simulations of low mass binaries find $\alpha_{\text{CEE}} \lesssim 0.4$ [see e.g. 242, 149, 59].

Calibration α_{CEE} to observations for massive binaries is much more challenging, as the formation of post-common-envelope systems formed from massive binaries are even more uncertain (e.g. X-ray binaries, milisecond pulsars, merging binary BHs). One of the very few physically motivated values for common envelope efficiency for massive binaries is from the hydrodynamical simulations of [94]. In this study, it was found that the envelope ejection of a NS-NS progenitor is possible, if $\alpha_{\mathrm{CEE}} \approx$ 2-5. Common envelope efficiencies larger than one, imply that there must be an additional energy source besides the orbital energy, for example nuclear energy generation during the CEE or accretion energy [377].

1.2.8 Orbital evolution due to stellar winds

In case of mass loss due to stellar winds, the specific angular momentum that is carried away is that of the donor, which implies $\gamma = M_{\mathrm{accretor}}/M_{\mathrm{donor}}$ and then the change in the orbit due to wind mass loss becomes (following from equation 1.14):

$$\frac{a}{a_i} = \left(\left[\frac{M_{\mathrm{donor}}}{M_{\mathrm{donor,i}}} \right]^{\beta} \frac{M_{\mathrm{accretor}}}{M_{\mathrm{accretor,i}}} \right)^{-2} \frac{M_{\mathrm{tot,i}}}{M_{\mathrm{tot}}}, \tag{1.29}$$

which, in case a negligible amount of stellar wind is accreted by the companion, reduces to:

$$\frac{a}{a_i} = \frac{M_{\mathrm{tot,i}}}{M_{\mathrm{tot}}}. \tag{1.30}$$

This implies that the semimajor axis widens due to stellar winds, given that the wind is fast, spherically symmetric, leaves the system in an adiabatic fashion and the companion star accretes a negligible amount from the stellar wind.

Stellar wind accretion by the companion is typically modelled by Bondi-Hoyle

accretion [39], which assumes spherical accretion with a rate that decreases with increasing terminal velocity of the stellar winds. If mass losses of massive stars are dominated by line-driven winds, the accretion typically is typically unimportant for the evolution of the orbit due to the high terminal velocities. Terminal velocities of dust driven winds of cool giants, could, however be as low as a few tens of km/s [see e.g 132], and in that case β can be up to $\sim 50\%$ [see e.g. 236].

1.2.9 Tides

Stars in binaries exert mutual gravitational force on each other. As according to Newton's theory, the gravitational force scales as $F_g \sim r^{-2}$, the pull is stronger on the surface facing to the companion than it is on the centre. Therefore, there exists a differential force on stars in binaries. This, along with the centrifugal force caused by the rotation causes the tidal force in binary systems.

Tides tend to deform celestial objects along the line connecting the centre of masses of the two stars in the binary. In case there are no dissipative forces in the stellar interior, this tidal bulge instantaneously rearranges itself as the stars are advancing in their orbit. This means that the star is always elongated on the line connecting the centre of masses. However, realistically energy is always dissipated inside the star, as it rearranges its elongated shape while orbiting. In that case, if the rotational period of the star is not synchronised with the orbital period, there will be a lag in the tidal bulge (i.e. the axis of elongation and the line connecting the centres of masses will not coincde). In this case tides will affect the orbital parameters [e.g. 394].

This is illustrated in the upper panel of Fig. 1.7. In this case, the rotational angular velocity is larger than instantaneous orbital angular velocity (i.e. $\Omega > \dot{\theta}$ as

shown in Fig. 1.7) and the tidal bulge is ahead of the line of centres. In the opposite situation (i.e. $\Omega < \dot{\theta}$) the axis of elongation will lag behind the line of centres. In both cases a torque will act on the star due to the tidal forces, which allows the exchange of rotational and angular momentum. Furthermore, tides also drain the total orbital energy of the system. The tidal interactions can lead to an dynamical instability, if

$$J_{\mathrm{rot}} > \frac{1}{3} J_{\mathrm{orbit}}, \tag{1.31}$$

that is the rotational angular momentum of the star is larger than one-third of the angular momentum of the orbit. In this case, the decay of orbit proceeds at an increasing rate and the stars eventually spiral into each other [63, 61, 140]. On the other hand, if $J_{\mathrm{rot}} \leq \frac{1}{3} J_{\mathrm{orbit}}$, then the binary system under tidal interactions evolves to an equilibrium state, which is characterised by circular orbits, a rotational frequency that is synchronised with the orbital freqeuncy and coplanarity [e.g. 11]. There is plenty of observational evidence of detached binary systems in a (near) equilibrium state, providing evidence of tidal interactions. The most well-known is of course the Earth-Moon system, which is almost perfectly tidally locked. Furthermore, astronomical surveys have also revealed that tidal equilibrium is also readily reached in many, detached, close stellar binaries [see e.g. 172, 77, 227, 228, 223, 203].

A model that quantitatively predicts the orbital evolution of the binary due to tidal interactions, and is commonly used by binary evolution codes was developed by [141]. Only small deviations in position and amplitude with respect to the equipontential surfaces are considered. Therefore, (R/r) can be treated as a small parameter (where R is the stellar radius and r is the orbital separation) and truncate any relevant expressions after the few leading powers. In this regime, the tidally deformed star can be described with three point masses: $M - 2\mu$ at the centre of mass of the star and two point masses with a mass μ at the surface of the star on the axis of the
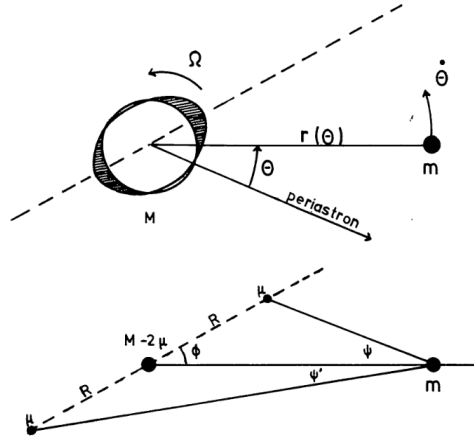
Figure 1.7: A schematic drawing of how tidal torque is exerted in a close binary. In the lower panel, the distorted star is represented by three point masses. Figure adopted [141]

elongation (shown in the lower panel of Fig. 1.7).

The model remains agnostic about the origin of dissipative processes in the stars. Instead, it assumes a constant time lag τ. This means that the shape of the tidally deformed star can be described by the equipotential surface that the star would have had a constant τ time ago. This implies $\mu = 1/2kmR^3r(t-\tau)^{-3}$, where k is the apsidal motion constant and m is the mass of the companion, $\phi = (\Omega - \dot{\theta})\tau$, where ϕ is the angle between the line along the elongation and the line connecting the centres of masses (see Fig. 1.7). Then the perturbing tidal force can be calculated by simply considering Newton's law for gravitation between the three points of mass and the companion, as shown in the lower panel of Fig. 1.7. This perturbing force is expanded in the powers of R/r and truncated to obtain only the leading orders. Then considering that the total angular momentum is conserved and considering the definition of the orbital energy, the rate of change of semimajor axis, eccentricity and angular velocity is determined as:

$$\frac{da}{dt} = -6\frac{k}{T}q(1+q)\left(\frac{R}{a}\right)^8 \frac{a}{(1-e^2)^{15/2}} \cdot \left(f_1(e^2) - (1-e^2)^{3/2}f_2(e^2)\frac{\Omega}{n}\right), \quad (1.32)$$

$$\frac{de}{dt} = -27\frac{k}{T}q(1+q)\left(\frac{R}{a}\right)^8 \frac{e}{(1-e^2)^{13/2}} \cdot \left(f_3(e^2) - \frac{11}{18}(1-e^2)^{3/2}f_4(e^2)\frac{\Omega}{n}\right), \quad (1.33)$$

$$\frac{d\Omega}{dt} = 3\frac{k}{T}\frac{q^2}{r_g^2}\left(\frac{R}{a}\right)^6 \frac{n}{(1-e^2)^6} \cdot \left(f_2(e^2) - (1-e^2)^{3/2}f_5(e^2)\frac{\Omega}{n}\right), \quad (1.34)$$

where $q = M/m$ is the mass ratio, $n = G^{1/2}(M+m)^{1/2}a^{-3/2}$ is the mean orbital angular velocity, r_g is the radius of gyration and can be defined in terms of the moment of inertia (I) as $r_g = I^{1/2}M^{-1/2}R^{-1}$, $f(e)$ are polynomial functions of eccentricity and can be found in [141], finally T is a characteristic timescale defined as

$$T = \frac{R^3}{GM\tau}, \quad (1.35)$$

and this parameter remains the largest uncertainty. For stars with deep convective envelope, convective damping due to turbulent viscosity is considered a very efficient dissipative process that could drive close binaries to their equilibrium point on timescales that are much shorter than the nuclear timescale [393]. For radiative stars, oscillations caused by tides could play an essential role in dissipating the orbital energy [392].

In the context of GW formation from isolated binaries, the most important question is whether tides are efficient enough to circularise the orbit by the onset of a mass transfer phase. In many binary evolution codes, it is assumed that the orbit is always circular at the onset of RLOF or that mass transfer rapidly circularises the orbit. This assumption is often due to necessity, since it remains challenging to model eccentric mass transfer episodes.

1.2.10 GW radiation

Energy carried away by GWs is a strong function of the orbital separation. GWs only affect the orbital evolution of massive stars and remnants appreciably, if their oribtal separation is equal or lower than a few tens of solar radii (e.g. see Fig. 1.9). This essentially means that GWs are only relevant for close orbit compact binaries. The equations governing the change in semimajor axis and eccentricity due to GWs are [266]:

$$\dot{a}_{\mathrm{gr}} = -\frac{64}{5}\ \frac{G^3 m_1 m_2 (m_1 + m_2)}{c^5 a^3 (1 - e^2)^{7/2}}\ \left(1 + \frac{73}{24}e^2 + \frac{37}{96}e^4\right), \qquad (1.36)$$

$$\dot{e}_{\mathrm{gr}} = -\frac{304}{15}e\frac{G^3 m_1 m_2 (m_1 + m_2)}{c^5 a^4 (1 - e^2)^{5/2}}\ \left(1 + \frac{121}{304}e^2\right). \qquad (1.37)$$

GWs tend to circularise and shirnk the orbit.

1.2.11 Physics of triple stars

In this section, we summarise the most relevant physics and types of interactions in triple stars. The discussion is restricted to hierarchical triples, as only such triple systems are dynamically stable and therefore remain bound for timescales that are relevant for stellar evolution. Hierarchical triples are systems which comprise an inner binary and an outer, distant tertiary star which orbits around the centre of the mass of the inner binary. A defining feature is that the outer orbital separation is much larger than inner orbital separation. A hierarchical tertiary is characterised
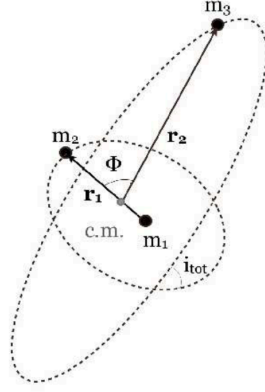
Figure 1.8: A schematic figure of a hierarchical triple. Figure adopted from [246].

by the masses of the two inner stars: m_1, m_2, the inner semimajor axis, eccentricity and argument of pericentre : $a_{\rm in}$, $e_{\rm in}$, $g_{\rm in}$, the tertiary mass $m_{\rm out}$, the outer orbital semimajor axis, eccentricity and argument of pericentre: $a_{\rm out}$, $e_{\rm out}$, $g_{\rm out}$, and the mutual inclination i [see Fig. 1.8 and see also e.g. 354].

A commonly used criteria for the dynamical stability of triples is from [220] and based on identifying the chaotic boundary:

$$\left(\frac{a_{\rm out}}{a_{\rm in}} \right)_{\rm crit} = \frac{2.8}{1 - e_{\rm out}} \left(1 - \frac{0.3i}{\pi} \right) \left(\frac{(1 + q_{\rm out})(1 + e_{\rm out})}{\sqrt{1 - e_{\rm out}}} \right)^{2/5}, \tag{1.38}$$

where $q_{\rm out} = m_{\rm outer}/(m_1 + m_2)$, the outer mass ratio. The triple is stable, if $a_{\rm out}/a_{\rm in} \geq (a_{\rm out}/a_{\rm in})_{\rm crit}$. This criteria also implies that hierarchical triples (i.e. with $a_{\rm out} \gg a_{\rm in}$) tend to be stable.

Because of the large outer orbital separation, the impact of the tertiary star on the inner binary is relatively weak. Consequently, the orbital evolution of hierarchical triples can be obtained via secular approximation. In this regime, the changes in the orbital parameters are slow compared to the orbital periods. This means that the inner and the outer orbit can be described as two, slowly evolving Keplerian

orbits [216]. The Hamiltonian of a secular triple can be given as [e.g. 123]:

$$H = -\frac{Gm_1 m_2}{2a_{\text{in}}} - \frac{Gm_{\text{out}}(m_1 + m_2)}{2a_{\text{out}}} - \frac{G}{a_{\text{outer}}} \sum_{l=2}^{\infty} \left(\frac{a_{\text{in}}}{a_{\text{out}}}\right)^l M_l \left(\frac{|\mathbf{r}_{\text{in}}|}{a_{\text{in}}}\right)^l \left(\frac{a_{\text{out}}}{|\mathbf{r}_{\text{out}}|}\right)^{l+1} P_l(\cos\Phi),$$

(1.39)

where $\mathbf{r}_{\text{in}}$, $\mathbf{r}_{\text{out}}$ are instantaneous separation vectors between the centre of masses of the inner stars and between the centre of the masses of the inner binary and the tertiary star, Φ is the angle between $\mathbf{r}_{\text{in}}$ and $\mathbf{r}_{\text{out}}$ (see also Fig. 1.8), P_l is the Legendre polynomial, and M_l is a coefficient defined as:

$$M_l = m_1 m_2 m_{\text{out}} \frac{m_1^{l-1} - (-m_2)^{l-1}}{(m_1 + m_2)^l}.$$

(1.40)

The first two terms in equation 1.39 are the Hamiltonian of the inner and outer orbit and the last term is the perturbation potential that describes the interactions between the two nested orbits. It is expressed as a power series of the ratio of the inner and outer semimajor axis. Since $a_{\text{in}}/a_{\text{out}}$ is small, it is sufficient to keep only the first few leading orders of l. Furthermore, the leading orders of the perturbation functions can be averaged over the inner and the outer orbit so that only the secular terms remain and any high frequency behaviour is filtered out [e.g. 359]. This averaging process shows that the orbital energy of the inner and the outer orbit (and therefore a_{in} and a_{out}) and the total angular momentum of the system is conserved [246].

1.2.12 von Zeipel-Lidov-Kozai oscillations

The secular equations of motions for the Hamiltonian presented in the previous section have been derived by several authors up to the quadrupole order [i.e $l = 2$, see e.g. 175, 195, 147, 160] and up to the octupole order [i.e. $l = 3$, see e.g. 196, 246].

The most remarkable feature of the solutions are the so-called ZLK oscillations [195, 175, 243]. If the relative inclination is sufficiently high, a mutual torque is exerted between the inner and the outer orbit, as a result of the orbit-averaged gravitational perturbation from the tertiary star. This leads to an exchange of angular momentum between the two orbits, while the orbital energy of each orbit (and therefore a_{in} and a_{out}) is conserved separately. The net result is that the eccentricity of the inner orbit and the mutual inclination will oscillate.

The behaviour of ZLK oscillations can be given in relatively simple analytical terms, if $m_2 \approx 0$, and $e_{\mathrm{out}} = 0$ [i.e. circular test particle approximation 195, 175, 246]. In this case, ZLK oscillations are induced, if the initial mutual inclination is $39.2° \leq i_{\mathrm{init}} \leq 140.8°$. Then, the eccentricity oscillations has a well-defined maximum. In case of an initial argument of pericenter of $g_{\mathrm{in}} = 90°$, this is [147]:

$$e_{\max} = \sqrt{1 - \frac{5}{3}\cos^2(i_{\mathrm{init}})}, \tag{1.41}$$

and the approximate timescale of the ZLK oscillations are [e.g. 147, 133, 160]:

$$t_{\mathrm{ZLK}} = \left(\frac{M_1 + M_2}{GM_{\mathrm{out}}^2}\right)^{1/2} \left(\frac{a_{\mathrm{out}}}{a_{\mathrm{in}}^{1/2}}\right)^3 (1 - e_{\mathrm{out}}^2)^{3/2}, \tag{1.42}$$

which implies the mass of the tertiary and $a_{\mathrm{out}}/a_{\mathrm{in}}$ does not influence the amplitude of the eccentricity oscillations, only sets the period of these oscillations. The amplitude of the oscillations, entirely depends on the mutual inclination, and in principle can reach extremely large values ($e_{\mathrm{in}} \approx 1$), which could even lead to stellar collision in the inner binary.

In more general cases (i.e. $m_2 \neq 0$ and/or $e_{\mathrm{out}} \neq 0$), the behaviour of the ZLK oscillations are qualitatively similar, and the eccentricity and inclination has always a well-defined minimum and maximum [246], if the Hamiltonian is dominated by

the quadrupole term. This occurs if the following term

$$\epsilon_{\text{oct}} = \frac{m_1 - m_2}{m_1 + m_2} \frac{a_{\text{in}}}{a_{\text{out}}} \frac{e_{\text{out}}}{1 - e_{\text{out}}^2},$$

(1.43)

is $|\epsilon_{\text{oct}}| \lesssim 0.01$. Otherwise, the octupole terms become important in the Hamiltonian, which could lead to an even qualitatively different behaviour than what is predicted by the test particle approximation. The maximum eccentricity might not be well defined and could reach extremely large values for a much larger parameter space. The orbital evolution could become chaotic and the mutual inclination can flip [see e.g. 35, 245, 196, 320].

1.2.13 ZLK oscillations coupled with other processes

ZLK oscillations are crucial to numerous astrophysical phenomena. When acting in concert with dissipative processes such as tides or gravitational waves, they are often associated with formation of short period binaries, planets or with triggering merger events. When high eccentricities are induced in the inner binary due to ZLK oscillations, the pericentre of the inner binary decreases, at which the dissipative processes become strong, and decrease the semimajor axis of the inner binary . This process has been studied in the context of planetary migration and formation of hot Jupiters [e.g. 387, 364, 245, 269], close stellar binaries [224, 164, 80, 87, 244], blue stragglers via stellar mergers [264], Type Ia supernova [158, 346, 118, 355, 340], double compact object mergers [e.g. 233, 35, 346, 16, 323, 19, 295, 117, 93, 333], and X-ray binaries in dense environments [151].

Furthermore, various stellar interactions can transition the triple into different dynamical regimes. Stellar winds can change the importance of octupole terms, as ϵ_{oct} in equation 1.43 depends on the mass ratio in the inner binary. Furthermore,

stellar winds can also change the timescale of the ZLK oscillations and can transition the binary into a dynamically unstable regime. This can be understood by considering how the inner and the outer orbit changes due to stellar winds in the triple:

$$\left(\frac{a_{\text{final}}}{a_{\text{init}}}\right)_{\text{in}} = \frac{M_{1,\text{init}} + M_{2,\text{init}}}{M_{1,\text{final}} + M_{2,\text{final}}},$$ (1.44)

and

$$\left(\frac{a_{\text{final}}}{a_{\text{init}}}\right)_{\text{out}} = \frac{M_{1,\text{init}} + M_{2,\text{init}} + M_{\text{out,init}}}{M_{1,\text{final}} + M_{2,\text{final}} + M_{\text{out,final}}},$$ (1.45)

which means that, if the relative wind mass loss rate (i.e. $\dot{M}/M$) in the inner binary is higher than that of the tertiary star, $a_{\text{in}}/a_{\text{out}}$ and q_{out} will increase. This can increase the timescale of ZLK oscillations or even trigger dynamical instability in the triple [163, 142, 265, 357].

If additional processes induce apsidal precession in the inner binary that proceeds on a much shorter timescale than the precession due to three-body dynamics, ZLK oscillations become suppressed. Such high rate precessions can be triggered by short range forces, such as tides, stellar rotation and GR effects [see e.g. 133, 80, 35, 87, 346, 71, 197, 269, 13]. In order to assess whether in a specific binary ZLK oscillations become quenched due to various short-range forces, in principle, one would have to solve the equation of motions in which all the relevant processes are taken into account. However, comparing characteristic timescales of ZLK oscillations and different short-range forces provide a simpler, approximative method to estimate, whether a triple is in a regime, where three-body dynamics are relevant or not [see e.g. 346, or Chapter 3 later.]

1.3 GW astronomy

GWs are propagating perturbations of the spacetime metric, which are generated by accelerated masses whose motion is not characterised by spherical symmetry [e.g. 209]. A few example of possible GW sources are compact binaries, rapidly rotating neutron stars with a bump on their surfaces and asymmetric SN explosions [e.g. 90, 136].

The very first detection of a GW signal was on September 14, 2015 [2]. The source of this GW transient was a merging binary BH with masses of about 36 and 29 $M_\odot$. Since then, detections of GWs from compact binary mergers have become a regular occurrence, and about 90 GW transients have been confirmed [see e.g. 6]. The overwhelming majority of these signals originate from binary BHs.

Predicting the gravitational wave signal from a merging compact binary is an extremely challenging task, that typically requires numerical relativity simulations, possibly combined with complex analytical methods [see e.g. 311]. Yet, useful insights can be drawn by considering possibly the simplest model: the Newtonian quadrupole formula for an inspiraling binary. In this case, the GW strain amplitude is proportional to [e.g. 209]:

$$h(t) \sim (GM_{\text{chirp}})^{5/3} D_L^{-1} f_{\text{GW}}^{2/3} \cos(2\pi f_{\text{GW}} t + \phi), \tag{1.46}$$

where h is the GW strain amplitude, $M_{\text{chirp}} = (m_1 m_2)^{3/5}/(m_1 + m_2)^{1/5}$ is the chirp mass, D_L is the luminosity distance, f_{GW} is the frequency of the GW and ϕ is a phase factor. The frequency of the GW is by a good approximation twice the rotational frequency of the binary, i.e. $f_{\text{GW}} = 2 f_{\text{binary}}$ [e.g. 209].

GWs carry orbital energy away from the system. The total energy radiated away

by GW from an inspiraling binary is [e.g. 90, 136]:

$$P_{\text{GW}} = \frac{32}{5} \frac{G^4 \mu^2}{c^5} \frac{M_{\text{tot}}^3}{a^5},$$ (1.47)

where μ is the reduced mass. This means that energy carried away by GWs scales as $\sim c^{-5} a^{-5}$. Therefore, the binary has to have an extremely short period for the GW radiation to have any non-negligible effect on the orbital evolution. Furthermore, equation 1.47 also implies that f_{binary} increases due to the orbital decay with time, and therefore so is f_{GW}. Since the amplitude of the GW strain is proportional to $f_{\text{GW}}^{2/3}$, both the frequency and the amplitude of the GW signal increases with time, as the orbit of the binary is shrinking due to gravitational radiation. This is the reason behind the characteristic *chirp signal* (shown in Fig. 1.11). The merger approximately occurs at a frequency [e.g. 209]:

$$f_{\text{GW,merger}} = 1.1\text{kHZ} \left(\frac{M_\odot}{M_{\text{tot}}} \right),$$ (1.48)

which is based on the assumption that the binaries plunge in, when they reach an orbital separation that is (approximately) associated with the innermost stable circular orbit of the system.

Equation 1.46 and 1.48 show that GWs from merging binaries sweep across a frequency range, which is primarily determined by the masses of the binary components. The frequency associated with the merger becomes lower with increasing component masses in the binary. This allows us to understand the position of different GW sources in the GW astronomy spectrum, as shown in Fig. 1.12. For example, while supermassive binaries generate orders of magnitude stronger GWs, they cannot be detected by ground-based GW observatories, as these systems never enter the frequency band of these detectors.

As it is hinted by equation 1.46, the GW signal contains direct information about the chirp mass and the luminosity distance of the binary. The chirp mass can be directly determined from the frequency evolution, and therefore, the luminosity distance can be derived from the amplitude evolution. This means the GW emitting coalescing binaries are standard candles [315]. Smaller scale variatons in the GW signal also contains information about the individual masses and spins of the binary components [which was neglected in equation 1.46, but apparent in the Post-Newtonian terms of waveforms, see e.g. 36]. To conclude, we can determine the merger rate of binary BHs and the mass, mass ratio and spin distributions of these objects. These measurements therefore provide invaluable clues how merging compact binaries are formed. Furthermore, as the properties of these GW transients could be significantly influenced by currently poorly understood stellar and binary physics, we can also use GW detections to test and to further constraint highly uncertain stellar physics models.

1.3.1 How do BH binaries merge?

In Fig. 1.9, we show the initial pericentre that equal mass compact binaries have, if they were to merge due to GWs exactly within the the age of the universe (which is assumed to be 13.5 Gyrs in this thesis). Typical merging stellar mass BH binaries, with BH masses of 5-50 $M_\odot$ cannot have an orbital separation larger than a few tens of solar radii. This stringent constraint on the maximum binary separation of GW progenitors makes it challenging for most massive binaries to form GW sources. Below, we summarise some of the proposed formation channels for GW transients from BH binary mergers.

- **Classical isolated binary channel:** Isolated binaries can form GW sources, if

they have sufficiently short initial periods such that mass transfer episodes will occur (compare Fig. 1.9 with 1.10). The key point in the formation of a short period binary BH is the second phase of mass transfer (i.e. mass transfer phase with a black hole accretor). This is the processs that has the potential to shrink the orbit sufficiently and form a short orbit compact binary. This can occur via CEE, or stable mass transfer. The latter scenario is possible, if the mass transfer rate occurs on a thermal timescale, and if the mass ratio of the system is relatively high. We discuss this channel in detail in Chapter 2. See e.g.[255, 69].

- **Chemically homogeneous evolution channel:** Chemically homogeneous evolution can be triggered in very close massive binaries with periods of few days. The rapid rotation induced by tidal locking triggers extremely efficient and fast mixing in the interiors of these stars. As a result, no chemical gradient builds up in the stellar interior, as the stars evolve. Consequently, they also do not expand significantly unlike their classical counterparts. Because of this property, these systems can remain detached despite their extremely short orbits, and form binary BHs and merge via GWs within the Hubble time. In Chapter 3, we investigate the evolution of these systems, triples with chemically homogeneously evolving inner stars. See e.g. [213, 401, 217].

- **Dynamical channels:** Merging binary BHs can be formed in dense environments, where dynamical interactions can create sufficiently tightly bound pairs from already existing BHs. Such interactions can take place in globular clusters [e.g. 183, 322, 278, 296, 68], in nuclear clusters [e.g. 18] or in AGN discs [e.g 226, 338, 21]. A defining feature of these channels is the non-negligible eccentricity that these systems can retain by the time they enter the LIGO/Virgo band and the isotropic distribution of their spins.[see e.g. 300].

- **Field triple channels:** This channel could be considered as a hybrid of the
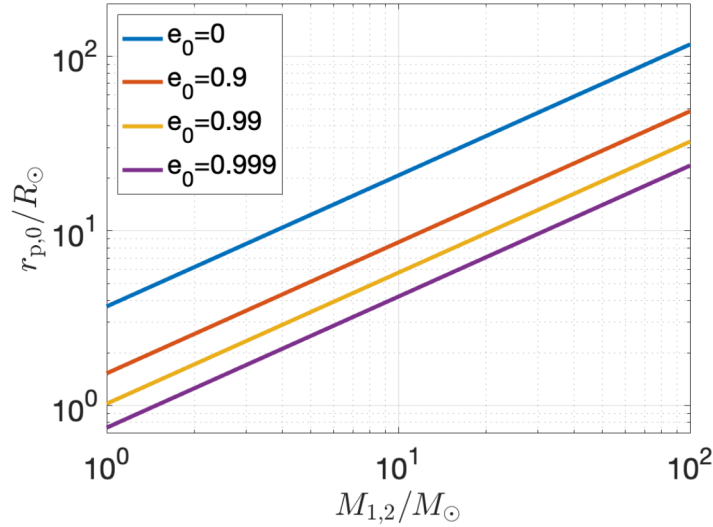
Figure 1.9: The pericentre of an equal mass binary, if it were to merge due GWs within the Hubble time. Figure adopted [211].

isolated binary channel and the dynamical channels. While the triple systems are isolated, dynamical interactions induced by the tertiary star can alter the evolution of the inner binary. For example, a combination of ZLK cycles and gravitational waves can bring the compact objects sufficiently close together, such that a compact binary merger occurs within the age of the Universe [e.g. 233, 35, 346, 16, 323, 19, 295, 117, 93, 333].

1.3.2 Demographics of observed merging binary BHs

The currently inferred merger rate of binary BHs is $R_{\mathrm{BBH}} = 28.3^{+13.9}_{-9.1}\,\mathrm{Gpc}^3\mathrm{yr}^{-1}$ [9]. In Fig. 1.13, masses of the merging binary black holes are shown which have been detected by the LIGO-Virgo-Kagra detector network until now. Most merging black holes have masses in the range of 15-30 $M_\odot$. A few merging black holes have masses above 50 $M_\odot$, which is in the predicted upper mass gap, hypothesised to originate due to pair-instability SN, which entirely disrupts its progenitor and leaves no remnant
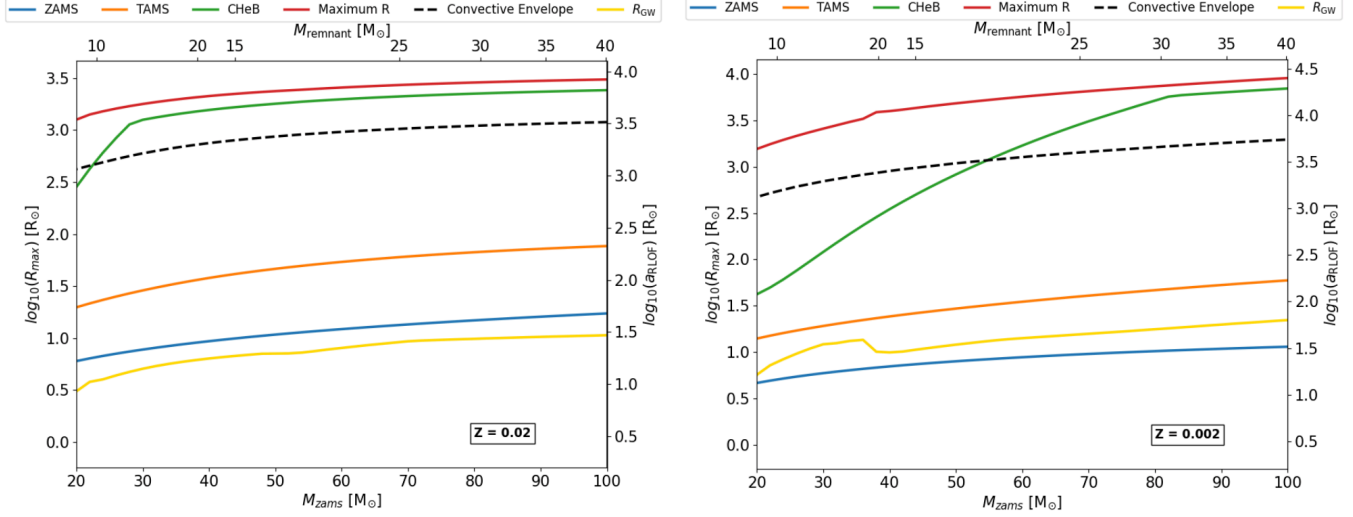
Figure 1.10: The maximum radial expansion of massive stars (shown on left y-axis) for different stellar evolutionary phases as a function of M_{ZAMS} (lower x-axis) at Z = 0.02 (left) and Z = 0.002 (right). Here 'TAMS' stands for terminal-age main sequence, 'CHeB' for core-helium burning, 'Maximum R' is the maximum stellar radius reached by the star and 'Convective envelope' shows the evolutionary stage at which the star develops a deep convective envelope. On the upper x-axis, we show the BH mass (here labelled as M_{remnant}) these massive stars would form, if they did not experience mass exchange throughout their lives. On the right y-axis, we show the equivalent orbital separation that an equal mass binary with masses of M_{ZAMS} would have, if it was about to fill its Roche-lobe at an evolutionary stage indicated by any of the lines. Therefore, the secondary y-axis gives an indication how wide the orbit has to be for a given binary in order to avoid Roche lobe overflow at different evolutionary stages (note, however, that that we did not take into account orbital widening due to stellar winds in this figure). The yellow line with the label R_{GW} indicates the maximum orbital separation that an equal mass BH-BH binary with a circular orbit and with a given M_{remnant} needs to have, if it were merge due to GWs just within the Hubble time. By comparing the R_{GW}, with the other lines, it is clear that GW progenitors from isolated binaries must originate from binaries that experience mass transfer episodes.

behind [e.g. 88]. One possible explanation for the origin of these objects is that they are a product of earlier black hole mergers [and therefore, a dense environment origin is favoured to an isolated scenario for these high mass systems, otherwise a subsequent merger would be difficult to explain, but see 369].

The observed merging binary black hole population also casts doubt on the existence of a lower mass gap [89], as BHs with masses lower than 5 $M_\odot$ have been detected (although distinguishing NS from BH based on GW signals remain extremely challenging). In Fig. 1.14, the inferred primary mass distribution and the mass ratio distribution of coalescing binary black holes are shown. The primary mass distribution shows a power-law like behaviour with a peak around $M_{\mathrm{BH}} = 10\,M_\odot$ and an overdensity bump around $M_{\mathrm{BH}} = 35\,M_\odot$. Once again, we see the apparent lack of the the upper mass-gap that is predicted by stellar evolutionary theory on pair instability SN. The origin of the peak near is $M_{\mathrm{BH}} = 10\,M_\odot$ is hard to explain with dynamical channels (e.g. globular cluster) and it is more consistent with the isolated binary channel. On the other hand, BHs with $M_{\mathrm{BH}} \gtrsim 50\,M_\odot$ are not predicted to form from isolated binaries, but could be formed in dense environments via hierarchical mergers. Current detections could therefore imply that there are multiple channels producing GW mergers [see 9, 396].
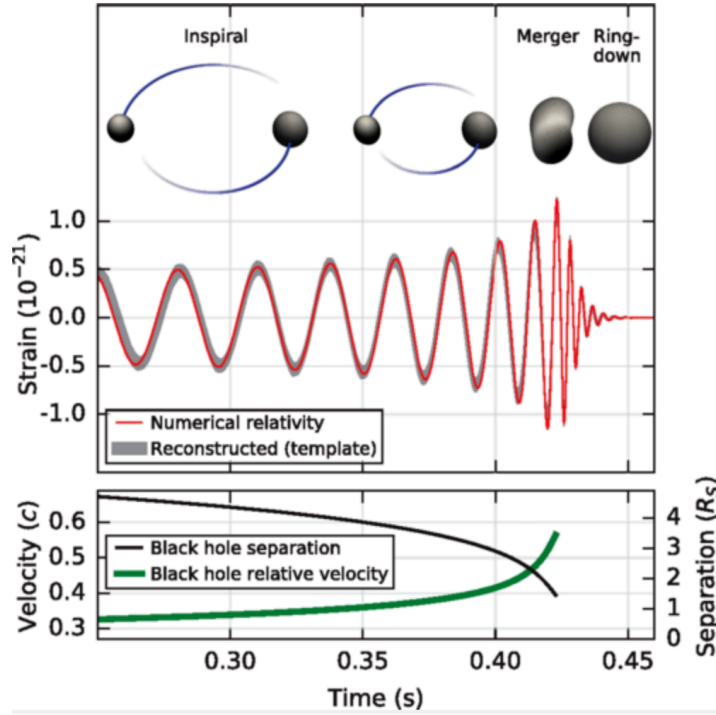
Figure 1.11: A schematic representation of the chirp signal and its relation to the orbital evolution of an inspiralling compact binary object. Figure adopted from [2].
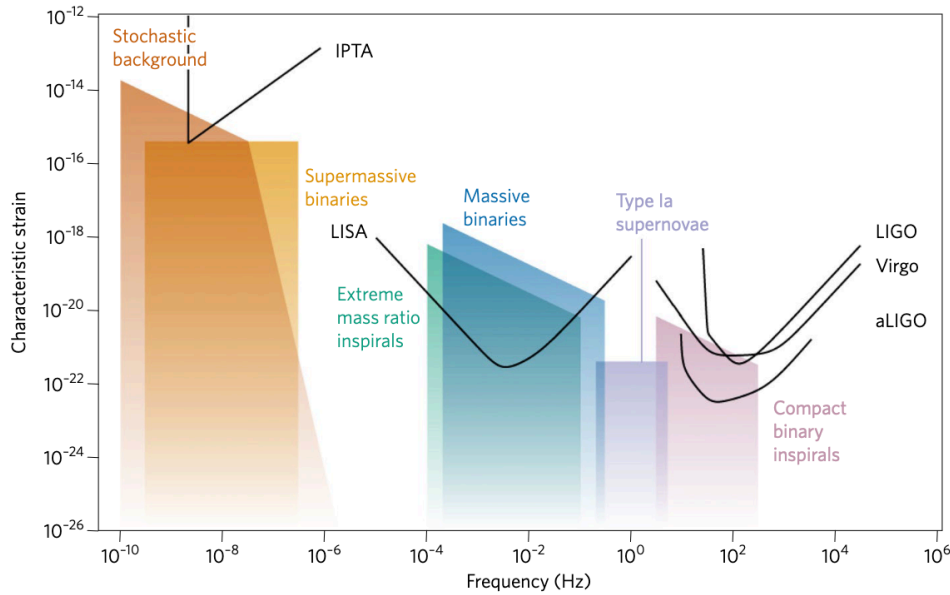
Figure 1.12: GW astronomy spectrum with potential GW sources and sensitivity curves of different GW detectors. Credit to Christopher Moore, Robert Cole and Christopher Berry, https://cplberry.com/2015/01/10/1408-0740/.
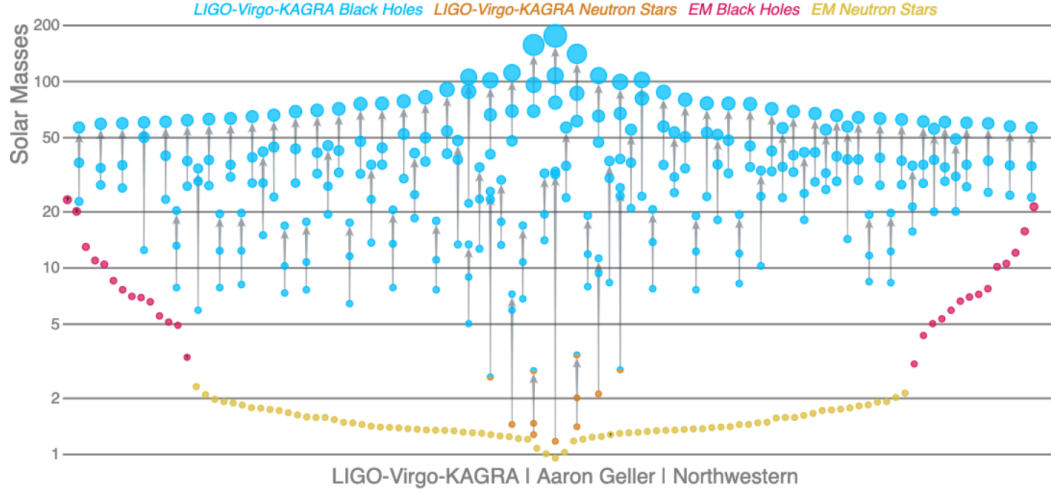
Figure 1.13: Masses of compact binaries detected via GWs [6], X-ray or radio. Credit to Aaron Geller, `https://media.ligo.northwestern.edu/gallery/masses-in-the-stellar-graveyard-with-error-bars`
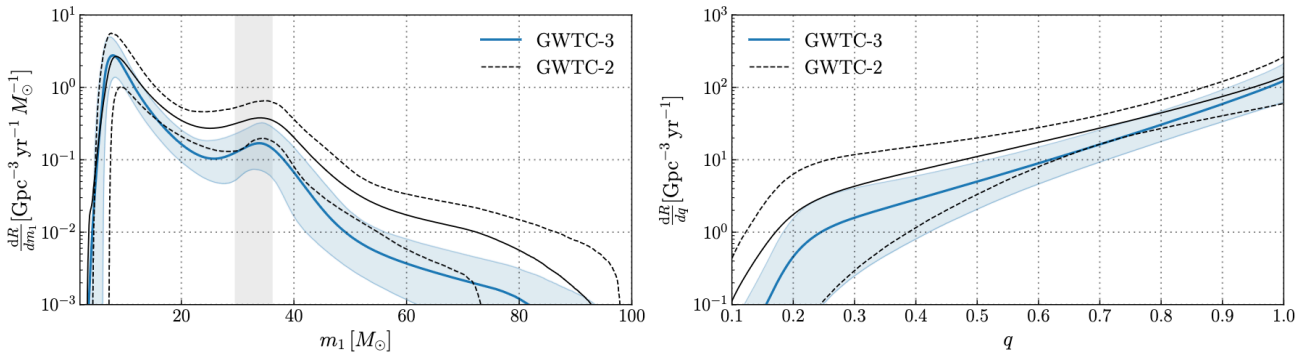
Figure 1.14: The inferred primary mass (left) and mass ratio (right) distribution of merging binary black holes based on GWTC-3. Figure adopted from [6]

Chapter 2

Importance of stable mass transfer and stellar winds in the isolated binary formation channel

authors: Andris Dorozsmai, Silvia Toonen

This chapter is a reformatted copy of Dorozsmai & Toonen 2023 [72], is published in MNRAS and available on arXiv with the number of 2207.08837 (see `https://arxiv.org/abs/2207.08837`). My contribution to this work was (i) to make updates to the binary evolution code, `SeBa`, regarding the modelling of stellar winds, mass transfer stability criteria, angular momentum loss and accretion efficiency during a stable phase of mass transfer (ii) to create different model variations and run the simulations, (iii) to develop a code for the data analysis of the population synthesis simulations and to interpret the results (v) to make the figures, (vi) and to write the manuscript. Silvia Toonen provided supervision for this project and provided feedback on the manuscript.

2.1 Abstract

The large number of gravitational wave (GW) detections have revealed the properties of the merging black hole binary population, but how such systems are formed is still heavily debated. Understanding the imprint of stellar physics on the observable GW population will shed light on how we can use the gravitational wave data, along with other observations, to constrain the poorly understood evolution of massive binaries. We perform a parameter study on the classical isolated binary formation channel with the population synthesis code SeBa to investigate how sensitive the properties of the coalescing binary black hole population are on the uncertainties related to first phase of mass transfer and stellar winds. We vary five assumptions: 1 and 2) the mass transfer efficiency and the angular momentum loss during the first mass transfer phase, 3) the mass transfer stability criteria for giant donors with radiative envelopes, 4) the effective temperature at which an evolved star develops a deep convective envelope, and 5) the mass loss rates of stellar winds. We find that current uncertainties related to first phase of mass transfer have a huge impact on the relative importance of different dominant channels, while the observable demographics of GW sources are not significantly affected. Our varied parameters have a complex, interrelated effect on the population properties of GW sources. Therefore, inference of massive binary physics from GW data alone remains extremely challenging, given the large uncertainties in our current models.

2.2 Introduction

Massive stars play an essential role in astrophysics. They are responsible for the chemical enrichment of the universe via stellar winds and supernovae. They are also progenitors of various interesting astrophysical phenomena, e.g. neutron stars,

black holes, gamma ray bursts (e.g. [187]). However, our understanding of these rare objects and short-lived lives is still incomplete. The population of merging compact binaries, observed as gravitational wave (GW) sources, offer a unique but indirect way to study the evolution of these objects. Since the first detection of GW, about a hundred merging binary black holes have been observed, which makes the inference of the population statistics of black hole-black hole binaries (BH-BH binaries) possible [8, 9].

As discussed in section 1.3, numerous formation channels of merging stellar mass binary black holes have been proposed in the last decades. These include formation scenarios involving isolated, interacting massive binaries (i.e. the classical isolated binary channel, see e.g. (e.g. [255]; [409];[361]; [69]; [229]; [27]; [82]; [230] [336]; [106]; [180]; [165]; [247]; [342]; [219]; [22]; [41]; [293]; [42]), massive binaries comprising chemically homogeneously evolving stars ([401]; [213]; [217]; [82]; [406]; [292]), or scenarios in which dynamical interactions play a key role in forming GW transients, e.g. in dense environments, such as globular clusters (e.g. [183]; [322]; [278]; [297]; [68]), nuclear clusters (e.g. [18]) AGN discs (e.g. [226]; [338]; [21]) or scenarios involving hierarchical, field triples (e.g. [323];[19]; [221];[369]; [334]). The possibility of merging binary black holes originating from population III stars ([23];[161]; [146]) or from primordial black holes ([31], [308]) has also been proposed and studied.

The classical isolated binary channel is perhaps the most studied formation path. In these scenario, typically two main sub-channels are identified (see also section 1.3.1). The first one is the CEE channel, in which the key step in the formation of close BH-BH binaries is the so-called common envelope evolution (CEE, e.g. [152]). Several, earlier population synthesis studies predicted a merger rate for this channel that is broadly consistent with the currently inferred LIGO rate [see e.g. 210], although these predictions are sensitively dependent on the highly uncertain common envelope efficiency and the binding energy of the envelope of the donor star.

However, recent detailed stellar evolutionary models of [168] and [219] showed that the binding energy of evolved stars with radiative envelopes could be underestimated by prescriptions commonly used by rapid population synthesis codes. Furthermore, a deep convective envelope could potentially be developed at a significantly cooler effective temperature ([167]) than previously assumed. These two developments would imply an appreciably lower predicted merger rate for this channel, possibly orders of magnitude lower than the currently inferred rate.

The second dominant channel (stable channel) involves two subsequent stable mass transfer episodes. The orbit of a binary experiencing a stable phase of mass transfer episode with black hole accretor can shrink significantly, if the mass ratio of the system is sufficiently high. This can lead to the formation of BH-BH binaries that merge due to GWs within the age of the universe [410]. Earlier studies did not predict this formation path to be significant [see e.g. 69, 27].However, the detailed simulations of [260] showed that a stable mass transfer episode in a binary comprising an evolved donor star with radiative envelope and a BH accretor is more readily achieved than previously assumed. Subsequent studies, with assumptions that are in agreement with the findings of Pavlovskii et al. [260], have shown that this formation path can be the dominant channel within the isolated binary scenario ([165], [251]; [407]; [99]; [22]; [219]; [14]; [42]).

The properties of GW sources from the two aforementioned channels are sensitively dependent on various, highly uncertain binary evolutionary phases (e.g. mass transfer episodes). This, in principle means that observations of merging binary black holes [e.g. 5, 9] could be used to constrain massive binary physics. Unfortunately, there are currently too many uncertainties in massive stellar evolution to draw any meaningful conclusion [see e.g. 30]. Nevertheless, it is still essential to understand how uncertainties of binary and stellar physics affect the observable properties of the merging binary black hole population in order to correctly interpret

the observed GW data in the future.

In this chapter, we perform a parameter study on the classical isolated binary channel, using a rapid population synthesis code, SeBa ([279], [353]). In the first part of this chapter, we study the uncertainties related to the first phase of mass transfer (i.e. mass transfer episodes between two hydrogen rich stars). For this, we test different assumptions on the angular momentum loss and the fraction of mass ejected during the mass transfer phase with a non-compact accretor. We also vary the mass transfer stability criteria of evolved stars with radiative envelopes and make different assumptions about the evolutionary stage at which giant stars develop convective envelopes to investigate the implications of studies such as [102]; [260]; [103]; [168]. We make model variations using all possible combinations of parameter variations. This allows us to explore the interrelated effects of uncertainties.

In the second part of this chapter, we investigate the effects of uncertainties in mass-loss rates of line-driven stellar winds. Both theoretical ([178]; [339]; [32]; [33]) and observational (e.g. [98]) studies suggest that mass loss rates of O/B stars could be overestimated by a factor of 2-3 by the prescription of [376], which is commonly used in stellar evolutionary codes. As we will see, the impact of lowered mass loss rates on GW sources significantly depends on our assumption of other, seemingly unrelated binary physics. Therefore, the second part of this chapter shows an example of the importance of interrelated effects of uncertain parameters and it highlights the dangers of devising strategies to infer stellar physics directly from GW data without performing a full parameter study.

The impact of the uncertainties in binary physics on the isolated binary channel has been extensively studied with population synthesis approaches in the recent years. However, most of such parameter studies typically concentrated on the episodes following the first phase of mass transfer. For example, the importance of

common envelope evolution was investigated by varying parameters related to the common envelope efficiency [e.g. 366, 22, 44], the binding energy of the donor star [e.g. 249, 366, 69, 335], and by making different assumptions on whether Hertzsprung gap donors can survive the common envelope phase [e.g. 69, 335, 54, 366, 43, 44]. The impact of core collapse was investigated by varying the magnitude of natal kicks received by the stellar remnant [e.g. 249, 335, 366, 43, 44, 105, 290], by applying different supernova mechanisms [e.g 69, 335, 366, 43, 44, 299, 408], and by varying the maximum neutron star mass [e.g. 69, 335, 43, 44]. Uncertainties regarding the second (stable) phase of mass transfer were studied by exploring the implications of super-Eddington accretion for BH accretors [e.g. 28, 22, 42].

On the other hand, a few studies also considered some of those parameters, which are investigated in this chapter. For example, the impact of mass transfer stability of donor stars crossing the Hertzsprung gap was studied in [366, 251, 408]. Furthermore, [249, 69, 43, 44, 30, 408] investigated the impact of different accretion efficiencies for mass transfer episodes with non-compact accretors, while [54, 366, 30] tested different assumptions on the angular momentum loss during non-conservative mass transfer episodes. The importance of stellar winds on the properties of merging compact objects was previously explored by [249, 69, 336, 286, 28, 29, 30, 43]. Clearly, many previous studies investigated the role of those parameters, which we also consider in this chapter. However, this was done typically in a different astrophysical context (e.g. to study the formation of merging double neutron star binaries, see [366, 54]) or to investigate the formation of specific systems see e.g. [29, 30]). More importantly, all of the above mentioned studies typically vary only one parameter with respect to their fiducial models and they never study systematically the importance of the first phase of mass transfer and how the related uncertainties can impact the population of GW sources.

This chapter is organised as following. In section 2.2.1, we briefly review the

classical isolated binary formation channel to introduce the terminology used in this chapter. In section 2.3, we describe the code used in this study. In section 2.4, we show our results that highlight the importance of uncertainties in the first mass transfer phase. In section 2.5, we show how decreasing the line-driven winds for O/B stars and/or WR stars by a factor of 3 can change the merging binary black hole population. Finally, in 2.6, we summarise our main findings.

2.2.1 The classical isolated binary formation channel

In this subsection, we provide a brief overview of the classical isolated formation channel for merging binary black holes. Our purpose is to introduce the terminology used in the rest of this chapter. For a detailed overview on this subject, see e.g. [280, 211, 215].

Black hole binaries with circularised orbits merge within the Hubble time (which we define here as 13.5 Gyrs), if their orbital separation is not larger than a few tens of solar radii ([266]; [211]). However, the radii of massive stars reaches orders of magnitude larger values than that during their evolution. Therefore, GW sources of the isolated binary channel must originate from interacting binaries.

We show a schematic drawing of the most common formation paths of GW sources according to our simulations in Fig. 2.1. At zero-age main sequence, the binaries are not interacting and their orbital separation widens due to stellar winds (stage 1). The initial primary star eventually fills its Roche-lobe and consequently the first phase of mass transfer is initiated (stage 2). In the dominant channels considered here, this mass transfer phase always occurs in a dynamically stable manner. This phase ends with the initial primary star losing its hydrogen envelope. At this stage, the donor star is a stripped helium star, and depending on the metallicity, it

could launch intense stellar winds and therefore may be observed as a Wolf-Rayet star (stage 3). The mass ratio and the orbit of the binary system at this stage depend on how much matter was accreted by the secondary and how much angular momentum was lost by the binary during the first phase of mass transfer. The stripped helium star eventually forms a black hole (stage 4). It is currently uncertain whether this occurs via a supernova or a direct collapse.

After the initial primary forms a compact object, the secondary star expands as well and initiates the second mass transfer phase (stage 5). Based on the mass ratio of the system and the envelope structure of the donor, this episode can occur in a stable (stage 5a) or unstable fashion (stage 5b or 5c). In case of the latter, a common envelope phase is initiated ([152]). As the common envelop ensuing the binary exerts friction on the system, the period is expected to dramatically decrease. If orbital energy is not used efficiently to unbind the envelope, the change in the orbital separation could be a few $\sim 1000\,R_\odot$. This process can lead to an efficient formation of merging binary black holes (i.e. CEE channel). We distinguish two subtypes of the common envelope channel based on the evolutionary phase of the donor star during the second phase of the mass transfer. In the first type (5b), the donor star has a radiative envelope (rCEE), while in the second (5c), the donor star has a deep convective envelope (cCEE). The mass transfer stability criteria is sensitively dependent on whether the envelope of the donor is mostly radiative or convective. We also note that the binding energy of the envelope could be significantly different for these two types of evolved stars.

If the second mass transfer phase occurs in a stable manner, the orbit can shrink sufficiently, and thus lead to the formation of a GW source, if the mass ratios of the binary at the onset of the mass transfer phase are relatively high (stage 5a). For example, the orbit of a binary with a mass ratio $q = M_{\mathrm{donor}}/M_{\mathrm{accretor}} \sim 3$ and $M_{\mathrm{accretor}} \approx 30\,M_\odot$ at the onset of the mass transfer phase, shrinks roughly by

$\sim 100\,R_\odot$, assuming the accretion rate of the black hole is Eddington limited. This implies that binaries with initial orbital separations of a few $\sim 100\,R_\odot$ can form GW sources efficiently via the stable channel.

In principle, GW sources could also be formed from systems, in which the first phase of mass transfer is dynamically unstable. However, we do not discuss this formation scenario in this chapter. This is because the merger rates associated with this formation scenario are negligible in our models.

By the time the second phase of mass transfer occurs, the initial primary star is typically already a black hole. We note that this can occur for a very large fraction of the parameter space, especially if rejuvenation of the accretor is taken into account after the first phase of mass transfer (see e.g. [358]). For example, systems with an initial primary mass of $M_{\mathrm{ZAMS,1}} = 100\,M_\odot$ can evolve in such a way, even if their initial mass ratio are as close to unity as $q_{\mathrm{ZAMS}} = M_{\mathrm{ZAMS,2}}/M_{\mathrm{ZAMS,1}} = 0.99$. We find that only those binaries form gravitational wave sources with non-negligible rates, in which the second phase of mass transfer occurs with a compact accretor. Therefore, in the rest of this chapter, when we mention the second phase of mass transfer, we always refer to mass transfer episodes with BH accretors.

2.3 `SeBa` and model variations

We use the rapid population synthesis code `SeBa` for our binary simulations[1] ([279], [353]). An up-to-date description of the code can be found in [353]. In the following sections, we only describe elements which are especially relevant for this study, or which have been changed with respect to [353]. The most relevant parameters related to stellar and binary physics used in all of our model variations are summarised in
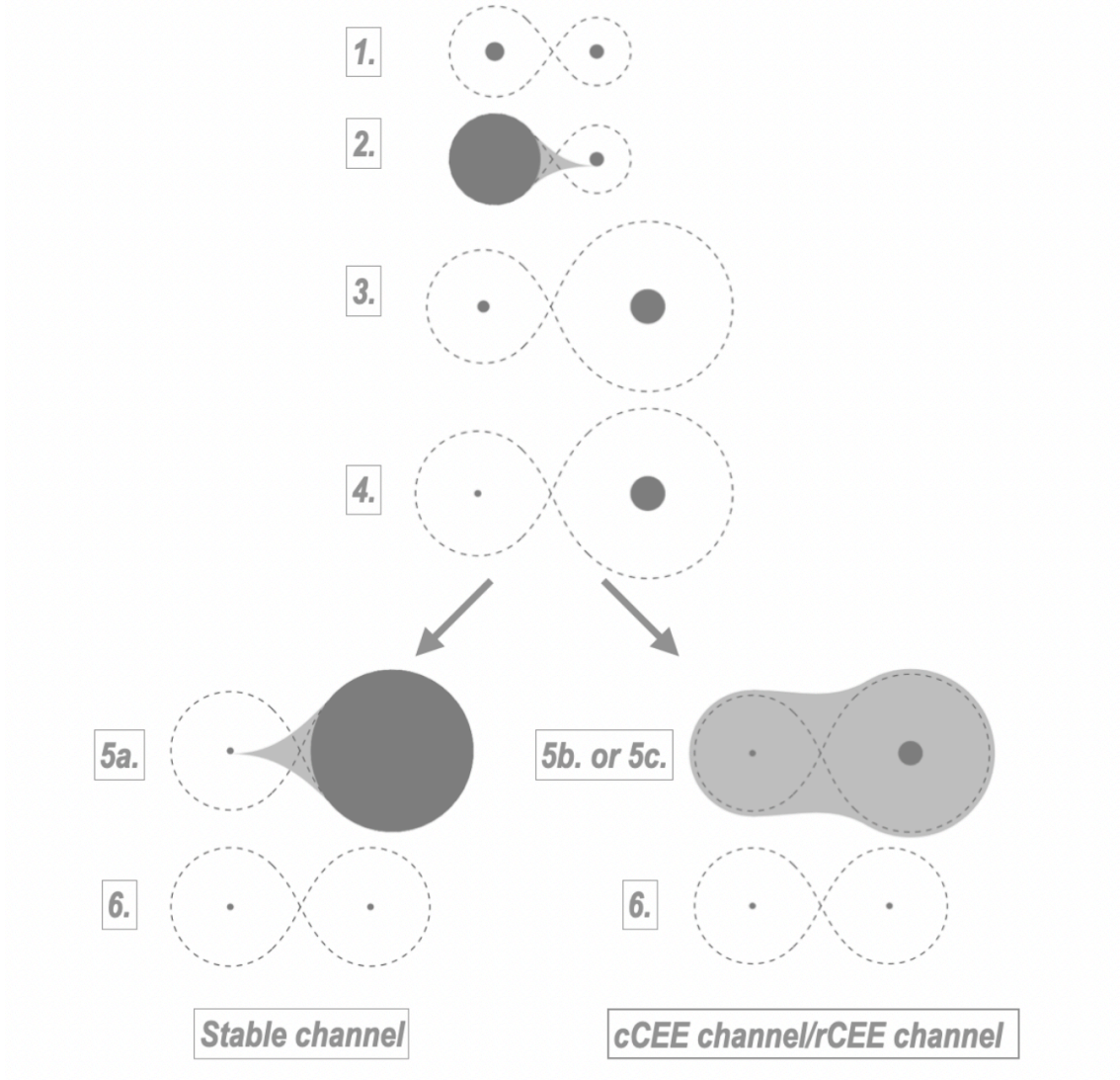
---

[1]https://github.com/amusecode/seba

Figure 2.1: The most common formation channels of gravitational wave sources from isolated binaries as predicted in this chapter. cCEE means that the dynamically unstable mass transfer is initiated by a giant donor, which has a deep convective envelope, whereas for rCEE the donor still has mostly a radiative envelope.

Table 2.1: Summary of the most important parameters in our rapid population synthesis simulation with SEBA. The top of the table shows the standard model used in this paper, while the bottom of the table shows the model variations. We run simulations on a metallicity grid Z = 0.0001, 0.0003, 0.0005, 0.0007, 0.001, 0.003, 0.005, 0.01, 0.02 with all possible combinations of model variations unless stated otherwise in section 2.3. For the detailed descriptions of stellar wind models see Table 2.3.7.

Parameters not varied in this paper		
Parameter	*Model/value*	*Label*
Single stellar tracks	Hurley et al. [138]	-
Tidal interactions	Orbits are circularised by the time of the	
mass transfer [279]	-	
SN prescription	Delayed model of [97]	-
Natal kick velocity distribution	Verbunt et al. [365]	-
Natal kick velocity scaling for BHs	$v_{\text{kick,BH}} = (1 - f) \cdot v_{\text{kick,NS}} \cdot (M_{\text{BH}}/M_{\text{NS}})^{-1}$	-
Common envelope treatment	α-formalism with $\alpha\lambda = 0.05$	-
Angular momentum loss mode with BH or NS accretor	$\gamma = M_d/M_a$	-
Accretion efficiency for BH and NS accretors	Eddington limited accretion	a
Model variations		
Parameter	*Model/value*	*Label*
Stellar wind model	1.) $f_{\text{wind}} = f_{\text{wind,WR}} = 1$ and $f_{\text{LBV}} = 1.5$	Model I
	2.) $f_{\text{wind}} = 1/3$, $f_{\text{wind,WR}} = 1$ and $f_{\text{LBV}} = 1.5$	Model II
	3.) $f_{\text{wind}} = f_{\text{wind,WR}} = 1/3$ and $f_{\text{LBV}} = 1.5$	Model III
Angular momentum loss mode with non-compact accretors	1.) $\gamma = 2.5$ (Portegies Zwart & Verbunt 279)	$\gamma = 2.5$
	2.) $\gamma = 1$ (Podsiadlowski et al. 272; Belczynski et al. 24)	$\gamma = 1$
Accretion efficiency of non-compact accretors	1.) $\beta = 0.3$	$\beta = 0.3$
	2.) $\beta = 0.7$	$\beta = 0.7$
Mass radius exponent of giants with radiative envelopes		
	1.) $\zeta_{\text{ad,rad}} = 4$	$\zeta_{\text{ad,rad}} = 4$
	2.) $\zeta_{\text{ad,rad}} = 7.5$	$\zeta_{\text{ad,rad}} = 7.5$
Boundary of deep convective envelope	1.) Prescription of Klencki et al. [168]	$T_{\text{eff,K}}$
	2.) convective above $\log_{10} T_{\text{eff}} = 3.73\,\text{K}$ (Belczynski et al. 24)	$T_{\text{eff,IT}}$

Table 2.1.

2.3.1   Treatment of binary interactions

In this section, we summarise how binary interactions are treated in `SeBa`. We assume tidal interactions circularise the orbit by the onset of the mass transfer ([279], see also discussion in section 1.2.9). Change in the orbital separation and eccentricity due to gravitational waves emission are calculated according to equations 1.36 and 1.37, based on [266].

A mass transfer episode occurs, if any of the stars in the binary fill their Roche-lobe. We calculate the Roche-lobe radius according to [78]. The evolution of the

orbital separation during a stable phase of mass transfer is determined according to equation 1.14.

Although, the mass transfer efficiency (β) and the angular momentum loss parameter (γ) is expected to depend on the parameters on the binary (see e.g. references in section 2.3.2), it is commonly assumed that these parameters are constant in rapid population synthesis codes [see e.g. 293, 24]. In this chapter, γ is assumed to be constant for a mass transfer episodes with non-compact accretors in all of our model variations. In this case, the orbital evolution due to mass exchange is determined by equation 1.15.

On the other hand, if the accretor is a black hole, we assume that the accretion is Eddington limited and that the specific angular momentum leaving the system is that of the accretor object, which implies $\gamma = M_{\mathrm{donor}}/M_{\mathrm{accretor}}$ (i.e. so-called isotropical reemission). The evolution of the orbital separation for such a mass transfer mode is determined by equation 1.16. For the systems considered here, Eddington limited accretion implies that $\beta \approx 0$, and in this case equation 1.17 becomes a good approximation for the orbital evolution due to this mass transfer mode. This exponential term in equation 1.17 reveals that if the mass ratio of the binary ($q = M_{\mathrm{donor}}/M_{\mathrm{accretor}}$) is sufficiently high, the orbit will experience significant shrinking. Therefore, in this case, a second phase of stable mass transfer could lead to the formation of a short period BH-BH systems that merge due to GWs within the Hubble time. We discuss the treatment of dynamically unstable mass transfer episodes in section 2.3.4.

When the stars in the binary system lose mass via stellar winds, we assume that a fraction of it is accreted via Bondi-Hoyle accretion [39], while the rest leaves the system with a specific angular momentum of the donor, which corresponds to $\gamma = M_a/M_d$. In this case, the change in the orbital separation is determined via

equation 1.29. Due to the high terminal velocities of the stellar winds of massive stars, however, the accretion of stellar winds are negligible. Therefore, by a good approximation, mass loss due to stellar winds leads to orbital widening as given by equation 1.30.

2.3.2 First phase of mass transfer

If the accretor is not a remnant, we assume that $\gamma = 2.5$, following [279]. We also test $\gamma = 1$, following [272] and [24]. In this study, we test two, constant values for mass transfer efficiency when the accretor is a non-compact object; $\beta = 0.3$ and $\beta = 0.7$. When the accretor is a neutron star or black hole, we assume that the accretion is Eddington-limited and $\gamma = M_{\mathrm{donor}}/M_{\mathrm{accretor}}$.

There are currently numerous uncertainties regarding mass transfer episodes with non-degenerate accretors [e.g. 187]. The fraction of the transferred mass that is eventually ejected from the binary and the specific angular momentum that is removed from the system depends on many factors. For example on whether an accretion disk is formed during the mass transfer episode [e.g. 202], on how efficiently the accretor star is spun up due to accretion [254], on whether accretion is possible above the critical rotation of the accretor star [277] and on the response of the radius of the accretor star on thermal timescale [see e.g. 275, 139, 293].

Detailed binary evolution models of massive stars indicate a low mass transfer efficiency ($\beta \approx 0.1$, on average) for mass transfer phases with evolved donors, if it is assumed that accretion is not possible above critical rotation [e.g. 191]. If the donor star is still on main sequence, tides can be sufficiently strong to counteract the spinning up, leading to higher mass transfer efficiencies (see e.g. [316]). These findings are broadly consistent with a few observational studies ([268]; [318] and

see also [402]). On the other hand, there are theoretical and observational studies, which conclude near-conservative mass transfers episodes among massive stars [e.g 312, 370], therefore a consensus regarding this physical process is still missing.

2.3.3 Mass transfer stability criteria and treatment of mass transfer

We determine the stability of mass transfer with the use of the so-called mass-radius exponents ([326] and see also equation 1.19). As explained in section , three different mass transfer modes can be distinguished: stable mass transfer on nuclear time scale ($\zeta_L \leq \min(\zeta_{ad}, \zeta_{eq})$), stable mass transfer on thermal timescale ($\zeta_{ad} \geq \zeta_L \geq \zeta_{eq}$.) and unstable mass transfer ($\zeta_L > \max(\zeta_{ad}, \zeta_{eq})$. In the first two cases, we assume that the mass transfer rate is $\dot{m} = M_d/\tau$, where τ is the nuclear timescale in the first and the thermal timescale in the second case. If the mass transfer is dynamically unstable, we assume common envelope evolution (see section 2.3.4).

As a major simplification, we assume a constant ζ_{ad} and ζ_{th} for a given stellar evolutionary phase (these are summarised in Table 2.2). Giants with deep convective envelopes tend to have low ζ_{ad}, possibly even negative. Therefore, donor stars of this type are likely to initiate unstable phases of mass transfers. At what stage the deep convective envelope develops in massive stars is still very uncertain. It is common to use effective temperature as a proxy for the evolutionary stage at which such an envelope is developed (we will note this as $T_{eff,boundary}$). We test two assumptions. First, that a deep convective envelope develops at an effective temperature $\log T_{eff} = 3.73\,K$, following [150] and [24]. In the second model variation, we follow the prescription of [167]. This prescription gives $T_{eff,boundary}$ as a function of luminosity and metallicity. The predicted values of $T_{eff,boundary}$ from [167] are typically considerably cooler than $\log(T_{eff}) = 3.73\,K$.

2.3.4 Common envelope evolution

In this study, we model common envelope evolution by adopting the energy formalism [e.g. 379, 409]. As the common envelope engulfs and exerts friction on the binary, the orbital separation starts to shrink. It is assumed that a fraction (α_{CE}) of the energy liberated from the orbital energy is used to unbind the envelope. Then the orbital separation by the end of the CEE phase is determined according to equation 1.28. Several studies published tabulated or fitted data for λ (i.e the parameter describing the structure of the envelope, see section 1.2.7). for a range of masses and evolutionary stages [e.g. 67, 388, 199, 57, 179, 168]. The values of these calculated λ parameters can vary over orders of magnitude, depending on the radius and the mass of the donor star and on the metallicity. [168] and [179] predict, however, that for sufficiently massive stars ($M_{\rm ZAMS} \gtrsim 30\,M_\odot$), λ varies only by a factor of a few ($\sim$2-5) as a function of stellar parameters and metallicity, once its radius has expanded sufficiently ($R \gtrsim 500$-$1000\,R_\odot$), given that the star still has mostly radiative envelopes (see e.g. Fig. 1 in [179] and Fig. C.3 in [168]).

In this study, we assume a constant $\lambda = 0.05$, which is in reasonable agreement with the results of [179] for stars with $M_{\rm ZAMS} \gtrsim 30\,M_\odot$ and $R \gtrsim 500\,R_\odot$. We note that we assume that Hertzsprung gap donors cannot survive CEE episodes [69]. This also implies that donor stars in GW progenitors typically have $R \gtrsim 500\,R_\odot$ at the onset of the CEE in our simulations. We assume $\alpha_{CE} = 1$.

2.3.5   Mass transfer episode types based on the evolutionary phase of the donor

We distinguish the following mass transfer phase types based on the evolutionary stage of the donor star.

Case A: the donor is a main sequence star (see e.g. [316]). If the period of the system is sufficiently short, the secondary might also fill its Roche-lobe, leading to the formation of contact systems ([274]; [380]; [231]). The outcome of Case A mass transfer phase is expected to be very different from those which start with an evolved giant donor (i.e Case B and Case C). As opposed to giants, main sequence stars do not have fully developed helium cores. During Case A mass transfer, fusion in the developing helium core is expected to halt because of the rapidly dropping central temperatures. Consequently, the mass of the naked helium star that is left after the end of Case A mass transfer phase is lower than for binaries experiencing mass transfer episodes with evolved donor stars (e.g. see [191]). In populaton synthesis codes like `SeBa`, it is challenging to model Case A mass transfer episodes accurately. There are two major reasons for this. Firstly, the stellar tracks of [138] do not track the mass of the developing helium core on the main sequence. The core mass is only determined at the start of the Hertzsprung gap phase. Secondly, a constant mass-radius exponent is assumed for a given stellar evolutionary phase (see subsection 2.3.3). This means that the radius response of the donor during a Case A mass transfer phase is assumed to be the same, regardless of how much mass had already left the star (i.e. even, if in principle most of the hydrogen rich mass had already left the star). The consequence of these two points is that, the amount of mass that is transferred to the accretor can be significantly overestimated, and the mass of the black hole that the donor eventually forms can be severely underestimated by codes like `SeBa`. For a different apporach in a binary population synthesis code, see e.g. [10]

or [180, 95], where in the last two, the stellar evolution is obtained by interpolating in tabulated data from a dense grid of detailed interacting stellar models. This approach allows for a more accurate modelling of Case A mass transfer episodes. To conclude, the outcome of Case A mass transfer episodes predicted by codes based on the stellar tracks of [138] should be treated with caution. Nevertheless, we still show such systems in this work for completeness.

Case B: the donor star is crossing the Hertzsprung gap. During this evolutionary phase of the donor star, a large and rapid increase in stellar radius occurs. The mass transfer phase ends with the donor losing its hydrogen envelope, leaving a naked helium star behind [but see 192]. Since the Hertzsprung gap phase lasts only for a few $\sim 10^4$ years, the helium core does not have sufficient time to significantly grow and therefore the mass of the helium star (and therefore the black hole that is eventually formed) is not strongly dependent on the exact initial separation of the binary. Furthermore, these systems are not significantly affected by LBV winds (assuming steady mass loss rates). As noted in section 2.3.4, we follow [69] and assume that binaries with donor stars crossing the Hertzsprung gap cannot survive CEE.

Case C: the donor star is in its core helium burning phase. We distinguish two sub-categories: (i) Case Cr: core helium burning donor star with radiative envelope, (ii) Case Cc: core helium burning donor star with deep convective envelope. We assume that the mass transfer stability criteria is the same for Case B and for Case Cr mass transfer phases (see Table 2.2). Yet, there are important differences in the predicted outcome of these two episodes, as the core helium burning phase lasts orders of magnitude longer with a slower expansion in radius. This means that for Case Cr mass transfers, the mass of the remnant that the donor star eventually forms is sensitively dependent on the initial separation, since the mass of the helium core can grow significantly during the core-helium burning phase. Moreover, the effects

of LBV winds are no longer negligible. Donor stars with deep convective envelopes have very different envelope structures and therefore different mass transfer stability criteria. As already mentioned, unstable mass transfer phases are more readily realised for these systems (see Table 2.2 and A.1).

2.3.6 Supernova and natal kicks

The mass of the remnant after core collapse is computed based on the delayed supernova model from [97] (see also Fig. 1.4). This prescription determines the remnant mass as a function of CO core mass, which in `SeBa` is obtained from the fits of [138]. The kick velocity for black holes is calculated as :

$$v_{\mathrm{BH}} = (1 - f_b) \left(\frac{M_{\mathrm{NS}}}{M_{\mathrm{BH}}} \right) v_{\mathrm{kick}} \tag{2.1}$$

Where f_b is the fallback (i.e. the fraction of matter that is initially ejected but then accreted by the compact object), M_{NS} is the canonical neutron star mass $M_{NS} = 1.4 M_\odot$ and v_{kick} is a random velocity kick drawn from the distribution inferred by [365] from proper motion measurements of pulsars. The distribution of [365] is a combination of two Maxwellian functions with velocity dispersions of $\sigma = 75\,\mathrm{km/s}$, and $\sigma = 315\,\mathrm{km/s}$, and weights of 0.42 and 0.58, respectively.

2.3.7 Stellar wind prescriptions

Massive stars lose a substantial fraction of their mass via stellar winds. We can roughly group stellar wind mechanisms into three groups; line-driven winds (which also includes Wolf-Rayet winds), winds of Luminous blue variables (LBVs), and dust-driven winds. Line-driven winds can be further distinguished based on whether

Table 2.2: Summary of the mass transfer stability criteria used in this study for each stellar evolutionary phase. For HG and CHeB stars with radiative envelopes we show two values (4 and 7.5) as we test both values in our study. HW87 stands for [130]

	Main sequence	Hertzsprung gap	Core helium burning phase	AGB phase	Helium star	Helium giant
ζ_{ad}	*4*	*4 or 7.5*	*For radiative envelope: 4 or 7.5* *For fully convective envelope: HW87*	*HW87*	*15*	*HW87*
ζ_{th}	*0.55*	*-2*	*For radiative envelope: -2* *For fully convective envelope: 0*	*0*	*1*	*-2*

they are optically thin (typically stellar winds of main sequence and evolved stars with hydrogen envelopes) or they are optically thick (line-driven winds of stripped helium stars, i.e. Wolf-Rayet winds). In the following, we briefly summarise the stellar wind prescriptions we use in this study, while Table 2.3.7 shows at what evolutionary stage these prescriptions are applied.

Line driven winds of O/B stars are modelled in `SeBa` using the mass-loss rates from [376], as long as the star is within the grid defined by [376], otherwise, the empirical formula from [248] is used. These mass-loss rates are applied until stars reach $T_{\text{eff}} \sim 8000K$ (see Table 2.3.7).

We note that [376] estimates the global metallicity dependence to be $\dot{M} \propto Z^{0.69}$ for O stars, by assuming a metallicity dependence of the final wind velocity to be $v_\infty \propto Z^{0.13}$, following [194]. This is consistent with the observations as shown by [237], although their results still depend on the findings of [194]. We note that however, [177] and [32] find weaker metallicity dependence of escape velocity, where in the latter, the exponent can even be negative for high luminosity stars. In `SeBa`, we assume $\dot{M} \propto Z^{0.85}$ (i.e. ignoring the metallicity dependence of v_∞), so that we are consistent with other population synthesis studies (e.g. [69, 214, 107, 336], but see e.g. [82] in which $\dot{M} \propto Z^{0.69}$ is used. We assumed that solar metallicity is Z = 0.02.

If a main-sequence star is outside of the grid defined by [376], in which case,

the empirical formula of [248] is used, we also assume a metallicity scaling $\sim Z^{0.85}$. We note that this is different from the what was originally suggested by [182] for this particular wind prescription, which is $\sim Z^{0.5}$. We do this so that there is a consistent metallicity dependence for optically thin line-driven winds.

LBV stars, stars beyond the Humphreys - Davidson limit, experience very high mass loss rates, in the order of $\dot{M}_{\mathrm{LBV}} \sim 10^{-5}$-$10^{-3} M_{\odot}\mathrm{yr}^{-1}$, although this is highly uncertain. Even less is known about their possible eruptions, in which huge amount of mass is lost in a very short time ([137]; [371]; [325]). For the mass-loss rates of LBV stars, we follow the assumption of [26], i.e. the mass loss rate is constant and has a value of $\dot{M}_{\mathrm{LBV}} = 1.5 \cdot 10^{-3} M_{\odot}\mathrm{yr}^{-1}$.

If the star becomes a cool giant (ie $T_{\mathrm{eff}} \leq 8000K$), we calculate the mass loss rate according to Reimer's empirical formula [285]. We compare it with the mass loss from [248] and we take the maximum value. For the mass loss rates of thermally pulsating AGB stars, we use the prescription of [363]. Mass loss rates for helium stars and helium giants (Wolf-Rayet star winds) are calculated according to [307].

In section 2.5, we investigate the impact of uncertainites in stellar winds on massive binaries that interact via mass exchange and on progenitors of GW sources. We test three stellar wind models, which are the following: 'Model I' with our standard stellar wind model ($f_{\mathrm{wind}} = f_{\mathrm{wind,WR}} = 1$), 'Model II' with the optically thin line driven winds scaled down by a factor 3 ($f_{\mathrm{wind}} = 1/3, f_{\mathrm{wind,WR}} = 1$) and 'Model III' where besides the optically thin line driven winds, Wolf-Rayet-like winds are also scaled down ($f_{\mathrm{wind}} = f_{\mathrm{wind,WR}} = 1/3$). For the exact description of our applied stellar winds prescriptions and scaling factors, see Table 2.3.7. With Model II, we aim to study the implications of [178]; [339]; [32] in a simplified way. These studies found that the prescription of [376] systematically overpredicts the mass loss by a factor $\sim 2-3$. With Model III. we investigate the general uncertainties in

the mass loss rates of stripped helium stars (see e.g. [307]). The latter becomes especially significant for interacting binaries, as envelope loss due to a mass transfer episode can significantly increase the time spent as a Wolf-Rayet star.

2.3.8 Initial conditions

Observations suggest that about half of the stars are in binaries (or in higher order, hierarchical systems) and this multiplicity fraction increases with increasing stellar mass [74] see also 1.2). In particular, [303] showed that the binary fraction reaches $f_b \simeq 0.7$ for stars in the mass range $M \simeq 15$-$60\,M_\odot$. The same observations showed that the orbital period distribution of these young, massive binaries favour short period systems:

$$f_p(\log p) \propto (\log p)^\pi, \qquad \text{for } \log p \in [0.15, 5.5], \tag{2.2}$$

here period, p is in days and $\pi = -0.55$. Although, other studies suggested somewhat flatter distributions (e.g. [171] or [76] based on observations of B stars in the Tarantula Nebula in the Large Magellanic Cloud).

According to [303], the mass ratio distribution of massive stars is nearly flat, $f_q \propto q^{-0.1}$, while the distribution of eccentricities follows $f_e \propto e^{-0.42}$. A similar mass ratio distribution is inferred by [171], while [76] finds $f_q \propto q^{-2.9}$ for B stars in the Tarantula Nebula, and [304] finds $f_q \propto q^{-1}$ or O stars in the Tarantula Nebula.

The effects of uncertainties in initial conditions were investigated by [399], and they found that only the changes in the initial mass function alters significantly the properties of the merging compact binary object population [but see 166]. There are observational and theoretical indications that the initial mass function might not

be universal [see 56, and references therein]. In our simulations, we assume these initial distributions are not correlated, however, although this might not be a valid assumption [see e.g. 235, 166].

In this chapter we used the following initial conditions for our simulations:

- Initial mass function: the initial mass of the primary is drawn from a distribution determined by [176]. In the mass range $M_{\mathrm{ZAMS}} = 20 - 100\,M_\odot$, this is $N_{\mathrm{IMF}}(M_{\mathrm{ZAMS}}) \simeq M_{\mathrm{ZAMS}}^{-2.3}$.

- Initial mass ratio distribution: we assume a uniform mass ratio distribution between 0.1 and 1, where the mass ratio is defined as $q = M_{\mathrm{ZAMS,2}}/M_{\mathrm{ZAMS,1}}$, that is the ratio of the mass of the initially secondary and the mass of the initially primary star. A flat distribution is in a reasonable agreement with observations of [303].

- Initial separation distribution: we assume a flat distribution in the logarithmic space of binary separation in the interval of $1R_\odot$-$10^4 R_\odot$; $N_a \simeq \log(a)$. This is equivalent to Opik's law, ie. a uniform distribution in $\log(p)$ [253].We note that since we sample from the distribution of semimajor axis, some of our systems have sub-day periods. However, we discard any systems that fill their Roche-lobe at zero-age main sequence and we do not take them into account for calculating event rates (see section A.1).

- Initial eccentricity distribution: the initial eccentricity assumed to follow a thermal distribution [126], i.e. $f_e \propto e$.

2.3.9 Simulation setup

In section 2.4, we explore the impact of uncertainties of first phase of mass transfer on the merging binary black hole population. We do this by varying four parameters in our simulations, namely:

1. γ, which expresses the specific angular momentum lost from the binary during a non-conservative mass transfer phase as a fraction of the total specific angular momentum of the binary. We vary γ only for non-compact accretors.

2. β, which describes the mass transfer accretion efficiency. We vary β only for non-compact accretors.

3. $\zeta_{\mathrm{ad,rad}}$, which is the mass-radius exponent for giant donors with radiative envelopes. It determines the boundary between stable and unstable mass transfer episodes.

4. $T_{\mathrm{eff,boundary}}$, which is the effective temperature at which a deep convective envelope is expected to develop.

The details of our model variations are summarised in Table 2.1. Using only our standard stellar wind model, we run simulations with all possible combinations of γ, β $\zeta_{\mathrm{ad,rad}}$ and $T_{\mathrm{eff,boundary}}$ (i.e 16 models in total, named M1..M16, see e.g. Table 2.3). We simulate 10^6 binaries at each value of our metallicity grid for each model variations. Our metallicity grid is defined as $Z = [0.02, 0.01, 0.005, 0.003, 0.001, 0.0007,$ $0.0005, 0.0003, 0.0001]$. To make comparisons with other studies easier, we have converted ζ to the critical mass ratio for each model variation in table $A.1$. We calculate the merger rate density in the local universe, as summarised in section A.1.

In section 2.5, in which we investigate the impact of uncertainties in mass loss

Table 2.3: A summary of our predicted rates for all of our model variation with our standard stellar wind models (i.e. Model I)

Model name	Model description	R_{stable} [Gpc^{-3}yr^{-1}]	R_{RCEE} [Gpc^{-3}yr^{-1}]	R_{CCEE} [Gpc^{-3}yr^{-1}]	R_{total} [Gpc^{-3}yr^{-1}]
M1	$\gamma = 2.5$, $\beta = 0.3$, $\zeta_{\text{ad,rad}} = 4$, T_{eff}-K	13.8	5.9	3.7	23.4
M2	$\gamma = 2.5$, $\beta = 0.7$, $\zeta_{\text{ad,rad}} = 4$, T_{eff}-K	10.2	8.7	7.5	26.4
M3	$\gamma = 2.5$, $\beta = 0.3$, $\zeta_{\text{ad,rad}} = 4$, T_{eff}-IT	13.4	0.7	5.0	19.1
M4	$\gamma = 2.5$, $\beta = 0.7$, $\zeta_{\text{ad,rad}} = 4$, T_{eff}-IT	9.1	0.9	11.0	21.0
M5	$\gamma = 2.5$, $\beta = 0.3$, $\zeta_{\text{ad,rad}} = 7.5$, T_{eff}-K	60	3.3	4.0	67.3
M6	$\gamma = 2.5$, $\beta = 0.7$, $\zeta_{\text{ad,rad}} = 7.5$, T_{eff}-K	88.9	4.2	7.8	100.9
M7	$\gamma = 2.5$, $\beta = 0.3$, $\zeta_{\text{ad,rad}} = 7.5$, T_{eff}-IT	53.9	0.6	5.0	59.5
M8	$\gamma = 2.5$, $\beta = 0.7$, $\zeta_{\text{ad,rad}} = 7.5$, T_{eff}-IT	77.4	0.3	10.6	88.3
M9	$\gamma = 1$, $\beta = 0.3$, $\zeta_{\text{ad,rad}} = 4$, T_{eff}-K	2.2	11.8	19.4	33.4
M10	$\gamma = 1$, $\beta = 0.7$, $\zeta_{\text{ad,rad}} = 4$, T_{eff}-K	2.4	12.8	15.0	30.2
M11	$\gamma = 1$, $\beta = 0.3$, $\zeta_{\text{ad,rad}} = 4$, T_{eff}-IT	2.1	3.5	42.2	47.8
M12	$\gamma = 1$, $\beta = 0.7$, $\zeta_{\text{ad,rad}} = 4$, T_{eff}-IT	2.4	1.4	24.2	28.0
M13	$\gamma = 1$, $\beta = 0.3$, $\zeta_{\text{ad,rad}} = 7.5$, T_{eff}-K	43.9	7.4	19.0	70.3
M14	$\gamma = 1$, $\beta = 0.7$, $\zeta_{\text{ad,rad}} = 7.5$, T_{eff}-K	73.3	6.0	13.8	93.1
M15	$\gamma = 1$, $\beta = 0.3$, $\zeta_{\text{ad,rad}} = 7.5$, T_{eff}-IT	45.8	3.1	40.7	89.6
M16	$\gamma = 1$, $\beta = 0.7$, $\zeta_{\text{ad,rad}} = 7.5$, T_{eff}-IT	76.0	0.6	25.1	101.7

rates due to stellar winds, we perform binary evolution simulations for 10^6 systems at metallicities Z = 0.02, 0.01 and 0.005. We test three stellar wind models (e.g. Model I, II, III, see section 2.3.7) and vary $\zeta_{\text{ad,rad}}$ and γ, while assuming the convective envelope prescription of [150] and $\beta = 0.3$.

We note, however, that with the metallicity specific star formation rate model that we assume in this study (see equations B.11 and A.6), GW progenitors formed at $Z \gtrsim 0.005$ do not contribute to the merger rate density in the local universe significantly. Consequently, in our models, different assumptions about mass loss rates of line-driven winds (which are only relevant at $Z \gtrsim 0.005$) also do not affect the demographics of GW sources at $z \sim 0$ significantly. However, whether merging binary black holes with masses $M_{\text{BH}} \sim 30\,M_\odot$ could be formed in an environment that is typical for the LMC and the SMC or even in the Milky Way (i.e. Z~0.02-0.005) remains an important and open question [see e.g. 330]. Furthermore, the models for metallicity-specific star formation rates, as well as the metallicity dependence of stellar winds are highly uncertain [see e.g. 53].
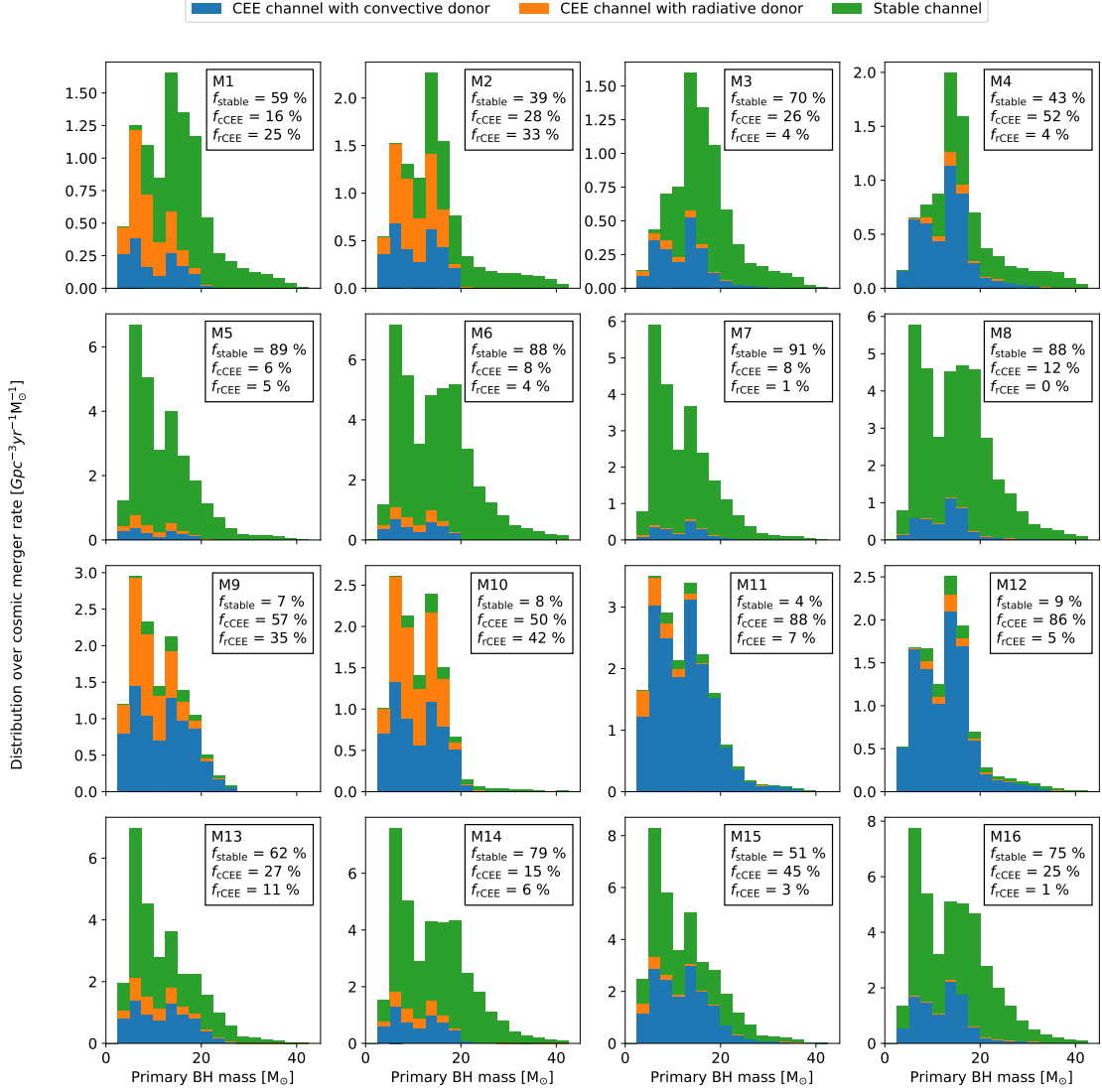
Figure 2.2: The mass distribution of the primary of the merging binary black hole in the local universe (z = 0) for all of our models with our standard stellar wind models (e.g. $f_{\mathrm{wind}} = f_{\mathrm{wind,WR}} = 1$, see Table 2.1). The distribution is shown by stacked histograms, where each colour indicates a different formation channel. In the legend on the upper right corner in each panel, we show the percentage of each channel. In Fig. A.10, we provide a comparison between these distributions and the primary mass distribution of BH-BH binaries as inferred from the the third LIGO–Virgo Gravitational-Wave Transient Catalog (GWTC-3) [9]
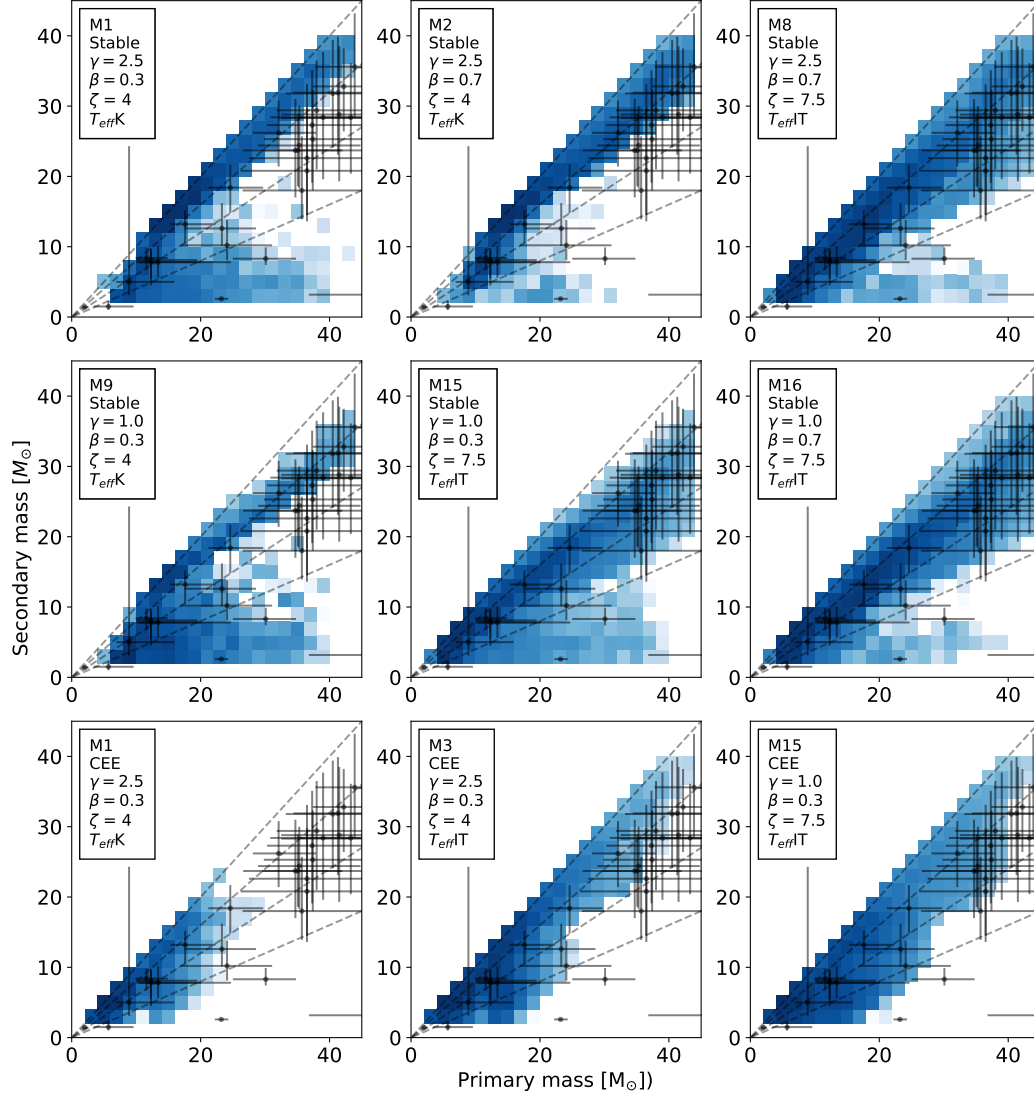
Figure 2.3: 2D Histograms that show the masses of the merging binary black holes for a few selected models at Z = 0.0007. Each histogram has been normalised to the merger efficiency of their own model variation. The dashed lines show constant mass ratios. We also show the observed GW detections from the third LIGO–Virgo Gravitational-Wave Transient Catalog (GWTC-3) and associated measurement uncertainties [9]. We do not show those detections, where any of the inferred merging black hole mass is above $M_{\mathrm{BH}} \geq 45\,M_{\odot}$.
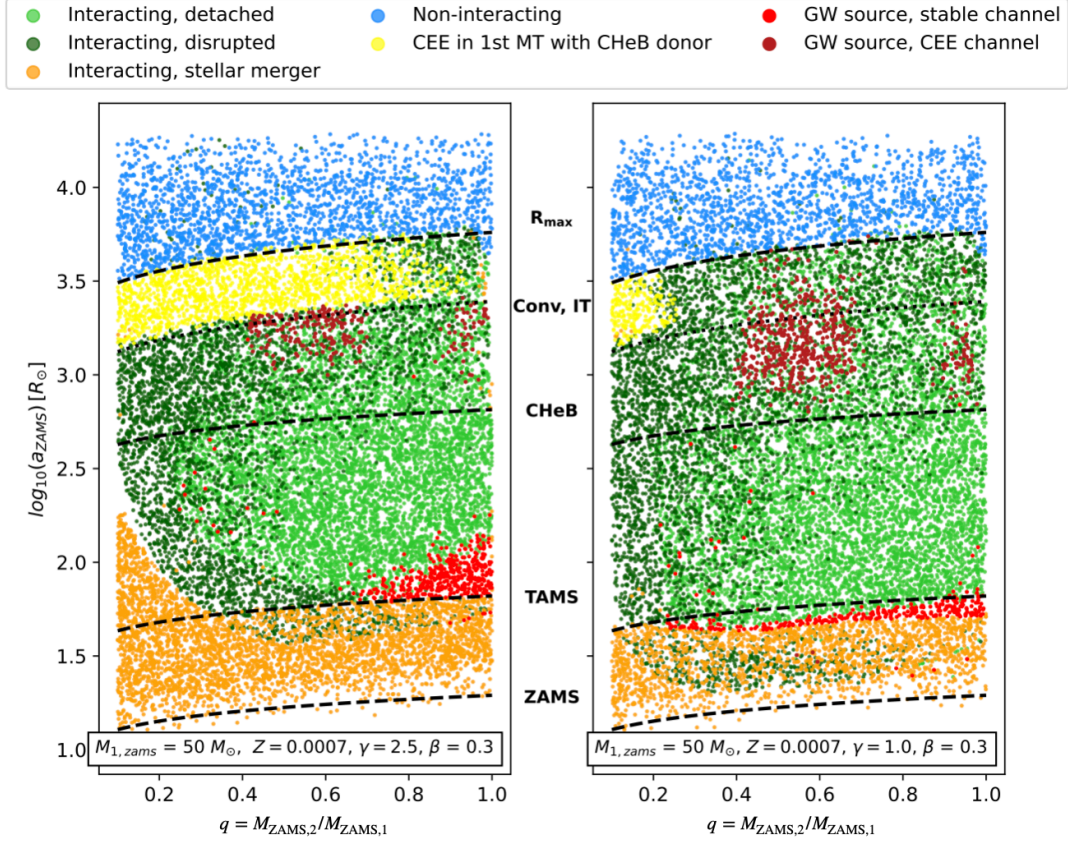
Figure 2.4: Our simulated binaries in the initial mass ratio - initial separation space. We show the orbital separation after tidal circularisation. The systems are simulated with the following parameters; $\beta = 0.3$, $\zeta_{ad,rad} = 7.5$. Furthermore, we have used the assumption of [150] regarding the development of deep convective envelopes. In the left panel we show systems with $\gamma = 2.5$, in the right with $\gamma = 1$. We show the outcome of each simulated binary with difference colours. We distinguish the following types; (i) interacting, detached: these binaries interact via mass transfer phases at least once and form detached BH-BH binaries which do not merge due to gravitational waves within Hubble time, (ii) interacting, disrupted: these binaries interact at least once and get disrupted due to the supernova kick of one of the binary components, (iii) interacting, stellar merger: these systems interact at least once and merge due to one of their mass transfer phases. Their first mass transfer phase is typically stable or unstable with a MS or HG donor, (iv) non-interacting: none of the stars fill their Roche-lobes, they either stay detached or get disrupted, (v) CEE in 1st MT with CHeB donor: these binaries have a core-helium burning donor at the onset of the first mass transfer phase, and they initiate a dynamically unstable mass transfer (vi) GW source, stable channel: gravitational wave progenitors evolving via two subsequent stable mass transfer phases, (vii) GW source, CEE channel: gravitational wave progenitors evolving via a stable and an unstable mass transfer phase.

2.4 Results: the impact of uncertainties in stable mass transfer

In Fig. 2.2, we show the primary mass distribution of merging binary black holes in the local universe (z = 0) for the three dominant channels: stable, rCEE, cCEE for all of our model variations. In Table 2.3, we show the corresponding predicted cosmic merger rate densities.

The total predicted merger rate densities (R_{total}) are in a broad agreement with the currently inferred rate from LIGO and Virgo observations [which is $R_{\text{GWTC3}} = 28.3^{+13.9}_{-9.1} \text{Gpc}^{-3}\text{yr}^{-1}$, see e.g. 6]. R_{total} of model variations with $\zeta_{\text{ad,rad}} = 4$ are within a factor of two of this inferred value, while R_{total} of model variations with $\zeta_{\text{ad,rad}} = 7.5$ are larger than the observed rate by a factor of 3-4. In Fig. A.10 and section A.4, we provide a comparison between the primary mass distribution of our models and inferred distribution from GWTC-3 [9].

Fig. 2.2 clearly demonstrates that the relative rate of each formation channel varies significantly with different model variations. Parameters γ and $\zeta_{\text{ad,rad}}$ have the largest impact. The stable channel dominates in 11 out of 16 model variations, and the cCEE channel dominates in the remaining 5. The rCEE channel is non-negligible only in 4 model variations. In 12 model variations, the vast majority of the most massive systems originate from the stable channel [in agreement with 407, 42].

While GW sources form most efficiently via the CEE channel in models M1-M3 (see e.g. $\zeta_{\text{ad,rad}} = 4$ and $\gamma = 2.5$ models in Fig. A.11), R_{total} is still dominated by the stable channel in these model variations. This is due to the relatively long formation times associated with the stable channel and the monotonic increase of the cosmic star formation rate up to $z \sim 2$ (see e.g. [205]). Most of the sources of the stable

channel are formed at higher redshifts than the sources of the CEE channel, and at these higher redshifts the star formation rate is also higher, which leads to an increased merger rate. [see similar conclusions in 247, 407]

Fig. 2.3 shows the predicted mass ratios distribution of GW sources and its dependence on primary BH mass. For relatively massive systems ($M_{\rm BH} \gtrsim 20\,M_\odot$), this distribution is dependent on the assumptions on the uncertain binary physics. The formation channels can yield a population of merging binary black holes with a relatively narrow range in mass ratios ($0.8 \lesssim q \lesssim 1.0$) or a moderately wide mass ratio distribution ($0.5 \lesssim q \lesssim 1.0$). The mass ratio distributions of the most massive GW sources of the stable channel is most sensitive to the assumed mass transfer stability parameter. In models with $\zeta_{\rm ad,rad} = 4$, the typical mass ratios are between $0.8 \lesssim q \lesssim 1.0$, while in models with $\zeta_{\rm ad,rad} = 7.5$, the mass ratio distribution becomes much broader, i.e. $0.5 \lesssim q \lesssim 1.0$. We notice smaller variations in the mass ratio distribution for the CEE channel with different assumptions in binary physics, though model variations with $\gamma = 1$ produce somewhat broader mass ratio distributions than models with $\gamma = 2.5$. The less massive systems generally have much wider mass ratio distributions in all model variations.

Overall, we do not notice significant variations in the merger rate density, BH mass range, or the shape of the mass distributions across different model variations. Our results, therefore, show that while the main GW observables do not depend sensitively on the uncertainties studied here, the relative importance of dominant channels do. In other words, the formation paths of the majority of GW progenitors can be entirely different depending on the assumptions on how the first phase of mass transfer proceeds and yet the predicted demographics of merging binary black holes are very similar [though we neglect spins in this study, see e.g. 22]. This highlights why it is extremely challenging to infer physics of massive binary evolution solely from GW observations, given the huge uncertainties in the current models.

Next, we briefly summarise the most important ways how uncertainties related to the first phase of mass transfer can affect the relative importance of the dominant GW formation channels, while in sections 2.4.1 - 2.4.4, we discuss these effects in detail.

1. The assumed angular momentum loss has a strong impact on which formation channel dominates. Typically, the stable channel dominates in models with $\gamma = 2.5$ (see e.g. first row in Fig. 2.2), while the cCEE channel dominates, if $\gamma = 1$, however the latter depends on the assumed $\zeta_{\mathrm{ad,rad}}$ as well (compare e.g. third and fourth row in Fig. 2.2).

2. An increased $\zeta_{\mathrm{ad,rad}}$ leads to a higher merger rate of the stable channel. However, this increase is only significant for relatively lower mass black holes ($M_{\mathrm{BH,1}} \lesssim 20\,M_\odot$). With lower mass transfer efficiencies (e.g. $\beta = 0.3$), we find that the merger rate of binary black holes with $M_{\mathrm{BH,1}} \gtrsim 20\,M_\odot$ is not affected at all, unless $\gamma = 1.0$.

3. The merger rate of the rCEE channel is only non-negligible with the convective envelope prescription of [167]. Furthermore, the GW sources of this channel comprise of relatively lower mass BHs (i.e $M_{\mathrm{BH,1}} \lesssim 20\,M_\odot$) in all of our model variations (see section 2.4.4).

2.4.1   The impact of angular momentum loss on the stable channel

As evident from Fig. 2.2, the merger rate density of the stable channel (R_{stable}) depends sensitively on the assumed angular momentum loss during the first phase of mass transfer (e.g. compare first with third row). In our $\gamma = 2.5$ models, this formation channel is particularly efficient and is typcially the dominant out of the three main formation paths considered here. On the other hand, in the $\gamma = 1$

models, the merger rate of this channel is negligible, unless the mass-loss exponent is increased, i.e. $\zeta_{\mathrm{ad,rad}} = 7.5$.

In order to understand the reason for the relation between γ and R_{stable}, we need to consider the following three important features of this formation channel:

1. *The progenitors of the stable channel have relatively short initial orbital separations.* For these systems, the largest values of a_{ZAMS} is a few hundred solar radii (shown in Fig. 2.4). If a_{ZAMS} is much larger than that, the orbit does not shrink sufficiently by two phases of stable mass transfer, such that a merging binary black hole would be formed.

2. *There is a minimum initial orbital separation for the binaries of the stable channel.* We identify a minimum a_{ZAMS} associated with this channel, below which binaries typically do not form GW sources. This minimum a_{ZAMS} roughly coincides with the separation at which the initial primary would fill its Roche-lobe just when it evolved off MS (see Fig. 2.4). If a_{ZAMS} is below this minimum value, the first phase of mass transfer (Case A) leads to a stellar merger eventually in the vast majority of cases (shown in Fig. 2.4). As explained in detail in section A.2.3, even if the initial orbit is wide enough for the system to survive the Case A mass transfer phase, the binary still likely merges in the subsequent mass transfer event. In this case, the first phase of Case A mass transfer leads to a less massive black hole from the initial primary (because the formation of the helium core is halted) and to a more massive secondary (because more mass is transferred to the accretor) with respect to systems experiencing a mass transfer episodes at later stages. This results in a relatively high mass ratio at the onset of the second phase of mass transfer ($q_{\mathrm{MT,2}}$) and such systems merge as a result of a dynamically unstable second phase of mass transfer (i.e. typically $q_{\mathrm{MT,2}} \gtrsim q_{\mathrm{crit}}$ with $\zeta_{\mathrm{ad,rad}} = 4$, where q_{crit}

is the critical mass ratio, i.e. the mass ratio above which the mass transfer episodes proceeds in a dynamically unstable fashion, see also Table A.1). To conclude, systems with a first phase of Case A mass transfer typically merge before forming BH-BH binaries [see also 100] and therefore, there exists a minimum initial separation associated with the stable channel. .

3. *The lower the angular momentum loss is, the wider the orbit becomes during the mass transfer phase.* This means that the orbital separation of binaries with $\gamma = 1$ typically widens more during the mass transfer phase than with $\gamma = 2.5$. The degree by which the orbit changes due to a first phase of (stable) mass transfer is primarily determined by the initial mass ratio (q_{ZAMS}), γ and β (see Fig. A.4). Systems that form GW sources via the stable channel typically have initially near equal masses ($0.7 \lesssim q_{\mathrm{ZAMS}} \lesssim 1.0$, but see e.g. [99]). This is because such binaries develop sufficiently large mass ratios by the onset of the second phase of mass transfer (see Fig. A.4), and therefore experience efficient orbital shrinking during a stable phase of mass transfer with a black hole accretor (see equation 3.16). For these initial mass ratio ranges, the orbit of the binary significantly widens in the $\gamma = 1$ models, while the net change in the orbital separation is very small in the $\gamma = 2.5$ models (see Fig. A.5). We note that, if q_{ZAMS} is very small, the orbit shrinks due to the first phase of mass transfer, even with $\gamma = 1$, but in that case $q_{\mathrm{MT},2}$ will be small and therefore the orbit will widen due to the second (stable) phase of mass transfer and no GW source will be formed (compare Fig. A.4 with Fig. A.5).

Considering these three points, it is possible to understand why the stable channel is inefficient with $\gamma = 1$. The orbit widens too much due to the first phase of mass transfer, even for those binaries that start out with the minimum a_{ZAMS} associated with this channel. Therefore, the binary black holes that eventually form this way are too wide to merge due to GWs within the Hubble time.

As shown in Fig. 2.2, stable channel can be efficient with $\gamma = 1$, if $\zeta_{\mathrm{ad,rad}} = 7.5$. In this case, the significant orbital widening due to the first mass transfer phase can be counteracted by the effect of the second phase of the mass transfer for sources with relatively large mass ratios at the onset of the second mass transfer ($3.2 \lesssim q_{\mathrm{MT,2}} \lesssim 5.5$, see equation 3.16). Such sources can form, if the first mass transfer phase is Case B and the mass transfer efficiency is relatively large (e.g. $\beta = 0.7$) or if the first mass transfer is (very late) Case A, which typically leads to large values of $q_{\mathrm{MT,2}}$.

The relationship between R_{stable} and γ is therefore dependent on the predicted outcome of Case A mass transfer episodes. We emphasise again our point in section 2.3.1, that the treatement of Case A mass transfer in stellar evolutionary codes based on [138], is extremely simplified and its predictions should be treated with caution. While we should expect that the prediction of large values $q_{\mathrm{MT,2}}$ following a Case A mass transfer phase is qualitatively true (and theferore a minimum a_{ZAMS} could indeed exist for the stable channel), whether indeed the vast majority of them would be above q_{crit} should be further investigated.

2.4.2 The impact of angular momentum loss on the CEE channel

Fig. 2.2 shows that the efficiency of the cCEE channel is also sensitively dependent on the assumed γ, although in an opposite way as for the stable channel. R_{cCEE} is about a factor of 8 larger with $\gamma = 1$ than with $\gamma = 2.5$ in our low mass transfer efficiency models. With $\beta = 0.7$, this difference is about a factor of two.

Below we explain the reason for this relationship. The binaries of the cCEE channel have a_{ZAMS} of a few thousand solar radii. Only in this case, the binaries are sufficiently wide by the onset of the second phase of mass transfer, such that the

donor star (i.e. the initial secondary star) fills its Roche-lobe with a deep convective envelope.

In general, binaries have wider orbital separations at the onset of the second phase of mass transfer ($a_{\mathrm{MT,2}}$) with $\gamma = 1$ than with $\gamma = 2.5$. Consequently, there are significantly more systems in the latter case for which the second phase of mass transfer is Case Cc (compare the top panels of Fig. A.7). This also leads to a higher R_{cCEE}, since in this channel the second phase of mass transfer is by definition Case Cc (see section 2.2.1). There are two reasons for this:

1. *The rate of unstable first phase of mass transfers of the widest interacting binaries sensitively depends on angular momentum loss.* The binaries with the longest periods that still exchange mass engage in Case Cc first phase of mass transfer (see Fig. 2.4). As shown in Fig. 2.4, in our low mass transfer efficiency model, the majority (~ 80 per cent) of Case Cc episodes occur in an dynamically unstable way, if $\gamma = 2.5$. For these binaries, the orbital separation drastically decreases due to the first phase of unstable mass transfer and these binaries typically do not form GW sources. On the other hand, the majority of the same mass transfer episodes are stable with $\gamma = 1$, and as a result, the orbit typically widens for these systems. This leads to larger values of $a_{\mathrm{MT,2}}$ and consequently a higher rate of Case Cc second phase of mass transfers compared to the models with $\gamma = 2.5$. Therefore, the critical mass ratio associated with a first phase of Case Cc mass transfer is sensitively dependent on the assumed γ and β, (see Fig. 2.4 and Table A.1). This can be understood by considering that with larger angular momentum loss, the orbit shrinks at a faster rate at the beginning of the mass transfer phase and therefore a dynamically unstable mass transfer phase is more easily instigated.

2. *The periods of binaries engaging in a first phase of Case Cr mass transfer tend*

to increase more with lower angular momentum loss. As a result, the number of binaries that have large $a_{\mathrm{MT},2}$ is higher in the models with $\gamma = 1$ with respect to models with $\gamma = 2.5$, and consequently, so is the rate of a second phase Case Cc mass transfer, since in wider binaries, the donor star fills its Roche-lobe at a later evolutionary stage and therefore it is more likely that this occurs when the star has already developed a deep convective envelope.

2.4.3   The impact of mass transfer stability parameter

Fig. 2.2 shows that R_{stable} increases and R_{rCEE} decreases with increasing $\zeta_{\mathrm{ad,rad}}$ (compare row 1 and 2, or row 3 and 4 of Fig. 2.2). This effect is not surprising; larger $\zeta_{\mathrm{ad,rad}}$ translates to larger q_{crit}, which implies a larger parameter space for stable mass transfer episodes, in case the donor star is evolved and has a radiative envelope. At the same time, the degree by which the orbital separation shrinks due to a stable phase of mass transfer significantly increases with increasing $q_{\mathrm{MT},2}$ (see e.g equation 3.16), which results in an efficient formation of GW sources via the stable channel. For example, with $q_{\mathrm{MT},2} = 3.2$ (i.e. q_{crit} at $\zeta_{\mathrm{ad,rad}} = 4$), the orbit shrinks typically by $\sim 200\ R_{\odot}$ due to a stable phase of mass transfer with a BH accretor, while the same with $q_{\mathrm{MT},2} = 5.5$ (i.e. q_{crit} at $\zeta_{\mathrm{ad,rad}} = 7.5$) is $\sim 1000\ R_{\odot}$. This means that the orbital shrinking due to a stable mass transfer with mass ratios $q_{\mathrm{MT},2} \gtrsim 5$ can be as efficient as due to common envelope evolution in our models.

However, Fig. 2.2 also shows that only the merger rate of relatively lower mass merging BH-BH binaries (i.e. $M_{\mathrm{BH},1} \lesssim 20\ M_{\odot}$) is significantly affected by an increased $\zeta_{\mathrm{ad,rad}}$ (and $\gamma = 2.5$). In particular, when we increase $\zeta_{\mathrm{ad,rad}}$ from 4 to 7.5, the merger rates of systems with $M_{\mathrm{BH},1} \gtrsim 20\ M_{\odot}$ remains practically unchanged in our low mass transfer efficiency model, and increases only by a factor of 3 in our high mass transfer efficiency models (while the R_{stable} for the entire mass range increases

almost by a factor of 9). The reason for this can be understood by inspecting Fig. A.6. At low metallicities, where we expect the vast majority of the GW progenitors to originate from, the maximum $q_{\mathrm{MT,2}}$ that binaries engaging in a first phase of Case B mass transfer develop significantly decreases with increasing $M_{\mathrm{ZAMS,1}}$. For example, at Z = 0.0007 and for binaries with $M_{\mathrm{ZAMS,1}} \gtrsim 60\,M_\odot$, this maximum of $q_{\mathrm{MT,2}}$ is about 3 and 3.5 for $\beta = 0.3$ and $\beta = 0.7$, respectively. Consequently, increasing $\zeta_{\mathrm{ad,rad}}$ from 4 to 7.5 (corresponding to increasing q_{crit} from 3.2 to 5) does not have a significant effect on R_{stable} for the most massive GW progenitors. An exception to this can bee seen in the model variations with $\gamma = 1$. In these models, the most massive GW sources of the stable channel have (a very late) Case A first phase of mass transfer, and develop $q_{\mathrm{MT,2}} \gtrsim 3.2$. In this case, increaseing $\zeta_{\mathrm{ad,rad}}$ affects the merger rate of the most massive binary black holes too (see last two panels in the 4th row of Fig. 2.2)

2.4.4 The impact of different convective envelope prescriptions

In our models with the convective envelope prescription of [167], the maximum primary mass of the BH-BH binaries of the cCEE channel is about $M_{\mathrm{BH,1}} \approx 20\,M_\odot$ (see e.g. first two columns of Fig. 2.2). This is about a factor of two lower than with the prescription of [150]. This is because the models of [167] predict that most massive stars (i.e. $M_{\mathrm{ZAMS}} \gtrsim 50\,M_\odot$) either never develop deep convective envelopes or they do at a late evolutionary stage, which is not followed by a significant expansion of stellar radius. This implies that the rate of Case Cc mass transfer episodes with donor stars with $M_{\mathrm{ZAMS}} \gtrsim 50\,M_\odot$ is negligible and therefore so is R_{cCEE} for $M_{\mathrm{BH,1}} \gtrsim 20\,M_\odot$.

The merger rate of rCEE is negligible with the prescription of [150]. In these models, stars develop a deep convective envelop soon after the onset of core-helium

burning. Therefore, the occurrence rate of a second phase of unstable Case Cr mass transfer is very low. This is no longer true for the models with the prescription of [167], in which the rCEE channel can account for up to 42 per cent of all mergers (see M10 in Fig. 2.2). However, the primary BH mass is always $M_{\mathrm{BH,1}} \lesssim 20\,M_\odot$ for this channel. This can be understood again by inspecting Fig. A.6. The maximum value of $q_{\mathrm{MT,2}}$ is either below or slightly above q_{crit} for the most massive systems experiencing a Case Cr mass transfer phase (depending on the assumed mass transfer efficiency). Therefore, very few binaries with $M_{\mathrm{1,ZAMS}} \gtrsim 50\,M_\odot$ initiate an unstable Case Cr phase. We can also see that the values of $q_{\mathrm{MT,2}}$ are considerably lower for Case C than for Case B mass transfer episodes. This is due to the strong LBV winds that decrease the mass ratios of the binaries over time. Therefore, metallicity independent LBV winds also contribute to the low R_{rCEE} in our models.

2.4.5 Comparison to earlier studies

Relatively early rapid population synthesis studies predicted that merging binary black holes overwhelmingly originate from the CEE channel [see e.g. 69, 27, 336], while the contribution from the stable channel is negligible. On the other hand, [247] found that the stable channel is the dominant source of merging binary black holes. Qualitatively similar results were found by several subsequent studies [i.e. 99, 251, 407]. A common interpretation for this difference is that in the latter studies, a significantly higher $\zeta_{\mathrm{ad,rad}}$ is assumed (or in case of detailed binary models, computed). For example, [247] assumes $\zeta_{\mathrm{ad,rad}} = 6.5$ following [102], which leads to higher rate of stable mass transfer episodes with significant orbital shrinkage when compared to, for example, [336].

Our results confirm that the value of $\zeta_{\mathrm{ad,rad}}$ indeed plays an important role for R_{stable} (see discussion in section 2.4.3). However, our models also suggest that the

significance of the stable channel is affected by the assumed angular momentum loss mode as well, and we expect this to be also the reason why the models of [27] predict a negligible R_{stable}. In particular, [27] assumes $\gamma = 1$ and a critical mass ratio of $q_{\mathrm{crit}} = 3$ for HG donors (for comparison, our assumed $\zeta_{\mathrm{ad,rad}} = 4$ is equivalent to $q_{\mathrm{crit}} = 3.2$, if the accretor is a BH). Therefore, the models of [27] are fairly similar to our M11 and M12 models (see Table 2.3). Our simulations of M11 and M12 indicate that the stable channel is essentially negligible, in broad agreement with [27]. However, in the models with a higher angular momentum loss (i.e. $\gamma = 2.5$), but with the same $\zeta_{\mathrm{ad,rad}}$, R_{stable} significantly increases and even dominates for $M_{\mathrm{BH},1} \gtrsim 25\,M_{\odot}$. In conclusion, the stable channel can embody a significant formation channel for merging binary black holes not only for $\zeta_{\mathrm{ad,rad}} \gtrsim 6.5$ but also for strong angular momentum loss modes such as $\gamma = 2.5$.

In the majority of our model variations, the most massive merging binary black holes originate from the stable channel (i.e. $M_{\mathrm{BH},1} \gtrsim 25\,M_{\odot}$) in broad agreement with [247]; [407] and [41]. In particular, our Fig. 2.2 can be directly compared to Fig. 5 of [407] and Fig. 7 of [42]. Our models generally agree more with that of [407] than with that of [42]. This is not surpising, as the models of [407] were generated by COMPAS [293], which also use the fitting formulae of [138]. Smaller differences between these models most likely can be attributed to different choices in binary physics assumptions of [407], such as $\zeta_{\mathrm{ad,rad}} = 6.5$, isotropic angular momentum loss mode, i.e. $\gamma = M_{\mathrm{d}}/M_{\mathrm{a}}$ and a mass transfer efficiency, which is related to the thermal timescale of the accretor star. The differences between our predictions and the results of [42] are more significant. While they predict that the stable channel dominates at high masses, the overall contribution of this channel is still small (~ 6.4 per cent). Furthermore, they find several other channels to be efficient, including ones in which only one phase of mass transfer occurs. These differences are most likely due to the following: i) their model is produced with BPASS [83, 331], which

uses detailed binary models, ii) they assume that if the accretor star accretes 5 per cent of its initial mass, it will evolve chemically homogeneously (which allows channels with only one mass transfer episode to be efficient), iii) they assume a super-Eddington accretion for BH accretors.

Furthermore, we find non-negligible differences in the reported final mass ratio distributions. In particular [42] finds that most systems from the stable channel have $q \lesssim 4$ (most likely can be attributed to their assumption of super-Eddington accretion rate), while [407] finds a relatively narrow range of $0.5 \lesssim q \lesssim 0.8$. On the other hand, the predicted mass ratios of the systems from the stable channel in our models typically peak at $q \approx 1$ and drop rapidly beyond $q \approx 0.8$ with $\zeta_{\mathrm{ad,rad}} = 4$ and beyond $q \approx 0.5$ with $\zeta_{\mathrm{ad,rad}} = 7.5$ (see Fig. 2.3). [407] finds a mass ratio distribution of the CEE sources in the range of $0.2 \lesssim q \lesssim 1.0$, which peaks around $q \approx 0.3$ and gradually decreases from that value with increasing q. While our predicted mass ratios for this channel are typically in the same range, they peak around $q \approx 1$ in all of our model variations.

2.4.6 Remark about predicted merger rate densities

The predicted merger rate densities for the 16 model variations discussed in the previous subsections have a relatively narrow range of $R_{\mathrm{total}} = 19.1\text{-}101.7$ Gpc^{3}yr^{-1}. This is a relatively small variaton in R_{total}, when compared to many previous population synthesis studies [where the typical variations in the predicted R_{total} can span several orders of magnitude, see e.g. 229, 70, 106, 28, 44]. Furthermore, our predicted rates are in a reasonably good agreement with the currently inferred merger rate density from LIGO and Virgo observations (i.e. $R_{\mathrm{GWTC3}} = 28.3^{13.9}_{-9.1}$ Gpc^{-3}yr^{-1}). Below, we discuss that this apparent agreement with observations is most likely a coincidence, and the small variations in the merger rate density is not in a disagree-

ment with previous studies. More importantly, our models should not be mistaken for accurate massive binary evolution models.

In Fig. 2.5 (which is an adopted version of Fig. 3 of [210]), we show the predicted R_{total} of merging binary black holes originating from the isolated binary channel from several population synthesis studies, including this one. A number of studies predict a large variation in R_{total}, which spans about two orders of magnitude [e.g. 70, 28, 395, 44]. However, in these studies, two orders of magnitude variations in R_{total} are typically only achieved, when assumptions regarding i) CEE physics, ii) the magnitude of the natal kick or iii) the metallicity specific star formation rate are varied. We do not vary any of the parameters related to the aforementioned processes. Studies that also do not perform such variations, typically find a range of R_{total} within one order of magnitude, i.e. similar to the range presented in this chapter [see e.g. 250, 251, 22, 319].

We finally note that the apparent agreement between the currently observed merger rate (i.e. $R_{\text{GWTC3}} = 28.3^{13.9}_{-9.1}\,\text{Gpc}^{-3}\text{yr}^{-1}$) and our predicted R_{total} is most likely a pure coincidence. Firstly, there are simply too many poorly understood elements in our models. Many of these significantly affect the predicted R_{total}, such as CEE, natal kick, star formation rate and the metallicity distribution of stars [for the latter and how the related uncertainties affect R_{total}, see 55, or "Chruslinska et al. 2019" in Fig. 2.5]. Secondly, models employed in this study should be regarded as toy models, which serve the purpose to explore how sensitive the demographics of merging BH-BH binaries are on certain poorly constrained processes. However, they are not sufficiently detailed nor accurate to reliably model the formation of GW sources. For example, many processes related to mass transfer are parametrised in an overly simplified way (i.e. constant β, λ, α_{CEE}, γ that do not depend on the parameters of the stars). Therefore, our models cannot precisely represent a sufficiently realistic evolutionary path of a given massive star population.
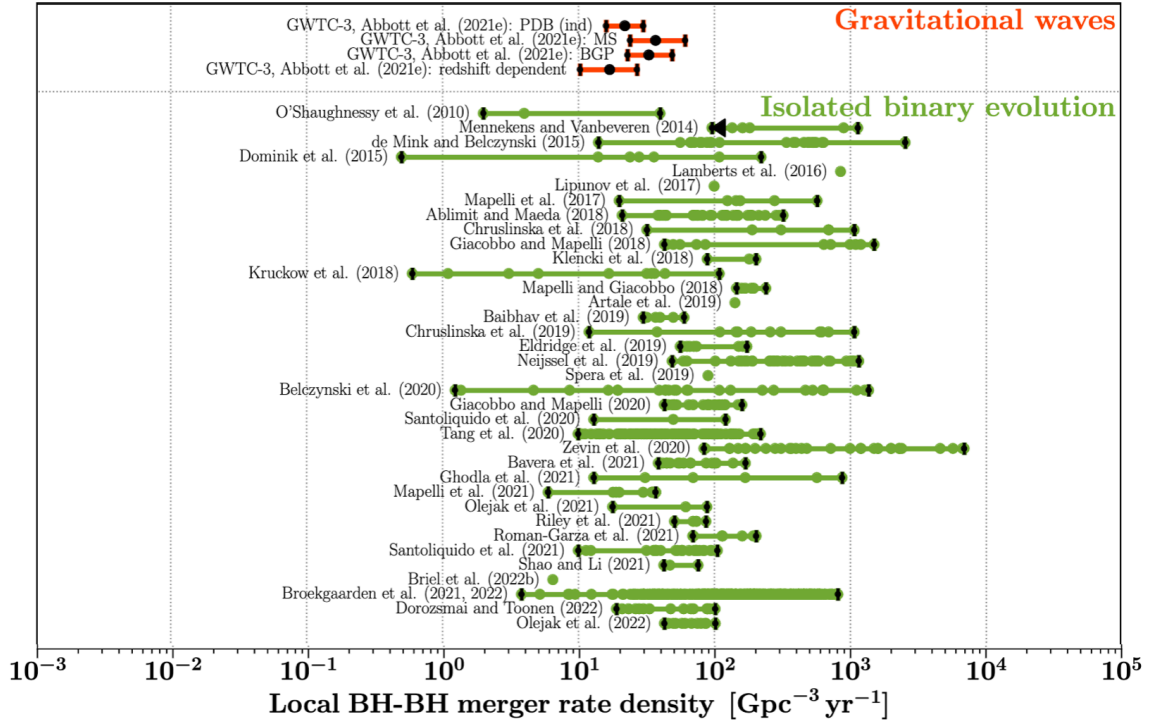
Figure 2.5: Figure adopted from [210], summarising the merger rate density predictions of merging binary black holes originating from the isolated binary channel at $z \approx 0$ from various population synthesis studies

2.5 Results: the impact of stellar winds

In this section, we investigate how different assumptions about mass loss rates of line-driven winds affect the evolution of interacting massive binaries (subsection 2.5.1) and progenitors of GW sources (subsection 2.5.2). We test three different models, these are Model I with $f_{\mathrm{wind}} = f_{\mathrm{wind,WR}} = 1$, Model II with $f_{\mathrm{wind}} = 1/3$, $f_{\mathrm{wind,WR}} = 1$, and finally Model III $f_{\mathrm{wind}} = f_{\mathrm{wind,WR}} = 1/3$. The three different stellar wind models are summarised in Table 2.3.7 (see also subsection 2.3.7). Finally, in subsection 2.5.3, we discuss the importance of LBV winds and the Humphreys-Davidson limit on GW sources.

2.5.1 The effects of stellar winds on binary evolution

In Figure 2.6, we show the remnant mass as a function of initial mass for single stars and for stars in interacting binaries at Z = 0.01. We see that stars in interacting binaries produce considerably lower mass black holes compared to their single counterparts.

There are two major reasons for this. Firstly, as the donor star loses its hydrogen envelope as a result of the mass transfer phase, its hydrogen-shell burning is halted and therefore so is the growth of its helium core. As the helium core is expected to grow only slightly during the very short Hertzsprung gap phase, but significantly during the core-helium burning phase (see later Fig. 2.7), the remnant mass depends on whether the system undergoes Case B or Case C mass transfer. In particular, at metallicities $Z \gtrsim 0.005$, the radial expansion after the onset of core helium burning of stars with $M_{\mathrm{ZAMS}} \gtrsim 40 M_{\odot}$ is negligible (Fig. A.1). Practically, all interacting massive binaries with $M_{\mathrm{ZAMS}} \gtrsim 40 M_{\odot}$ initiate Case A or Case B mass
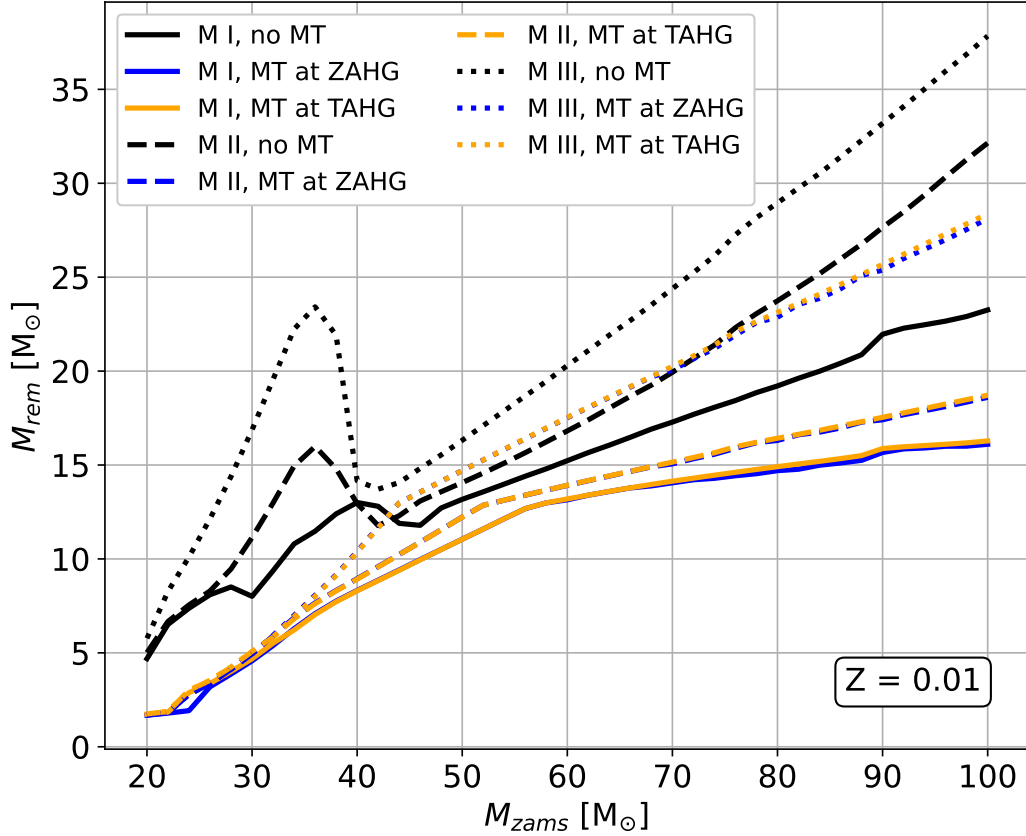
Figure 2.6: The mass of the remnant as a function of initial mass at Z = 0.01 for stars in interacting binaries and single stars for our three stellar wind models. Model I shown by solid lines, Model II shown by dashed lines and Model III shown by dotted lines. The black lines show the remnant mass for single stars (e.g. their hydrogen envelope is not stripped as a result of a mass transfer episode), the blue lines show the remnant mass for stars, which lose their envelopes just at the moment when they cross the Hertzsprung gap (e.g. at zero-age Hertzsprung gap), the yellow lines show stars, which lose their envelopes at the end of the Hertzsprung gap phase (e.g. terminal-age Hertzsprung gap gap). Here we ignored the accretion by the BH in an eventual second phase of mass transfer, which is a valid assumption, if the accretion is Eddington-limited
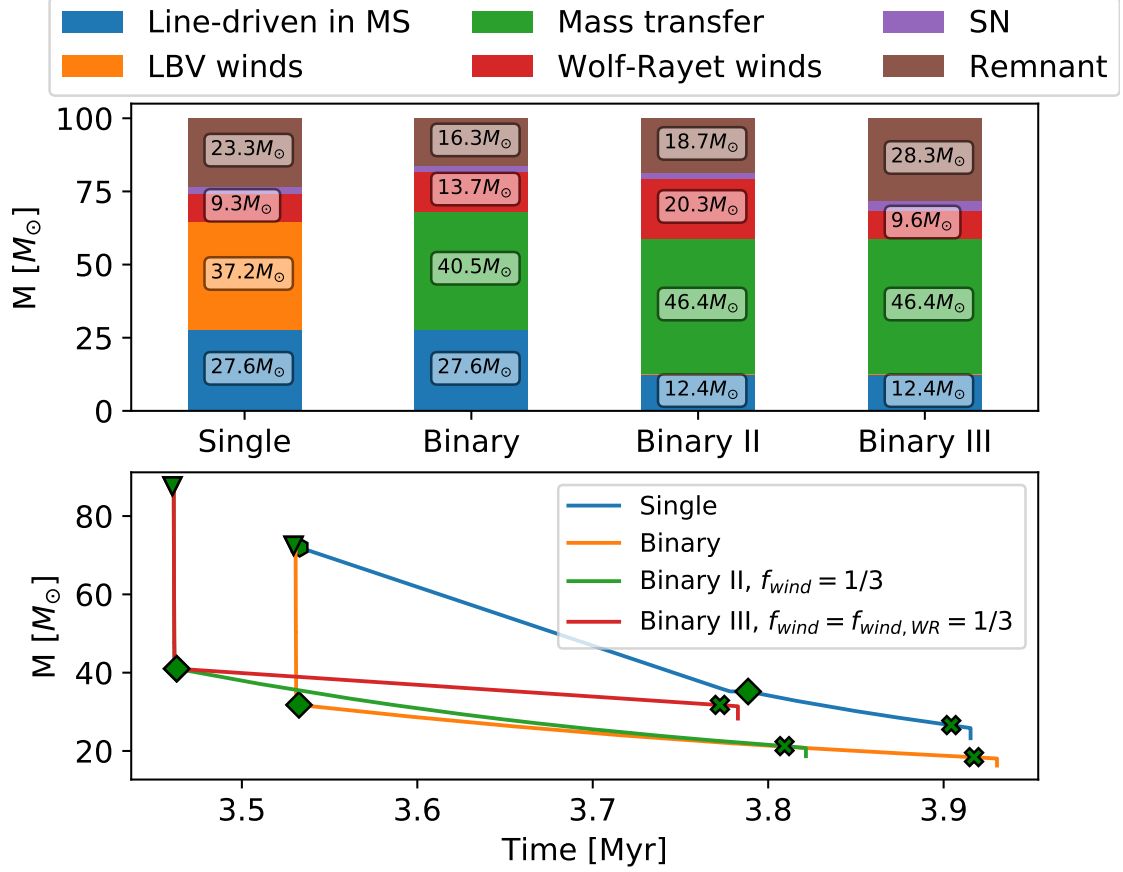
Figure 2.7: The importance of stellar winds with and without binary interactions are compared by showing the evolution of a star with an initial mass of $M_{\mathrm{ZAMS,1}} = 100 M_\odot$ at metallicity $Z = 0.01$ as a single star, and as a binary with a companion of $M_{\mathrm{ZAMS,2}} = 90 M_\odot$ and with an initial orbital separation of $a_{\mathrm{ZAMS}} = 400 R_\odot$. We show the binaries for three different stellar wind models. Labels 'Binary', 'Binary II' and 'Binary III' correspond to Model I ($f_{\mathrm{wind}} = 1$), Model II ($f_{\mathrm{wind}} = 1/3$) and Model III $f_{\mathrm{wind}} = f_{\mathrm{wind,WR}} = 1/3$), respectively. We assume circular orbits. The top panel shows the remnant mass and the mass lost due to different mechanisms. The bottom panel shows the mass of the stars as a function of time. The green symbols indicate the starting points of different stellar evolutionary phases; triangle: hydrogen-shell burning phase, hexagon: core helium burning phase, diamond: helium star, cross: helium giant. For clarity, we also show the curves starting from the hydrogen-shell burning phase.
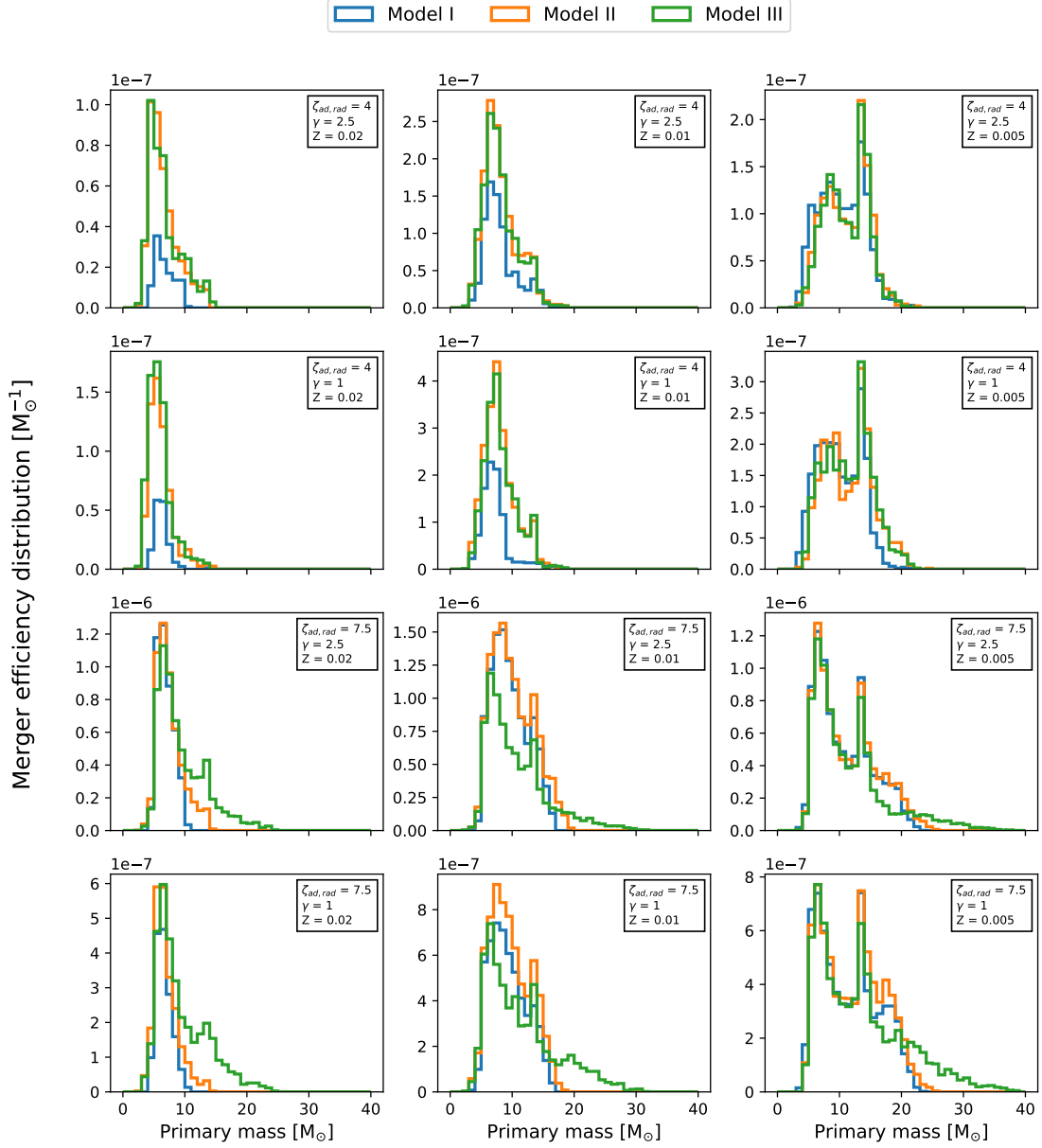
Figure 2.8: The primary mass distribution of merging binary black holes for different stellar wind models and different assumptions for mass transfer stability criteria for giants with radiative donors ($\zeta_{\mathrm{ad,rad}}$) and angular momentum loss during mass transfer with non-compact accretor (γ) at metallicities Z = 0.02, 0.01 and 0.005. For all models shown here the convective envelope prescription of [150] and $\beta = 0.3$ is assumed. This histograms are normalised to the merger efficiency.

transfer episodes at these metallicities. Consequently, the yellow curves in Fig. 2.6 (corresponding to systems initiating mass transfer at the end of the Hertzsprung gap phase of the donor star) show approximately the maximum remnant mass that stars with $M_{\mathrm{ZAMS}} \gtrsim 40 M_{\odot}$ from interacting binaries can have at Z = 0.01. Because of the early envelope stripping, the helium cores of the donor stars cannot grow significantly via hydrogen shell burning. As a result, they also form less massive remnants than their non-interacting counterparts.

Secondly, the lifetime of the Wolf-Rayet phase of a star in an interacting binary increases compared to that of the single star. The primary star in the interacting binary spends most, if not all of its core helium burning lifetime as a stripped helium star. As a consequence, the star in the binary ends up losing more mass due to Wolf-Rayet winds than its single counterpart. Since the Wolf-Rayet winds directly affect the mass of the helium core, the mass of the black hole sensitively depends on total mass lost during this evolutionary phase. The single star also loses a significant amount of mass via LBV winds. However, this impacts only the hydrogen envelope, and not the mass of the helium core.

The difference between interacting and non-interactive binary evolution is illustrated in Fig. 2.7, where we compare the evolution of a single star with an initial mass of $M_{\mathrm{ZAMS}} = 100 \, M_{\odot}$, with the evolution of a binary with the same primary mass as the mass of the single star. The mass of the black hole originating from single stellar evolution is appreciably higher ($M_{\mathrm{BH}} = 23.3 \, M_{\odot}$) than the black hole formed through binary evolution ($M_{\mathrm{BH}} = 16.2 \, M_{\odot}$, but also compare the black with the yellow lines in Fig. 2.6). In the lower panel of Fig. 2.7, we compare the evolution of the masses of these two systems starting from the Hertzsprung gap phase. During this phase, the helium core of the single star grows only slightly, from $M_{\mathrm{core}} \sim 31.2 \, M_{\odot}$ to $M_{\mathrm{core}} \sim 31.7 \, M_{\odot}$ (also compare the blue with the yellow lines in Fig. 2.6), while it increases up to $M_{\mathrm{core}} \sim 35.2 \, M_{\odot}$ by the end of the core helium burning. As previ-

ously mentioned, at these metallicities, the most massive binaries are only expected to undergo Case C mass transfer phase in negligible numbers. This implies that the masses of stripped helium stars ($M_{\mathrm{HE,binary}}$), which evolve from an MS star with $M_{\mathrm{ZAMS}} = 100\,M_\odot$ in an interacting binary is not above $M_{\mathrm{HE,binary}} \sim 31.7\,M_\odot$ for the vast majority of the cases. The single star also loses its envelope eventually, mostly due to LBV winds. However, this occurs well after the onset of the core helium burning phase. During this phase, the mass of the helium core can grow uninterrupted. As a result, a more massive helium star is formed, e.g. in this case $M_{\mathrm{HE,single}} = 35.2 M_\odot$.

We also see that while in Model II single stars form appreciably more massive BHs than in Model I, this difference is much smaller for interacting binaries. As shown in Fig. 2.7, in Model II, the primary star of the binary system develops a more massive helium core before the envelope loss ($M_{\mathrm{HE,binary}} \approx 40.3\,M_\odot$) than in Model I ($M_{\mathrm{HE,binary}} \approx 31.7\,M_\odot$). However, this stripped star in the interacting binary loses an enormous amount of mass via Wolf-Rayet winds and ends up with a black hole that is only about $2.4\,M_\odot$ more massive than the black hole evolving from the same system in Model I (compare the solid lines with the dashed lines in Fig. 2.6). The decrease in the difference in remnant masses for interacting binary systems compared to single systems is the result of the increased amount of mass lost during the Wolf Rayet phase ($\sim 20.3\,M_\odot$ as opposed to $\sim 13.7\,M_\odot$). In Fig. 2.7, we also show the evolution of the binary with Model III, in which the Wolf-Rayet winds are also scaled down by a factor of three. In this case, the mass of the final black hole is about $M_{\mathrm{BH}} \sim 28.3\,M_\odot$, which is about $10\,M_\odot$ more than than the black hole forming in the binary with Model I (compare the solid lines with dotted lines in Fig. 2.6).
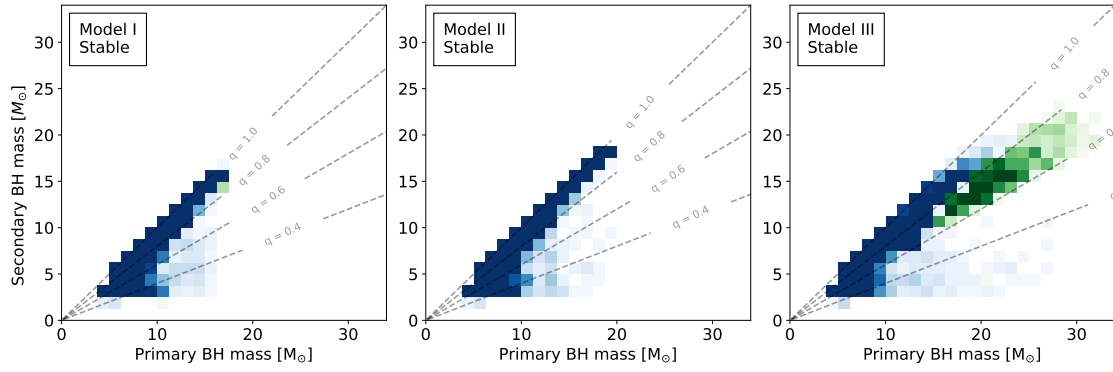
Figure 2.9: 2D histograms of masses of the merging binary black holes for the three stellar wind models at $Z = 0.01$. We have separated sources that have Case A first mass transfer phase (green) and sources that have Case B first mass transfer phase (blue). The histograms have been normalised to the merger efficiency at $Z = 0.01$.

2.5.2 The effect of stellar winds on merging binary black holes

In this subsection, we discuss how the maximum mass of merging binary black holes are affected with different stellar wind models. In Fig. 2.8, we show the primary mass distribution of merging binary black holes for all of our three stellar wind models and with different values of $\zeta_{ad,rad}$ and γ at metallicities $Z = 0.02, 0.01, 0.005$. The difference in the maximum mass in Model I and Model II is only $\sim 4\,M_\odot$ and therefore not significant. This is not surprising, as we found similar results for interacting binaries in section 2.5.1.

Whether the most massive black holes in Model III form GW sources depends on what we assume about the mass transfer stability criteria for giants with radiative donors. With $\zeta_{ad,rad} = 4$, the most massive systems in Model III form BH-BH binaries that are too wide to merge within Hubble time, or experience stellar merger and never form BH-BH binaries. Therefore, in that case, the maximum masses of the GW sources do not differ significantly between Model II and Model III. However, with $\zeta_{ad,rad} = 7.5$, the primary masses of merging binary black holes can reach up to $M_{\rm BH} \sim 30\,M_\odot$ for Model III at $Z = 0.01$, which is significantly larger than that

of the most massive GW progenitors in Model II ($M_{\mathrm{BH}} \sim 20\,M_\odot$). In order to understand this in more detail, let us consider how the most massive merging black hole binaries are formed at metallicties $Z \gtrsim 0.005$:

- *The most massive GW sources form via the stable channel.* This is due to our assumption that envelope ejection during CEE is only possible with core-helium burning donors. At such high metallcities the expansion of radius in such donors is negligible for $M_{\mathrm{ZAMS}} \gtrsim 40\,M_\odot$ (see Fig. A.1) and therefore so are the rates of Case C mass transfer events for such systems.

- *Binaries with the most massive stars only form GW source, if they have* $q_{\mathrm{MT},2} \gtrsim$ *4-5.* The orbit only shrinks efficiently due to a stable phase of mass transfer with a BH accretor, if $q_{\mathrm{MT},2}$ is large (see equation 3.16). In relatively high metallicity environments ($Z \gtrsim 0.005$), the orbital separations of binaries with the most massive initial masses are typically so wide at the onset of the second phase of mass transfer due to stellar winds (see Figure A.9), that only systems with $q_{\mathrm{MT},2} \gtrsim$ 4-5 form BH-BH binaries that merge within the Hubble time.

Considering these two points, we can understand why binaries with the most massive stars do not form GW sources with $\zeta_{\mathrm{ad,rad}} = 4$. In these model variations $q_{\mathrm{crit}} = 3.2$ at the onset of the second mass transfer phase (see Table A.1). Consequently, a binary with $q_{\mathrm{MT},2} \approx$ 4-5 experiences an unstable phase of mass transfer and the system merges before it could form a BH-BH binary. If $q \lesssim q_{\mathrm{crit}}$, then the BH-BH binary that is formed is too wide to merge within the Hubble time.

In Fig. 2.9, we show a 2D histograms of the masses of the merging binary black holes at Z = 0.01 for each stellar wind model. We distinguish sources based on the type of the first mass transfer episode (Case A is shown by green and Case B is shown

by blue). The most massive systems in Model I and Model II experience a Case B first phase of mass transfer. The most massive black holes from these models have mass ratios $0.8 \lesssim q_{\mathrm{final}} \lesssim 1.0$. On the other hand, the gravitational wave sources with the most massive primaries are predicted to form in a very different way in Model III. These binaries have their first mass transfers with (late) main sequence donors and the mass ratio distribution of the merging binary black holes are in the range of $0.6 \lesssim q_{\mathrm{final}} \lesssim 0.8$. In Figure A.9, we show typically formation histories of the most massive merging binary black holes from each mode and we discuss their evolution in detail in section A.3.

2.5.3 The effect of LBV winds on the merging binary black hole population

Stars that cross the Humphreys-Davidson limit are predicted to lose a significant amount of mass via LBV stellar winds. However, the underlying mechanism for the mass loss, the predicted mass loss rates and its metallicity dependence are extremely uncertain [see e.g. 325].

If the progenitors of merging binary black holes have sufficiently wide initial orbital separations, such that the donor stars cross the Humphreys-Davidson limit, before they initiate a mass transfer episode, then LBV winds will affect the demographics of this merging binary black hole population. This can occur in the following ways. Firstly, the range of the mass ratio distribution is decreased to lower values at the onset of the second mass transfer by the LBV mass loss rates. This affects the number of mergers of the rCEE channel (see also e.g. Fig. A.6 and discussion in section 2.4.4). Secondly, intense mass loss rates widen the orbit. This can increase the number of binary black holes which are too wide to merge
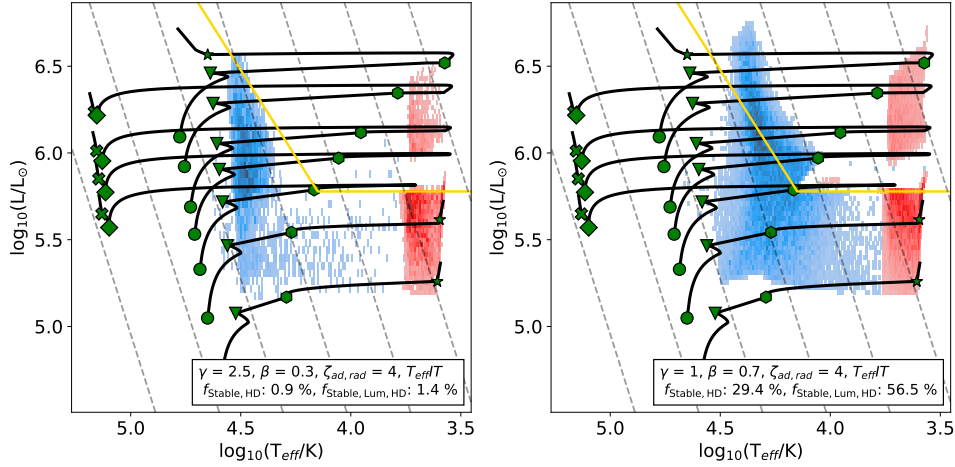
Figure 2.10: We show the positions of the donor stars at the onset of the second mass transfer phase of GW progenitors in the HD diagram at Z = 0.0007 with 2D histograms for two different model variations. The blue 2D histogram shows the systems of the stable channel, while the red shows the systems of the CEE channel. The yellow line shows the Humphreys-Davidson limit. We also show a few stellar tracks with the same masses as in Fig. A.1, as well as the their most importnt evolutionary steps with green shapes (see Fig. A.1). In the legend $f_{\mathrm{Stable,HD}}$, expresses the number of systems in the stable channel, in which any of the stars cross the Humphreys-Davidson as a fraction of all stable channel GW sources. $f_{\mathrm{Stable,LumHD}}$ is the same but expressed as a fraction of only those stable channel sources, in which any of the stars in the binary would cross the Humphreys-Davidson limit, if it evolved without any binary interactions

within Hubble time. Finally, extremely high LBV mass loss rates can also affect the maximum size that the stars eventually reach. In principle, if the mass loss rates are sufficiently high ($\dot{M}_{\mathrm{LBV}} \sim 10^{-3} M_{\odot}\mathrm{yr}^{-1}$), the red-ward evolution of massive stars could be truncated by LBV winds, as they would lose their hydrogen-rich envelopes soon after the onset of core-helium burning.

The latter is why LBV winds have been associated with the lack of observed red super giants above luminosities of $\log(\mathrm{L/L_{\odot}} \approx 5.8$ (see e.g. [186], but also see [128]; [108]; [302] for different possible scenarios). In the context of gravitational wave progenitors, [229] found that, if the LBV mass loss rate is in the order of $\dot{M}_{\mathrm{LBV}} = 10^{-3} M_{\odot}\mathrm{yr}^{-1}$ or higher, the merger rate of binary black holes drastically decreases. However, we show that, if the BH-BH mergers are dominated by the

stable channel, then this is not necessarily true. This is because for such binaries both of the mass transfer phases occur in relatively small orbits, typically when the donor is at the beginning of its hydrogen shell burning phase. Therefore, stars in a large fraction of these systems never cross the Humphreys-Davidson limit.

In Fig. 2.10, we show the donor stars at the onset of the second phase of mass transfer in the Hertzsprung-Russel diagram for the stable and the CEE channel at Z = 0.0007 for two model variations. We chose these particular models because they have the lowest and the largest number of GW progenitors of the stable channel, in which any of the stars cross the Humphreys-Davidson limit during their evolution. We also show the percentage of the binaries in the stable channel, in which any of the stars evolves beyond the Humphreys-Davidson limit ($f_{\mathrm{Stable,HD}}$). These are $f_{\mathrm{Stable,HD}} = 0.9$ per cent in the model with $\gamma = 2.5$ and $f_{\mathrm{Stable,HD}} = 29.4$ per cent in the model with $\gamma = 1$. This already indicates that in some of our model variations, only a negligible number of GW progenitors of the stable channel is affected by LBV winds. We note that this fraction is dependent on the mass of the stars, In particular, in the model with the $\gamma = 1$, all stars with donor mass above 80 $M_{\odot}$ initiate the mass transfer phase after they crossed the Huprheys-Davidson limit.

We also show f_{StableHD} for all model variations at all metallcities in Fig. A.12. This clearly demonstrates that especially at lower metallicties (at which most GW sources are predicted to originate from), the majority of the systems in the stable channel never become LBV stars.

As evident from Fig. 2.10, the most massive GW progenitors in the CEE channel initiate the second phase of mass transfer well beyond the Humphreys-Davidson limit, since the donors of these systems typically have a deep convective envelope before they fill their Roche-lobes.

If the LBV mass loss rates were a magnitude higher than our assumed value, all binaries in the CEE channel with stars that cross the Humphreys-Davidson limit would lose their hydrogen rich envelopes before those would become mostly convective. This would decrease the predicted merger rate and the maximum black hole mass of this formation channel, broadly consistent with [229]. On the other hand, this is not the case for the stable channel, as a significant fraction of these systems never evolve beyond the Humphreys-Davidson limit. Even those systems which do, the stars of these binaries typically spend there less than ~ 10 per cent of their Hertzsprung gap lifetime. This means that even, if the mass loss rate is $\dot{M}_{\mathrm{LBV}} = 10^{-3} \, M_{\odot}\mathrm{yr}^{-1}$, the donor would only lose $\sim 1 \, M_{\odot}$ mass, and therefore the predictions for the stable channel are little affected by a steady, intense LBV mass loss. We show this in Fig A.13, where we determined the mass that would be lost by the donor stars of the stable channel due to LBV wind with a mass loss rate of $\dot{M}_{\mathrm{LBV}} = 10^{-3} \, M_{\odot}\mathrm{yr}^{-1}$ for the $\gamma = 2.5$, $\beta = 0.3$ models at each metallicity. We see that even with such an enormous mass loss rate, the vastr majority of the donor stars would only lose 1-2 $M_{\odot}$.

2.6 Conclusion

We performed a parameter study on the classical isolated binary formation channel of gravitational sources. Our primary aim was to investigate how sensitively the demographics of merging binary black holes depend on current uncertainties related to the first phase of mass transfer (between two hydrogen rich stars) and on stellar winds. For this, we used the rapid population synthesis code `SeBa` to simulate the evolution of massive binaries over a metallicity range $Z = 0.0001 - 0.02$ with several model variations each with different assumptions about the binary physics. In the first part of this chapter (section 2.4), we varied the (i) angular momentum loss

and (ii) the mass transfer efficiency during first phase of mass transfer, (iii) the mass transfer stability criteria for giants donors with radiative envelopes and (iv) the effective temperature at which evolved stars develop deep convective envelopes. In the second part of this chapter (section 2.5), we also varied the mass loss rates of line-driven winds (see Table 2.1 for an overview for all of our model variations).

We find that current uncertainties related to the first phase of (stable) mass transfer have a huge impact on the relative importance of different dominant channels, while the observable properties (i.e. merger rate, mass and mass ratio distribution) of merging binary black holes are not significantly affected. This implies that models with different binary physics assumptions might yield the same predicted demographics of merging binary black holes, the origin of the majority of GW progenitors could be entirely different. This shows why it is very challenging to infer physics of massive binary evolution solely from GW observations in a meaningful way, given the large uncertainties in our current models (see also [30]).

In order to break the degeneracy between the uncertain parameters and the predicted population of merging binary black holes, it is clear that we have to analyse the gravitational wave data along with electromagnetic observations. In particular, regarding the first mass transfer phase, observations of WR-O/B binaries and high mass X-ray binaries could offer invaluable clues about how the first mass transfer episode proceeds. Especially an extensive catalogue of the former type would be useful, as these systems have not yet experienced core-collapse, and their mass ratios and orbital separations are directly related to the mass transfer efficiency and the angular momentum carried away by the expelled matter.

In our model variations, we identify two dominant evolutionary paths, one involves two stable mass transfer phases (stable channel), and one in which a stable mass transfer episode is followed by an unstable mass transfer phase (CEE channel

with two variant: cCEE and rCEE, see see Fig. 2.1). Below, we summarise our most important results:

- *Impact of angular momentum loss on the dominant channels (section 2.4.1 and 2.4.1):* The assumed angular momentum loss during the first phase of mass transfer determines how the orbital separation changes during mass exchange and has an indirect effect on the rate of stable and unstable mass transfer phases. Consequently, it has also a strong impact on the merger rate of different formation channels. We find that typically the stable channel dominates in our models with $\gamma = (dJ/dM_{\mathrm{tot}})/(J/M_{\mathrm{tot}}) = 2.5$, while, the merger rate of cCEE channel remains low. On the other hand, in our models with $\gamma = 1$, the merger rate of the stable channel is typically negligible, while the cCEE channel is efficient.

- *Impact of mass transfer stability criteria (section 2.4.3):* The merger rate of the stable channel increases with increasing $\zeta_{\mathrm{ad,rad}}$. This is because the degree of orbital shrinkage due to a stable mass transfer phase with a black hole accretor becomes substantially more efficient with increasing mass ratios. However, we find that only the merger rate of relatively lower mass BH-BH binaries is significantly affected (i.e. $M_{\mathrm{BH}} \lesssim 20\,M_{\odot}$), when $\zeta_{\mathrm{ad,rad}}$ is increased from 4 to 7.5 (corresponding to a q_{crit} of 3.2 and 5.5). This is because at lower metallicities (which are the most relevant for GW sources), the maximum mass ratios of the most massive binaries at the onset of the second mass transfer phase is limited to 3-3.5, depending on the mass transfer efficiency.

- *Line driven stellar winds (section 2.5.1 and 2.5.2):* Although, decreasing the mass loss rates of optically thin line driven winds by a factor of three significantly increases the masses of the black holes formed without mass exchange (see Fig. A.1), we do not find an appreciable difference in the masses of merging binary black holes (Fig. 2.8). The primary reason for this is that stars

in interacting binaries experience a longer Wolf-Rayet phase due to envelope stripping than their single counterparts. Although, with weaker winds on the main sequence, stars develop a more massive helium core, they also experience significantly higher Wolf-Rayet mass loss rates after the envelope stripping (since the more massive helium core will be more luminous after envelope loss, and this leads to considerably higher mass loss rates). However, if the Wolf-Rayet mass loss rates are simultaneously decreased too, we find a significant increase in the masses of gravitational wave sources, but only in the model variations with $\zeta_{\mathrm{ad,rad}} = 7.5$.

- *LBV winds (section 2.5.3):* Intense LBV mass loss rates can have significant effect on the CEE channel. If the mass loss rates are above $\dot{M}_{\mathrm{LBV}} \sim 10^{-3}\,M_{\odot}\mathrm{yr}^{-1}$, the merger rate of the CEE channel becomes negligible. On the other hand, the stable channel is not appreciably affected, as these binaries have so short periods, such that their envelopes are stripped as a result of a mass transfer episode before or very soon after they cross the Humphreys-Davidson limit.

Chapter 3

Stellar triples with chemically homogeneously evolving inner binaries

authors: Andris Dorozsmai, Silvia Toonen, Alejandro Vigna-Gomez, Selma de Mink, Floris Kummer

This chapter is a reformatted copy of Dorozsmai et. al 2023 [73], published in MNRAS (https://academic.oup.com/mnras/article/527/4/9782/7469482) and available on arXiv with the number of 2307.04793 (see https://arxiv.org/abs/2307.04793). My contribution to this work was (i) to implement chemically homogeneously evolving stars and contact (inner) binaries in the triple evolution code, TRES, (ii) to execute the simulations, (iii) to develop a code for the data analysis of the population synthesis simulations, to formulate strategies for post-processing to interpret the results, (v) to make the figures, (vi) and to write the manuscript. This project was originally proposed by Silvia Toonen and Selma de Mink. The triple evolution code, TRES, was developed by Silvia Toonen. Silvia Toonen, Alejandro Vigna-Gomez, Selma de Mink and Floris Kummer provided a substantial amount

of scientific advice, and helped me to significantly improve the structure and the quality of the manuscript.

3.1 Abstract

Observations suggest that massive stellar triples are common. However, their evolution is not yet fully understood. We investigate the evolution of hierarchical triples in which the stars of the inner binary experience chemically homogeneous evolution (CHE), particularly to understand the role of the tertiary star in the formation of gravitational-wave (GW) sources. We use the triple-star rapid population synthesis code `TRES` to determine the evolution of these systems at two representative metallicities: $Z = 0.005$ and $Z = 0.0005$. About half of all triples harbouring a CHE inner binary (CHE triples) experience tertiary mass transfer (TMT) episodes, an event which is rare for classically evolving stars. In the majority of TMT episodes, the inner binary consists of two main-sequence stars (58-60 per cent) or two black holes (BHs, 24-31 per cent). Additionally, we explore the role of von Zeipel-Lidov-Kozai (ZLK) oscillations for CHE triples. ZLK oscillations can result in eccentric stellar mergers or lead to the formation of eccentric compact binaries in systems with initial outer pericenters smaller than $\sim 1200\ R_{\odot}$. Approximately 24-30 per cent of CHE triples form GW sources, and in 31 per cent of these, the tertiary star plays a significant role and leads to configurations that are not predicted for isolated binaries. We conclude that the evolution of CHE binaries can be affected by a close tertiary companion, resulting in astronomical transients such as BH-BH binaries that merge via GW emission orders of magnitude faster than their isolated binary counterparts and tertiary-driven massive stellar mergers.

3.2 Introduction

An accurate and detailed understanding of the evolution of massive stars is essential for various important open questions in astrophysics, such as nucleosynthesis of heavy elements, the origin of supernova events, gamma-ray bursts, and GW sources (e.g. [187]). Observational evidence shows that the fraction of stars in hierarchical triples or in higher-order multiple-stellar systems increases with the mass of the primary star ([85, 305]). In particular, [235] showed that the majority of O-type stars reside either in triple or quadruple stellar systems. This implies that in order to understand the evolution of massive stars, and to correctly interpret the various astrophysical phenomena related to them, we need to consider stellar interactions in hierarchical triples.

The evolution of hierarchical triples involves a complex interplay between three-body dynamics, stellar evolution, and stellar interactions [e.g. 354]. Three-body interactions can result in e.g. ZLK oscillations [411, 195, 175, 243], a secular effect where the eccentricity of the inner binary can be significantly enhanced as a result of dynamics. ZLK oscillations coupled with various dissipative processes (e.g., tides, GWs) can shrink the orbit [e.g. 224, 87, 346] and prompt the merger of the inner binary [e.g. 264, 368]. These type of mergers can result in astronomical transient events such as Type Ia supernova [e.g. 158, 355, 340] or double compact object mergers [e.g. 16, 19, 295, 117, 93, 333]. Furthermore, stellar evolution can affect the orbital dynamics of the triple. For example, radial expansion and mass loss can prompt ZLK oscillations or dynamical instabilities [265, 320, 232, 357, 121].

Population synthesis studies of stellar triples show that the inner binaries in hierarchical triples have increased stellar interactions compared to isolated binaries [e.g. 356, 334, 120]. Similarly, tertiary-driven dynamics could play an essential role

in double compact object mergers. While GW sources detected by the LIGO/Virgo collaboration [LVC, e.g. 4, 3, 7, 345] have been studied in the context of stellar triples, this has been done so far only in a limited parameter space. For example, for systems in which the inner binary is wide enough such that interaction between the two stars in the form of mass exchange can be neglected [e.g. 323, 19, 295, 93, 367, 222], or in which the stars of the inner binary merge during the main sequence [333]. There are still major uncertainties and a need to explore and to understand the population of merging binary BHs from hierarchical triples.

In this paper, we focus on the evolution of hierarchical triples in which the stars of the inner binaries are chemically homogeneously evolving. CHE stars have been discussed in the context of rapidly-rotating stars [207, 389, 390], which can experience enhanced mixing during the MS stage. This mixing allows hydrogen-rich matter in the radiative envelope to be deposited into the convective core, where it is fused to helium. At the same time, helium is mixed throughout the star. This prevents the build-up of a chemical gradient inside the star and the classical core-envelope structure. As a result, the stars remain very compact over their lifetime. CHE has been proposed to occur in very close binaries where the tidal deformation of both stars is strong and they are forced to rotate rapidly [403, 329]. More recently, CHE binaries received renewed interest as they have been proposed as a new pathway to form BH binaries that can merge within the age of the universe [401, 213, 217, 406, 292]. Recently, [367] studied triples with CHE inner binaries in the context of sequential merging BH-BHs with masses that fall in the pair-instability mass gap. Specifically, they considered sequential mergers of hierarchical co-planar triples, a simplified approach which neglected three-body dynamics. In this paper, we remove the constraints of co-planarity and explore, for the first time, the evolution of massive stellar triples with CHE inner binaries in the entire parameter space. As isolated CHE binaries are known to be promising GW progenitors, we will mostly focus on

the role of the tertiary star in the evolution of the inner binary in the context of GW astronomy.

This paper is structured as follows. In section 3.3, we introduce TRES, the triple evolutionary code we use in this study, and the adaptations we have made to model CHE and contact binaries. In section 3.4, we discuss the results of our population synthesis in TRES and identify the most important evolutionary channels. In section 3.5, we show that the initial parameters of the tertiary star are sufficient to predict the evolutionary channel of each system. Finally, in section 3.6, we use analytical and numerical methods to explore our synthetic population of stellar triples in the context of GW sources.

3.3 Methodology

We use TRES to simulate the evolution of our hierarchical triples [see 354, for a detailed description of the code]. TRES couples secular dynamics of stellar triples with stellar evolution, and takes into account additional physical processes such as stellar interactions and dissipative processes.

TRES determines the evolution of each star by using the fitting formulae of [138] to the stellar tracks of [276] from the rapid binary synthesis code SeBa [279, 353], while interactions between the stars are determined by TRES. TRES treats three-body dynamics in the following way. For secular evolution, we include secular three body dynamics (subscript '3b') including quadrupole ([123]) and octupole terms ([91] with corrections of [246]). Regarding the additional physical processes, we take into account: i) general relativistic effects (GR) and GW emission [subscript 'GR' 266, 35], ii) tidal friction [subscript 'TF' 139], iii) the effects of stellar winds

under the assumptions of fast, adiabatic wind at the mass loss rate provided by SeBa (subscript 'wind'), iv) precession due to ZLK, GR, tides [subscript 'tides' 324] and intrinsic stellar rotation [subscript 'rotate' 87], and v) the change in the stellar rotation due to stellar evolution based on spin angular momentum conservation (subscript 'I'). This gives rise to a set of first-order ordinary differential equations, that are solved numerically. These equations are:

$$
\begin{cases}
\dot{a}_{\mathrm{in}} & = \quad \dot{a}_{\mathrm{in,GR}} + \dot{a}_{\mathrm{in,TF}} + \dot{a}_{\mathrm{in,wind}} \\[4pt]
\dot{a}_{\mathrm{out}} & = \quad \dot{a}_{\mathrm{out,GR}} + \dot{a}_{\mathrm{out,TF}} + \dot{a}_{\mathrm{out,wind}} \\[4pt]
\dot{e}_{\mathrm{in}} & = \quad \dot{e}_{\mathrm{in,3b}} + \dot{e}_{\mathrm{in,GR}} + \dot{e}_{\mathrm{in,TF}} \\[4pt]
\dot{e}_{\mathrm{out}} & = \quad \dot{e}_{\mathrm{out,3b}} + \dot{e}_{\mathrm{out,GR}} + \dot{e}_{\mathrm{out,TF}} \\[4pt]
\dot{g}_{\mathrm{in}} & = \quad \dot{g}_{\mathrm{in,3b}} + \dot{g}_{\mathrm{in,GR}} + \dot{g}_{\mathrm{in,tides}} + \dot{g}_{\mathrm{in,rotate}} \\[4pt]
\dot{g}_{\mathrm{out}} & = \quad \dot{g}_{\mathrm{out,3b}} + \dot{g}_{\mathrm{out,GR}} + \dot{g}_{\mathrm{out,tides}} + \dot{g}_{\mathrm{out,rotate}} \\[4pt]
\dot{h}_{\mathrm{in}} & = \quad \dot{h}_{\mathrm{in,3b}} \\[4pt]
\dot{\theta} & = \quad \frac{-1}{J_{\mathrm{b,in}} J_{\mathrm{b,out}}} [\dot{J}_{\mathrm{b,in}}(J_{\mathrm{b,in}} + J_{\mathrm{b,out}}\theta) + \dot{J}_{\mathrm{b,out}}(J_{\mathrm{b,out}} + J_{\mathrm{b,in}}\theta)] \\[4pt]
\dot{\Omega}_1 & = \quad \dot{\Omega}_{1,\mathrm{TF}} + \dot{\Omega}_{1,\mathrm{I}} + \dot{\Omega}_{1,\mathrm{wind}} \\[4pt]
\dot{\Omega}_2 & = \quad \dot{\Omega}_{2,\mathrm{TF}} + \dot{\Omega}_{2,\mathrm{I}} + \dot{\Omega}_{2,\mathrm{wind}} \\[4pt]
\dot{\Omega}_3 & = \quad \dot{\Omega}_{3,\mathrm{TF}} + \dot{\Omega}_{3,\mathrm{I}} + \dot{\Omega}_{3,\mathrm{wind}}
\end{cases}
\tag{3.1}
$$

where a, e, g, h and J_b represent the semimajor axis, eccentricity, argument of pericenter, line of ascending nodes, and the orbital angular momentum for the inner (subscript 'in') and outer (subscript 'out') orbit. The dot represents the time derivatives. Lastly $\theta \equiv \cos(i)$, where i is the mutual inclination between the inner and outer orbit, and $\Omega_1, \Omega_2, \Omega_3$ the spin frequency of the primary, secondary and tertiary star respectively. Per definition the primary and secondary stars are the stars in the inner binary, with the primary star initially more massive than the secondary star, and the tertiary star orbits the inner binary.

We highlight three aspects of the orbital evolution of hierarchical triples that are

particularly relevant for the systems we study in this paper. Firstly, if the apsidal precession of the inner binary due to short range forces, such as tides ($\dot{g}_{\rm in,tides}$) and GR effects ($\dot{g}_{\rm in,GR}$) occurs on a much shorter timescale than the precession due to three-body dynamics ($\dot{g}_{\rm in,3b}$), ZLK oscillations will be quenched [see e.g. 133, 80, 35, 87, 346, 71, 197, 269, 13]. The timescale of ZLK oscilations can be approximated as [e.g. 147, 133, 160]:

$$t_{\rm ZLK} = \left(\frac{M_1 + M_2}{GM_{\rm out}^2}\right)^{1/2} \left(\frac{a_{\rm out}}{a_{\rm in}^{1/2}}\right)^3 (1 - e_{\rm out}^2)^{3/2}. \tag{3.2}$$

The timescale related to the apsidal precession due to tides are [e.g. 324, 197]:

$$t_{\rm tides} = \left(\frac{M_1}{15k_{\rm am}\mu_{\rm in}^{1/2}M_2}\right)\left(\frac{a_{\rm in}^{11/2}}{R_1^5}\right)\left(\frac{(1-e_{\rm in}^2)^5}{1+\frac{3}{2}e_{\rm in}^2+\frac{1}{8}e_{\rm in}^4}\right), \tag{3.3}$$

where $k_{\rm am}$ the apsidal motion constant, which we assume to be 0.0144 for MS and helium stars, $\mu_{\rm in} = G(M_1 + M_2)$, i.e. the standard gravitational parameter for the inner binary and R_1 is the radius of the inner star. The timescale related to precession due to general relativistic effects is [e.g. 234, 35, 233]:

$$t_{\rm GR} = \frac{c^2}{3\mu_{\rm in}^{3/2}}a_{\rm in}^{5/2}(1 - e_{\rm in}^2). \tag{3.4}$$

If $t_{\rm ZLK} \gg \min(t_{\rm GR}, t_{\rm tides})$, then three-body dynamics are suppressed. If the timescales are comparable, then the maximum eccentricity induced by the ZLK oscillations is diminished. In principle, rotation-induced oblateness in the inner binary also induces apsidal precession [$g_{\rm in,rot}$, see e.g. 87]. However, as long as the rotational period of the inner stars is not shorter than the orbital period (which is true for all systems considered here), $\dot{g}_{\rm tides} \gg \dot{g}_{\rm rot}$ and therefore precession due to stellar rotation does not play a role in suppressing three-body dynamics [197].

Secondly, octupole terms in the three-body dynamics are typically negligible

for CHE triples, as the mass ratio of the inner binary is always very close to one. Finally, we estimate the time it takes for the inner binary to merge due to GWs following [266], if the tertiary is dynamically decoupled from the inner binary. If ZLK oscillations are still relevant during the inspiral phase, we follow the approximation of [233]:

$$t_{\mathrm{GW}} \approx t_{\mathrm{GW,Peters}}(a_{\mathrm{in}}, e_{\mathrm{in,max}})(1 - e_{\mathrm{in,max}})^{-1/2}, \tag{3.5}$$

where t_{GW} is the time required for the merger, $t_{\mathrm{GW,Peters}}$ is the time to merger based on the relation of [266], $e_{\mathrm{in,max}}$ is the maximum eccentricity reached during ZLK oscillations and a_{in} is the initial inner semimajor axis. The approximation in equation 3.5 is based on [381] and it neglects the effects of precession due GR. When the latter is taken into account, [346] finds that equation 3.5 underestimates the actual merger timescale typically by a factor of 2-3.

3.3.1   Modelling of chemically homogeneous evolution

We follow [292] in order to incorporate CHE stars in `TRES`. That means that we assume a star evolves chemically homogeneously, if the angular frequency of the spin of the star is above a certain critical value, i.e. $\omega_{\mathrm{star}} > \omega_{\mathrm{CHE,crit}}$. [292] provides a fit to this critical value based on `MESA` [261] models at different masses and metallicities. In order to determine whether a star evolves chemically homogeneously, we check whether our simulated star is spinning above $\omega_{\mathrm{CHE,crit}}$ at every timestep. If a star meets this criterion we do not evolve its radius during that timestep. We assume that the star by the end of core hydrogen burning forms a helium star with a mass $M_{\mathrm{He,ZAMS}} = M_{\mathrm{TAMS}}$, where $M_{\mathrm{He,ZAMS}}$ is the initial mass of the helium star and M_{TAMS} is the terminal age main sequence mass of the star. With these assumptions, CHE stars experience an instantaneous drop in radii at the end of their MS phase

[compare main sequence stellar evolution with helium star evolution in 138]. This is a simplification of the results of detailed simulations of CHE stars, where the latter suggests a gradual contraction of the radius during the MS [e.g. 207]. If a CHE star loses angular momentum (e.g. due to stellar winds), its rotational frequency decreases. If the frequency reduces to below the critical value, we assume the evolution of the star transitions back to the classical non-CHE case.

For simplicity, we only consider systems in which the stars of the inner binary are CHE from zero-age main sequence (ZAMS). Stars that do not evolve chemically homogeneously from ZAMS could, in theory, become CHE if they attained a sufficiently high-spin frequency before a significant chemical gradient is built up in their interior. This can be achieved for example, if a star is spun up by accretion during a mass transfer event [e.g., 48, 105]. We neglect such systems in this study.

3.3.2 Contact binaries

We follow the implementation of [292] for modelling contact binaries [which is based on the models of 217]. We assume that contact binaries, i.e. binaries in which both stars fill their Roche-lobes, can maintain co-rotation and consequently survive the contact phase without merging as long as neither of the stars fill the outer Lagrangian points (L2 and L3). For contact binaries, [217] finds that mass is transferred between the two stars back and forth until they reach an equal mass ratio. We follow [217] and approximate the L2 point as

$$\frac{R_{\mathrm{L2,2}} - R_{\mathrm{RL,2}}}{R_{\mathrm{RL,2}}} = 0.299 \tan^{-1}(1.84 \mathrm{q}^{0.397}), \tag{3.6}$$

where $R_{\mathrm{RL,2}}$ is the Roche-lobe radius of the secondary star, which we approximate following [78].

If the stars in the inner binary are in contact but without filling their L2 points, we assume that the masses of the binary equalise via a fully conservative mass transfer phase. We follow [292] and assume this mass equalisation occurs instantaneously and readjust the orbit of the inner binary as [see, e.g. 326]:

$$\frac{a_{\text{fin}}}{a_{\text{init}}} = \left(\frac{M_{1,\text{init}} M_{2,\text{init}}}{M_{1,\text{fin}} M_{2,\text{fin}}} \right)^2 , \tag{3.7}$$

where a_{init}, a_{fin} are the initial and the final orbital separation and $M_{1,\text{init}}$, $M_{2,\text{init}}$ are the initial masses of the primary and the secondary, respectively. The final masses are $M_{1,\text{fin}} = M_{2,\text{fin}} = 1/2 \cdot (M_{1,\text{init}} + M_{2,\text{init}})$ by definition. The assumption of mass equalisation for contact binaries results in the prediction of the CHE channel leading to mostly equal-mass binary BH mergers [e.g. 217].

3.3.3 Stellar winds

The mass loss rates of stellar winds and their effects on the evolution of the star are determined by `SeBa` [138, 353], while the effects on the orbit of the triple are determined by `TRES` (equation 3.1). In this study, we use the same implementation of stellar winds for massive stars as in Chapter 2 with one difference; the mass loss rates of helium stars and giants are calculated according to the empirical formula of [116] instead of [307].

For reference, we summarise the mass loss rates prescriptions used in this study. For MS stars, we follow [376], if $T_{\text{eff}} \leq 50$ kK and [248], if $T_{\text{eff}} > 50$ kK. For evolved stars crossing the Hertzsprung gap or core helium burning (CHeB) stars, we follow [376], if $T_{\text{eff}} \geq 8$ kK or the maximum between [248] and [285], if $T_{\text{eff}} < 8$ kK. For evolved stars beyond the Humphreys-Davidson limit, we assume $\dot{M}_{\text{LBV}} = 1.5 \cdot 10^{-4}\ M_{\odot}\text{yr}^{-1}$ [25]. For Asymptotic Giant Brach stars and double shell burning

supergiants, we calculate the maximum between [248], [285] and [363]. Finally, for helium stars we follow the empirical form from [116] in the form $\dot{M}_{\mathrm{WR}} = 0.5 \cdot 10^{-13} \cdot$ $\left(\frac{L}{L_\odot}\right)^{1.5} \left(\frac{Z}{Z_\odot}\right)^{0.86}$ with a clumping factor of $\eta = 0.5$ from [115] and a metallicity scaling of $\dot{M}_{WR} \sim Z^{0.86}$ [374].

In order to compute the change in the orbit due to stellar winds, we assume stellar winds are spherically symmetric and fast compared to the orbital velocity; additionally, we neglect wind accretion by the companions. In that case the inner and the outer orbit of the triple widens as

$$\dot{a}_{\mathrm{in,wind}} = \left(\frac{a_{\mathrm{final}}}{a_{\mathrm{init}}}\right)_{\mathrm{in}} = \frac{M_{1,\mathrm{init}} + M_{2,\mathrm{init}}}{M_{1,\mathrm{final}} + M_{2,\mathrm{final}}}, \tag{3.8}$$

and

$$\dot{a}_{\mathrm{out,wind}} = \left(\frac{a_{\mathrm{final}}}{a_{\mathrm{init}}}\right)_{\mathrm{out}} = \frac{M_{1,\mathrm{init}} + M_{2,\mathrm{init}} + M_{3,\mathrm{init}}}{M_{1,\mathrm{final}} + M_{2,\mathrm{final}} + M_{3,\mathrm{final}}}, \tag{3.9}$$

where subscripts 'init' and 'final' refer to properties before and after the stellar winds carried mass away from the stars in a given timestep. We assume that the eccentricity remains unchanged by stellar winds [134, 135].

We neglect stellar wind accretion by the other stars in the triple system [see e.g. 39]. Neglecting accretion is justified for line-driven winds due to their large terminal velocities [see e.g. 376]. The assumptions of a fast and spherically symmetric wind might not always be valid [e.g. 45], and rapidly rotating stars might not have fully symmetric outflows [104]. Particularly, stellar winds in certain binary-configurations might even lead to orbital shrinking [314].

3.3.4 Remnant formation

The mass of the compact object remnant is computed based on the delayed super-nova model from [97] (i.e. same as in Chapter 2). The natal kick velocity for BHs is calculated the same way as in Chapter 2, i.e. according to equation 2.1. We determine the change in the inner and outer orbit due to the core collapse of any of the stars in the triple system based on the formalism developed in [270].

Models of [97] predict that the most massive stars collapse directly (typically $M_{\mathrm{ZAMS}} \gtrsim 40\,M_\odot$), without any ejecta, and the only mass loss during the remnant formation is due to neutrino losses, which is assumed to be 10 per cent of the pre-core-collapse mass of the star. Additionally, we assume that the neutrino emission is spherically symmetrical and do not impart natal kicks onto the BH. In this case, the orbit is only changed due to the instantaneous mass loss [e.g. via Blaauw kick, see 34]. We note that, if the pre-core-collapse orbit is circular, a Blaauw kick due to neutrino losses does not lead to a significant change in the inner orbital elements. However, this is no longer the case for eccentric pre-core-collapse orbits. In particular, if the core collapse occurs near the pericenter, the orbit can become significantly wider [e.g. 129].

By the onset of core-oxygen burning, the core temperatures of the most massive stars can reach above $T_{\mathrm{core}} \sim 3 \times 10^9\,K$. Under these conditions, the emitted gamma-ray photons in the core are energetic enough to form electron-positron pairs. This leads to pair-instability (see e.g. [92], [283], [20], [96]). Depending on the mass of the star, this instability can result in a pulsation pair instability supernova, in which the star experiences a series of pulsations leading to severe mass loss [i.e. or PPISN, see e.g. 391, 217, 384, 287], or pair instability supernova, in which the star is completely disrupted and no remnant is formed [PISN, see e.g. 391, 217, 384, 287]. For the treatment of pair-instability in massive stars, we follow [337]. If the mass

of the helium star pre-core-collapse is $M_{\mathrm{HE,pre-SN}} \geq 35\,M_\odot$, the star is assumed to undergo PPISN, and its remnant mass is determined by the fitting formula of [337], based on the detailed stellar simulations of [218]. If $60 \leq M_{\mathrm{HE,pre-SN}} \leq 130\,M_\odot$, we assume the star undergoes PISN, and leaves no remnant behind. In principle, if $M_{\mathrm{HE,pre-SN}} \geq 130\,M_\odot$, photo-disintegration prevents the pair instability supernova to occur and the star collapses directly into a BH ([38], [385], [124], [406]), however this does not occur for any of our simulated systems.

3.3.5 Tertiary mass transfer (TMT) episodes

If the tertiary star fills its Roche-lobe, it will transfer mass to the inner binary. There have been some efforts to study and model this process [405, 193, 60, 109, 328, 239], but this complex scenario remains to be fully understood.

In order to calculate the Roche-lobe of the tertiary star, we assume the inner binary can be approximated as a point mass and estimate the Roche radius with the fitting formula of [78]. This assumption is valid in the regime where the orbital separation of the outer star is much larger than that of the inner binary (e.g. $a_{\mathrm{out}} \gg a_{\mathrm{in}}$). TRES determines the stability of TMT based on extrapolating typical methods from binary star evolution, i.e. by using critical mass ratios [see e.g. 354]. This parameter is defined as $q_{\mathrm{crit}} = M_{\mathrm{donor}}/M_{\mathrm{accetor}}$, i.e. the ratio of the mass of the donor and the mass of the accretor star at the onset of the mass transfer episode. The mass transfer phase is assumed to be dynamically unstable, if the mass ratio of the system is above the critical mass ratio, i.e. $q > q_{\mathrm{crit}}$. We obtain q_{crit} for each stellar evolutionary stage from [139] and [57]. We quote these values for the two most common donor types in our simulations [a complete description of our assumptions about q_{crit} can be found in 354]. These are $q_{\mathrm{crit}} = 3$ and $q_{\mathrm{crit}} = (1.37 + 2[M_{\mathrm{donor,core}}/M_{\mathrm{donor}}]^5)/2.13$ for Hertzsprung gap stars (i.e. hydrogen shell burning

stars which have not regained thermal equilibrium yet) and core helium burning (CHeB) stars, respectively. The term in the squared bracket is the core mass to total mass ratio of the donor. If this equals to ~ 0.45 - 0.65, which is fairly typical for massive CHeB stars (see Chapter 2), then $q_{\mathrm{crit}} \approx 0.7$-$0.75$. This reflects the assumption made by [138], CHeB stars tend to have deep convective envelopes [cf. 167], and are therefore more likely to experience unstable mass transfer episodes [e.g. 130].

Stable TMT could be accompanied with the formation of a circumbinary disc or it could occur in a ballistic accretion fashion. These two types could lead to significantly different evolution of the inner orbit [405]. We assume that TMT occurs via ballistic accretion, if $a_{\mathrm{in}}(1 + e_{\mathrm{in}}) \geq R_{\mathrm{cd}}$ at the onset of the TMT phase, where R_{cd} is (i.e. adapting the fitting formulas for mass transferring binaries of [201] and [362] to triples, see also equation 1.18):

$$R_{\mathrm{cd}} = 0.0425 \, a_{\mathrm{out}}(1 - e_{\mathrm{out}}) \left[\frac{1}{q_{\mathrm{out}}} \left(1 + \frac{1}{q_{\mathrm{out}}} \right) \right]^{1/4}. \tag{3.10}$$

TMT: Evolution of the inner orbit

If the tertiary star fills its Roche-lobe, `TRES` stops the simulation of the system. However, when discussing potential GW progenitors (Section 3.6), we determine the orbital evolution due to TMT by applying simplified assumptions, if the mass transfer episode is dynamically stable. In this subsection we describe our assumptions about the evolution of the inner orbit during a stable phase of TMT, while in subsection 3.3.5 we discuss the evolution of the outer orbit.

We distinguish three particular TMT configuration cases, based on the evolutionary stage of the inner binary and on whether or not the transferred mass forms

a circumbinary disc around the inner binary:

1. an inner binary with compact objects and with ballistic accretion,

2. an inner binary with compact objects and with a circumbinary disc,

3. a non-compact inner binary.

(i) *An inner binary with compact objects and with ballistic accretion.* Hydrodynamical simulations of [405] showed that in case of a TMT episode with ballistic accretion, the transferred mass eventually engulfs the inner binary and exerts friction on it. This leads to a scenario that could be considered similar to the common-envelope evolution of binaries [see section 1.2.7 or e.g. 255, 152], since in both cases drag forces exerted by a gaseous medium supplied from the donor star lead to the orbital shrinking of the binary. Inspired by this similarity, [405] applied a modified version of α-formalism [originally developed for common-envelope evolution, see equation 1.28 or e.g. 360, 398, 67] to model the inner binary evolution of triples experiencing TMT [see also 119]. For the configuration case (i), we take the same approach.

Below we explain how the post-mass-transfer inner orbit is determined based on this formalism in detail. $\Delta M_{\mathrm{trnsf}}$ is the mass that is transferred from the tertiary in a timestep Δt. When $\Delta M_{\mathrm{trnsf}}$ ends up encompassing the inner binary, it has binding energy of E_{bind}. As the inner orbit is shrinking due to the friction during the TMT episode, the orbital energy of the inner binary changes by ΔE_{orb}. We assume that a fraction (α_{TMT}) of ΔE_{orb} is used to unbind $\Delta M_{\mathrm{trnsf}}$. We can write an equation expressing the energy balance as:

$$\alpha_{\mathrm{TMT}}\Delta E_{\mathrm{orb}} = E_{\mathrm{bind}}, \tag{3.11}$$

with

$$\Delta E_{\rm orb} = \frac{G M_1 M_2}{2 a_{\rm in,fin}} - \frac{G \left(M_1 + \Delta M_{\rm trnsf}/2\right)\left(M_2 + \Delta M_{\rm trnsf}/2\right)}{2 a_{\rm in,init}}, \tag{3.12}$$

and

$$E_{\rm bind} = \frac{-G(M_1 + M_2)\Delta M_{\rm trnsf}}{\lambda_{\rm TMT} a_{\rm init}}, \tag{3.13}$$

where $\lambda_{\rm TMT}$ is a parameter related to the structure of $\Delta M_{\rm trnsf}$, parameterising its binding energy, $a_{\rm in,init}$ is the initial orbital separation before $\Delta M_{\rm trnsf}$ is transferred to the inner binary and $a_{\rm in,fin}$ is the final orbital separation after $\Delta M_{\rm trnsf}$ is expelled from the inner binary. We assume that the total mass transferred to the inner binary throughout the entire TMT episode equals to the mass of the hydrogen envelope of the tertiary $M_{\rm out,env}$ (but see [192]). Then assuming a constant $\alpha_{\rm TMT}$ and $\lambda_{\rm TMT}$, the orbit changes due to the entire TMT episode as:

$$\frac{a_{\rm in,fin}}{a_{\rm in,init}} = \frac{M_1 M_2}{\frac{2(M_1+M_2)M_{\rm out,env}}{\alpha_{\rm TMT}\lambda_{\rm TMT}} + \left(M_1 + \frac{M_{\rm out,env}}{2}\right)\left(M_2 + \frac{M_{\rm out,env}}{2}\right)}. \tag{3.14}$$

As both $\alpha_{\rm TMT}$ and $\lambda_{\rm TMT}$ are unknown, we combine them and try three different values: $\alpha_{\rm TMT}\lambda_{\rm TMT} = 0.05, 0.5, 5$. Here $\alpha_{\rm TMT}\lambda_{\rm TMT} = 5$ is the fiducial value used in [119], which is in a good agreement with the hydrodynamical simulations of [405], in which the inner stars are on the MS during the TMT episode. We note that we neglect the possibility of TMT episode with ballistic accretion transitioning to a TMT episode with a circumbinary disc.

Additionally, for configuration type (i), we assume that the inner binaries circularise as a result of the mass transfer phase (as $a_{\rm in,new} = a_{\rm in}(1 - e_{\rm in})$). We note that this assumption might not be correct for highly eccentric inner binaries. For example, [110] showed that binaries at the onset of common-envelope events with

$e \gtrsim 0.95$ might retain eccentricities as high as $e \sim 0.2$.

(ii) *An inner binary with compact objects with circumbinary disc.* If a circumbinary disc is formed during a mass transfer phase towards an inner BH-BH binary we assume that the orbit of the inner binary remains unchanged. The actual physics underlying such a process are very complex [see 185, for a review on circumbinary accretion from gaseous medium]. The circumbinary disc may exert a torque on the inner binary and extract angular momentum from it, while the accreted matter can transfer angular momentum onto the inner binary. Furthermore, the circumbinary disc and the inner binary could be tidally distorted by the tertiary star.

It is commonly assumed that circumbinary accretion of a BH-BH binary from a gaseous medium leads to the shrinking of its orbit due to the torques exerted by the circumbinary disc and due to dynamical friction of the gas (e.g. [21, 338, 17, 347, 75, 226, 301]). However, a consensus regarding this physical process is still missing, with some hydrodynamical simulations suggesting that accretion from circumbinary disc could even lead to to orbital widening instead of orbital decay [e.g. 240, 238].

(iii) *A non-compact inner binary.* If the mass transfer occurs with a MS-MS accretor, we assume that this results in the merger of the inner binary. We make this assumption because these binaries have very short periods and a sizeable fraction of them are in contact and most likely they would expand due to TMT, overfilling their L2 point, which would lead to a merger (see later subsection 3.6). As we discuss in in subsection 3.6, we do not consider GW sources from those triple systems, in which the TMT occurs towards a binary with evolved (i.e. non-MS), non-compact stars.

We do not model unstable phases of TMT (as we will show later, they are very rare among the systems we discuss in this paper) . We note, however, that during

this type of mass transfer episode, the outer orbital separation is predicted to rapidly decrease due to the common-envelope-like evolution in triple system; this could result in a regime where the secular approximation from the triple is no longer valid [e.g. 109, 60, 328].

TMT: Evolution of the outer orbit

When determining the evolution of the outer orbit due to a stable phase of TMT, we apply the same method for all accretor types, irrespective of whether a circumbinary disc is formed. We calculate the evolution of the outer orbit during the TMT phase, based on the following relation:

$$\frac{\dot{a}_{\text{out}}}{a_{\text{out}}} = -2\frac{\dot{M_3}}{M_3}\left[1 - \beta\frac{M_3}{M_1 + M_2} - (1-\beta)\left(\gamma + \frac{1}{2}\right)\frac{M_3}{M_{\text{tot}}}\right], \tag{3.15}$$

where β is the fraction of mass accreted by the inner binary, γ is the specific angular momentum lost from the system as a fraction of the specific angular momentum of the triple and $\dot{M_3}$ is the mass transfer rate from the tertiary star. Equation 3.15 can be derived from angular momentum arguments. It is an adaptation of the relation describing the orbital evolution of a circular, mass transferring binary comprised of point particles [see equation 1.14 or e.g. 326], applied to a triple experiencing a TMT episode. This adaptation is valid, if the tertiary star is sufficiently far away from the inner binary, such that the inner binary can be treated as a point particle with a mass of $M_1 + M_2$. We assume that eventually all the transferred mass is isotropically expelled from the triple ($\beta = 0$), from near the inner binary. This expelled matter thus carries away a specific angular momentum that is equal to that of the inner binary ($\gamma = M_3/(M_1 + M_2)$, see also [119], for a similar approach). In this case

137

equation 3.15 can be expressed as

$$\frac{a_{\text{out,fin}}}{a_{\text{out,init}}} = \frac{M_{\text{tot,init}}}{M_{\text{tot,fin}}} \left(\frac{M_{3,\text{init}}}{M_{3,\text{fin}}}\right)^2 \exp\left(2\frac{M_{3,\text{fin}} - M_{3,\text{init}}}{M_1 + M_2}\right). \tag{3.16}$$

In case of BH-BH inner accretors, these assumptions might be valid, as the accretion rate of BHs might be capped by the Eddington-limit, and most of the mass could indeed be expelled from the system, for example in the form of a jet (e.g. [159, 410]) . On the other hand, MS stars are likely to accrete more efficiently, and therefore $\beta = 0$ might no longer be a good approximation.

3.3.6 Initial conditions

We sample 10^5 triples at two representative (moderate and low) metallicities: Z = 0.005 and Z = 0.0005. We simulate each hierarchical triples from ZAMS. After drawing the parameters for a given triple system, we further check, if it is dynamically stable [based on the criteria of 220] or if the stars in the inner binary are CHE at ZAMS. If any of the two criteria are not met, we do not evolve the triple system and only take it into account for the normalisation of event rate calculations. We terminate the simulation of a triple system when either a Hubble time (assumed to be 13.5 Gyrs) has passed, or when the tertiary star fills its Roche lobe, a merger occurs, a dynamical instability occurs or if any of the stars becomes unbound from the triple. We also stop the simulation, if any of the stars in the inner binary transitions back from CHE to classical evolution. That is, we only consider triples in which the stars of the inner binary chemically homogeneously evolve throughout their entire MS lifetimes. We refer to this population as *CHE triple population*.

In this study, we motivate the choice of the initial distributions of the parameters of the inner binaries based on recent surveys of massive binaries [e.g. 303, 171]. In

such surveys, a possible tertiary companion is not always unequivocally identified and therefore it is not clear whether the inferred distributions also hold for triples or only for isolated binaries.

We assume the ZAMS mass of the primary star ($M_{1,\mathrm{ZAMS}}$) follows the power-law mass distribution of [176], i.e. $N \sim M_{ZAMS}^{-2.3}$ for $M_{\mathrm{ZAMS}} \geq 0.5\, M_\odot$ and $N \sim M_{ZAMS}^{-1.3}$ for $M_{\mathrm{ZAMS}} < 0.5\, M_\odot$. We sample $M_{1,\mathrm{ZAMS}}$ from a mass range of 20-100 $M_\odot$. The lower limit approximately coincides with the lowest initial mass at which CHE is still possible in a tidally locked binary [e.g. 292], while the upper limit is roughly the maximum mass at which the stellar tracks used in TRES are still reasonably accurate. We assume a flat inner mass-ratio (i.e. $q_{\mathrm{in,ZAMS}} = M_{2,\mathrm{ZAMS}}/M_{1,\mathrm{ZAMS}}$) distribution, which is in broad agreement with [303]. We restrict the range of $q_{\mathrm{in,ZAMS}}$ to 0.7-1 given that inner binaries in which both of the stars are chemically homogeneously evolving and have $q_{\mathrm{in}} \leq 0.7$ would merge early during the MS (where we found the lower limit of 0.7 from our simulations). We sample the inner semimajor axis from a log-uniform distribution ([253]; and in broad agreement with [303]) in the range of 16 to 40 $R_\odot$. We assume that the inner binaries are tidally locked at ZAMS. This has three implications: i) the inner binaries have circular orbits, ii) their rotational angular frequency is synchronised with the orbital angular frequency, and iii) the spins of the stars are aligned with the orbital angular momentum vector.

We draw the properties of the outer binary from the same distributions that we assume for the inner binaries, with the exception of outer eccentricities. Observations of hierarchical multiple systems of galactic solar-type stars support the assumption that the distributions of the initial parameters of the inner and the outer binaries are the same [350, 351]. We sample the outer semimajor axis from a loguniform distribution in the range of 100 to $10^5\ R_\odot$. We assume that the distribution of the outer mass ratio (i.e. $q_{\mathrm{out,ZAMS}} = M_{\mathrm{out,ZAMS}}/(M_{1,\mathrm{ZAMS}} + M_{2,\mathrm{ZAMS}})$) is flat on a range of 0.1 to 1, furthermore the mass of the tertiary is restricted to a range of 5-100 $M_\odot$.

We assume non-spinning tertiary stars. The eccentricities of the outer orbit are drawn from a thermal distribution [e.g 126]. The mutual inclination between the inner and outer orbit is assumed to be uniform in $\cos(i_{\mathrm{ZAMS}})$, where i_{ZAMS} is the initial inclination (i.e. an assumption that there is no preferred orientation of the orbits and they form randomly). The initial argument of the pericenter is assumed to be uniformly distributed between $-\pi$ and π.

In Section 3.6, we compare our CHE triple population to a CHE isolated binary population. To this end, we also perform population synthesis of isolated binaries with CHE stars. We sample 10^5 isolated binaries at $Z = 0.005$ and $Z = 0.0005$ and evolve them with `TRES`. We sample from the same initial distributions that we assumed for the inner binaries of our triple population. Similarly to the triple population, we discard systems that are not CHE at ZAMS and stop the simulation, if a Hubble time has passed, or if any of the stars in the binary transitions from CHE to classical evolution. We only analyse binaries, in which the stars remain CHE throughout their entire MS lifetime (hereafter *CHE binaries*).

Throughout the paper, we estimate birth rate and merger rate densities of different evolutionary channels (discussed in detail in appendix, section B.2). In order to determine each of these quantities, one must know how common single and multiple stellar systems are. We assume two different stellar populations, with different binary and triple fractions. In the first, we assume that about 73 per cent of massive stars are found in triples [with multiplicity fractions of $f_{\mathrm{single}} = 0.06$, $f_{\mathrm{binary}} = 0.21$, $f_{\mathrm{triple}} = 0.73$, see e.g. 235][1], whereas in the second test population, we assume there are no triples and about 70 per cent of massive stars are in binaries [$f_{\mathrm{single}} = 0.3$,

---

[1][235] finds that 73 per cent of O stars are either in triples or quadrupoles. Therefore $f_{\mathrm{triple}} = 0.73$ should be considered as a rough upper limit. We also note that [351] finds that there is a strong correlation between the inner period and the triple multiplicity; among solar type stellar systems, 96 per cent of the spectroscopic binaries with periods less than 3 days has a tertiary companion. Therefore CHE triples, which have also inner binaries with periods of few days, could have exceptionally high triple fractions too.

Table 3.1: An overview of our sampled triples based on the evolutionary type of the inner binary. For the definitions of the different categories, see text in section 3.4.1.

	Z = 0.005		Z = 0.0005		Combined
	% of simulation	% of CHE at ZAMS	% of simulation	% of CHE at ZAMS	Birth rate [Gpc^{-3}yr^{-1}]
CHE at ZAMS	10.3	100	9.9	100	13.7
- *CHE triple*	7.6	73.5	7.5	75.7	9.6
- *Transition to classical evolution*	1.6	15.5	0	0	1.9
- *Merges during contact phase*	0.9	9	1.7	17.5	1.4
- *Simulation error*	0.2	2	0.6	6.7	0.2

$f_{\mathrm{binary}} = 0.7$, $f_{\mathrm{triple}} = 0$, see e.g.   303] [2].

3.4   Results of population synthesis simulations

In Table 3.4, we provide an overview of our sampled systems based on the evolutionary type of the inner binary. Out of our sampled population of triples, only about 10 per cent of the triples have an inner binary where both stars evolve chemically homogeneously from ZAMS (CHE at ZAMS triples, see Table 3.4), and we follow the further evolution only for these triples. About 75 per cent of CHE at ZAMS triples qualify as CHE triples and we focus on these systems for the majority of the paper. For the remaining 25 per cent, we distinguish three scenarios:

- **The inner stars transition to classical evolution**. As the orbit of the inner binary widens due to stellar winds, the rotational frequencies of the inner stars decrease, because the stellar tides enforce synchronization between the stellar spins and the (new longer) orbital period. If the inner orbit widens sufficiently, the angular rotational frequencies of the inner stars drop below ω_{CHE} and therefore these stars transition to classical evolution. This occurs only in our moderate metallicity model (15.5 per cent of all CHE at ZAMS triples at Z = 0.005 and 0 per cent at Z = 0.0005).

---

[2]Strictly speaking, [303] did not make any statements about triple fractions, but they found that 70 per cent of massive stars have companions that are sufficiently close such that mass exchange will occur some time in their evolution.

- **The inner binary does not survive the contact phase during the MS phase of the inner stars**. We assume a merger takes place when both stars overflow their outer Lagrangian point during the contact phase. This occurs during mass equalization in the contact phase or due to GW emission, which lead to shrinkage of the inner orbit. As orbital widening due to stellar winds prevent mergers, the process occurs more efficiently at low metallicities (about 9 per cent of all CHE at ZAMS triples at Z = 0.005 metallicity and 17.5 per cent at Z=0.0005).

- **Computational issue.** Finally, we note that the simulation of about 2 (6.7) per cent of CHE at ZAMS triples fails at Z = 0.005 (Z = 0.0005). This can occur because either no solution is found for the secular orbital evolution of the system, or the computation time exceeds the allowed CPU time (which is 5000 seconds per system). Computational issues arise more often for systems that are close to the dynamical instability (i.e. have low $a_{\mathrm{out}}/a_{\mathrm{in}}$). Therefore, our estimates for the occurrence rates of systems, in which stellar merger due to ZLK oscillations or dynamical instability occurs should be considered as a lower limit (see next subsection).

3.4.1 Main evolutionary outcomes

In Table 3.2, we show the most common evolutionary outcomes for CHE triples. We distinguish 5 different evolutionary channels.:

- **No post-MS mass transfer phase:** During the MS, it may be in a contact, but the system does not experience any other form of mass transfer events. The inner binary eventually forms a BH-BH binary in all these triples.

- **Stellar merger of the inner binary due to ZLK:** Stellar merger occurs in the

142

Table 3.2: A summary of the different channels (in bold font) and their sub-channels (in normal font) identified of CHE triples. The rows with bold fonts in the second and third column express the number of systems in each channel as a percentage of all CHE triple systems. The rows with normal fonts in the second and third column express the number of systems in each sub-channel as a percentage of all systems in their respective main channel. See equation B.8 and the accompanying discussion in appendix B.2 for the definition of birth rate density.

Channel	% at Z = 0.005	% Z = 0.0005	Birth rate density [Gpc^{-3}yr^{-1}]
No post-MS MT	**27.2**	**10.8**	**2.3**
- Inner binary evolution decoupled from tertiary	97.4	98.6	2.2
- Driven by three-body dynamics	2.6	1.4	0.1
Stellar merger of the inner binary due to KL	**3.3**	**2.5**	**0.4**
- double helium star accretor	74.7	58.5	0.3
- helium star-MS accretor	7.9	35	0.04
- helium star-BH accretor	17.4	6.5	0.06
Tertiary mass transfer	**55.4**	**52.1**	**5.2**
- MS-MS accretor	58	60.8	3.1
- BH-BH accretor	30.9	24.3	1.5
- Other types of accretors	11.1	14.9	0.6
Unbound systems	**10.7**	**34**	**1.4**
- Core collapse SN	100	16	0.9
- (P)PISN	0	84	0.5
Dynamical instability	**3.5**	**0.6**	**0.3**

inner binary due to ZLK oscillations.

- **Tertiary mass transfer (TMT):** The tertiary star fills its Roche lobe.

- **Unbound systems:** This evolutionary outcome takes place, if any of the stars becomes unbound from the system. This occurs when a stellar remnant is formed in the system, with three major subtypes: (i) natal kick imparted onto the remnant object during the SN explosion, (ii) instantaneous mass loss during pulsational PISN, or (iii) complete disruption of the star due to PISN.

- **Dynamical instability:** These systems eventually become dynamically unstable, where the secular approximation is no longer valid.

We discuss these channels in detail in sections 3.4.3 - 3.4.13.

3.4.2 Examples for the evolution of a few selected systems

In the following, we present the evolution of a few selected systems from some of the channels introduced in section 3.4.1. In all of these example systems, the initial parameters of the inner binary are the same: $M_{1,\mathrm{ZAMS}} = M_{2,\mathrm{ZAMS}} = 70\,M_\odot$, $a_{\mathrm{in,ZAMS}} = 22.4\,R_\odot$. These have been specifically chosen such that this system would form a GW source via the binary CHE channel within the Hubble time, if it was an isolated binary (i.e. in about 8.9 Gyrs). The inner binary is tidally locked and therefore $e_{\mathrm{in,ZAMS}} = 0$. The stars of the inner binary are in contact from ZAMS and equalise in mass soon after ZAMS. The initial mutual inclination is $i_{\mathrm{ZAMS}} = 90°$ in all systems discussed below, which allows for ZLK oscillations to develop, unless they are suppressed by short range forces [see e.g. 197].

In order to understand the evolutionary paths of CHE triples introduced below, we first show which configurations of CHE triples lead to efficient ZLK oscillations (see Fig. 3.1). We evolve the previously introduced CHE inner binary as an isolated system, and take four snapshots during different evolutionary stages (ZAMS, end of MS, at the onset of core collapse, and at the formation of an inner BH-BH binary). For each snapshot, we show a range of possible tertiary companions to this inner binary with different tertiary masses (M_{out}) and outer semi major axes (a_{out}) and identify those regions, where three-body dynamics are relevant.

As shown in the leftmost panel, precession due to tides completely suppresses three-body dynamics when the inner stars are still on the MS for almost the entire parameter space of CHE triples. The limited number of triples for which this is not true typically become dynamically unstable later in the evolution (e.g. compare panel 1 with panel 4). By the time of hydrogen depletion in the inner stars, the stellar radii of CHE stars shrinks typically by a factor of 3-5 with respect to their ZAMS value. Therefore, at this stage tides become less efficient (since $t_{\mathrm{tides}} \sim R^{-5}$,

see equation 3.3) and precession due to GR becomes the major limitation to three-body dynamics. For the systems shown in Fig. 3.1, ZLK oscillations occur only, if $a_{\mathrm{out}} \lesssim 500\,R_\odot$. During the CHeB phase of the inner stars, the typical timescale of precession due to GR further increases, as a result of the strong Wolf-Rayet winds that significantly widen the inner orbit. As long as the inner orbit widens faster than the outer orbit (which is always true if the tertiary star is the initially least massive star in the system), the timescale related to ZLK oscillations will not significantly increase. Therefore during this stage, the parameter space where three-body dynamics are relevant increases. This is also shown in the rightmost panel of Fig. 3.1; by the time the inner binary forms BHs, triples with $a_{\mathrm{out}} \lesssim 2000\,R_\odot$ will develop ZLK oscillations.

Example for stellar merger of the inner binary due to ZLK oscillations

First, we discuss the evolution of a CHE triple, in which the inner binary merges as a double helium star due to strong ZLK oscillations (shown in Fig. 3.2). This triple has a tertiary with an initial mass of $M_{\mathrm{out,ZAMS}} = 32.1\,M_\odot$ and a circular outer orbit with $a_{\mathrm{out,ZAMS}} = 200\,R_\odot$. As indicated by Fig. 3.1, when the stars of the close inner binary are still on the MS, precession associated with strong tides suppresses the effects of the three-body dynamics [see also e.g. 368]. At 3.9 Myrs, the stars of the inner binary evolve off the MS. By this time, these stars had lost a small amount of mass due to stellar winds and the inner orbit had widened by only 2 per cent as a result. Similarly, the outer orbit also widens only by a negligible amount. Consequently, the timescale of the ZLK oscillations does not change significantly. On the other hand, the tidal effects become much weaker, as the radii of the stars had decreased by a factor of 5 with respect to their ZAMS value. As a result, the ZLK oscillations are no longer suppressed (see also second panel of Fig 3.1). At this stage, there are two competing mechanisms that drive the evolution of the pericenter: ZLK

oscillations and the strong Wolf-Rayet-like winds, which decrease and increase the pericenter, respectively. For this triple, the ZLK timescale is extremely short (few years) and a large inner eccentricity of $e_{\rm in} \approx 0.65$ is reached shortly after the onset of CHeB, during which the orbital widening due to stellar winds is negligible. At this stage, the pericenter becomes sufficiently small such that the helium stars fill their Roche-lobes at the point of closest approach. We assume this results in the merger of the inner binary.

Example for TMT towards an eccentric BH-BH binary

The next triple we discuss experiences a TMT episode towards an eccentric BH-BH inner binary (shown in Fig 3.3). This system has the same parameters as the previously discussed triple, but with a slightly larger initial outer semimajor axes: $a_{\rm out,ZAMS} = 421\,R_\odot$. When the inner stars evolve off MS, ZLK oscillations are quenched by precession due to GR (compare the second panels of Fig. 3.1 and Fig. 3.3). Three-body dynamics become later effective, as the orbit of the inner binary widens significantly and faster than the outer orbit due to strong WR winds (compare the third panels of Fig. 3.1 and Fig. 3.3, although by this stage the parameters of the inner binary differ slightly). As a result $t_{\rm GR}$ increases by a factor of 5, while $t_{\rm ZLK}$ barely changes. As ZLK cycles become only effective once the inner orbit has sufficiently widened, the inner binary does not come into contact despite reaching similarly high inner eccentricities as in the previous system.

As the stars of the inner binary have the same mass, they co-evolve, and they become stellar remnants at the same time. This occurs around 4.2 Myr, when the inner eccentricity is $e_{\rm in,max} = 0.75$. Since core-collapse occurs in an eccentric orbit, a large range of possbile post-supernova orbits is possible ($a_{\rm in} = 42\text{-}186\,R_\odot$) depending on where exactly the stars are in their orbit. In the particular example shown in Fig

3.3, the core collapse occurs while both stars are near the pericenter (which is less likely as they spend more time near the apocenter). This leads to an inner semi-major axis of $a_{\rm in} = 171\,R_\odot$ after BH-BH formation. As the outer orbit is circular at the onset of the core-collapse, it only widens by a moderate amount. As the inner period to outer period ratio has increased by a factor of 7, the timescale of the ZLK oscillations also further decrease, making the three-body dynamics even more relevant for the further evolution of the system. The evolution of this triple therefore demonstrates, that if the ZLK oscillations are strong enough to induce eccentricities before the formation of an inner BH-BH binary, the importance of three-body dynamics can be significantly increased during the last stages of the evolution of the triple, depending on (i) where the inner stars are in their orbit when the formation of the compact objects occur and (ii) on the eccentricity of the outer orbit.

After the formation of the inner BH-BH binary, the tertiary star evolves off the MS, and at 6.1 Myr fills its Roche-lobe and transfers mass to the highly eccentric ($e_{\rm in} = 0.94$) BH-BH binary at a highly inclined orbit (i = 71.5°). At this stage, we stop the simulation (but see later section 3.6, where we predict the further evolution of some of these systems). We note, however, that even if the TMT episode does not affect the inner binary, it still merges due to GWs about a factor of 8 faster than its isolated binary counterpart due to the high eccentricities induced by the ZLK oscillations.

Example for TMT towards a circular BH-BH binary

Next, we show the evolution of a CHE triple, which also experiences a TMT episode towards a BH-BH binary, but in which three-body dynamics remain suppressed throughout the entire evolution. The initial outer semimajor axis is $a_{\rm out,ZAMS} =$

$1069\,R_\odot$. For this system the timescales of the ZLK oscillations remain too long with respect to the timescale associated with precession due to GR effects throughout the entire post-MS phase. At the onset of core-collapse, at which the parameter space for ZLK oscillations is typically the largest for CHE triples with inner binaries composed of non-compact objects, the outer semimajor axis is $a_{\rm out,ZAMS} = 1720\,R_\odot$ and the tertiary mass is $M_{\rm out} = 31.9\,M_\odot$. The third panel in Fig. 3.1 implies that the three-body dynamics is just quenched by the relativistic precession at this stage. Therefore, the inner orbit remains circular when the BHs are formed, and the inner orbit only widens moderately due to BH formation. The inner and the outer orbit after the formation of a BH-BH binary are $a_{\rm in} = 46.6\,R_\odot$ and $a_{\rm out} = 1860\,R_\odot$ and therefore the ZLK oscillations remain quenched. At 6 Myr, the tertiary reaches a radius of $547\,R_\odot$ and fills its Roche-lobe while crossing the Hertzsprung gap. The last two examples suggest (and we will show in section 3.5 that this is generally true for the vast majority of CHE triples) that three-body dynamics are only relevant for the evolution of CHE triples, if the tertiary star is on a sufficiently short orbit, such that it will eventually fill its Roche-lobe and initiate a TMT episode. Conversely, if the tertiary star remains detached throughout the evolution of the triple, the inner binary evolves effectively as an isolated binary for the vast majority of CHE triples.

3.4.3 No post-MS mass transfer

In no post-MS mass transfer triples, the tertiary star remains bound and detached, while the stars of the inner binary form a BH-BH binary. The inner stars are in contact in the majority of the cases (e.g. around 90 per cent at $Z = 0.005$). There are no other mass transfer phases during the evolution of these systems (by definition). About 27 per cent of CHE triples evolve this way in our moderate metallicity model (see Table 3.2). This decreases to 11 per cent at $Z = 0.0005$. The main reason for
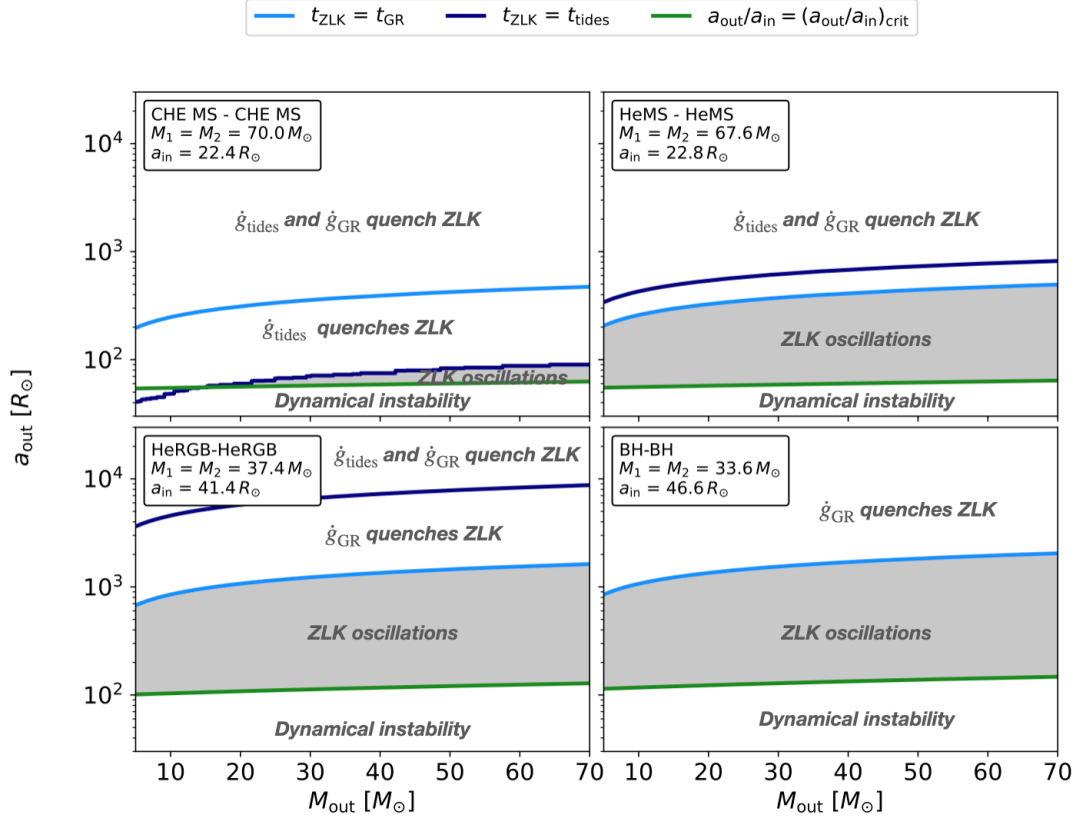
Figure 3.1: We illustrate the parameter space where ZLK oscillations develop for typical CHE triples at different evolutionary stages at Z = 0.005. Each panel represents triples with a specific inner binary (with masses M_1, M_2 and inner separation a_{in} as indicated in the top left of each panel) but with varying tertiary masses, M_{out} (x-axis) and outer semimajor axes, a_{out} (y-axis, logscale). The parameters of the inner binary in each panel are the same as that of an isolated CHE binary with $M_{1,ZAMS} = M_{2,ZAMS} = 70\,M_\odot$, $a_{ZAMS} = 22.4\,R_\odot$ at different evolutionary stages (see text in section 3.4.2). First panel: two CHE main sequence stars at zero-age main sequence, second panel: helium stars at the onset of core-helium burning (HeMS), third panel: two helium stars at the end of core-helium burning (HeRGB), fourth panel: at the formation of a BH-BH inner binary. We assume circular inner and outer orbits and a mutual inclination of i = 90°. The light blue and the dark blue lines show regions, where the ZLK timescale equals to the timescale of apsidal precession due to tides and GR effects, respectively (see equation 3.2, 3.4, and 3.3). Consequently, triples above any of these two lines do not exhibit ZLK oscillations, as they are quenched by these short range forces. The green line represents the boundary of dynamical instability. The shaded grey region represents triples where ZLK oscillations are effective.
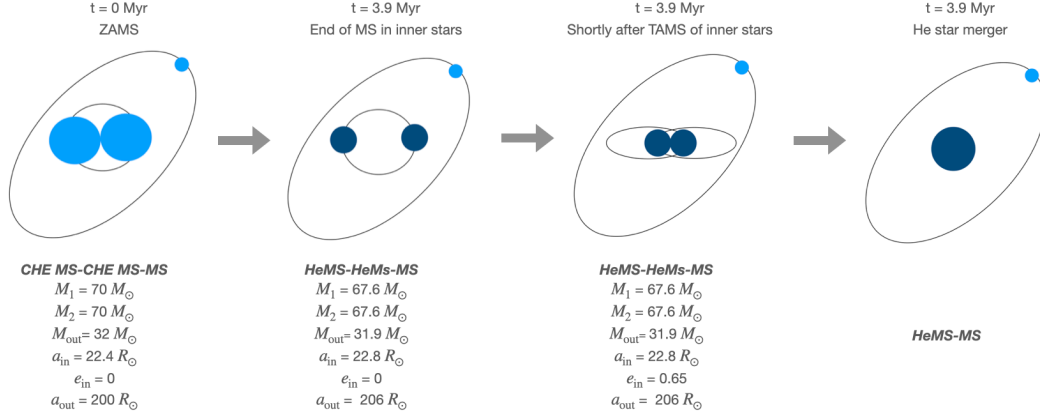
Figure 3.2: A schematic drawing showing the evolution of a triple system in which the stars in the inner binary experience stellar merger due to ZLK oscillations. The first line below each drawing shows the evolutionary stage of each star. The first is for the primary, the second is for the secondary, and the third is for the tertiary star. CHE MS refers to a chemically homogeneously evolving MS star, HeMS to a core-helium burning helium star, and HeRGB to a helium star that has finished core-helium burning. The parameters of the triple at ZAMS are: $M_{1,\mathrm{ZAMS}} = M_{2,\mathrm{ZAMS}} = 70\,M_\odot$, $a_{\mathrm{in,ZAMS}} = 22.4\,R_\odot$, $i_{\mathrm{ZAMS}} = 90°$, $M_{\mathrm{out,ZAMS}} = 32.1\,M_\odot$, $a_{\mathrm{out,ZAMS}} = 200\,R_\odot$, $e_{\mathrm{out}} = 0$. The outer eccentricity remains $e_{\mathrm{out}} \lesssim 0.01$ throughout the evolution.
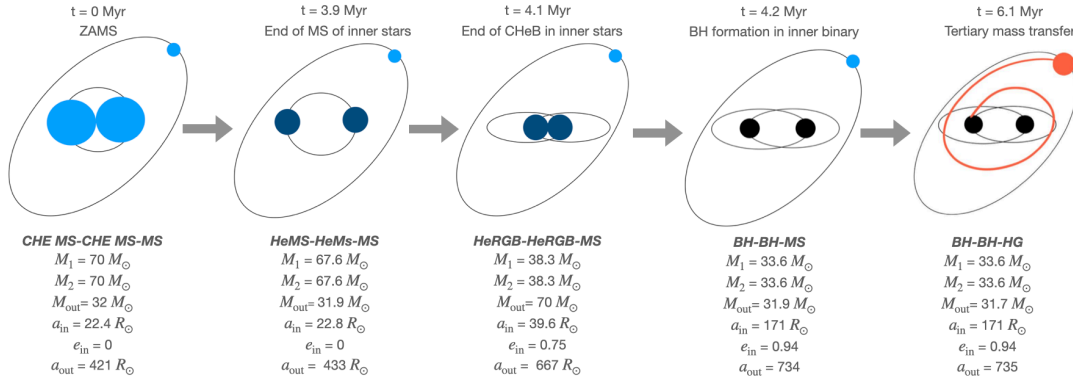

Figure 3.3: A schematic drawing showing the evolution of a triple system with that eventually experiences a TMT episode (i.e. the most common evolutionary outcome, see Table 3.2). The triple system with the following initial parameters: $M_{1,\mathrm{ZAMS}} = M_{2,\mathrm{ZAMS}} = 70\,M_\odot$, $a_{\mathrm{in,ZAMS}} = 22.4\,R_\odot$, $i_{\mathrm{ZAMS}} = 90°$, $M_{\mathrm{out,ZAMS}} = 32.1\,M_\odot$, $a_{\mathrm{out,ZAMS}} = 200\,R_\odot$, $e_{\mathrm{out}} = 0$. The outer eccentricity remains $e_{\mathrm{out}} \lesssim 0.01$ throughout the evolution.

this difference is the larger number of PISN that occurs at lower metallicities, which prevent the formation of BHs.

After the formation of the BH-BH binary, the system may merge due to GW emission within a Hubble time. This occurs for all systems of this type at $Z = 0.0005$. However at $Z = 0.005$, the stellar winds are strong enough such that 32 per cent of the inner binaries of these triples end up with orbits that are too wide to merge within a Hubble time due to GW emission. We note that these are not necessarily all of the GW sources from our simulations, as triples in other channels discussed here can also potentially form merging binary BHs (see discussion in section 3.6).

For the majority of these triples (> 97 per cent), the inner binary evolves essentially unaffected by the tertiary star (see also section 3.5). Therefore, the properties of the inner binaries of this channel are nearly indistinguishable from those of isolated CHE binaries. The initial outer pericenters of the triples of this channel are large enough such that the outer star remains detached (i.e. $a_{\mathrm{p,out,ZAMS}} \gtrsim 2000$-$3000\,R_\odot$ at Z $= 0.005$, see also section 3.5). At such large tertiary separations, the three-body dynamics remain suppressed during the entire evolution of the triple.

The properties of the subgroup in which three-body dynamics drive the evolution of the inner binary are very different. Firstly, they have very short initial outer pericenters (i.e, $a_{\mathrm{p,out,ZAMS}} \approx 100$-$700\,R_\odot$), and secondly, the tertiary has a relatively low mass (typically $M_{\mathrm{out,ZAMS}} = 10$-$30\,M_\odot$). In these systems, the ZLK oscillations drive the eccentricity of the inner BH-BH binary up to large values (e.g. $e_{\mathrm{in}} \gtrsim 0.7$-$0.9$). Above a given eccentricity, the GW emission becomes so efficient that the inner binary decouples from the tertiary and it plunges due to GWs [see e.g. 323, 295]. These systems typically have a relatively low-mass tertiary star compared to the stars in the inner binary, such that the inner binary merges as a BH-BH binary due to GW emission before the tertiary star would evolve off the MS and fill its Roche-

lobe. Overall, the parameter space for this subgroup is very small, and therefore we predict a negligible GW merger rate (see later discussion in section 3.6).

3.4.4 Stellar merger of the inner binary due to ZLK

In this scenario, the inner binary merges due to three-body dynamics, before it would form a BH-BH binary. At $Z = 0.005$, about 3.3 per cent of the CHE triple population evolves this way. In our low metallicity model, this fraction decreases slightly, to 2.2 per cent. This is because at lower metallicities, the inner period to outer period ratio increases less due to the weaker stellar winds, and therefore ZLK oscillations remain less efficient (see equation 3.2).

Mergers in this channel occur in inner binaries, in which one or both of the stars have already evolved off MS, otherwise the strong tidal effects typically quench the ZLK oscillations (see section 3.4.2). As shown in Table 3.2, most of the merger occurs between two helium stars (59-75 per cent). The rest occurs between a helium star - MS star or helium star - BH binaries. The majority of the double helium star mergers (>90 per cent) originate from triples, in which the stars in the inner binary were in contact during MS and co-evolved. This also implies that the majority of them have equal masses at the time of the merger. The masses of these helium inner stars typically range from 29 to 94 $M_{\odot}$ at $Z = 0.005$.

The outer orbital period of the triples from this channel has to be sufficiently short, such that the ZLK oscillations are strong enough such that they prompt the inner binary to merge. The outer pericenter at the moment of the merger typically ranges from 100 to 200 $R_{\odot}$ and it does not exceeds 700 $R_{\odot}$. The eccentricities of the inner binary at the moment of the merger typically have values of $e_{\rm in} \approx 0.5$-0.9. For all of these triples, the tertiary is a MS star at the time of the merger and less

massive than the stars of the inner binary, otherwise it would evolve faster than the stars in the inner binary and would fill its Roche-lobe, while the inner stars are still on MS. If the outer orbit does not significantly change after the merger, the tertiary star is expected to transfer mass to the merger product, once it evolved off the MS.

3.4.5   Systems with tertiary mass transfer (TMT)

Among CHE triples, this is the most common evolutionary pathway. In these systems, the outer star eventually initiates a mass transfer phase while the inner binary is detached or in contact. Approximately 55 (52) per cent at $Z = 0.005$ ($Z = 0.0005$) of all CHE triples experience this type of evolution (see Table 3.2). This means that a TMT episode would eventually occur in about 40 per cent of all stellar systems containing a binary with CHE stars (with $f_{\text{binary}} = 0.21$, $f_{\text{triple}} = 0.73$). While systems containing binaries with CHE stars are rare (see e.g. typical birth rates in Table 3.4), they form GW sources very efficiently [e.g. 213, 401, 217]. Therefore, our predictions suggest that the evolution of a non-negligible fraction of potential GW progenitors could experience a TMT episode. This is an interesting result, as TMT is thought to be very uncommon for classically evolving hierarchical triples, which would have implied that they play a limited role in important astrophysical phenomena [see e.g. 405, 356, 120, 184]. In particular [356] found that about 1 per cent of triples with primaries in the intermediate mass range belong to this evolutionary channel. Similarly, [405] predicts that about only 1 per cent of the observed 725 triples in the catalogue of [349] would eventually initiate TMT.

In the following sections (3.4.6-3.4.11), we discuss the properties of the triples of this channel at the onset of TMT. While predicting the outcome of a TMT episode is currently extremely challenging, highlighting several important aspects of these systems (e.g. dynamical stability of TMT, timescales of TMT epsiodes, the amount

of transferred mass, the type of accretors, etc.) helps to better understand the nature of these systems and the role they potentially play in the evolution of GW progenitors.

3.4.6   Donors of TMT episodes

Here, we discuss the stellar evolutionary stage of the donor star at the onset of the mass transfer episode, as it is highly relevant for determining if the mass transfer episode occurs in a dynamically stable or unstable way [which has a dramatic effect on the outcome of the TMT, compare e.g. 405, 110].

In particular, convective envelopes can be developed by core-helium-burning or asymptotic giant branch stars. Mass transfer episodes initiated by such cool-giant donors with deep convective envelopes are more likely to occur in a dynamically unstable way than mass transfer phases initiated by giant donors with mostly radiative envelopes [e.g., 130, 326, 167].

At $Z = 0.005$, around 80 per cent of the donors of TMT systems are stars crossing the Hertzsprung gap. At this metallicity, the largest expansion in the radius of the star occurs during this evolutionary phase, which makes binary interaction during this stage the most likely. The second most common donor type is a CHeB star with 11.3 per cent, while the rest are either stars on the first giant branch (when the tertiary $M_{\mathrm{out,ZAMS}} \lesssim 8\,M_\odot$) or stars on the asymptotic giant branch.

At lower metallicities, CHeB donors are more prevalent. At $Z = 0.0005$, only 58 per cent of the tertiary donors are HG stars while 40 per cent are CHeB stars; this is because the onset of CHeB occurs at a higher effective temperature with respect to systems at Z = 0.005. Consequently, at lower metallicities, the onset of CHeB
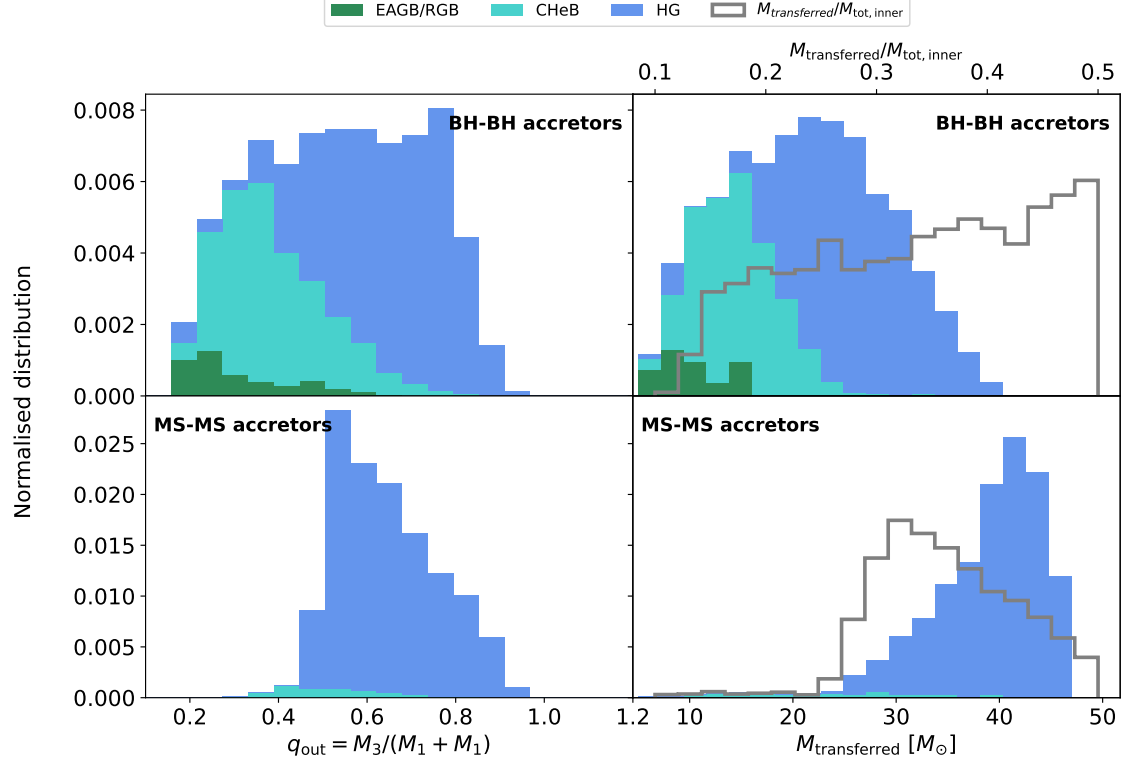
Figure 3.4: We show the properties of the donor star at the onset of tertiary mass transfer episode. The right panels show the amount of mass transferred from the tertiary to the inner binary for systems undergoing TMT at Z = 0.005, and the left panels show the outer mass ratio, $q_{\mathrm{out}} = M_{\mathrm{out}}/(M_1+M_2)$, at the onset of the tertiary mass transfer phase. Different colours correspond to different evolutionary stages of the donor as shown by the legend. We exclude cases where the donor is a MS star. Furthermore, we distinguish BH-BH inner binaries (upper panels) and MS-MS inner binaries (lower panels), which are the main types of accreting systems. The unfilled histogram in the panels on the right show the transferred mass as a fraction of the total mass of the inner binary for all donor types. All histograms shown have been normalised with respect to the population of CHE evolving triples.

is followed by a larger increase in radius with respect to their higher metallicity counterparts (see e.g. Fig. 1.10). This in turn implies that stars are more likely to fill their Roche-lobes at this evolutionary stage.

3.4.7   Stability of TMT episodes

The vast majority of mass transfer episodes in this channel occur in a dynamically stable way (99.9 per cent at Z = 0.005 and 98.8 per cent at Z = 0.0005). This is due to the relatively low mass ratios at the onset of the mass transfer phase (i.e. typically $q_{\mathrm{out}} < q_{\mathrm{crit}}$, see left panel of Fig. 3.4 for our moderate metallicity model, and Fig. B.1 for our low metallicity model). Typical mass ratios for systems with HG donors are $q_{\mathrm{out}} = 0.4$-0.8, while for CHeB donors, they are $q_{\mathrm{out}} = 0.3$-0.5 . The values for CHeB donors are smaller because of the strong LBV winds that CHeB star experience decrease the mass ratios over time. Unstable mass transfer phases exclusively occur with CHeB donors in our simulations.

These low mass ratios also imply that the expansion due to stellar evolution drives the TMT episodes [e.g. 326]. Consequently, we expect TMT episodes with HG donors to last 10^4 yrs, while TMT epiosdes with CHeB donor could last much longer up to 10^5-10^4 years.

3.4.8   Accretors of TMT episodes

In this subsection, we discuss the type of accretors of TMT episodes. The evolutionary stage of the inner binaries has a crucial role in the outcome of TMT episodes. If the inner binary comprises CHE MS stars, a TMT episode probably leads to the merger, as CHE binaries have very short periods and the majority of them are in

contact at the onset of the TMT [see also 40]. On the other hand, if the inner binary consists of BHs, TMT epsiode is unlikely to lead to a merger by itself, however, in principle, could be a source of (observable) X-ray emission [e.g. 156].

As shown in Table 3.2, the two most common types of accretors are MS-MS and BH-BH binaries. In only 11-15 per cent of CHE triples experience TMT with different accretors, such as an inner binary consisting of two helium stars or a helium star with a MS or BH companion.

We highlight the relatively large fraction of BH-BH accretors (24-31 per cent of CHE triples experiencing TMT). For classically evolving triples, mass transfer towards a BH-BH binary is highly unlikely. Firstly, in systems in which a TMT episode were to occur towards a BH-BH inner binary, the stars of the inner binary need to be more massive than the tertiary, such that they form BHs before the outer star fills its Roche-lobe. Secondly, the outer star has to be sufficiently close, otherwise it would remain detached throughout its evolution. This, in turn, puts a limit on the largest possible inner orbit, if the system is to remain dynamically stable. The maximum inner orbit for such systems is so small that classically evolving inner stars (which eventually expand) would initiate mass transfer and would most likely merge, which would reduce the triple to a binary and a tertiary mass transfer would never occur [see e.g. Fig. 14 in 356]. On the other hand, if the triple has CHE inner stars, the stars will not expand and not merge with one another, instead the system will evolve to contain a BH-BH binary by the time the tertiary fills its Roche-lobe.

3.4.9 Mass transferred towards the inner binary

We discuss the amount of mass that is transferred during the TMT episode. This is an important aspect, as the relative transferred mass determines the angular

momentum reservoir available to change the orbit of the inner binary.

Assuming that the entire envelope of the donor star is transferred towards the inner binary, the amount of transferred mass ranges between 1-40 $M_\odot$ for BH-BH accretors and between 10-50 $M_\odot$ for MS-MS accretors (see right panel of Fig. 3.4 for Z = 0.005 and B.1 in section of B.1 of Appendix for Z = 0.0005). Systems with MS-MS accretors typically receive a larger amount of mass than BH-BH accretors, because the tertiary star is typically more massive in the former case. This is because for the tertiary to fill its Roche lobe while the inner stars are still on the MS, the initial tertiary star needs to be evolve faster and hence be more massive than the MS stars. The relative transferred mass expressed as a fraction of the total mass of the inner binary (i.e. $M_{\mathrm{transferred}}/M_{\mathrm{tot,inner}}$) has the same maximum value (~ 0.5) for both BH-BH and MS-MS accretors (see grey histogram in right panel of Fig. 3.4).

3.4.10 Formation of circumbinary disc

We discuss how common it is for TMT systems to develop a circumbinary disc at the onset of the mass transfer episode. As explained in section 3.3.5, whether a TMT episode is accompanied by a formation of a circumbinary disc can have important consequences for the evolution of the inner orbit.

We find that about 63 per cent of all TMT systems develop circumbinary discs in our moderate metallicity model, while in the rest TMT proceeds in a ballistic fashion. Systems in which a circumbinary disc is formed during the TMT phase typically have larger outer pericenters at the onset of the mass transfer ($a_{\mathrm{p,out}} \approx$ 300-6000 $R_\odot$) than in those where TMT proceeds in a ballistic manner ($a_{\mathrm{p,out}} \approx$ 100-600 $R_\odot$).

TMT with a circumbinary disc is more prevalent at lower metallcities. About 74 per cent of all TMT systems develop circumbinary discs at Z = 0.0005. This occurs because the ratio of the inner and the outer orbital separation decreases less by the onset of the mass transfer phase due to weaker stellar winds (see equation 3.10).

TMT episodes with inner BH-BH binaries are somewhat more likely to occur in a ballistic fashion than with MS-MS inner binaries. About 45 (23) per cent of TMT systems with BH-BH inner binaries do not develop circumbinary discs at Z = 0.005 (Z = 0.0005), while 32 (27) per cent of TMT episodes with MS-MS inner binaries occur in a ballistic fashion. This is mainly because the inner apocenter to outer pericenter ratios at the onset of TMT are typically higher for inner BH-BHs than for inner MS-MS binaries (see equation 3.10). This difference is due to Wolf-Rayet winds, supernova kicks and possible ZLK oscillations that BH-BH inner binaries experienced prior to the TMT episode.

3.4.11   Three-body dynamics prior to TMT

Three-body dynamics can increase the eccentricities of the inner binary. This can, for example significantly decrease the coalescence time due to GWs [e.g. 233, 35, 381, 346].

Three-body dynamics is almost always suppressed during the MS phase of the inner binaries due to the strong tides (see also section 3.4.2). Consequently, the inner orbits of TMT systems with MS-MS inner binaries are always circular at the onset of the mass transfer episode. On the other hand, this is no longer the case when the inner stars are in their post-MS.

In Fig. 3.5, we show the cumulative distribution of the inner binary eccentricities

at the onset of the mass transfer phase of TMT systems with BH-BH accretors at Z = 0.005. We see that systems without circumbinary discs tend to have eccentric inner orbits at the onset of mass transfer. The high eccentricities are caused by ZLK cycles during the post-MS evolution of the inner binary. About 40 per cent of such triples have $e_{in} \gtrsim 0.4$ at this stage. This is in contrast with the systems with circumbinary discs; about 90 per cent of the systems have eccentricities $e_{in} \lesssim 0.1$. The difference is due to the smaller inner period to outer period ratios that systems without circumbinary discs have (see equation 3.2). In our low metallcity model, high eccentricites at the onset of TMT are much less common (see Fig. B.2 in section of B.1 of Appendix). For these systems the inner period to outer period ratio does not increase significantly because of the weak stellar winds.

3.4.12 Unbound systems

In this channel, one of the stars in the triple becomes unbound as a result of core-collapse. We distinguish systems based on whether this occurs via PISN or via classical core collapse [e.g. 97]. As shown in Table 3.2, PISN does not occur in our moderate metallicity model, whereas at Z = 0.0005, it becomes quite prevalent; about 84 per cent of the unbound systems occur due to PISN.

If the triples becomes unbound as a result of a classical core-collapse, we further distinguish whether it is due to the core-collapse occuring in the inner binary (97 per cent of all classical core-collapse systems at Z = 0.005 and 99 at Z = 0.0005) or of the tertiary star (3 per cent at Z = 0.005 or 1 per cent at Z = 0.0005). As the inner binary consists of CHE stars, they have large initial masses (i.e. $M_{ZAMS} \gtrsim 30\,M_{\odot}$) and furthermore they develop more massive CO cores than their classically evolving counterparts. Therefore, they get weak (if any) natal kicks when they form BHs according to our implemented natal kick prescription. Yet weak natal kicks, or even
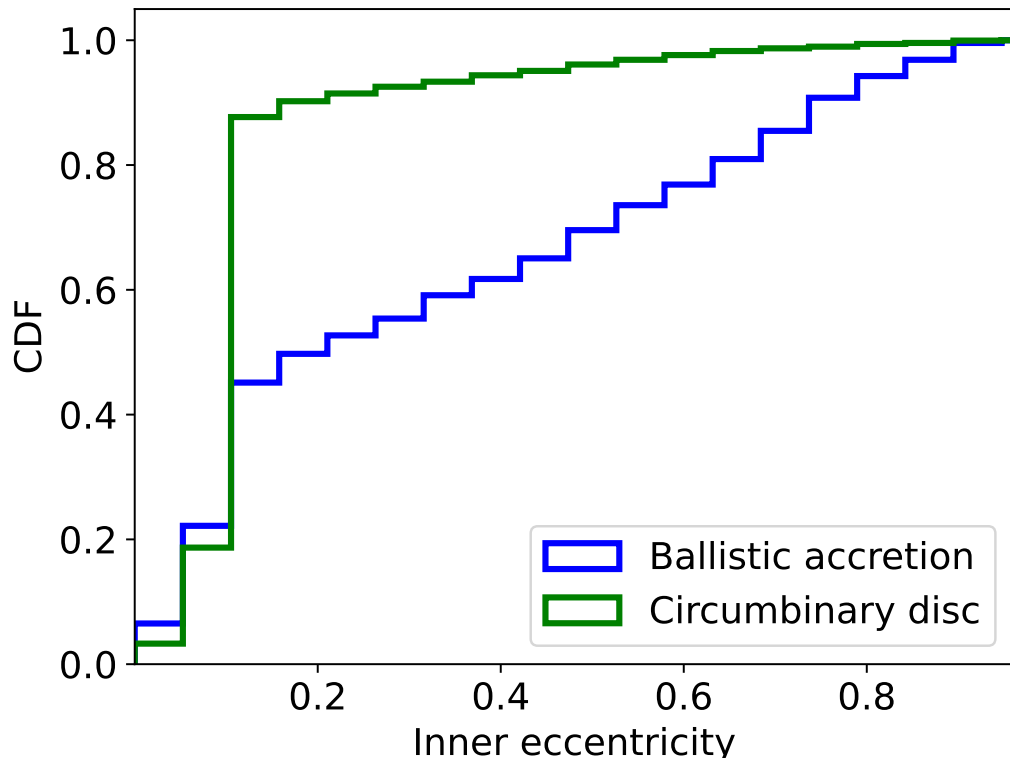
Figure 3.5: The cumulative distribution of the inner binary eccentricities of systems experiencing TMT with BH-BH accretors at the onset of the mass transfer phase at Z = 0.005. The green curve shows the systems with circumbinary discs formed during the mass transfer phase. The blue curve shows the systems where ballistic accretion occurs.

completely symmetrical instantaneous mass loss due to neutrino losses [which we assume to be 10 per cent of the pre-collapse mass according to 97] can unbind the tertiary star, if the outer star has high eccentricities. We find that in systems in which one of the stars becomes unbound due to the core-collapse in the inner binary, the outer eccentricities are large, about 70 per cent of them $e_{\mathrm{out}} \geq 0.8$. In the vast majority of the cases (about 99 per cent of such unbound systems), only the tertiary is ejected, while the inner binary remains bound.

If the triple becomes unbound due to the core-collapse of the tertiary star and with low outer eccentricity, it almost always occurs as a result of a strong natal kick. Consequently, most of such unbound systems have initial tertiary masses of $M_{\mathrm{out,ZAMS}} \approx 8\text{-}25\,M_{\odot}$ (see also discussion in section 3.5), as these systems are expecetd to receive the largest kicks according the supernova prescription of [97] .

3.4.13 Systems which become dynamically unstable

These triples typically have very short initial outer pericenters ($a_{\mathrm{p,out,ZAMS}} \approx 70\text{-}400\,R_{\odot}$) and therefore are very close to the stability limit at ZAMS. Such systems can transition to non-secular or non-hierarchical evolution, if $a_{\mathrm{in}}/a_{\mathrm{out}}$, e_{out} or q_{out}, significantly increases during evolution [see 220]. Among CHE triples, there are primarily two processes that can trigger this change: stellar winds and core collapse.

If the relative wind mass loss rate (e.g. $\dot{M}/M$) in the inner binary is higher than that of the tertiary star, $a_{\mathrm{in}}/a_{\mathrm{out}}$ and q_{out} will increase, which can prompt the triple to experience a dynamical instability [see also 163, 142, 265, 357]. 30 per cent of the systems of this channel destabilise due to stellar winds and the destabilisation occurs when the stars of the inner binary are in their post-MS phase. At this stage, the inner stars experience strong Wolf-Rayet winds, while the tertiary star is still

on the MS with significantly lower mass loss rates.

In the remaining 70 per cent, the instability sets in due to the collapse of the core of one of the stars. We find that this only occurs when BH formation takes place in the inner binary. As noted in section 3.3.4, CHE stars typically form BHs via direct collapse, such that q_{out} only increases slightly. Furthermore, the direct collapse is expected to be accompanied by a weak Blauw-kick due to neutrino losses such that $a_{\mathrm{in}}/a_{\mathrm{out}}$ and e_{out} only increase significantly, if the inner or the outer pre-core-collapse orbits are eccentric, respectively. The pre-core-collapse inner orbit is eccentric in 72 per cent of the systems of this channel. And the eccentricity is caused by ZLK oscillations. In the remaining 28 per cent, three body-dynamics is not efficient in driving up the eccentricity because the mutual inclination is outside of the critical Kozai range [see e.g. 243]. Therefore, the core collapse occurs when the inner orbit is circular. These systems still become unstable during the BH formation, because 1) either $a_{\mathrm{in}}/a_{\mathrm{out}}$ already increased strongly due to stellar wind mass losses before the BH formation or 2) the outer orbit is eccentric and the core collapse occurs while the tertiary star is near the outer pericenter (leading to a significant increase in e_{out}).

The occurrence rate of this channel is strongly dependent on metallicity (3.5 per cent of all CHE triples at Z = 0.005 and 0.7 per cent at Z = 0.0005, see Table 3.2). This dependence is due to the reduced strength of stellar winds and ZLK oscillations (which are responsible for any eccentricity in CHE inner binaries) at lower metallicities.

3.5 The origin of each evolutionary channel

In this section, we discuss the initial parameters of the triples from each evolutionary channel introduced in section 3.4.1. We find that initial parameters can be used as a proxy to determine the final evolutionary outcome of CHE triples. In particular, the evolutionary outcome can be parameterised by the initial mass and orbital separation of the tertiary star. The parameters of the inner binary play a less important role in this regard, as the parameter space for CHE inner binaries is already quite reduced. We illustrate this in the left panel of Fig. 3.6 by showing an ensemble of CHE triples at $Z = 0.005$, in which the parameters of the inner binary are the same, but the mass and the orbital separation of the tertiary star are varied (therefore this grid represents only a small subset of the entire CHE population discussed in section 3.4.1). The inner binary consists of two 70 $M_\odot$ stars with a circular initial orbit with $a_{\rm in,ZAMS} = 22.4\,R_\odot$ (similar to the example systems discussed in section 3.4.2). The initial tertiary mass ranges from 5 to 100 $M_\odot$, while $a_{\rm out,ZAMS}$ ranges from 200 to $10^4\,R_\odot$.

3.5.1 Initial parameters of systems of different evolutionary channels

The majority of the triples shown in the left panel of Fig. 3.6 experience TMT episodes. Their initial outer orbital separations are relatively short and range roughly from 100 to 3300 $R_\odot$. The evolutionary phase of the inner stars at the onset of the TMT episode depends on the initial mass of the tertiary star. For the systems shown in the left panel of Fig. 3.6, the inner binary at the onset of TMT comprise of BHs, if $M_{\rm out,ZAMS} \lesssim 59\,M_\odot$, helium stars, if $59\,M_\odot \lesssim M_{\rm out,ZAMS} \leq 70\,M_\odot$, and MS stars, if $M_{\rm out,ZAMS} \geq 70\,M_\odot$. The majority (53 per cent) of the TMT systems

in the left panel of Fig. 3.6 have a BH-BH inner binaries. For the entire population of CHE triples presented in section 3.4.1, the same percentage is smaller (i.e 31 per cent) at the same metallicity (see Table 3.4). As shown in Fig. 3.7, this quantity (i.e. the ratio of the number of TMT systems with BH-BH inner binaries and the number of all TMT system) scales proportionally to the initial mass of the secondary star in the inner binary. This means that TMT episodes occur more frequently with BH-BH accretors among CHE triples with more massive inner stars. This is due to our assumptions about the initial distribution of the triples (section 3.3.6). If the TMT occurs towards a BH-BH inner binary, the tertiary has to be initially the least massive in the triple. With increasing $M_{2,\text{ZAMS}}$, the fraction of triples for which $M_{2,\text{ZAMS}} > M_{\text{out,ZAMS}}$ increases because of our assumptions of a maximum initial stellar mass of $M_{\text{ZAMS,max}} = 100\,M_\odot$ and a flat outer mass ratio distribution.

In 15 per cent of the triples shown in the left panel of Fig. 3.6, the inner binary merges before BH formation or before a TMT episode occurs. All such mergers in the grid occur between two helium stars, and are due to ZLK oscillations that arise when the stars of the inner binary evolve off the MS. The initial outer orbital separations in this channel are very short, i.e. 200 to 241 $R_\odot$, while the tertiary masses range between $32 \leq M_{\text{out,ZAMS}}/M_\odot \leq 68$. For lower tertiary masses ($M_{\text{out,ZAMS}} < 32\,M_\odot$), the ZLK oscillations are not strong enough to boost the inner eccentricity and cause a mass transfer episode in the inner binary. For larger tertiary masses ($M_{\text{out,ZAMS}} > 70\,M_\odot$), the tertiary typically fills its Roche-lobe before the stars of the inner binary evolve off the MS. However, during the main sequence phase of the inner stars, the effects of ZLK cycles are quenched and consequently no mergers are prompted by three-body dynamics before the tertiary initiates a TMT episode.

Triples of the no post-MS MT channel in the left panel of Fig. 3.6 have initial outer orbits $a_{\text{out}} \gtrsim 2000\text{-}3000\,R_\odot$. Their initial tertiary mass is also typically outside

of the range of $\sim$8-25 $M_\odot$, such that the system does not dissociate due to SN kicks. As we show in the next subsection, three-body dynamics are not important for the evolution of these systems.

In the lower panel of Fig. 3.8, we show the inital pericenter ($a_{\mathrm{outer,ZAMS}}$) distribution of the entire CHE triple population for each evolutionary channel at Z = 0.005. As it can be seen, the range of initial pericenters are in agreement with those shown in Fig. 3.6 for all channels except for the unbound systems (since for the unbound systems, the outer eccentricity plays a crucial role, as explained in section 3.4.12, and in the grid we assume circular outer orbits). This again confirms that the parameters of the tertiary star play the most important role in determining the evolutionary path of a CHE triple. As evident from comparing the lower panels of Fig. 3.8 and Fig. B.4, the range of $a_{\mathrm{outer,ZAMS}}$ of systems with TMT episodes increases with decreasing metallicity. At lower metallicity, the stellar winds are weaker and consequently, the outer orbit widens less. Therefore, the maximum $a_{\mathrm{outer,ZAMS}}$ at which the tertiary stars can still fill their Roche-lobes also increases with decreasing metallicity.

3.5.2 Initial parameters of triples with three-body dynamics

In the right panel of Fig. 3.6, we show the maximum eccentricities that the inner binaries reach during their evolution ($e_{\mathrm{in,max}}$). About 29 per cent of the triples shown in the right panel of Fig. 3.6 reach $e_{\mathrm{in,max}} \geq 0.4$ due to ZLK cycles. In all of these triples, the tertiary star eventually fills its Roche-lobe (although in some cases, the inner binary merges first).

For the systems shown in Fig. 3.6, ZLK cycles are efficient when $a_{\mathrm{out,ZAMS}} \lesssim$ 1200 $R_\odot$ and $M_{\mathrm{out,ZAMS}} \lesssim 70\,M_\odot$. When the outer orbit is $a_{\mathrm{out,ZAMS}} \gtrsim 1200\,R_\odot$, the

ZLK cycles are quenched by various short range forces (e.g. precession caused by tides or general relativistic effects). If $a_{\mathrm{out,ZAMS}} \lesssim 1200\,R_\odot$ but $M_{\mathrm{out,ZAMS}} \gtrsim 70\,M_\odot$, the tertiary star fills its Roche-lobe while the stars in the inner binary are still on the MS. The inner binaries of these triples do not develop high eccentricities, as ZLK cycles are quenched during MS due to strong tides (see section 3.4.2), and TMT episode with MS-MS accretors are expected to result in the merger of the inner binary (see section 3.6).

The right panel of Fig. 3.6 also shows that $e_{\mathrm{in,max}}$ does not decrease smoothly with increasing outer orbital separations, instead it drops rather abruptly across $a_{\mathrm{out,ZAMS}} \approx 1200\,R_\odot$. Triples with $a_{\mathrm{out,ZAMS}} \approx 1200\,R_\odot$ reach very large inner eccentricities ($e_{\mathrm{in,max}} \approx 0.9$), while at slightly larger orbital separations (i.e. $a_{\mathrm{out,ZAMS}} \approx 1500\,R_\odot$) the ZLK cycles are completely quenched.

These above mentioned effects are qualitatively also true for the entire CHE triple population presented in section 3.4.1 (see upper panel of Fig. 3.8). At Z = 0.005, the ZLK oscillations are only efficient, if $a_{\mathrm{p,out,ZAMS}} \lesssim 1200\,R_\odot$. This implies that three-body dynamics are only relevant for those triples, in which the tertiary star would eventually fill its Roche-lobe (compare the upper and lower panels of Fig. 3.8). Consequently, if the tertiary in a CHE triple remains detached throughout its evolution, the evolution of the inner binary will almost always be kinetically decoupled from the tertiary star (This is essentially the both TMT and ZLK oscillations require small outer orbits.. If $a_{\mathrm{p,out,ZAMS}} \lesssim 1200\,R_\odot$, a wide range of inner eccentricites are possible ($e_{\mathrm{in,max}}$ = 0-0.9) for all $a_{\mathrm{p,out,ZAMS}}$. In this case, the value of $e_{\mathrm{in,max}}$ is primarily determined by the mutual inclination of the triple [see also e.g. 13].

In our low metallicity model ($Z = 0.0005$) the maximum initial outer pericenter at which three-body dynamics are still relevant is lower compared to our moderate
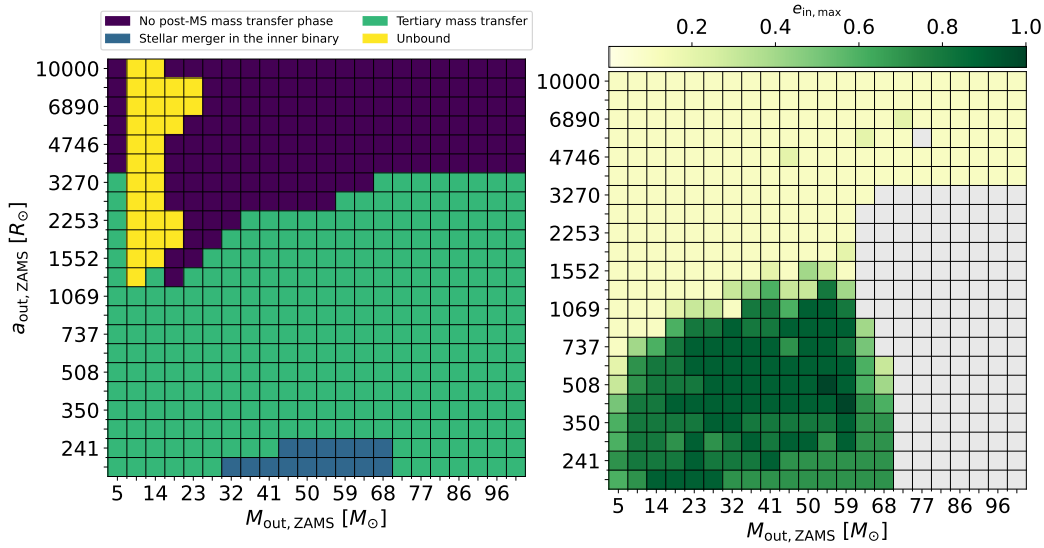
Figure 3.6: Left panel: we show the evolutionary outcome of collection of triples with fixed inner binary parameters and different parameters for the tertiary at a metallicity $Z = 0.005$. The parameters of the inner binary are the same for each system shown in the grid, i.e. $M_{1,\mathrm{ZAMS}} = M_{2,\mathrm{ZAMS}} = 70, M_\odot$, $a_{\mathrm{in,ZAMS}} = 22.4\,R_\odot$, $e_{\mathrm{in}} = 0$. The initial tertiary mass M_{out} ranges from 5 to $100\,M_\odot$ on a linear scale, while $a_{\mathrm{out,ZAMS}}$ ranges from 200 to $1000\,R_\odot$ on a logarithmic scale. We assume zero outer eccentricity and an initial inclination of 90°. Right panel: we show the maximum eccentricity of the inner binary reached during the evolution. The parameters of the inner binary are the same as in left panel

metallicity model (right panel in Fig. B.4 in section B.1 of Appendix). At such low metallicities, stellar winds do not widen the orbit of the inner binary significantly and thus the timescales of the ZLK cycles do not decrease as much as at Z = 0.005.

3.6   Gravitational waves sources

We now discuss the possible formation channels of GW sources that originate from CHE triples and their properties. In section 3.6.1 we predict the merger rate densities and compare them to that of GW sources from isolated CHE binaries. For this, we assume two test populations with different stellar multiplicity fractions. One population is composed of only single and binary stellar systems (i.e. with stellar
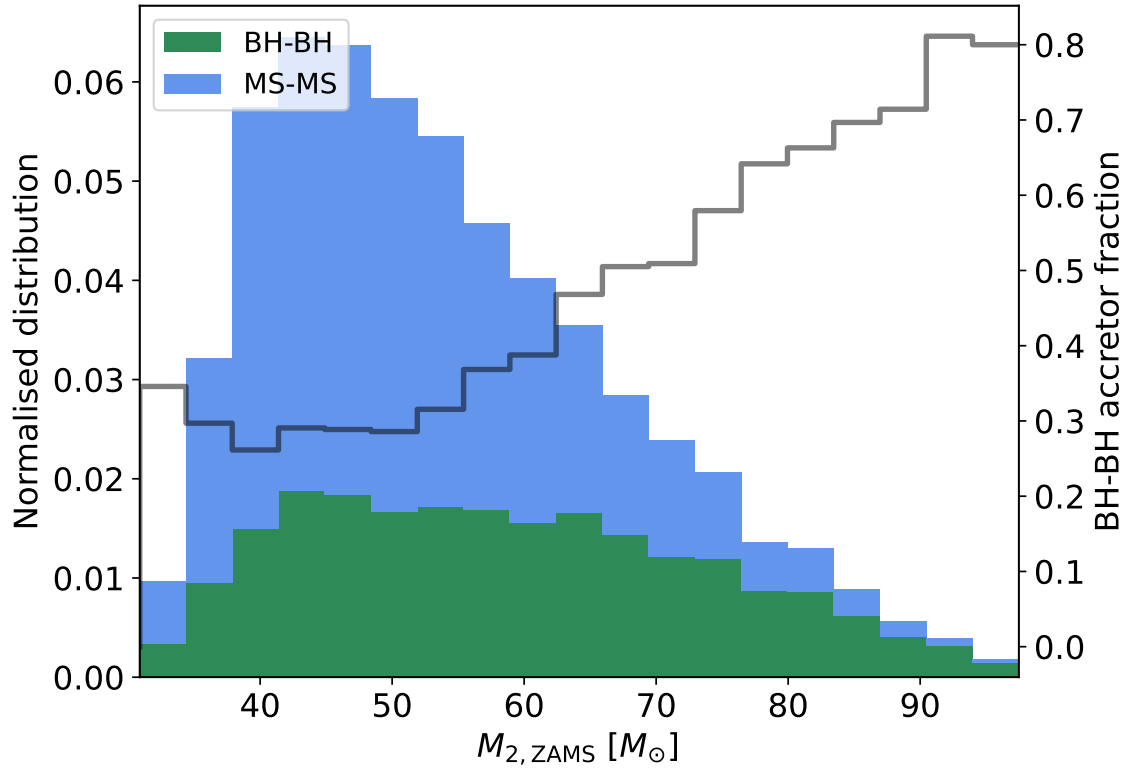
Figure 3.7: The distribution of the initial secondary masses of the entire CHE triple population that undergo tertiary mass transfer at $Z = 0.005$. We only show those systems which have either BH-BH or MS-MS accretors. The grey unfilled histogram, with the corresponding secondary x-axis on the right hand side, shows the number of systems with BH-BH accretors as a fraction of all systems undergoing tertiary mass transfer phases.
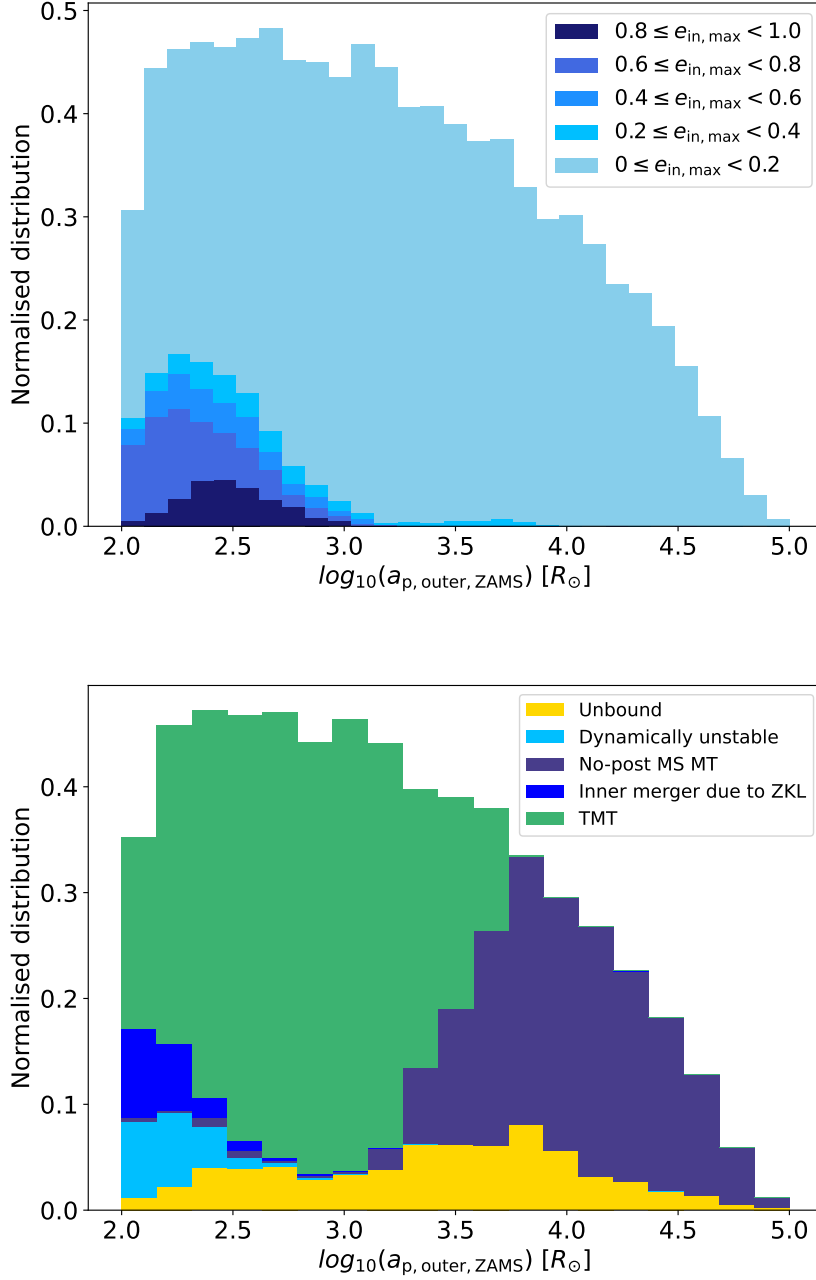
Figure 3.8: Upper panel: The distribution of the initial pericenter of a few selected evolutionary types of the entire CHE triple population at Z = 0.005. The histograms have been normalised to the full population of the CHE evolving triples. The histograms shown are stacked. Each colour represents a different evolutionary type. For clarity we do not show all the types introduced in section 3.4.1, see text for discussion. Lower panel: The distribution of the initial outer pericenter of the entire CHE triple population at Z = 0.005. We distinguish systems based on the maximum eccentricity of the inner binary reached during their evolution. The histograms are normalised to one and stacked.

multiplicity fractions at ZAMS of $f_{\text{single}} = 0.3$, $f_{\text{binary}} = 0.7$, $f_{\text{triple}} = 0$), in the other triples dominate ($f_{\text{single}} = 0.06$, $f_{\text{binary}} = 0.21$, $f_{\text{triple}} = 0.73$).

In sections 3.6.2 - 3.6.5 we discuss the properties of each GW formation channel from CHE triples and binaries. These predictions are based on the synthetic populations discussed previously, and in cases where the simulations are stopped before the formation of a BH-BH binary, we predict the further evolution of CHE triples beyond the stopping conditions (Section 3.3.6) by applying simple assumptions (as detailed below).

The four main identified formation channels of GW sources within our CHE triple population are (see also Fig. 3.9):

- **Effectively isolated inner binary:** For such triples, three-body dynamics is suppressed by various short-range forces and the tertiary star remains detached throughout the entire evolution. The inner binary therefore evolves effectively as an isolated binary and the properties of these GW sources are indistinguishable from those of the CHE binary channel. There are two ways these systems can form: i) with the tertiary star bound to the triple (systems from the no post-MS MT channel, see section 3.4.3) and ii) systems in which the tertiary star becomes unbound from the triple (from the unbound channel discussed in section 3.4.12). For the latter, we assume that the orbit of the inner binary is not affected by the tertiary unbinding from the triple system.

- **TMT with a BH-BH accretor:** This channel comprises systems in which the tertiary star fills its Roche-lobe when the inner binary is a BH-BH binary. The inner binary components do not coalesce during the TMT phase, but will merge afterwards due to GW emission. In these systems, the tertiary star can affect the evolution of the inner binary in two major ways, via the TMT
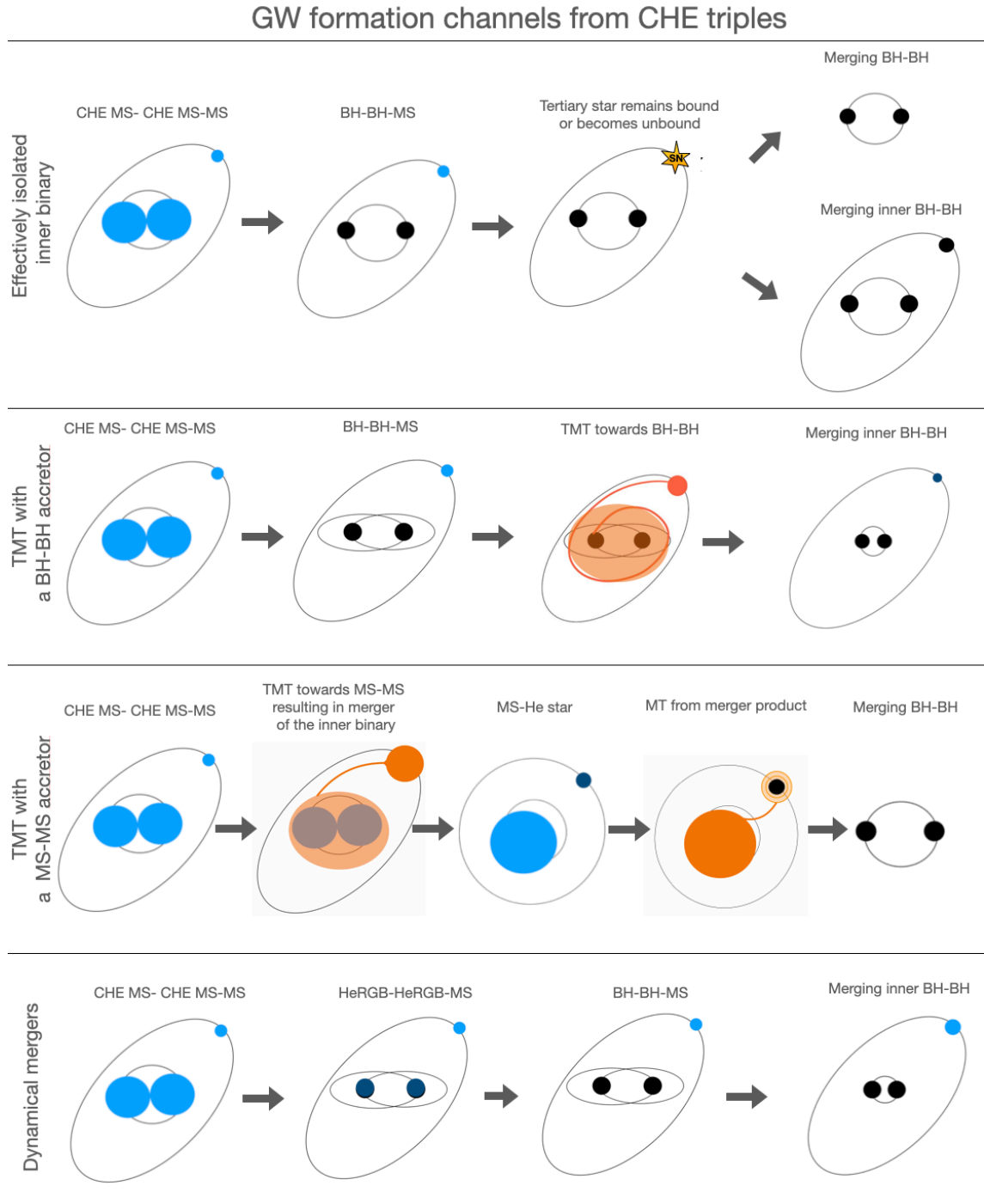
Figure 3.9: The possible formation channels of merging binary BHs from our CHE triples population.

episode and via three-body dynamics (see section 3.4.5). In section 3.3.5, we introduced our assumptions regarding the evolution of the inner orbit during a TMT episode.

- **TMT with a MS-MS accretor:** In this scenario, there are two sequential mergers taking place in the system [see also e.g. 333]. First, the inner binary merges when the stars are still on the MS as a result of mass transfer from the tertiary to the inner binary. This reduces the triple to a binary. We assume that the merger product of the inner binary evolves further in a classical way (as opposed to CHE). Consequently, the merger product expands and eventually fills its Roche-lobe and transfers mass to the initial tertiary star. The orbit shrinks due to this second phase of mass transfer and as a result, a merging double compact object is formed. The second phase of mass transfer is essential. Systems in which no mass transfer takes place after the inner binary merger might form detached BH-BH binaries but are too wide to merge due to GWs within the Hubble time. We note that double MS mergers among CHE triples typically occur due to TMT episodes as three-body dynamics are suppressed during the MS phase.

- **Dynamical mergers:** In the triples of this channel, ZLK oscillations are very efficient and drive up the inner eccentricities to $e_{\mathrm{in}} \approx 0.6$-$0.9$ after the stars of the inner binary have become BHs. Such systems merge due to GW emission within a few Myrs. The tertiary remains detached until the inner binary merges and therefore these triples belong to the no post-MS MT channel. As discussed in section 3.4.3, these systems are rare.

We ignore the possibility of GW source forming in a CHE triple through a stellar merger that do not occur between two MS stars. Such mergers can occur due to TMT or three-body dynamics with (i) helium star-MS binaries or (ii) double helium star binaries. We justify the omission of the first type, as they are relatively rare. This
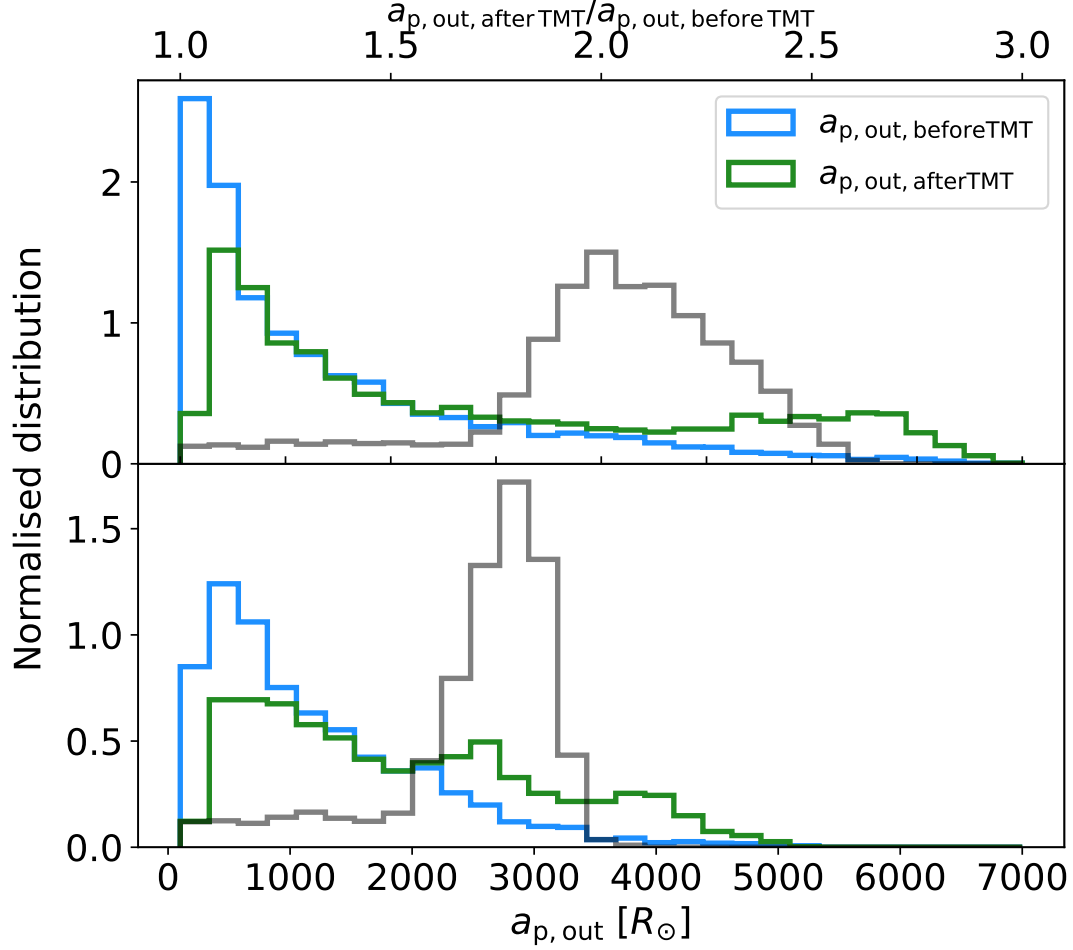
Figure 3.10: The pericenter of the outer orbit before and at the onset of TMT for MS-MS inner (upper panel) and BH-BH inner binary accretors (lower panel) as calculated with equation 3.16 at Z = 0.005. The grey line shows the ratio of the pericentre after the TMT and at the before the TMT episode (i.e. $a_{\mathrm{p,out,afterTMT}}/a_{\mathrm{p,out,beforeTMT}}$ with the corresponding values shown in the upper x-axis). We note that for we have normalised these distributions to 10^4 (such that the numbers on the y-axis are in the order of unity).

Table 3.3: Summary of the statistics of GW sources from the population with triples (with $f_{\text{single}} = 0.06$, $f_{\text{binary}} = 0.21$, $f_{\text{triple}} = 0.73$), and from the population without triples (with $f_{\text{single}} = 0.3$, $f_{\text{binary}} = 0.7$, $f_{\text{triple}} = 0$). The 'of all CHE systems' is the number of systems, expressed as a fraction of all systems containing a binary that contains two, tidally-locked CHE stars. Formation efficiency gives the number of systems expressed as a faction of all stellar systems (see equation B.1). Merger rate density is the merger rate density in the local universe (see equation B.15).

	of all CHE systems at Z = 0.005 [%]	of all CHE systems at Z = 0.0005 [%]	Formation efficiency at Z = 0.005	Formation efficiency at Z = 0.0005	Merger rate density [Gpc^{-3}yr^{-1}]
Population with triples					
CHE triple channels:	**29.1/31.9**	**23.7/23.7**	**$6.9 \cdot 10^{-7}/7.2 \cdot 10^{-7}$**	**$9.2 \cdot 10^{-7}$**	**12.7/11.8**
- Effectively isolated inner binary	19.3	12	$4.6 \cdot 10^{-7}$	$3.0 \cdot 10^{-7}$	8.8
- TMT with BBH & BA (sc. 1/sc. 2)	3.8/6.6	2.3/2.3	$9 \cdot 10^{-8}/1.2 \cdot 10^{-7}$	$5.8 \cdot 10^{-8}/\, 5.8 \cdot 10^{-8}$	1.4/0.5
- TMT with BBH & CBD	5.9	7.8	$1.4 \cdot 10^{-7}$	$1.9 \cdot 10^{-7}$	2.4
- TMT with MS-MS channel	0.3	5	$6 \cdot 10^{-9}$	$1.2 \cdot 10^{-7}$	0.2
- Dynamical mergers	0.2	0.1	$4 \cdot 10^{-9}$	$2.0 \cdot 10^{-9}$	0.05
CHE binaries	**8.7**	**12.9**	**$7.2 \cdot 10^{-7}$**	**$5.2 \cdot 10^{-7}$**	**11**
Population without triples					
CHE binaries	**65**	**88.6**	**$1.2 \cdot 10^{-6}$**	**$1.2 \cdot 10^{-6}$**	**44.2**

type of merger occurs in 0.2-2 per cent of all CHE triples depending on metallicity. For the second type, the merger product is a helium star, it is not expected to significantly expand and it is unlikely to ever fill its Roche-lobe. Without a phase of mass transfer that leads to orbital shrinkage, the binary remains too wide to merge within a Hubble time. However, if the merger remnant can accrete matter during the TMT phase it could regain a hydrogen-rich envelope, and expand later in its evolution. For simplicity, we neglect this scenario.

3.6.1 Rates of GW mergers

In the population without triples, the predicted merger rate density is $R_{\text{merger}} = 44.2 \, \text{Gpc}^{-3}\text{yr}^{-1}$ (see Table 3.3). This is about a factor of two higher than predicted by [292], giving a rough agreement given the simplicity of our rate calculation (see discussion in Appendix B.2). The total merger rate density of the population containing triples is $R_{\text{merger}} = 23 \, \text{Gpc}^{-3}\text{yr}^{-1}$. This is about a factor of two lower than that of the population without triples. There are two reasons for this difference. Firstly, stellar mergers frequently occur in CHE triples, preventing the formation of

compact BH-BH binaries. While all CHE binaries form BH-BH binaries, only about 60 (45) per cent of CHE triples form (inner) BH-BH binaries at Z = 0.005 (Z = 0.0005).

Secondly, the number of systems formed in the population with triples is always lower per unit stellar mass formed than in the population without triples, as triple systems, on average, have larger total masses than binaries and/or single stars.

In the population with triples, about half of the GW mergers are from formation channels involving CHE originate from triples. The role of the tertiary is negligible for 69 per cent of GW progenitors from CHE triples. In the remaining 31 per cent, the evolution of the inner binary is affected by the tertiary star via TMT and/or three-body dynamics.

3.6.2   Isolated binaries

At $Z = 0.005$, about 68 per cent of the CHE binary population forms a BH-BH binary that merges within the Hubble time, while at $Z = 0.0005$, all CHE binaries merge due to GWs within the age of the universe. In our moderate metallicity model, the delay times of these BH-BH binaries from this population ranges from 3 to 50 Gyr (and therefore the delay time of GW sources ranges from 3 to 13.5 Gyr). In our low metallicity model, the delay times are considerably shorter, ranging roughly from 100 to 600 Myrs. At Z = 0.005, only those binaries merge which were in contact during their MS phase. At Z = 0.0005, about 97 per cent of all GW progenitors were in contact during their MS phase. Since we assume such binaries equalise in mass, we predict that the vast majority of GW sources consist of equal mass black hole binaries from this population (in broad agreement with [217]). The masses of the merging binary black holes from this channel range from 20 to 42 $M_\odot$ at Z =

0.005 and 33 to 54 $M_\odot$ at Z = 0.0005.

3.6.3   Effectively isolated inner binaries

This is the dominant channel among CHE triples with a predicted merger rate density of 8.8 $\mathrm{Gpc}^{-3}\mathrm{yr}^{-1}$. At Z = 0.005 (Z = 0.0005), about 19 (12) per cent of all CHE systems (e.g CHE binaries and CHE triples, see section 3.3.6) are expected to form GW sources via this channel. In 53 per cent of the GW progenitors of this channel, the tertiary star becomes unbound by the time both stars in the inner binaries form BHs. This percentage drops to 38 per cent at Z = 0.0005.

The demographics of this channel are nearly indistinguishable from the isolated binary population. The merger efficiency of this channel, which we define as the GW sources as a fraction of BH-BH inner binaries formed via a certain channel, is 68 per cent. Unsurprisingly, this is the same as the merger efficiency of the isolated CHE binary channel. Similarly to the CHE binary case, the majority of the inner binaries of these triples were also in contact during their MS phase and therefore this channel also produces overwhelmingly equal mass mergers.

3.6.4   TMT with a BH-BH accretor

This is the dominant formation channel in which the evolution of the inner binary is affected by the tertiary star. The predicted merger rate density is $R_{\mathrm{merger}} = 3.8$ $\mathrm{Gpc}^{-3}\mathrm{yr}^{-1}$, which accounts for about 16 per cent of all GW mergers from CHE systems. About 10 per cent of all CHE systems form merging binary BHs via this channel.

With our simplistic models of TMT (see subsection 3.3.5), we predict that the outer orbit widens as a result of the TMT episode for all triples considered in this study. In the lower panel of Fig. 3.10, we show how the outer pericenter changes after the mass transfer phase for triples experiencing TMT with a BH-BH inner binary accretor for our moderate metallicity model (and in the lower panel of Fig. B.5 for our low metallicity model). The orbital separations widen typically by a factor 1.5-2.

Even, if the inner orbit remains unchanged due to TMT, the outer orbit widens so much, such that three body-dynamics become typically negligible after the TMT episode for the majoirty of these triples. For example, at $Z = 0.005$, in those TMT systems, in which ZKL oscillation are effective prior to the mass transfer event, 70 per cent of the inner binaries become decoupled from the tertiary star after the TMT episode. If the evolution of the inner BH-BH inner binary is decoupled from the tertiary, its orbital evolution is solely determined by the emission of GWs (and therefore the coalescence time can be determined according to [266], otherwise, we use equation 3.5).

As noted in section 3.3.5, we make different assumptions about the evolution of the inner orbit based on whether a circumbinary disc is formed during TMT. We therefore discuss the properties of GW sources from these two subtypes separately.

Accretion through a circumbinary disc

The predicted merger rate of this channel is 2.4 Gpc^{-3}yr^{-1}. The merger rate efficiency is just 6 per cent higher than the merger rate efficiency from isolated binaries. The slight increase is due to the small number of eccentric inner binaries at the onset of the mass transfer ($\sim$10 per cent of systems undergoing TMT with BH-BH

accretors and circumbinary discs have e_{in}>0.4, see Fig. 3.5). The small difference is not surprising as we have assumed here that the orbit of the inner binary does not change due to circumbinary disc accretion. However, if circumbinary disc accretion leads to a significant increase (decrease) in the inner period, the compact object merger fraction decreases (increases) significantly as well. Clearly, better models are required to understand circumbinary accretion of a BH binary from a mass transferring tertiary star.

Ballistic accretion

The properties of these GW sources depend on how the inner binary evolves due to TMT. If we simplistically assume that that the inner orbit does not change (i.e. *Scenario 1*, see section 3.3.5), then the merger rate density of this channel in the local universe is $R_{merger} = 1.4$ Gpc^{3}yr^{-1}. In this case about 3.8 (2.3) per cent of all stellar systems containing a CHE binary form GW sources via this channel at Z = 0.005 (Z = 0.0005). The merger efficiency of this channel is 75 per cent at Z = 0.005, which is slightly higher than that of the CHE binary population (68 per cent). As discussed in section 3.4.5, a considerable fraction of these sources have high eccentricities, namely, 48 per cent with $e_{in} \gtrsim 0.4$ at Z = 0.005 and 10 per cent at Z = 0.0005. This results in shorter delay times and more mergers with respect to the isolated CHE binary channel (top left panel of Fig. 3.11).

If the orbital evolution can be described by equation 3.14 (i.e. *Scenario 2*, see section 3.3.5), then the inner pericenters of BH-BH binaries decrease by 1-3 orders of magnitude due to the TMT episode, depending on the efficiency parameter α_{TMT}. In this case, all inner bineries become dynamically decoupled from the tertiary star after the TMT episode. As shown in the left panel of Fig. 3.12, the peak of the orbital separation distribution shifts from 32 $R_{\odot}$ to 25, 5 and 1 $R_{\odot}$ with $\alpha_{TMT} = 0.05, 5, 5$.

With such short periods, nearly all (i.e. typically $\gtrsim 99$ per cent) of the inner binaries eventually emerge. However, none of the inner binaries merge during the mass transfer, in fact they merge due to GW emission afterwards. In Fig. 3.11, we show that the typical delay times in *Scenario 2* are also orders of magnitude shorter with respect to that of isolated CHE binaries. With $\alpha_{\mathrm{TMT}} = 0.05$, the delay times of these GW sources is dominated by the stellar evolution. Such timescales could make TMT episodes relevant in young clusters in which star-formation is still active. Even when assuming a weaker friction exerted by the transferred mass (i.e. $\alpha_{\mathrm{TMT}}\lambda_{\mathrm{TMT}} = 5$) resulting in the smallest orbital shrinkage in our models, most of the BHs merge within a few hundred Myr at $Z = 0.005$.

Despite the higher merger efficiency, the predicted merger rate density for *Scenario 2* is considerably lower (i.e. $R_{\mathrm{merger}} = 0.5\,\mathrm{Gpc}^{-3}\mathrm{yr}^{-1}$) than in *Scenario 1*. This is due to the extremely short delay times, implying the progenitor stars must have formed recently, when the cosmic star formation rate is low [e.g. 206]. As the cosmic star formation rate is expected to increase strongly from $z = 0$ to $z = 2$, we expect the merger rate density of this channel to be significantly higher at $z \approx 2$ than at $z = 0$. This would make these sources more relevant for third-generation GW detectors.

We mention two interesting aspects of this channel. Firstly, depending on the efficiency parameter of the TMT episode, these systems could be in the LISA frequency band [12] during the mass transfer phase. In the right panel panel of Fig. 3.12, we show the frequency at which the BH-BH binaries emit GWs after the mass transfer episode. With $\alpha_{\mathrm{TMT}} = 0.5$, about half, and with $\alpha_{\mathrm{TMT}} = 0.05$, all of our systems enter the mHZ regime during the mass transfer phase. The evolution through the LISA frequency range would be primarily driven by gas dynamics instead of GW emission [see also 288]. Such sources would be detectable by LISA, if the corresponding luminosity distances are not larger than $\sim 10\,\mathrm{kpc}$ and $\sim 10^4\,\mathrm{kpc}$ in case

of $\alpha_{\mathrm{TMT}} = 0.5$ and $\alpha_{\mathrm{TMT}} = 0.05$, respectively [see e.g. Fig. 1 in 12].

Secondly, a TMT episode could be accompanied by a detectable electromagnetic signal, as the transferred mass is expected to heat up when it reaches the inner BH binary. If the delay time between this signal and the GW merger is within the lifetimes of typical observing missions, then the GW merger could be associated with this electromagnetic counterpart [see also e.g. 400]. We find that the time between the end of the TMT episode and the GW merger in case of $\alpha_{\mathrm{TMT}}\lambda_{\mathrm{TMT}} = 0.05$ is shorter than a year for 6 per cent of these sources at Z = 0.0005. This implies that in this case a electromagnetic counterpart could be detected, shortly before the GW merger. This is in contrast with the possible electromagnetic signatures associated with BH mergers in AGN discs, where the electromagnetic counterpart would occur after the GW merger [see e.g. 225]

3.6.5 TMT with a MS-MS accretor

This channel has a low merger rate density of $R_{\mathrm{merger}} = 0.2\,\mathrm{Gpc^{-3}yr^{-1}}$. Even though 25 per cent of all systems containing a CHE binary experience a double MS merger in the inner binary at Z = 0.005, only 1.1 per cent of them form merging binary BHs. This low merging efficiency is due to two reasons. Firstly, if the mass transfer episode between the merger product and the tertiary star proceeds in a dynamically unstable way, the process mostly ends in stellar merger and no double compact binary is formed. Secondly, if the same mass transfer proceeds instead in a stable way, the binary BH typically has too wide orbit to merge within the Hubble time. We note, however, that these predictions are sensitively dependent on uncertain stellar physics (such as the efficiency of CEE phase, mass-loss radius exponent and binding energy of stars with $M_{\mathrm{ZAMS}} \gtrsim 100\,M_{\odot}$). We also note that the merger efficiency is significantly higher in our low metallicity model, 12.3 per cent of triples with double

MS merger forms merging binary BHs. As the merger efficiency seems to increase with decreasing metallicity, and we only calculate the merger rate density based on two metallicities, it is likely that we underestimate the merger rate density for this channel (see more detailed explanation in Appendix section B.2).

In case of a TMT episode with a MS-MS accretor, we always assume that the inner binary merges due to the mass transfer phase. We justify this assumption by the fact that CHE MS-MS binaries tend to be on very close orbits ($\sim$20-30 $R_\odot$) compared to their stellar radii ($\sim$5-10 $R_\odot$). A significant fraction of them are already in contact. Furthermore, these stars may swell up as a result of accretion, this type mass transfer event is likely to end in merger [e.g. 40, 193].

The merger product is a rejuvenated MS star with a mass of $M_{1+2} = M_1 + M_2$. This means that we neglect any accretion during TMT and we assume a fully conservative merger without mass outflows. At Z = 0.005, the mass of the inner binary merger remnant M_{1+2} ranges from 65 to 188 $M_\odot$. The distribution has a peak around $\sim 100\,M_\odot$. At Z = 0.0005, the mass of the merger product ranges from 70 $M_\odot$ to 190 $M_\odot$.

The orbital separations after the TMT episode are shown in the upper panel of Fig. 3.10 (and Fig. B.5 for our low metallicity model). We can see that the outer orbit widens typically by a factor of 1.7-2.5 and the orbital separations range from 150 to 6800 $R_\odot$. While the ranges are similar at both metallicities, at Z = 0.0005, the typical orbital separations are significantly shorter.

Most of the systems experience a second phase of mass transfer after the TMT episode (62 per cent at Z = 0.005 and 96 per cent at Z = 0.0005) and typically the donor star is on the Hertzsprung gap during this second phase of mass transfer (about 99 per cent at Z = 0.005, and about 86 per cent at Z = 0.0005). More evolved

donor stars are not expected to occur frequently, as the onset of CHeB occurs at a cooler effective temperature with increasing mass and followed by a less significant subsequent radial expansion [138]. In particular for $M_{\mathrm{ZAMS}} \gtrsim 100\,M_{\odot}$, stars are predicted to expand negligibly after the CHeB, even at low metallicities.

Regarding the stability of the mass transfer between the merger remnant and the initial tertiary, we find that it occurs in a dynamically unstable manner in 66 (30) per cent of cases at Z = 0.005 (Z = 0.0005). We assume that CE phases with a donor star on the Hertzsprung gap result in a merger, following [69] [but see also 167, 219]. At both metallicities, binary BHs are only produced when the second phase of mass transfer proceeds in a stable manner. Furthermore, in order to form a GW source, the orbit needs to be compact enough ($a_{\mathrm{out}} \lesssim 1000\,R_{\odot}$) at the onset of the second mass transfer event. This only occurs in about 5 per cent (30 per cent) of systems with stable mass transfer at Z = 0.005 (Z = 0.0005).

This is the only GW formation channel of CHE triples that yields a significantly different mass and mass ratio distributions than the CHE binary channel. The masses of the merging binary BHs range from 16 to 27 $M_{\odot}$ at Z = 0.005 and 17 to 54 $M_{\odot}$ at Z = 0.0005. The mass ratios range from 0.7 to 0.8 at Z = 0.005 and 0.5 to 1.0 at Z = 0.0005. All other channels produce merging binary BHs with masses that range from 20 to 42 at Z = 0.005 and 33 to 54 at Z = 0.0005. The vast majority ($\gtrsim$ 90 per cent) of these systems have equal masses, as the inner binaries had been in contact during their MS phase.

3.6.6 Dynamical mergers

The merger rate density of this channel is very low, $R_{\mathrm{merger}} = 0.05$ Gpc^{-3}yr^{-1}. The delay times of these systems are very short and range from 4 to 20 Myrs. Similarly
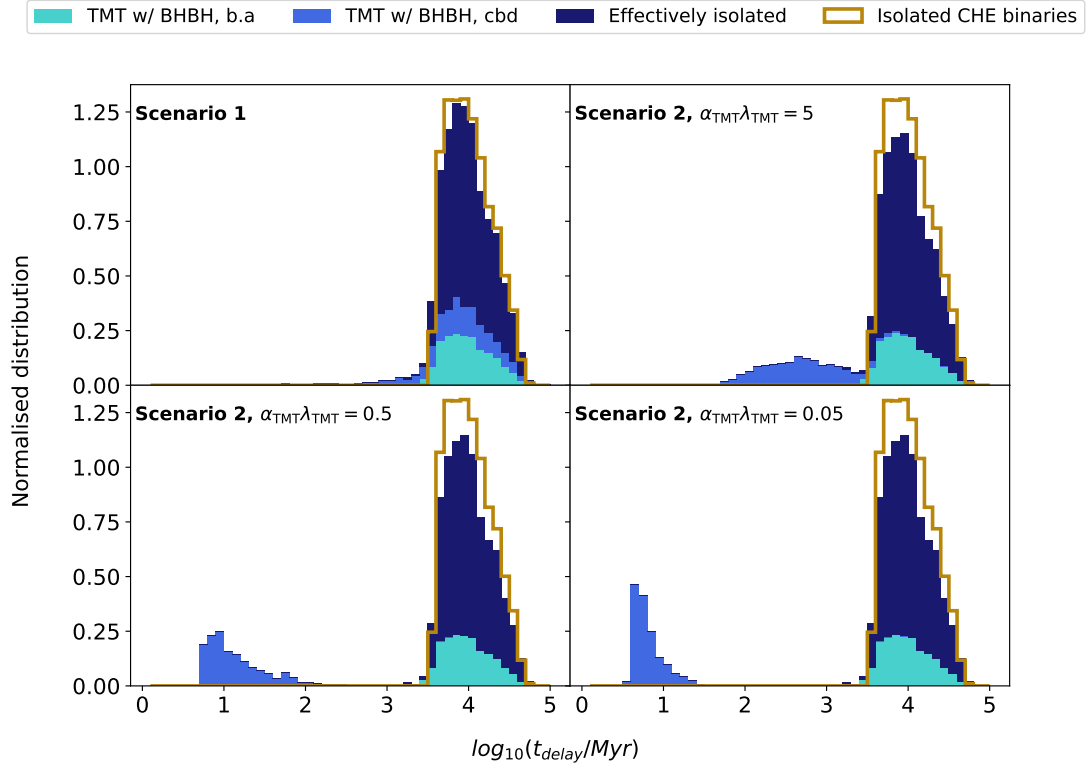
Figure 3.11: The time delay distribution of the GW sources from the CHE triple population shown by a stacked histogram. As a comparison, we also show the time delay distribution of the GW sources from CHE isolated binaries at the same metallicity (gold). The different colours of the stacked histograms refer to different evolutionary paths of the triples (shown by the legend in the top of the panel)
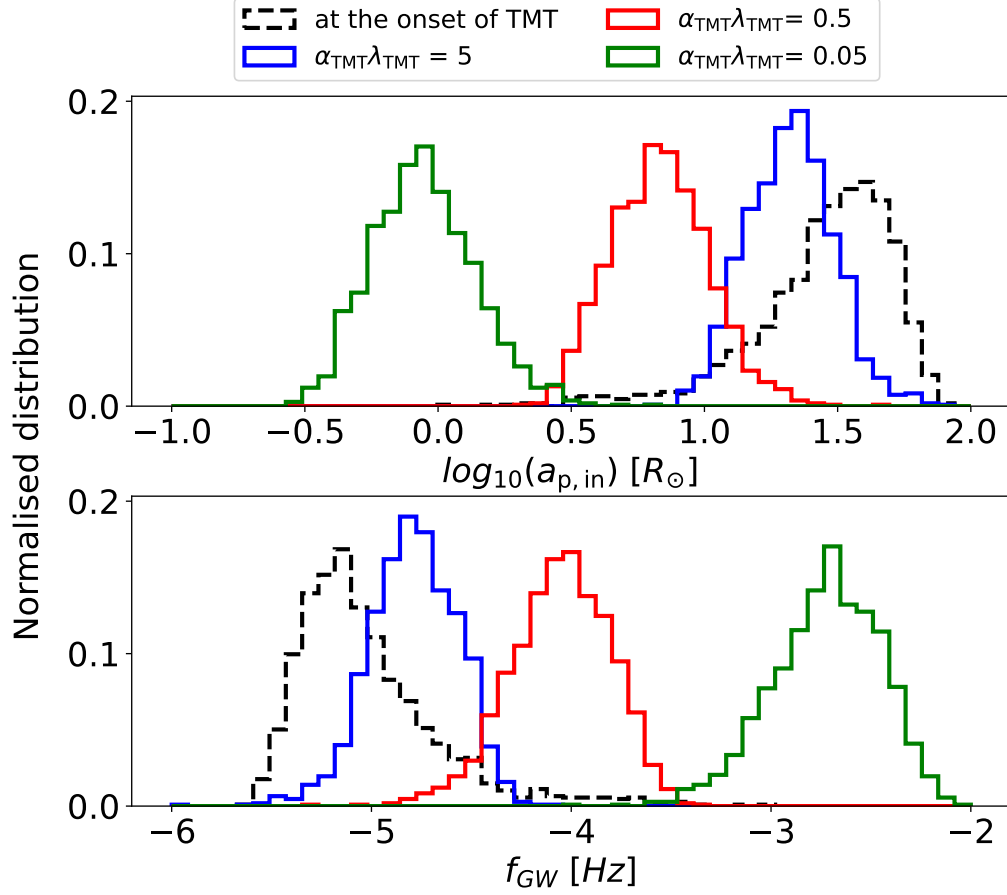
Figure 3.12: Orbital parameters of GW sources that evolve through the TMT channel with BH-BH accretors and ballistic accretion at Z=0.005. In the upper panel we show the inner pericenter of the inner BH-BH binary ($a_{p,in}$). The black line represents $a_{p,in}$ at the onset of TMT. The coloured lines show the orbital characteristics at the end of the mass transfer for *scenario 2*, where the change in the orbit has been estimated using an energy formalism with three different values of $\alpha_{TMT}\lambda_{TMT}$ (equation 3.12 and 3.13). Lower panel: we show the frequency of the GW radiated by the inner BH-BH binary before and after the tertiary mass transfer phase.

to the GW progenitors that have experienced TMT episodes with ballistic accretion, the short delay times imply that the merger rate density could be about an order of magnitude larger at z $\approx$ 2. About 25 per cent of these systems have eccentricities $e_{\text{in}} \gtrsim 10^{-4}$ when the characteristic GW frequency reaches 10 Hz, making eccentricities detectable by third-generation detectors [200].

For all systems, the tertiary star is still on the MS when the inner binary merges due to GWs with outer pericenters of $a_{\text{p,out}} \approx 120\text{-}790\,R_\odot$. It is therefore expected that the initial tertiary star will eventually fill its Roche-lobe, once it evolves of the MS.

3.7 Conclusion

We studied the evolution of hierarchical triples with CHE stars in the inner binary with a rapid populations synthesis approach. We performed simulations with the triple population synthesis code `TRES` at two representative metallicities: Z = 0.005 and Z = 0.0005. We showed that the evolution of CHE stars can be altered by the presence of a tertiary star in several ways. This can potentially lead to a formation of a number of diverse and unique astrophysical phenomena, e.g. TMT phases with BH-BH accretors, highly eccentric mergers of helium stars, and mergers of binary BHs with very short (few Myrs) delay times.

To summarise our main findings:

1. **Tertiary mass transfer (TMT) episodes are common among CHE triples:** Unlike in classically evolving hierarchical triples, we predict that a TMT phase is very common among CHE triples. The tertiary star fills its Roche-lobe in

about 50 per cent of all triples with CHE inner binaries. The same fraction for classically evolving systems is predicted to be a few percent at best [see e.g. 405, 356, 120, 184]. We find that the mass transfer episodes initiated by the tertiary star typically occurs in a dynamically stable way.

2. **BH-BH inner binaries that accrete from the tertiary star are also common:** About 31 (24) per cent of the tertiary-driven mass-transfer episodes occur with BH-BH accretors at Z = 0.005 (Z = 0.0005). Previous population synthesis studies suggest that such a scenario is probably not possible for triples with classically evolving stars [see e.g. 356, 120]. Therefore, mass transfer towards a BH-BH inner binary represents a unique scenario for triples (or higher-order multiples) with CHE stars in the inner binaries. An exciting prospect would be a possible EM counterpart from such an event [e.g. 400].

3. **Importance of three-body dynamics:** ZLK oscillations can be effective for CHE triples, if the stars in the inner binary have evolved off the MS (otherwise precession due to strong tides quench ZLK cycles) and if the initial outer pericenter is $a_{\mathrm{p,outer,ZAMS}} \lesssim 2000 \, R_\odot$ (otherwise ZLK cycles are quenched by various short range forces throughout the entire evolution of the inner binary). ZLK oscillations are only present in those CHE triples, in which the outer pericenter is so short that the tertiary star would eventually fill its Roche-lobe. The inner eccentricities of these systems can reach values up to $e_{\mathrm{in,max}} \sim 0.9$ (upper panel of Fig. 3.8). The effects of three-body dynamics are negligible for those CHE triples in which the triple remains detached. In this case, the inner binary evolves effectively as an isolated binary.

4. **Three-body dynamics can drive the inner binary to a stellar merger:** In about 3 per cent of CHE triples, the inner binary merges before BH-BH formation. The most common type is a merger of a double helium star binary, that comes into contact in a highly eccentric orbit (Table 3.2).

5. **CHE triples form GW sources efficiently:** About 30 (24) per cent of the CHE triple population forms BH binaries that merge due to GWs within Hubble time at Z = 0.005 (Z = 0.0005). We predict a merger rate density of GW sources from CHE triples of $R_{\mathrm{merger}} \approx 12\,\mathrm{Gpc}^{-3}\mathrm{yr}^{-1}$ (Table 3.3). We also predict that about half of the GW sources from CHE systems originate from triples. In 69 per cent of all GW sources from CHE triples, the inner binary evolves effectively as an isolated binary and therefore its properties are indistinguishable from those of CHE binaries. In the remaining 31 per cent, the evolution of the GW progenitor is affected by three-body dynamics and/or TMT episodes.

6. **Tertiary mass transfer and three-body dynamics could lead to the formation of BH-BH binaries that merge within Myrs**

   The vast majority of those GW progenitors of CHE triples, in which the evolution of the inner binary is not decoupled from the tertiary object, experience a TMT episode with a BH-BH inner binary. In this case, we model the evolution of the inner binary during the TMT phase with energy arguments [following 405, see also subsection 3.3.5] and with different assumptions on how efficiently the transferred mass shrinks the orbit of the inner binary. We find typical values for the delay time of these GW sources of few hundred Myrs and few Myrs in our model variation with the least and the most orbital shrinkage, respectively.

Chapter 4

Conclusion and recommendations

In this thesis, I studied the evolution of massive stars in binary and triple systems in the context of gravitational wave astronomy with a rapid population synthesis approach. The studies presented here take one of the first necessary steps toward resolving the following important open questions in modern astrophysics; what is the origin of merging stellar mass black hole binaries and how much can we can learn about massive star evolution using gravitational wave astronomy. This first step is to explore how the demographics of merging binary black holes depend on uncertain physics of multiple systems of massive stars. Such an exploration allows us i) to identify features in the demographics of merging binary black holes that could potentially aid us in inferring information about the poorly understood evolutionary processes of massive stars, ii) to understand which aspects of stellar evolution models need the most urgent improvements to allow for a correct interpretation of merging binary black hole statistics in a stellar physics context, iii) to understand what type of complimentary, electromagnetic observations of massive stars should be combined with the gravitational wave observations in order to improve our understanding about massive star evolution.

In Chapter 2, I showed that the first phase of stable mass transfer for isolated massive binaries plays an important role in determining the dominant formation channel for merging binary black holes but its related uncertainties do not affect the most important GW observables significantly, such as merger rate, mass and mass ratio distributions. This highlights one of the many challenges to use detections of GW transients to learn about the origin of compact binary mergers and the evolution of their progenitors. In order to overcome this particular challenge, an extensive catalogue of WR-O/B binaries with solutions for mass ratios and orbital periods would be indispensable. Comparing the mass ratio and period distribution of WR-O/B binaries to those of ZAMS systems would reveal invaluable clues about the (average) mass transfer efficiency and angular momentum loss mode during a mass transfer episode between two hydrogen rich stars. At the same time, more realistic mass transfer models need to be implemented in binary evolution codes and their astrophysical implications should be thoroughly explored (i.e. models in which the choice of the mass transfer efficiency and angular momentum loss are determined by physically motivated processes, rather than assuming a constant value throughout the entire mass exchange episode, as commonly assumed in rapid population synthesis codes).

An additional, important recommendation, following from the results presented in Chapter 2, is to improve the modelling of Case A mass transfer episodes for massive binaries and to investigate the long term evolution of systems experiencing such mass transfer phases. In Chapter 2, we have shown that numerous defining features in the demographics of merging binary black holes arise due to our predictions that the majority of binaries, which experience Case A mass transfer episodes would eventually merge. However, Case A mass transfer episodes in rapid population synthesis codes are typically modelled in an extremely simplified way (including in this thesis as well) and therefore, it is imperative to explore the role of this mass transfer

mode in the context of GW astronomy with more realistic models.

In Chapter 3, I studied the evolution of massive stellar triples in which the inner binaries consist of chemically homogeneously evolving stars (i.e. CHE stars). Earlier studies showed that isolated binaries comprising CHE stars can form short orbit binary black holes that merge due to GWs within the Hubble time and therefore, these systems have been proposed as promising GW source progenitors. I show that when such a binary system is part of a hierarchical triple, the presence of the tertiary star is predicted to significantly influence the evolution of the inner binary in various ways. It affects the demographics of GW sources originating from these systems. Furthermore, it also leads to the formation of unique astrophysical events, such as tertiary mass transfer (TMT) towards the inner binary consisting of black holes or helium stars, or mergers of double helium stars driven by three-body dynamics. In particular, I show that the relative rate of TMT episodes among such triples is predicted to be remarkably high and therefore such mass transfer episodes can play an important role in the formation of GW sources. This means that TMT, a currently poorly understood process, needs to be studied in more detail. In particular, hydrodynamical simulations of TMT episodes would deliver very important insights for the field of GW astronomy. Finally, I note that the triples studied in Chapter 3 can lead to the merger of massive, rapidly rotating helium stars with non-negligible event rates. This could potentially provide a viable formation path for ultra-long gamma ray bursts. The feasibility of this proposed formation channel should be explored in a more detailed study.

Appendix A

Appendix to Chapter 2

In this section, we briefly summarise how single massive stars evolve with our three different stellar wind models (for description of these models, see section 2.3.7). Although, the impact of stellar winds on single massive stars has already been studied [see e.g. 26, 286], we give this summary so that the results of 2.5.1 and 2.5.2 can be contrasted to the results from single stellar evolution.

In order to understand the importance of different stellar wind prescriptions, we show where different stellar wind mechanisms dominate in the the Hertzsprung-Russel diagram in Fig. A.1, along with the predicted mass loss rates throughout the evolution of a few selected massive stars.

In Fig. A.2, we show the mass lost due to the different wind mechanisms as a fraction of the initial mass for single stars at metallicities $Z = 0.02$ and $Z = 0.005$. Up to $M_{\mathrm{ZAMS}} = 20\,M_{\odot}$, the mass of the remnant is almost completely determined by the mass lost due to supernova and dust-driven winds. Above $M_{\mathrm{ZAMS}} = 40$-$50\,M_{\odot}$, only a negligible amount of mass is lost during remnant formation as our model [delayed model from 97] predicts direct collapse. This implies that no mass
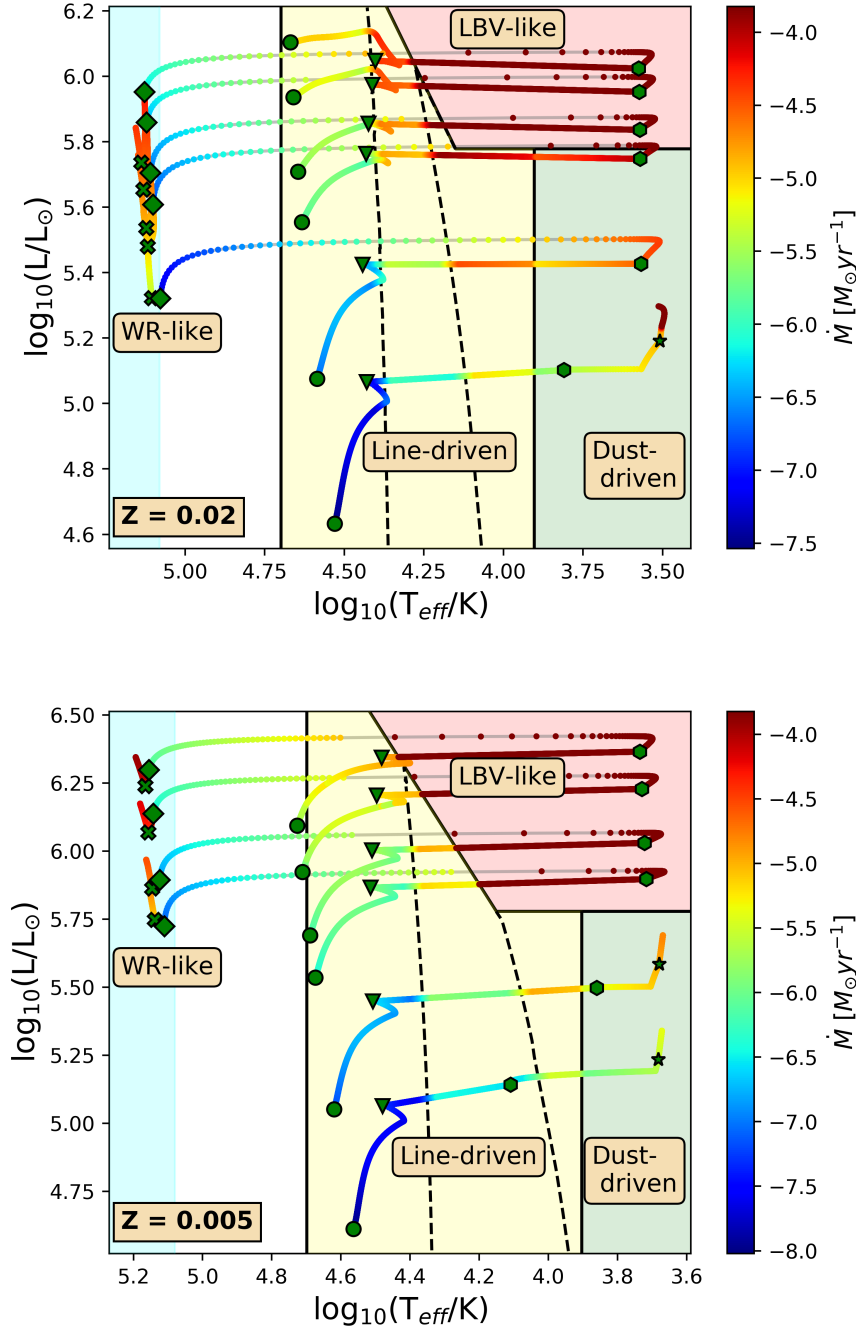
Figure A.1: Hertzsprung-Russel diagrams for massive stars with the mass-loss rate colour-coded in the tracks. The stars have $M_{\mathrm{ZAMS}} = 20, 30, 50, 60, 80, 100\ M_{\odot}$. Different shaded regions denote different stellar wind mechanisms operating on stars. Within the 'Line-Driven' range, the two dashed lines show where the first and the second bi-stability jump occurs. Green figures indicate the starting points of different stellar evolutionary phases; circle: main-sequence, triangle: hydrogen-shell burning phase, hexagon: core helium burning phase, star: AGB, diamond: helium star, cross: helium giant.
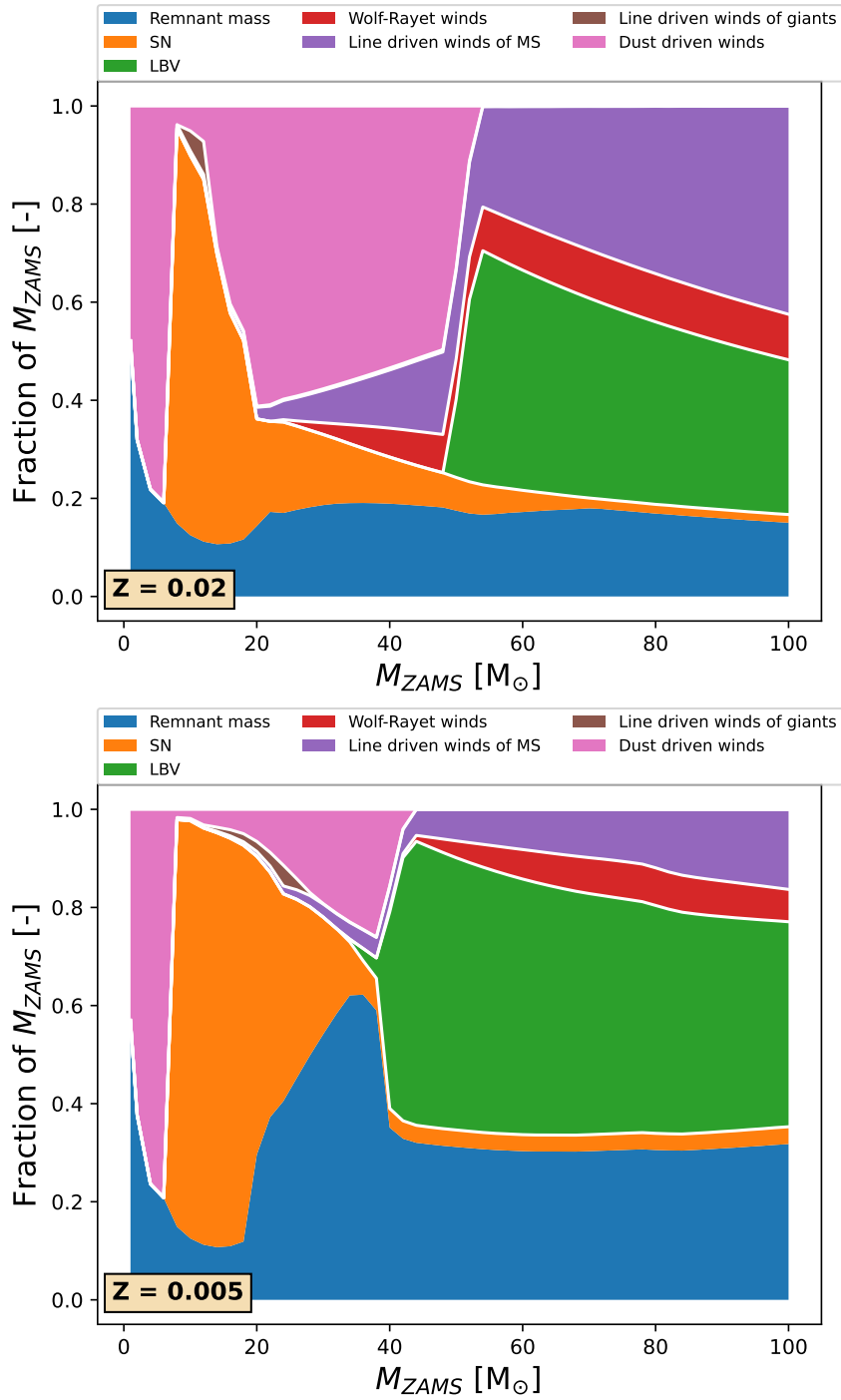
Figure A.2: Fraction of mass lost due to different mass loss mechanisms during the entire life of a non-interacting star at Z = 0.02 and Z = 0.005 as a function of zero-age main sequence mass.

is ejected in the process and the only mass loss is due to neutrino losses, which is assumed to be 10 per cent of the proto-NS mass.

The mass loss due to line-driven winds during the main-sequence phase is substantially more significant for stars with initial masses above $M_{\mathrm{ZAMS}} = 40\text{-}50\,M_\odot$. Furthermore, the stars in this mass range eventually cross the Humphreys-Davidson limit, which leads to severe mass losses during the LBV phase. The masses of black holes which form via direct collapse (i.e. from progenitors with $M_{\mathrm{ZAMS}} \gtrsim 40\,M_\odot$) end up losing 20-40 per cent of their initial mass via line-driven winds during their main sequence phase. This already indicates that lowering the optically thin line-driven winds by a factor of three can have significant effect on the mass spectrum of the most massive black holes.

In Fig. A.3, we show the mass spectrum of black holes formed from single stars for a wide range of metallicities for Model I and Model II [for comparison see 26, 106]. Model II produces moderately more massive black holes in the mass range $40\,M_\odot \lesssim M_{\mathrm{ZAMS}} \lesssim 70\,M_\odot$ compared to the standard wind model at metallicities $Z \gtrsim 0.005$. However, above $M_{\mathrm{ZAMS}} \gtrsim 70\,M_\odot$, the differences become increasingly more appreciable. In particular, the most massive star we simulated ($M_{\mathrm{ZAMS}} = 100\,M_\odot$) using Model I yields $M_{\mathrm{BH}} \approx 14 M_\odot$ at solar metallicity. This increases up to $M_{\mathrm{BH}} \approx 24 M_\odot$ for the Model II. At $Z = 0.01$ black holes even as massive as $M_{\mathrm{BH}} \gtrsim 30\,M_\odot$ are formed in Model II. Since the initial masses of massive stars follow a distribution of $N \sim M_{\mathrm{ZAMS}}^{-2.3}$ ([176]), we therefore expect that only the high mass tail of the black hole mass distribution would be affected significantly when scaling down optically thin line driven stellar winds. Below $Z \approx 0.002$, the differences between the two stellar wind models become negligible.
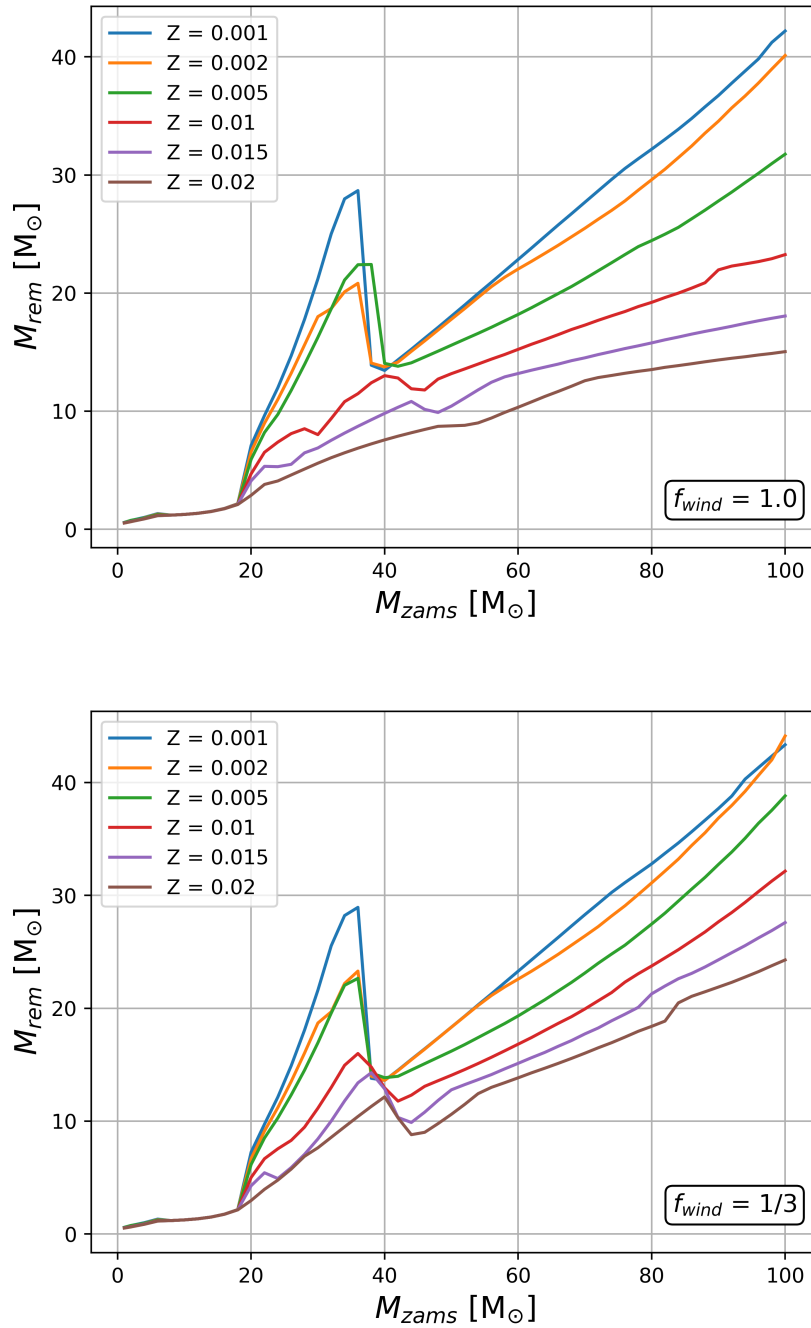
Figure A.3: Zero age main sequence mass and remnant mass functions for different metallicities for single stellar evolution. We assume that black hole formation occurs above $M_{\mathrm{ZAMS}} = 20 M_{\odot}$.

A.1   Merger rate density in the local universe

The merger rate density is an important characteristics of a synthetic population of GW sources, as it allows comparison to the catalogue of gravitational wave (GW) source detections made by LIGO and Virgo [e.g. 6]. We calculate the merger rate density in the local universe (i.e. $z \approx 0$) for all of our model variations presented in section 2.4. In order to determine this quantity, we follow a formalism similar to the one outlined in [70].

First, we define the merger efficiency as the number of mergers originating from a black hole binary with masses $M_{\mathrm{BH},1}$ and $M_{\mathrm{BH},2}$ at metallicity Z as the fraction of the full parameter space (i.e as the fraction of all the stars born, assuming the initial conditions introduced in subsection 2.3.8):

$$\epsilon_{\mathrm{mer}}(M_{\mathrm{BH},1}, M_{\mathrm{BH},2}, Z) = f_{\mathrm{pm}} \cdot \frac{N_{\mathrm{merger}}}{N_{\mathrm{simulated}}}, \tag{A.1}$$

where N_{merger} is the number of mergers originating from a BH binary with given masses at a given metallicity, $N_{\mathrm{simulated}}$ is the number of sampled systems in our simulation and f_{pm} is the simulated parameter space as a fraction of the complete parameter space. We determine the latter as:

$$f_{\mathrm{pm}} = f_{\mathrm{bin}} \cdot \int_{1\,R_\odot}^{10^4\,R_\odot} f_{\mathrm{a}}(a)da \cdot \int_{0.1}^{1} f_{\mathrm{q}}(q)dq \cdot \int_{20\,\mathrm{M}_\odot}^{100\,M_\odot} N_{\mathrm{IMF}}(M)dM, \tag{A.2}$$

here N_{IMF} is the normalised initial mass function of [176], and has been normalised in an interval of $0.08\,M_\odot$-$100\,M_\odot$, f_q is the normalised mass ratio distribution, which has been normalised in the interval of 0-1, and f_a is the normalised semimajor axis distribution, which has been normalised between 10-$10^6\,R_\odot$, f_{bin} is the binary fraction, which we assume to be 0.7, following [303].

A.1. Merger rate density in the local universe

The merger efficiency can be converted to a merger rate density by assuming a metallicity specific star formation density model $\text{SFRd}^*(Z, z)$:

$$\frac{dN}{dV\,dz\,dt} = \iiiint \frac{\text{SFRd}^*(Z, z_{\text{ZAMS}})}{\tilde{M}} \cdot \epsilon_{\text{mer}} dZ\,dM_{\text{BH,1}}\,dM_{\text{BH,2}}\,dt_{\text{d}}, \tag{A.3}$$

where t_{d} is the so-called delay time, which is the time between the zero-age main sequence of the stars in the binary and the time of the merger due to GWs, z_{ZAMS} is the redshift at zero-age main sequence and it is a function of the time delay, $\tilde{M}$ is the average mass of all stellar systems born, such that $\text{SFRd}(Z, z)^*/\tilde{M}$ gives the average number of stars born at redshift z and in the metallicity bin centred around Z.

Delay time can be directly obtained from the population synthesis simulations. In order to determine z_{ZAMS} for a given z and delay time, we use the relationship for lookback time:

$$t_d = \frac{1}{H_0} \int_z^{z_{\text{ZAMS}}} \frac{dz'}{(1 + z')E(z')} dz', \tag{A.4}$$

where $E(z) = \sqrt{\Omega_m(1 + z)^3 + \Omega_\lambda}$, with $\Omega_M = 0.3$, $\Omega_\lambda = 0.7$ and $H_0 = 70 \text{kms}^{-1}\text{Mpc}^{-1}$.

The star formation rate density in a metallicity bin centered at Z with a width of $2\Delta Z$ is $\int_{Z_{\text{min}}}^{Z_{\text{max}}} \text{SFRd}(z) \cdot f_{\text{met}}(Z, z)\,dZ$, where Z_{min} and Z_{max} are the minimum and the maximum metallicity values as defined by $2\Delta Z$. Here $f_{\text{met}}(Z, z)$ gives the distribution of metallicities of binaries at redshift z as:

$$f_{\text{met}}(Z, z) = \frac{1}{\sigma\sqrt{2\pi}} \exp\left(\frac{(\log_{10}(Z) - \mu(z))^2}{2\sigma^2}\right), \tag{A.5}$$

where $\sigma = 0.5$ and the mean metallicity varies with redshift as given by [206]:

$$\mu(z) = \log_{10}(Z_\odot \cdot 10^{0.153 - 0.074z^{1.34}}) - 0.5ln(10)\sigma^2, \tag{A.6}$$

Table A.1: Conversion between the mass transfer stability criteria for giants and the critical mass ratio ($q_{\mathrm{crit}} = M_d/M_a$) for different assumptions on the mass transfer efficiency and the angular momentum loss mode during the mass transfer phase. The last column reflects a binary with a black hole accretor whose mass accretion is Eddington-limited and the expelled mass having the specific angular momentum of the accretor. Donors with radiative envelopes are characterised by $\zeta_{\mathrm{ad,rad}}$, whereas donors with convective envelopes are described by ζ_{HW}. For the latter, we assume a core mass to total mass ratio of 0.45-0.63, which we find is typical for giants at $\log(T_{\mathrm{eff}}) \approx 3.73\,\mathrm{K}$ with initial masses $M_{\mathrm{ZAMS}} = 50$ - $100\,M_\odot$ with a metallicity independent LBV mass loss rate of $\dot{M}_{\mathrm{LBV}} = 1.5 \cdot 10^{-4} M_\odot \mathrm{yr}^{-1}$.

Mass transfer stability criteria	Angular momentum loss				
	$\gamma = 2.5$		$\gamma = 1.0$		$\gamma = M_d/M_a$
	Mass transfer efficiency				
	$\beta = 0.3$	$\beta = 0.7$	$\beta = 0.3$	$\beta = 0.7$	*Eddington limited accretion*
q_{crit} with $\zeta_{\mathrm{ad,rad}} = 4$	3.8	2.9	6.2	3.4	3.2
q_{crit} with $\zeta_{\mathrm{ad,rad}} = 7.5$	8.7	5.2	11.6	5.7	5.5
q_{crit} with $\zeta_{\mathrm{ad}} = \zeta_{\mathrm{HW}}$	$0.9 - 0.7$	$0.9 - 1.1$	$1.5 - 1.9$	$1.1 - 1.4$	$1.4 - 1.7$

where we took $Z_\odot = 0.02$. Furthermore, the star formation rate density SFRd(z) is given by [205]:

$$\mathrm{SFRd}(z) = \frac{0.01 \cdot (1+z)^{2.6}}{1 + ((1+z)/3.2)^{6.2}}\, M_\odot \mathrm{yr}^{-1} \mathrm{Mpc}^{-3}. \tag{A.7}$$

We note again that the metallicity specific cosmic star formation rate is very uncertain and this uncertainty has an important impact on the predicted merging binary black hole population [see e.g. 56, 342, 41, 53]

A.2 The effect of the first phase of mass transfer

In this subsection, we discuss in detail how the first phase of mass transfer affects the mass ratio and orbital separation distributions of binaries. In the following, we restrict the discussion to sources with $M_{\mathrm{ZAMS},1} \gtrsim 45\,M_\odot$ at $Z = 0.0007$. We do this so that the the impact of the first mass transfer can be more easily understood, since at this metallicity the stellar winds are negligible and for this mass range the orbit is not modified by any natal kicks. Therefore the impact of the first mass transfer

can be more easily understood.. However, we note that results presented here are still qualitatively true for all binaries.

In the next section, we present examples for Case B and Case C mass transfer episodes. For this, we assume that the donor fills its Roche-lobe when it reaches the midpoint of its Hertzsprung gap lifetime. As noted in subsection 2.3.1, the outcome of Case B mass transfer epsidoe is not sensitivey dependent on when exactly the Roche-lobe overflow occurs (or equivalently, on the initial orbital separation).

For the examples of Case C mass transfer episodes, we assume that the donor fills its Roche-lobe when it reaches an effective temperature of $\log(\mathrm{T_{eff}}) = 3.73\,\mathrm{K}$. The latter criteria does not strictly imply that the donor is in its core helium burning phase. In particular, at $Z = 0.0007$, binaries with $M_{\mathrm{ZAMS,1}} \gtrsim 90\,M_\odot$ are still in their Hertzsprung gap phase at this effective temperature. Nevertheless, we still choose this criteria, as we find that it is fairly typical for GW sources of the CEE channel to initiate the first mass transfer phase at this stage. We also note, that outcome of the Case C mass transfer phases is more sensitively dependent the initial separation (see discussion 2.3.1).

The distribution of mass ratios and orbital separation of massive binaries at the onset of the second phase of mass transfer are distinct for each formation channel. Therefore, the distribution of these parameters helps us to understand the importance of each channel. The shape of this distribution is primarily determined by the initial conditions and the first phase of mass transfer. The progenitors of each sub-channel introduced in section 2.2.1 have the following range of mass ratios at the onset of the second phase of mass transfer:

- cCEE channel: in this scenario the second phase of mass transfer is Case C, unstable and the donor star has a deep convective envelope, i.e. $q_{\mathrm{MT,2}} > q_{\mathrm{crit}}$

with $\zeta_{\text{ad}} = \zeta_{\text{HW}}$

- rCEE channel: the second phase of mass transfer is Case C, unstable but the donor star has a radiative envelope, i.e. $q_{\text{MT},2} > q_{\text{crit}}$ with $\zeta_{\text{ad}} = \zeta_{\text{ad,rad}}$.

- stable channel: The binary has a relatively short period (i.e. Case B first phase of mass transfer). The binary has a relatively large $q_{\text{MT},2}$. The orbit only then can shrink efficiently due to a stable mass transfer (see Equation 3.16). This means there is a minimum value of $q_{\text{MT},2}$ associated with this channel (for a given $M_{\text{ZAMS},1}$). This value depends on γ and β and on the predicted outcome Case A mass transfer episodes in a complicated way, but it is typically $q_{\text{MT},2,\text{min}} \gtrsim 2.2$ for at $Z \lesssim 0.005$ (see Fig. A.7). Therefore: $q_{\text{MT},2,\text{min}} < q_{\text{MT},2} < q_{\text{crit}}$ with $\zeta_{\text{ad}} = \zeta_{\text{ad,rad}}$.

We note that a stable phase of mass transfer does not typically change the orbit by orders of magnitude. Therefore, the types of the first and the second phases of mass transfers are the same in most cases. For example, most CEE sources have a Case C first phase of mass transfer.

A.2.1 Effect on the mass ratio

In the left panel of Fig. A.4, we show the relation between the initial mass ratio $q_{\text{ZAMS}} \equiv M_{\text{ZAMS},2}/M_{\text{ZAMS},1}$ and that at the onset of the second mass transfer phase $q_{\text{MT},2} \equiv M_d/M_a$. This figure shows the effect of different mass transfer efficiencies and different initial masses for Case B and Case C mass transfer types.

Fig. A.4 tells us what fraction of the binaries can potentially form sources of each channel, and what their initial mass ratio range is. For example, as we will see, GW sources of the stable channel typically require $2.2 \lesssim q_{\text{MT},2} \leq q_{\text{crit}}$. If $\beta = 0.3$,
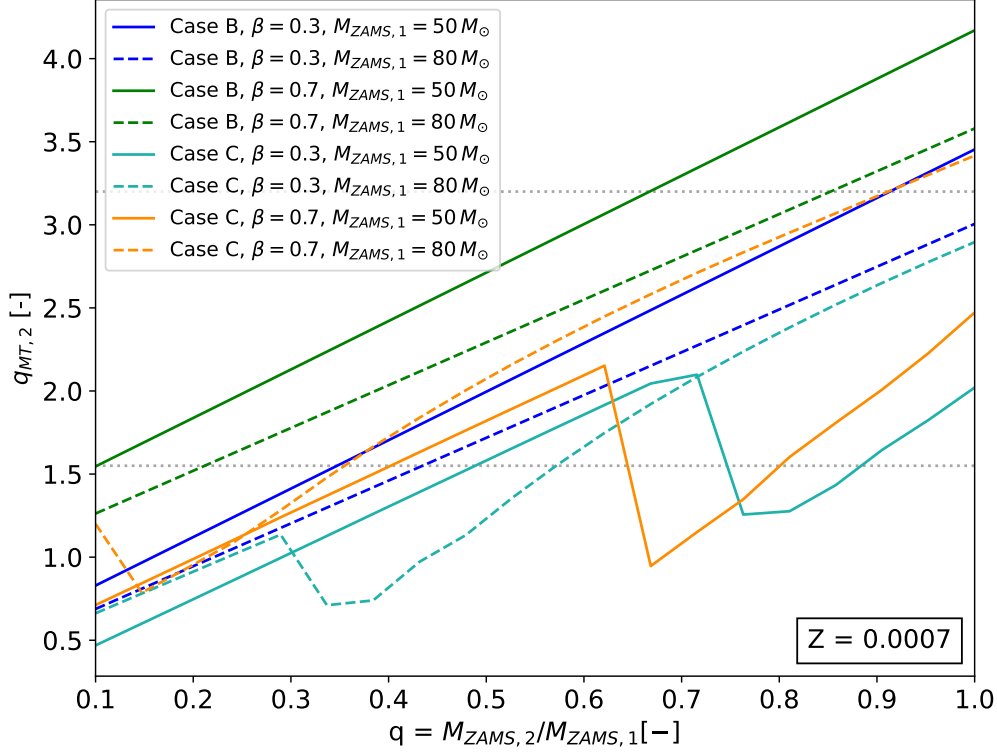
Figure A.4: the relationship between the initial mass ratio ($q_{\mathrm{ZAMS}} = M_{\mathrm{ZAMS,2}}/M_{\mathrm{ZAMS,1}}$) and the mass ratio at the onset of the second mass transfer phase ($q_{\mathrm{MT,2}} = M_d/M_a$). We have neglected the effects of supernova but not the stellar winds. We show these relations for different mass transfer types, mass transfer efficiencies and initial masses. For Case B, we assume that the mass transfer phase starts at the half of the Hertzsprung gap phase lifetime of the donor. In the other case, we assume that the mass transfer phase occurs just before when the donor reaches an effective temperature of $\log_{10} \mathrm{T_{eff}} = 3.73$K. This coincides with the stage where donors develop deep convective envelopes according to [150]. For the majority of the binaries, this occurs with a core-helium burning donor ($M_{\mathrm{ZAMS,1}} \gtrsim 90 M_\odot$ at Z = 0.0007). We chose this criteria, because we find that most of the GW sources from the CEE channel roughly initiate their first mass transfer phase at this stage.
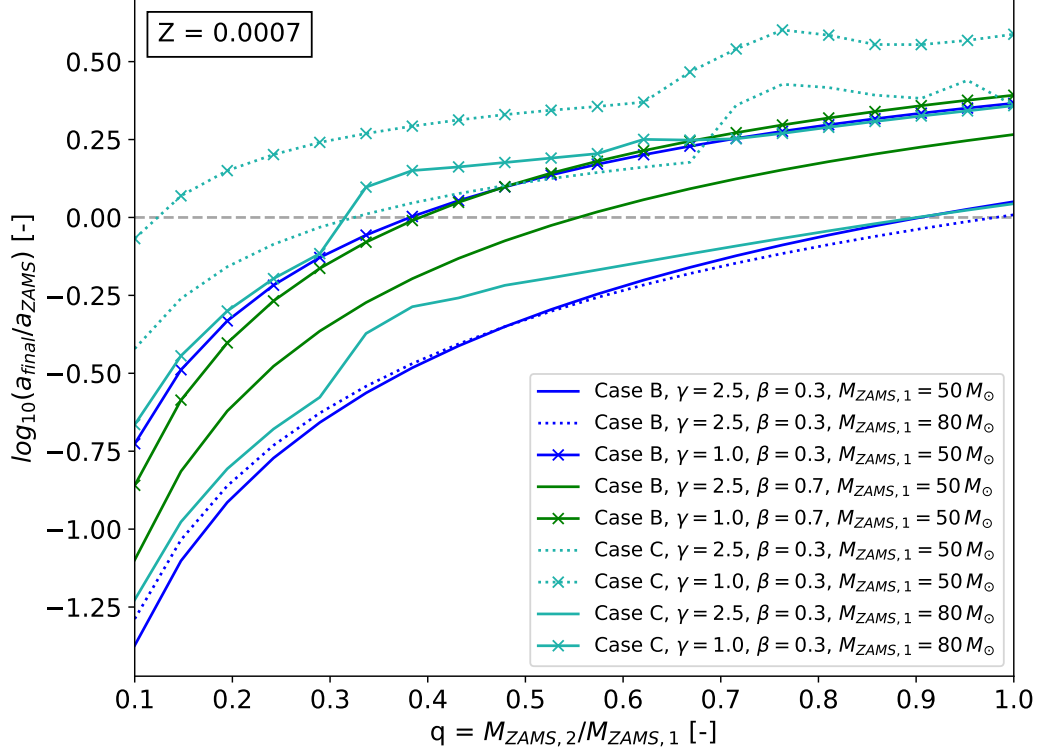
Figure A.5: The relationship between the the initial mass ratio and the shift in the orbital separation in log space for different different mass transfer types, mass transfer efficiencies, angular momentum losses and initial masses. Here we have always assume stable mass transfer phase regardless of the assumed $\zeta_{\mathrm{ad,rad}}$. We have neglected the effects of supernova but not the stellar winds. The upper horizontal, dotted line shows $q_{\mathrm{crit}} = 3.2$, which corresponds to the critical mass ratio for a mass transfer phase with black hole accretor and giant donors with radiative envelopes with $\zeta_{\mathrm{ad,rad}} = 4$. The lower bottom line show the critical mass ratio when the donor has a deep convective envelope. See Table A.1
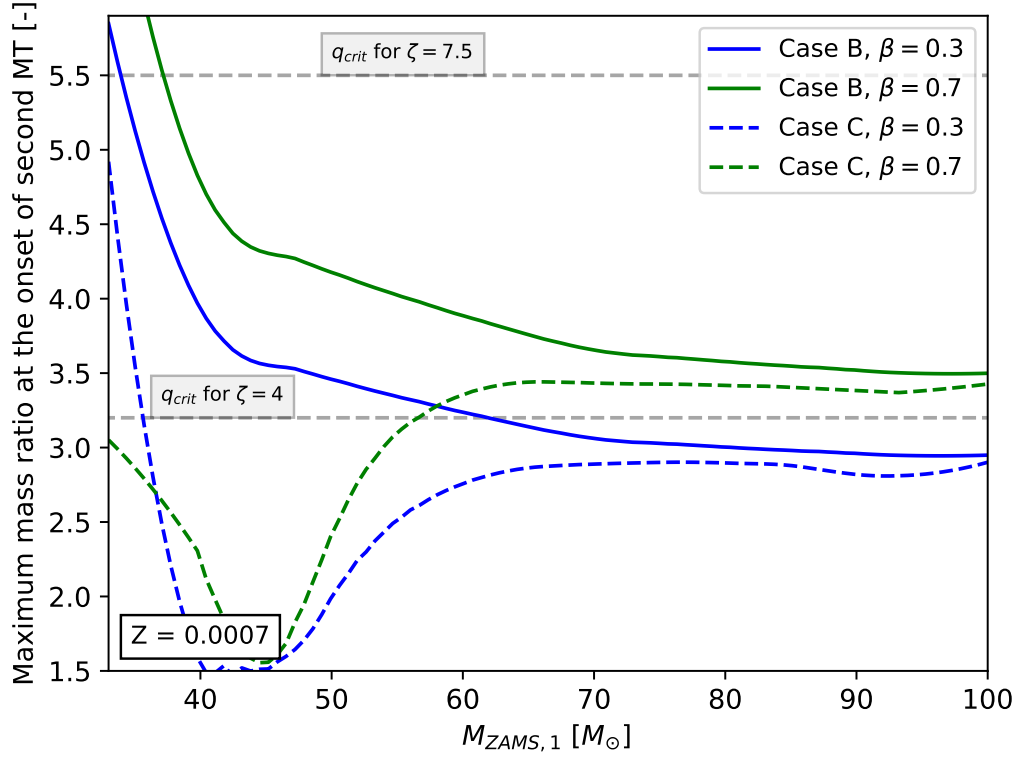
Figure A.6: The estimated maximum value of mass ratio at the onset of the second mass transfer phase ($q_{\mathrm{MT},2} = M_d/M_a$) that a system can reach with a given initial primary mass, mass transfer efficiency and mass transfer phase type. The maximum $q_{\mathrm{MT},2}$ is achieved by binaries that have initially near equal masses. How exactly we defined 'Case B' and 'Case C' mass transfer episode types are explained in the caption of Fig. A.4.

A.2. The effect of the first phase of mass transfer

we expect the most massive sources of the stable channel to evolve from binaries with $q_{\mathrm{ZAMS}} \gtrsim 0.8$. On the other hand, the formation via the rCEE channel, which requires $q_{\mathrm{MT},2} > q_{\mathrm{crit}}$, is not possible at all with mass transfer efficiencies as low as $\beta = 0.3$. Even if $\beta = 0.7$, the formation becomes only possible if $q_{\mathrm{ZAMS}} \gtrsim 0.85$ and $M_{\mathrm{ZAMS},1} \gtrsim 60\,M_\odot$.

We can see that the curves for Case C mass transfer episodes do not have a simple linear relationship, as is the case for Case B. Instead a dip can be observed in the curves at a given range of initial mass ratio. The position of this dip shifts to lower values with increasing mass. This is due to the effect of LBV mass loss. The dip occurs at the lowest initial mass ratio at which the secondary star is still massive enough after the first mass transfer phase, such that it evolves beyond the Humphreys-Davidson limit and eventually loses a significant fraction of its envelope before the onset of the second phase of the mass transfer. At the same time, the mass of the accretor black hole at the second mass transfer phase (formed by the initial primary star) is not significantly affected by LBV winds. This implies that the range of distribution of $q_{\mathrm{MT},2}$ of binaries with a Case C first phase of mass transfer are narrowed down by the LBV winds.

The maximum $q_{\mathrm{MT},2}$ that can be reached by binaries at Z = 0.0007 is shown in Fig. A.6. The maximum $q_{\mathrm{MT},2}$ is given as a function of $M_{\mathrm{ZAMS},1}$ for a given mass transfer efficiency and mass transfer type. The maximum occurs for near equal mass binaries. We expect the results to depend only weakly on the metallicity as long as $Z \lesssim 0.002$, because the $M_{\mathrm{ZAMS}} - M_{\mathrm{BH}}$ relation does not significantly change at this metallicity range (see discussion later in section 2.5).

We can use Fig. A.6 to asses the importance of $\zeta_{\mathrm{ad,rad}}$. A higher $\zeta_{\mathrm{ad,rad}}$ implies a higher critical mass ratio and thereby increases the parameter space for stable mass transfer phase. The degree of orbital shrinkage during stable phase of mass

transfer with a black hole accretor increases exponentially with increasing mass ratio (Equation 3.16). Hence, we may expect that the merger rate of the stable channel could increase significantly with increasing $\zeta_{\mathrm{ad,rad}}$. However, we also have to take into account the limit on the maximum mass ratio at the onset of the second phase of mass transfer. This value is determined by β and the $M_{\mathrm{ZAMS}} - M_{\mathrm{BH}}$ relation. The maximum mass ratio of binaries with Case B mass transfer phase is below 3.2, if $M_{\mathrm{ZAMS,1}} \gtrsim 60\,M_{\odot}$ and $\beta = 0.3$. Therefore, in our low mass transfer efficiency models, increasing $\zeta_{\mathrm{ad,rad}}$ from 4 to 7.5 only affects the evolution of binaries with $M_{\mathrm{ZAMS,1}} \lesssim 60\,M_{\odot}$.

Fig. A.6 also shows the importance of the mass transfer efficiency on the rCEE channel. We find that with low accretion efficiencies, the formation of GW sources via the rCEE channel is not possible for almost the entire mass range. This can be seen from Fig. A.6 as the curve for Case C mass transfer for $\beta \leq 0.3$ and $\zeta_{\mathrm{ad,rad}} = 4$ is below the critical mass ratio for $M_{\mathrm{ZAMS,1}} \gtrsim 40\,M_{\odot}$. If $\zeta_{\mathrm{ad,rad}}$ is increased up to 7.5, then the formation of such systems become impossible even with larger mass transfer efficiencies.

A.2.2 The effect on the orbital separations

The relationship between the initial orbital separation and the orbital separation at the onset of the second phase of mass transfer ($a_{\mathrm{MT,2}}$) can be approximated as:

$$\frac{a_{\mathrm{MT,2}}}{a_{init}} = f_{\mathrm{wind,post-MT,1}} \cdot f_{\mathrm{MT,1}} \cdot f_{\mathrm{wind,pre-MT,1}}, \tag{A.8}$$

if the effects of supernova are negligible. Here, $f_{\mathrm{wind,post-MT,1}}$ and $f_{\mathrm{wind,pre-MT,1}}$ describes by what factor the orbit widens due to stellar winds from the birth of the binary until the onset of the first mass transfer phase and from the end of

A.2. The effect of the first phase of mass transfer

the first mass transfer phase until the onset of the second mass transfer phase, respectively. These changes in orbit are described by Equation 1.30. The terms $f_{\mathrm{wind,post-MT,1}}$ and $f_{\mathrm{wind,pre-MT,1}}$ are negligible for binaries evolving through Case B mass transfer at metallicities $Z \lesssim 0.005$. On the other hand, if the first mass transfer phase is a Case C, then LBV winds contribute to the widening of the orbit appreciably at all metallicities. The term $f_{\mathrm{MT,1}}$ is the change in the orbit during the first mass transfer phase. In principle, these are due to the combined effects of stellar winds and the mass transfer phase itself. However, the effects of the former are typically negligible especially if the mass transfer episode proceeds on thermal timescale. The change in the orbit due to the mass transfer episode is determined by Equation 1.15. In all cases, $f_{\mathrm{MT,1}}$ is the dominant term, i.e. $|f_{\mathrm{MT,1}}| \gg \max(|f_{\mathrm{wind,post-MT,1}}|, |f_{\mathrm{wind,pre-MT,1}}|)$.

In the right panel of Fig. A.4, we show $\log(a_{\mathrm{MT,2}}/a_{\mathrm{initial}})$ as a function of q_{ZAMS} for several model variants and for both Case B and Case C mass transfer types. We see that for Case B mass transfer phase, the change in the orbital separation is mostly determined by the mass ratio of the system, and it is only very weakly independent of the masses of the binary. The latter no longer holds if the first mass transfer phase is a Case C. Here the mass of the initially primary star does affect the amount of orbital widening. There is an upward shift in the curves of $\log(a_{\mathrm{2ndMT}}/a_{\mathrm{initial}})$ for donor stars with strong LBV winds. This effect is reduced for more massive donor stars, as the amount of mass lost due to LBV winds before the onset of the second mass transfer phase (at $\log T_{\mathrm{eff}} = 3.73 \, \mathrm{K}$) decreases with increasing initial mass.

In general, the orbital separations of systems with low initial mass ratios shrink, whereas the opposite is true for binaries with mass ratios close to one. This is also clear from Equation 1.15, which shows that as long as $M_d > M_a$ the separation of the system decreases during the mass transfer phase. Where the turnover occurs between widening and shrinking, however, is dependent on the assumed angular

momentum loss mode γ and accretion efficiency β. As we increase β, the effect of the first mass transfer phase starts to converge to the fully conservative case, and therefore the difference between the angular momentum loss becomes less important.

In the context of GW sources, there is an important point to make regarding the stable channel. In the initial mass ratio range, where we expect the GW sources of stable channel to originate from (i.e. from relatively similar initial masses), the model with $\gamma = 2.5$ and $\beta = 0.3$ shows only an insignificant change in the orbit. The largest widening occurs in models with $\gamma = 1$. This shows why the stable channel is the most efficient in the $\gamma = 2.5$ and $\beta = 0.3$ model, and why it is typically inefficient with $\gamma = 1$.

A.2.3 Case A mass transfer episode

The outcome of a Case A mass transfer phase is much more sensitively dependent on the initial separation and the mass ratio than that of the previously discussed mass transfer types (see also subsection 2.3.5). This means that it is challenging to show simple relations for these kind of systems as we did in Fig. A.4 and A.6 for Case B and Case C.

To demonstrate typical outcomes of Case A mass transfer phases, we show the evolution of a few selected binaries until the second mass transfer phase as simulated by `SeBa` in Fig. A.8. These results show two important characteristics of systems evolving through a first phase of Case A mass transfer. Firstly, they develop $q_{\mathrm{MT},2}$ that are significantly larger than that of their Case B counterparts. These mass ratios are often above q_{crit}. Secondly, if they survive the Case A mass transfer phase, their orbit widens more compared to systems with Case B mass transfers. These two points imply that the majority of these systems initiate an unstable second phase of

mass transfer with an HG donor, which results in stellar merger. All of the systems shown in Fig. A.8 would indeed merge with $\zeta_{ad,rad} = 4$, while one of them would merge with $\zeta_{ad,rad} = 7.5$ as a result of the second mass transfer phase. We, however, stress again that such results from rapid population synthesis codes following the stellar tracks of [138] should be treated with caution. These stellar tracks do not track the developing helium core during main sequence and consequently the mass of the stripped donor after the Case A mass transfer might be severely underestimated.

A.3   Evolution of massive binaries with different stellar wind models

Here, we discuss the evolution of the systems, which form merging binary black holes with the most massive black hole binary in each of our stellar wind models. In order to gain a more detailed understanding of the combined effect of $\zeta_{ad,rad}$ and different stellar wind models, we show the typical formation histories of sources with the most massive primary black holes for each of our stellar wind models in the Appendix in Fig. A.9,. In these scenarios, we assume $\gamma = 2.5$, $\beta = 0.3$ and $\zeta_{ad,rad} = 7.5$. Fig. A.9 shows that the formation path of the most massive sources in Model I and Model II are fairly similar. The evolution starts out with an almost equal mass binary, as this leads to the highest mass ratios at the onset of the second mass transfer phase. On the other hand, the minimum initial separation (so that the first mass transfer is Case B) of such sources is different. Decreasing the optically thin stellar winds by a factor of three increases the radii of stars at the end of the main sequence. In particular, at Z = 0.01, for $M_{ZAMS} = 100\,M_\odot$, R_{TAMS} can increase from $83.2\,R_\odot$ to $110\,R_\odot$ when switching from Model I to Model II. Therefore, binaries of Model II need to start out with a higher initial separation, because of their larger R_{TAMS}. It
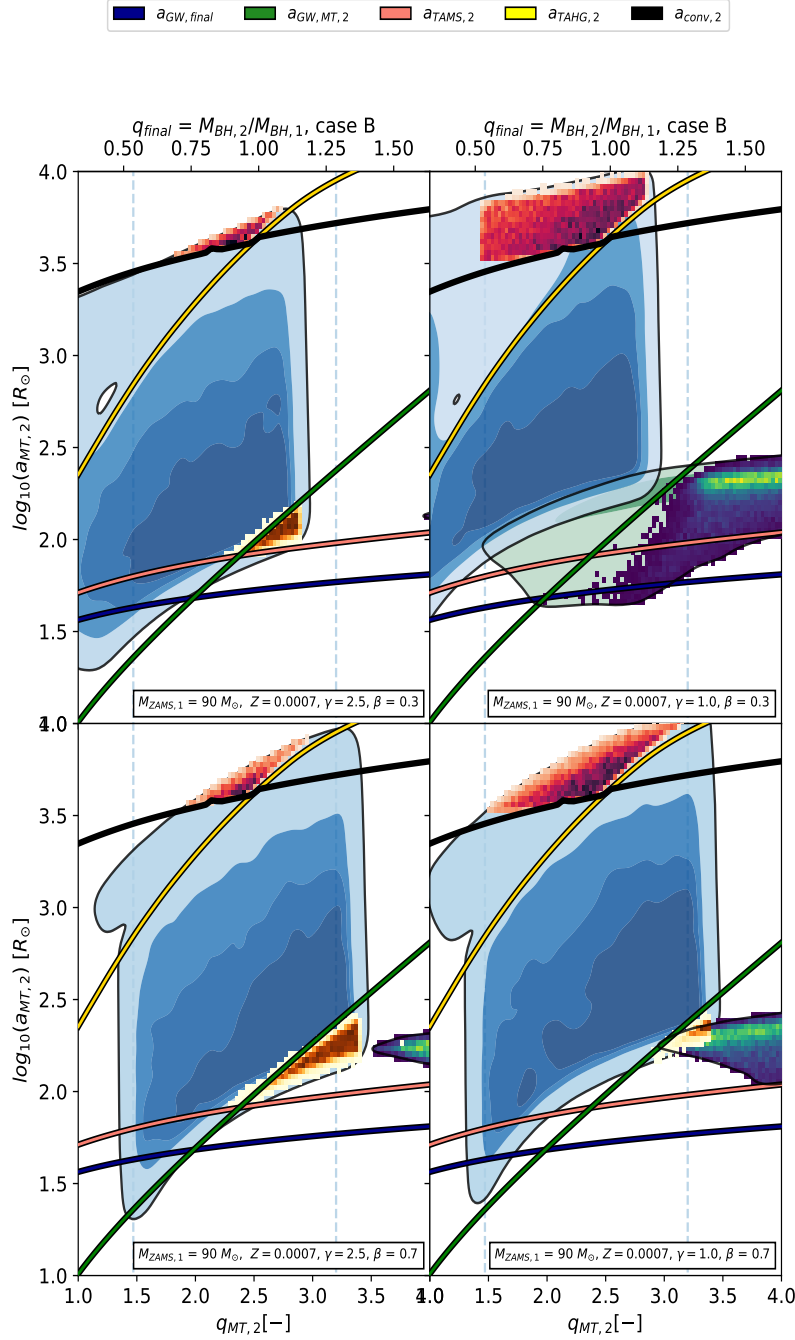
Figure A.7: We show the density contours of BH-star binaries, at the onset of the second phase of mass transfer in the mass ratio - orbital separation space for four different model variations. Contours with blue colour denote binaries for which the first phase of mass transfer is either Case B or Case C, while contours with green colour show systems for which this is Case A. See text for more information

is also confirmed, that these sources indeed require large mass ratios of $q \sim 4 - 5$ at the onset of the second mass transfer. The formation of such systems is not possible in the $\zeta_{\mathrm{ad,rad}} = 4$ model as they would undergo unstable mass transfer and would merge during CEE. We note that primary masses of $\sim 16 - 18\,M_\odot$ for Model I with $\zeta_{\mathrm{ad,rad}} = 4$ can still be seen in Fig. 2.8, however these systems have secondary black hole masses $M_2 \sim 5 - 7\,M_\odot$. The formation of such systems is possible because they start out with a high initial mass ratio and therefore the orbit significantly shrinks after the first mass transfer (even if $\gamma = 1$).

Binaries with initial parameters as shown for Model II in Fig. A.9 do not form GW sources in Model III. The evolutionary path of such a binary would be exactly the same as for Model II until the formation of the first naked helium star. However, because of the decreased Wolf-Rayet-like mass loss rates, the initial primary star forms a $28.0\,M_\odot$ black hole. The intially secondary star becomes a $93.5\,M_\odot$ massive HG giant at the start of the second mass transfer. The mass ratio of 3.3 is not sufficiently high enough to shrink the orbital separation ($\sim 420\,R_\odot$) enough so that the $28.0\,M_\odot$ - $30.5\,M_\odot$ BH-BH would merge within Hubble time.

Instead, the sources with the most massive primaries in Model III form with similar initial masses as in Model II but at shorter orbital separations ($a \sim 180 - 200\,R_\odot$). At such a separation the first mass transfer occurs with a MS donor. As explained earlier, this halts the growth of the helium core. It is predicted that the mass transfer episode proceeds while the donor eventually evolves off the main sequence and it finally ends with the HG donor losing its hydrogen envelope, leaving behind a $26.8\,M_\odot$ massive naked helium star. With the lowered Wolf-Rayet-like winds, this collapses into a $19.8\,M_\odot$ black hole. At the beginning of the second mass transfer, the donor star is a $96.3\,M_\odot$ HG giant. The mass ratio ~ 4.9 is high enough to shrink the orbital separation ($a \sim 370.8\,R_\odot$) significantly. The same system in Model II would have a larger mass ratio because of the lower mass of the black

Stage	Illustration	Case A, example 1			Case A, example 2			Case A, example 3			Case B, example 1		
		$M_1\,[M_\odot]$	$M_2\,[M_\odot]$	$a\,[R_\odot]$	$M_1\,[M_\odot]$	$M_2\,[M_\odot]$	$a\,[R_\odot]$	$M_1\,[M_\odot]$	$M_2\,[M_\odot]$	$a\,[R_\odot]$	$M_1\,[M_\odot]$	$M_2\,[M_\odot]$	$a\,[R_\odot]$
Stage-1 (MS-MS)		50	49.5	55	50	49.5	45	50	10	45	50	49.5	100
Stage-3 (HeMS-MS)		14.8	59.2	180.8	11.8	60.1	205.9	9.3	22.0	38.6	19.1	57.9	232.5
Stage-5 (BH-HG)		13.3	58.9	183.9	8.1	59.7	156.0	4.8	21.9	55.6	17.2	57.6	200.7

Figure A.8: A summary of the evolution of a few selected binaries going through Case A mass transfer phases compared with a binary evolving through a Case B mass transfer episode. We assume $\gamma = 1$ and $\beta = 0.3$. We only show the evolution until the initial secondary fills its Roche-lobe The numbers denoting the evolutionary stage are the same as shown in Fig. 2.1. Therefore Stage 1 refers to the binary at its birth, Stage 2 is at the end of the second mass transfer phase and Stage 3 is just before the second mass transfer episode. We note that for Case A binaries the first mass transfer phase is interrupted at the end of the main sequence of the donor, as its radius starts shrinking. Shortly after, the radius starts to expand rapidly again with the beginning of the Hertzsprung gap phase and therefore refills its Roche-lobe. This second stage ends with the donor losing its hydrogen envelope. For Case A binaries stage 3 refers to stage when the donor becomes a stripped helium star.

hole ($M_1 \approx 14.9\,M_\odot$) and the mass transfer would become unstable, which results in a stellar merger. As systems with such high masses always require mass ratios $q_{\mathrm{MT},2} > 4$, it is clear why there is such a huge difference in the maximum masses of merging binary black holes between $\zeta_{\mathrm{ad,rad}} = 4$ and $\zeta_{\mathrm{ad,rad}} = 7.5$ for Model III.
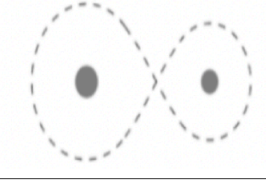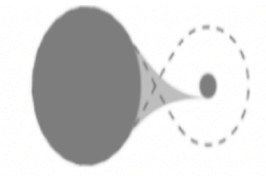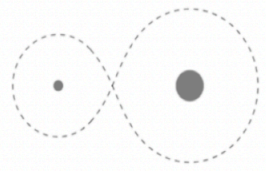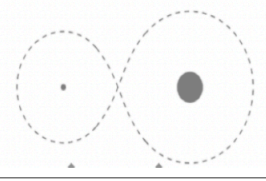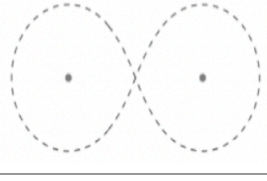
Stage	Illustration	Model I			Model II			Model III		
		$M_1\,[M_\odot]$	$M_2\,[M_\odot]$	$a\,[R_\odot]$	$M_1\,[M_\odot]$	$M_2\,[M_\odot]$	$a\,[R_\odot]$	$M_1\,[M_\odot]$	$M_2\,[M_\odot]$	$a\,[R_\odot]$
Stage 1 (MS - MS)		99.4	97.8	167.8	99.0	96.4	330.6	98.8	96.1	196.4
Stage 2 (MS/HG-MS)		72.2	71.9	229.8	86.9	85.3	375.3	88.3	86.4 (*)	219.1
Stage 3 (HeMS-MS)		31.6	84.0	235.0	40.7	99.1	363.7	26.8	103.3	295.9
Stage 4 (BH-MS)		16.2	77.9	281.1	18.6	95.6	444.3	19.8	99.6	367.8
Stage 6 (BH-BH)		16.2	16.6	23.4	18.6	19.6	28.4	19.8 3	30.5	23.4

Figure A.9: Typical formation histories of merging binary black holes with the most massive primary black holes according to our three different stellar wind models. For brevity, we only show a few stages of the most important steps in the evolution of these systems. The stage numbers correspond to the evolutionary stages as shown in Fig. 2.1. For all the sources here, we assume $\gamma = 2.5$, $\beta = 0.3$ and $\zeta_{\mathrm{ad,rad}} = 7.5$. The asterisk for Stage 2 for Model III means that the first mass transfer phase is Case A
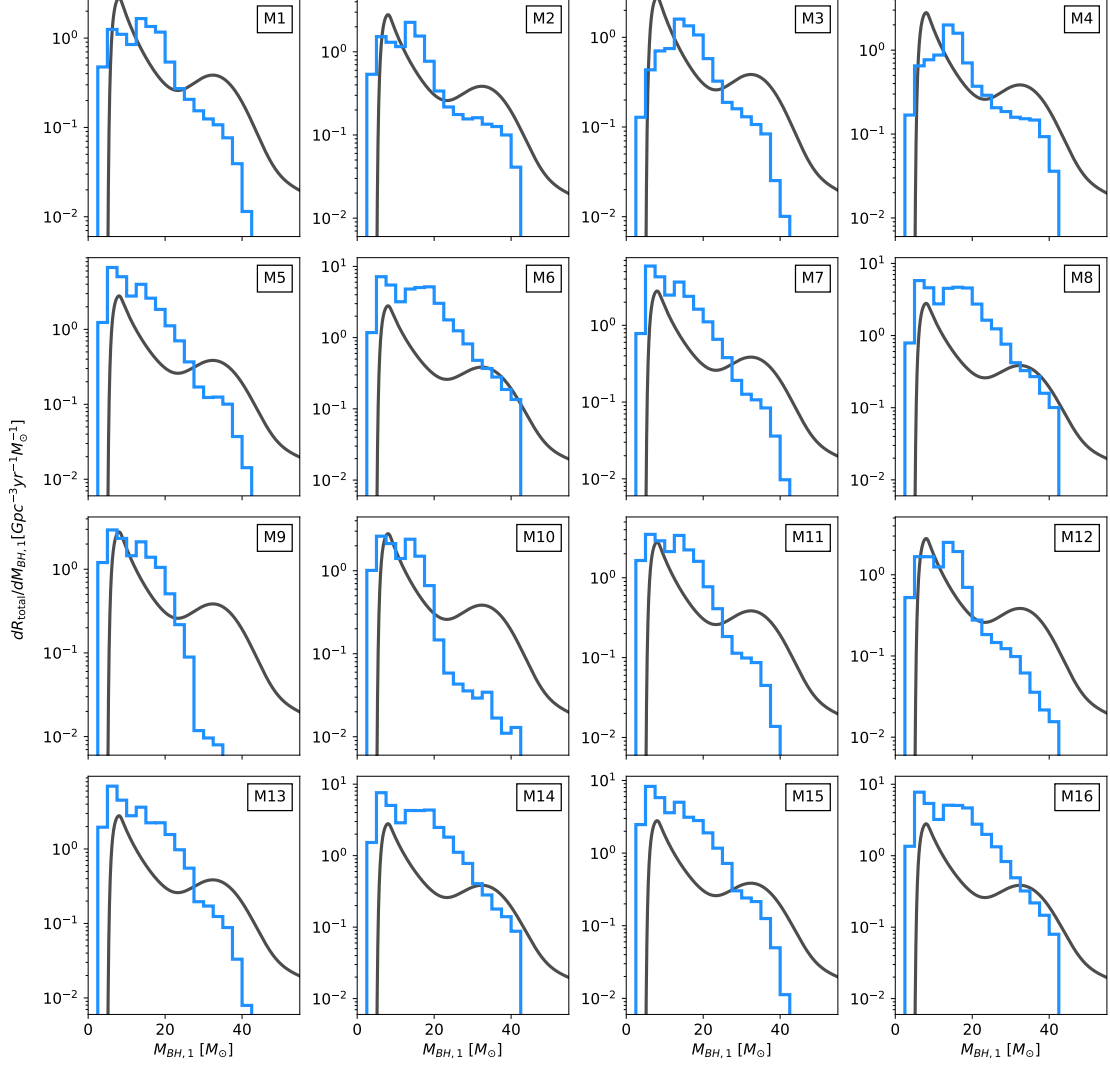
213

Figure A.10: We compare the distribution of primary BH masses of our 16 different model variations (blue) discussed in section 2.4 (see also Table 2.3) with the inferred primary mass distribution of BH-BH binaries of the GWTC-3 catalogue [9], based on the "Power Law + Peak" model (black).
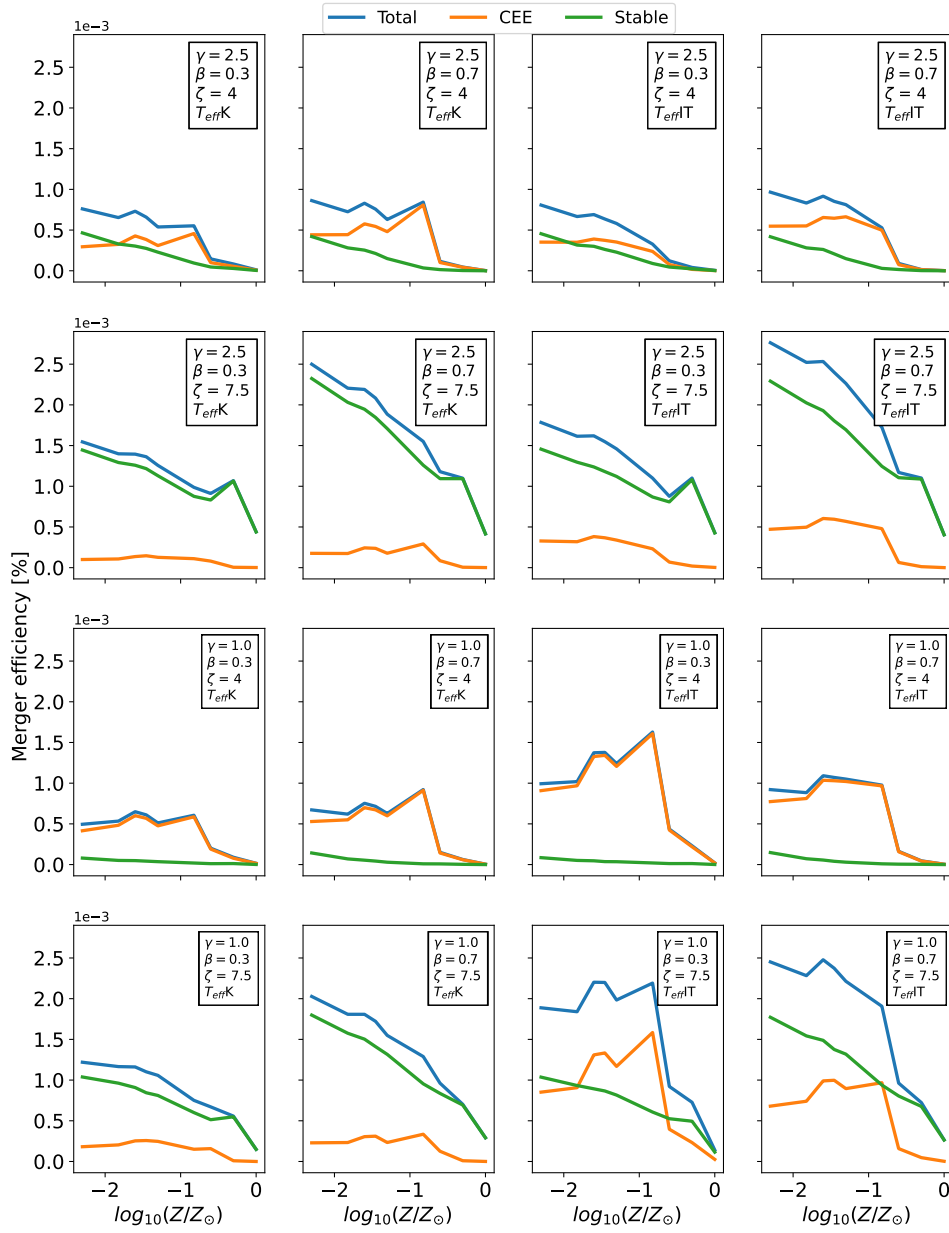.

Figure A.11: Merger rate efficiencies of merging binary black holes our different model variations as a function of metallicity. We consider those systems merging binary black holes, for which the time between zero-age main sequence and merger due to GWs is equal or less than the 14 Gyr. Merger rate efficiency is defined in Equation A.1.
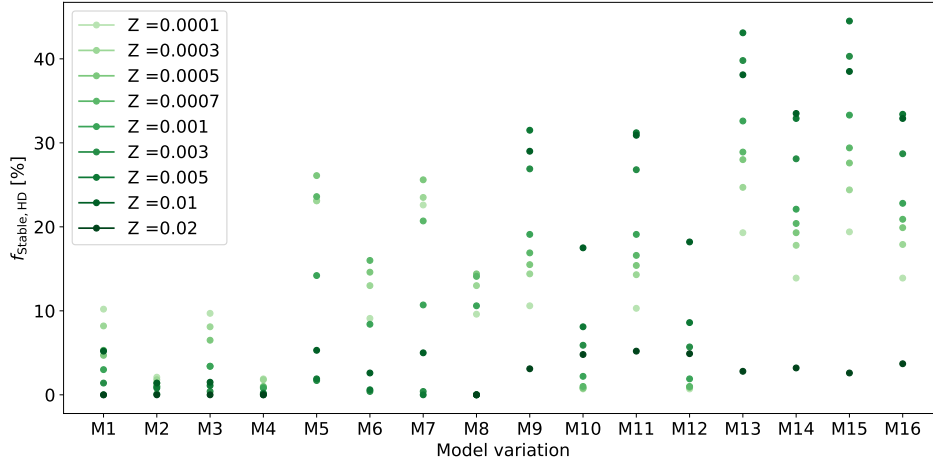.

Figure A.12: The percentage of the binaries in the stable channel, in which any of the stars evolves beyond the Humprheys-Davidson limit for all of our model variations at each metallicity. See Table 2.3 for the meaning of the labels of the model variations.
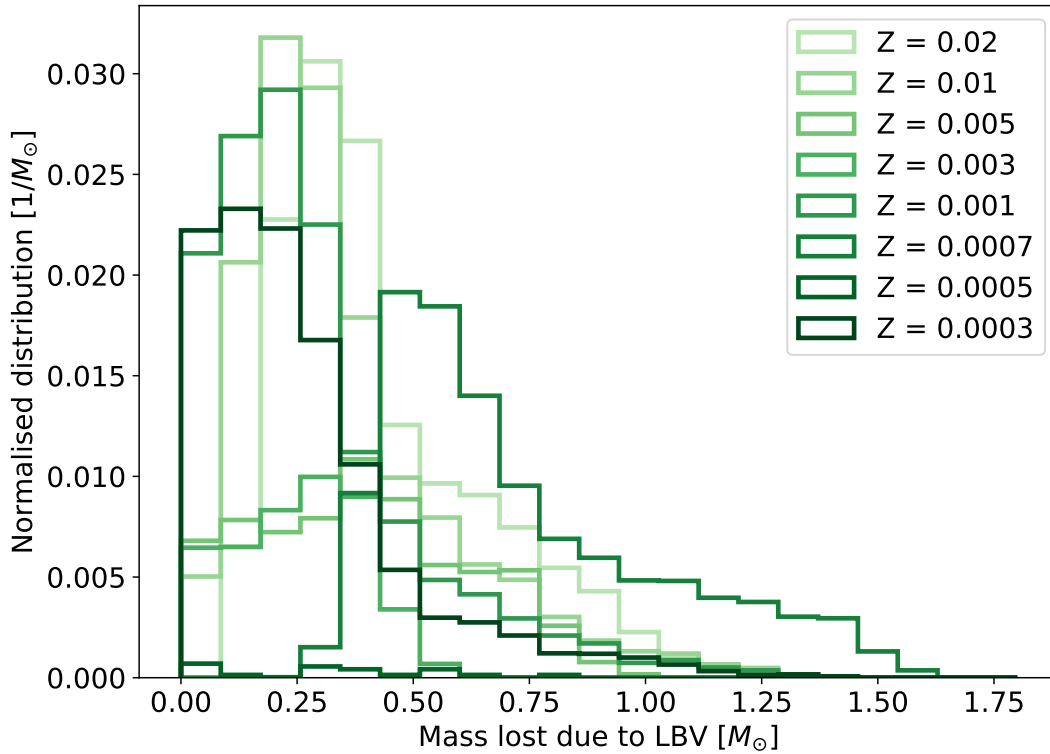

Figure A.13: The estimated total mass lost due to LBV winds with $\dot{M}_{\mathrm{LBV}} = 10^3 M_\odot \mathrm{yr}^{-1}$ of those stars in the systems of the stable channel sources, which cross eventually the Humprheys-Davidson limit in the $\gamma = 2.5$, $\beta = 0.3$, $\zeta_{\mathrm{ad,rad}} = 4$, T_{eff}IT model variation.

A.4   Additional figures

In this subsection, we present additional figures that are helpful (but not necessary) to understand the main results of this work. In Fig. A.7 , We show the density contours of BH-star binaries, at the onset of the second phase of mass transfer in the mass ratio - orbital separation space for four different model variations. Contours with blue colour denote binaries for which the first phase of mass transfer is either Case B or Case C, while contours with green colour show systems for which this is Case A. In this figure, we limit our population to systems for which the initial primary star had a mass of $M_{\mathrm{ZAMS},1} = 90\,M_\odot$. The metallicity is $Z = 0.0007$ and the convective envelope prescription is of [150]. The $a_{\mathrm{GW,final}}$ line shows the separation that binaries have by the time they form BH-BH binaries, if they were to merge due to GW just within Hubble time. For this, we estimate the remnant mass of the donor assuming that the second phase of mass transfer takes place at the midpoint of the hydrogen shell burning phase. The $a_{\mathrm{GW,MT},2}$ line indicates the separation that the same binaries have at the onset of the second phase of mass transfer. We assume stable mass transfer (i.e. Equation 3.16) and we neglect the effect of supernova kick on the orbit. The $a_{\mathrm{TAMS},2}$ line indicates the orbital separation at which the second phase of mass transfer occurs when the donor just evolved off the main sequence. The $a_{\mathrm{TAHG},2}$ is the orbital separation at which the second mass transfer phase occurs with a donor, which just evolved off the Hertzsprung gap phase, while $a_{\mathrm{conv},2}$ is the orbital separation at which the donor fills its Roche lobe just before it develops a deep convective envelope. Furthermore we also show 2D histograms of the GW sources; CEE channel (dark red), stable channel with Case B second mass transfer phase (orange), stable channel with Case A second mass transfer phase (blue). These histograms have been normalised to one. In Fig. A.10, we compare the primary BH mass distributions of our models (shown in Table 2.3) with the inferred distribution of the GWTC-3 catalog [9]. We represent the inferred

distribution with the "Power Law + Peak" model (see e.g. equation B4 in [9]). The values of the model parameters are: $\alpha = -3.5$, $m_{\mathrm{min}} = 4.6\,M_\odot$, $m_{\mathrm{max}} = 86\,M_\odot$, $\lambda_{\mathrm{peak}} = 0.038$, $\mu_m = 34\,M_\odot$, $\sigma_m = 5.7\,M_\odot$, $\delta_m = 4.82\,M_\odot$. For simplicity, we ignored uncertainties. We normalised the distribution to the inferred merger rate density of BH-BH mergers; $R_{\mathrm{GWTC3}} = 28.3\,\mathrm{Gpc}^{-3}\mathrm{yr}^{-1}$. While the upper end of the inferred distribution reaches $M_{\mathrm{BH,1}} = 86\,M_\odot$, the maximum BH mass of our model variations is only $M_{\mathrm{BH,1}} = 42\,M_\odot$, since we do not sample stars more massive than $M_{\mathrm{ZAMS}} = 100\,M_\odot$. To make the comparison easier, we only show the figures up to $M_{\mathrm{BH,1}} = 60, M_\odot$. None of our models can reproduce the peak at $34\,M_\odot$. If this feature is indeed related to (pulsational) pair instability supernova [PPISN 88, 218], then this is not surprising . Firstly, we do not model PPISN in this study. Secondly, since we do not consider stars with $M_{\mathrm{ZAMS}} > 100\,M_\odot$, our PPISN rate would be negligible in any case. All of our models, except M9-M10, yield distributions that are broadly similar to the power-law component of the inferred distribution. M9-M10 exhibit much steeper decrease at $M_{\mathrm{BH,1}} \gtrsim 20\,M_\odot$. Models M5-M16 have a peak around $M_{\mathrm{BH,1}} \approx 10\,M_\odot$, similarly to the inferred distribution. On the other hand, for models M1-M4, this peak occurs at somewhat higher masses ($M_{\mathrm{BH,1}} \approx 15\text{-}20\,M_\odot$), which is not supported by observations.

In Fig. A.11, we show the merging efficiency of each of our model variations (with standard stellar wind models) at each simulated metallicity. In Figure A.12, we show the number of binaries of the stable channel in which any of the stars cross the Humphreys-Davidson limit, expressed as a fraction of all systems in the stable channel. In Figure A.13, we show the estimated total mass lost due to LBV winds with a mass loss rate of $\dot{M}_{\mathrm{LBV}} = 10^3 M_\odot\mathrm{yr}^{-1}$ of those stars in the systems of the stable channel sources, which cross eventually the Humprheys-Davidson limit in the $\gamma = 2.5$, $\beta = 0.3$, $\zeta_{\mathrm{ad,rad}} = 4$, T_{eff}IT model variation. In Fig. A.7, we show density contours, which reflect the mass ratios and orbital separations of binaries at

the onset of the second phase of mass transfer. These binaries were simulated with SeBa at a metallicity $Z = 0.0007$. In Fig. A.7, we limit the initial primary mass to $M_{\mathrm{ZAMS},1} = 90\,M_\odot$. We show four model variations with different assumptions on γ and β. At this stage, the initial primary star has already formed a black hole. If the first phase of mass transfer is Case B, then the mass of the black hole is $M_{\mathrm{BH},1} = 35.44\,M_\odot$. We distinguish binaries for which the first phase of mass transfer is Case A (shown by the green contour, hereafter 'Case A binaries') and for which it is Case B or Case C (shown by the blue contour, hereafter 'Case B binaries' and 'Case C binaries', respectively). We also show the progenitors of GW sources as 2D histograms over the contours. We distinguish three types: CEE channel, stable channel with Case B binaries ('stable Case B', hereafter) and stable channel with Case A binaries ('stable Case A').

Appendix B

Appendix to Chapter 3

B.1   Additional figures

In this section, we present the low metallicity model (i.e. Z = 0.0005) counterparts of some of the figures presented in the main text. In Fig. 3.4, we show the mass ratios at the onset of TMT and the amount of (relative) mass transferred towards the inner binary. In Fig. B.2, we show the cumulative distribution of eccentricities for CHE triples that experience TMT at the onset of the mass transfer phase. In B.3, we show the $M_{2,\mathrm{ZAMS}}$ distribution of TMT sources, distinguishing them based on the evolutionary phase of the inner binary. In Fig. B.4 we show the distribution of initial inner pericenters of CHE triples, distinguishing systems based on the maxium inner eccentricity reached during evolution (left panel), and the based on the evolutionary channel (right panel). In Fig B.5, we show the outer pericentre before and after the TMT episode for systems with MS-MS inner binaries (upper panel) and BH-BH inner binaries (lower panel) at the onset of the mass transfer phase.
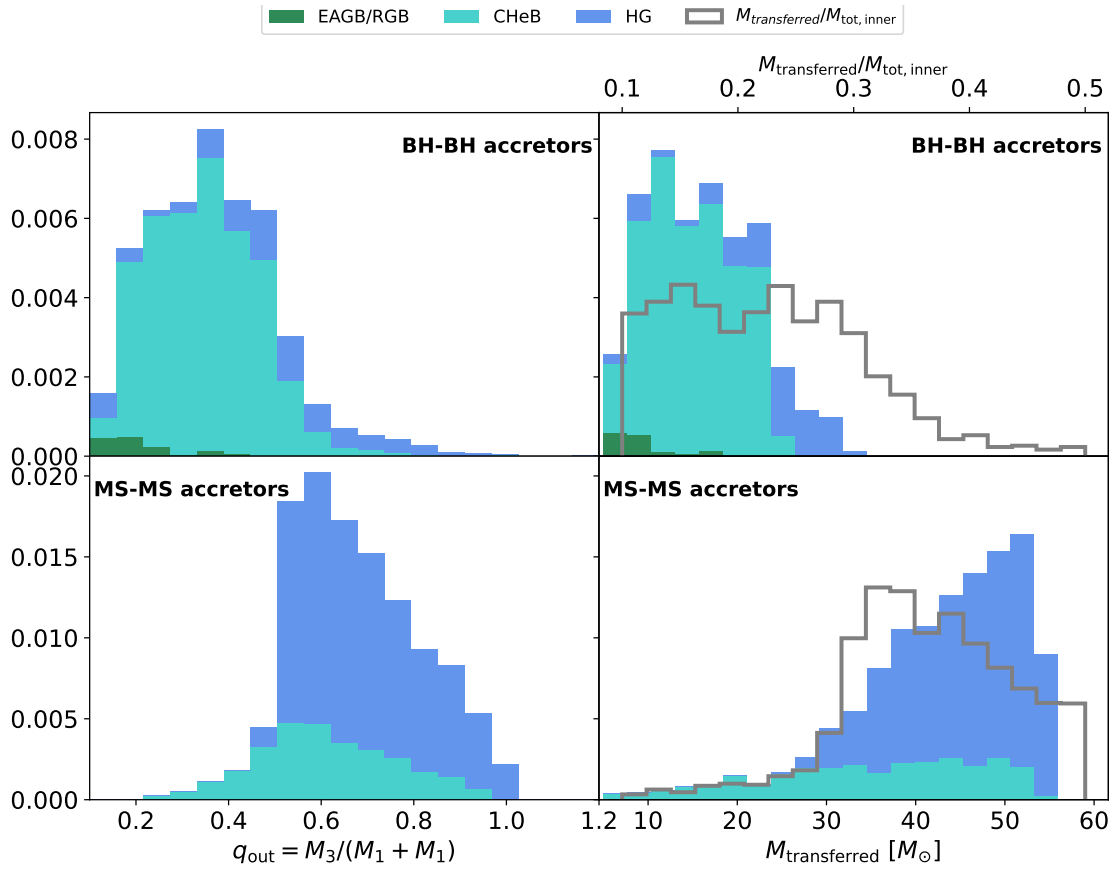
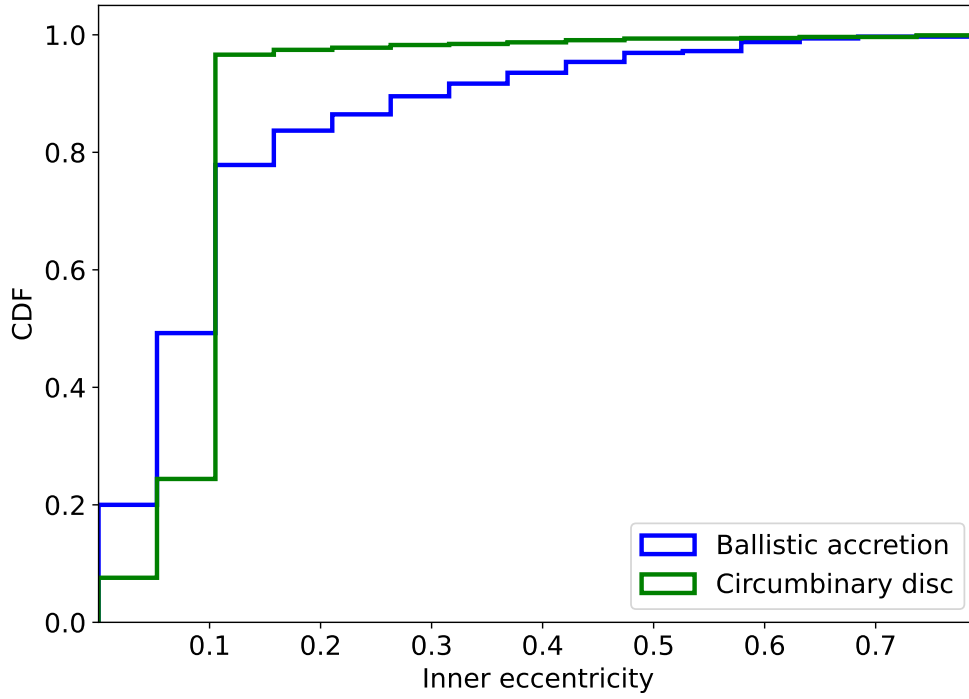Figure B.1: The same figure as Fig. 3.4 but for our model at Z = 0.0005.

Figure B.2: The same figure as Fig. 3.5 but for our model at Z = 0.0005.
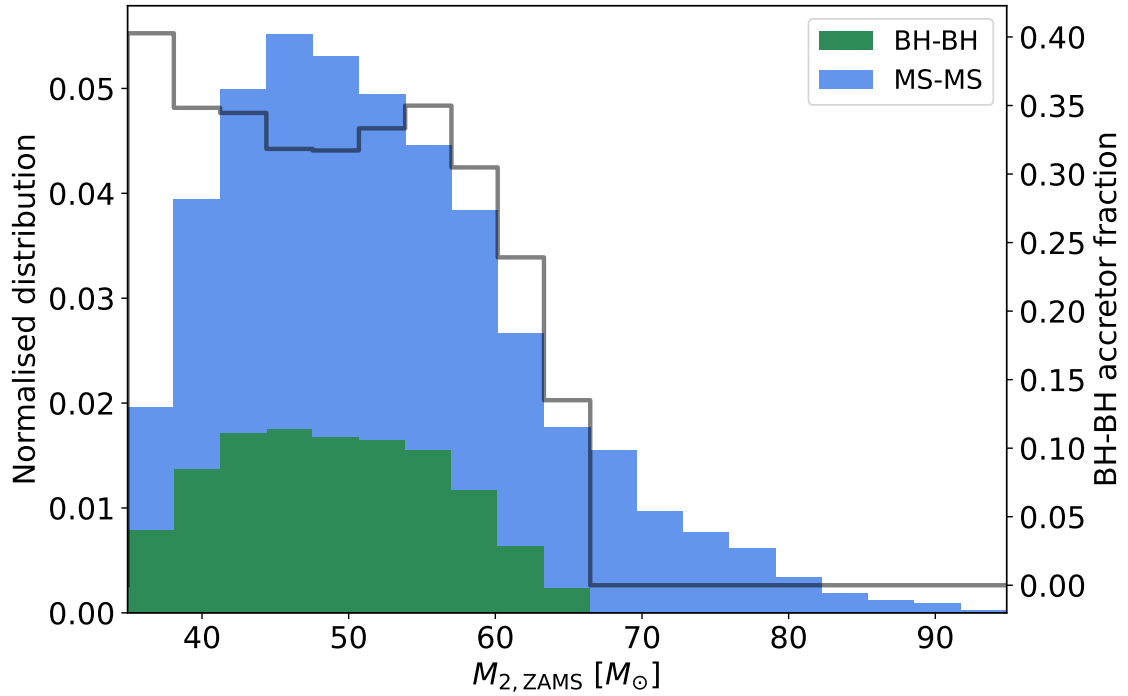

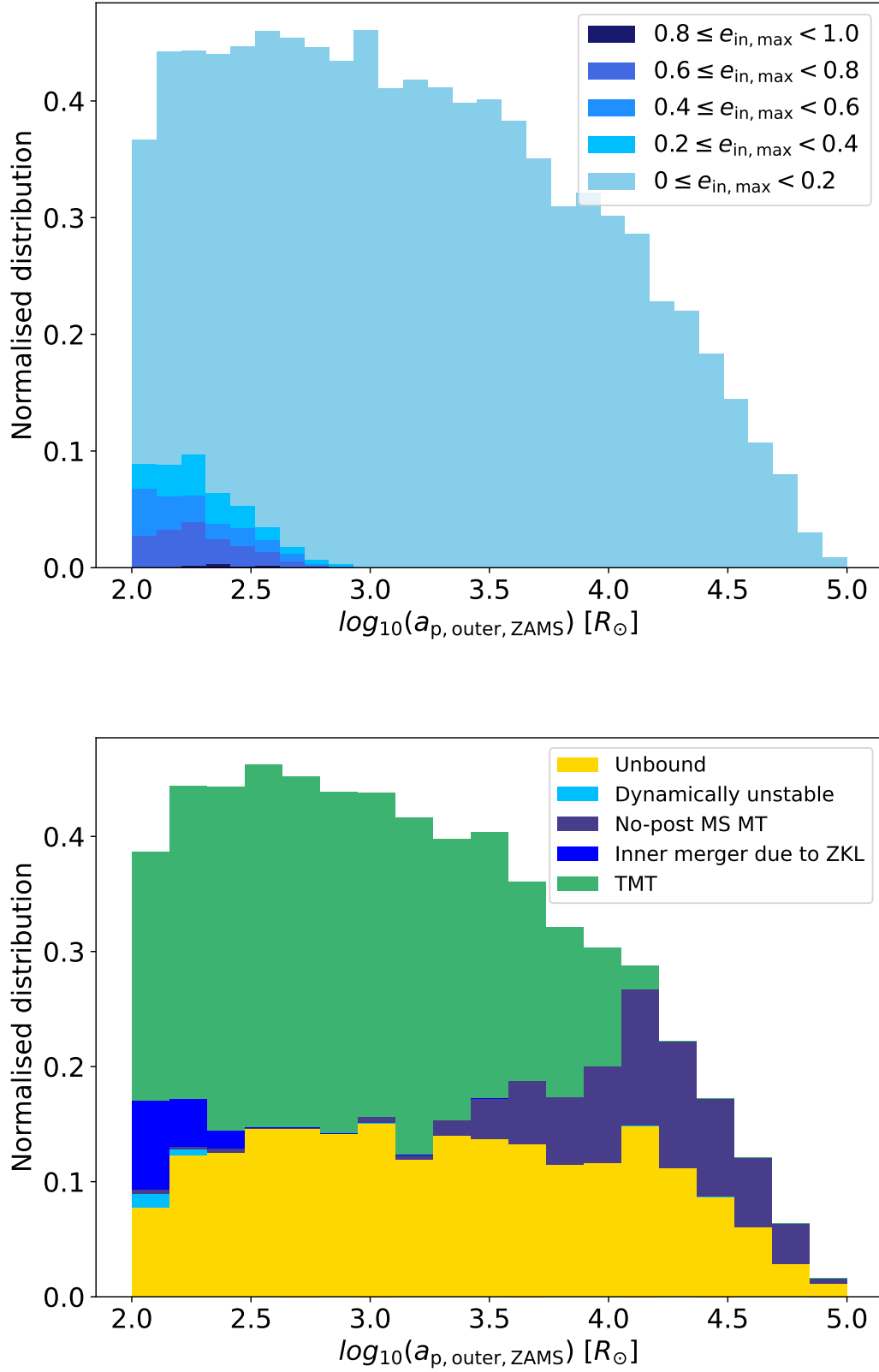Figure B.3: The same as Fig. 3.7 but for our model at Z = 0.0005

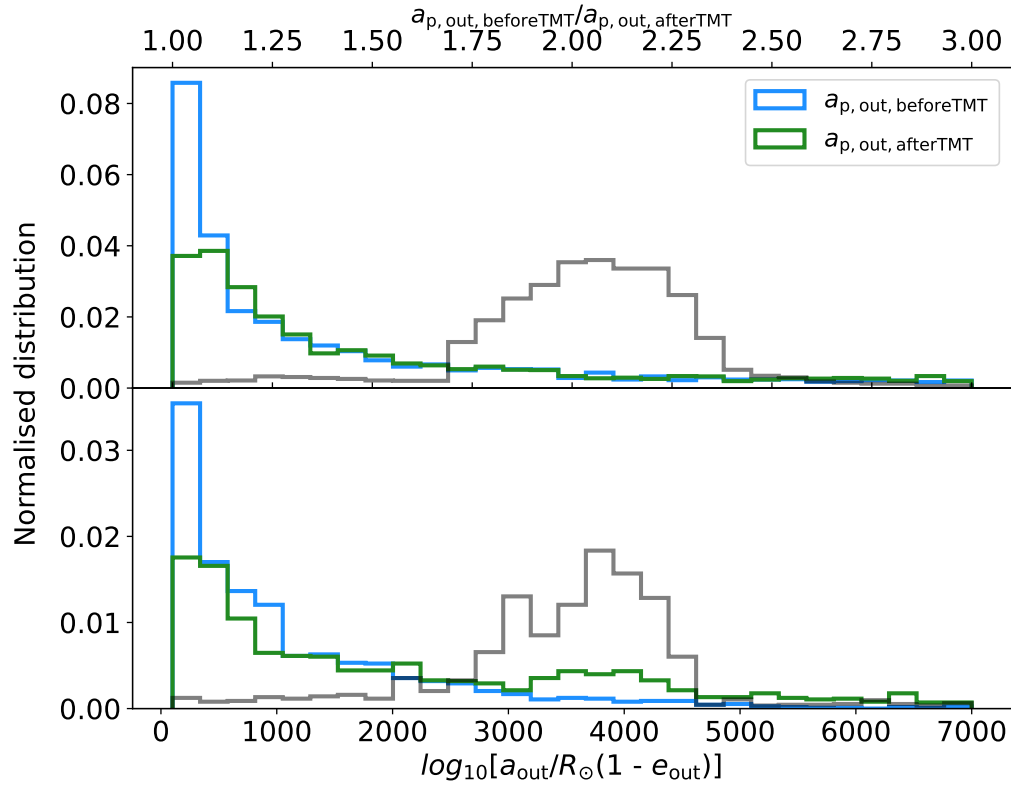Figure B.4: The same as Fig. 3.8 but at Z = 0.0005

Figure B.5: The orbital separation of the outer orbit before and at the onset of TMT for MS-MS inner (upper panel) and BH-BH inner binary accretors (lower panel) as calculated with equation 3.16 at Z = 0.0005.

B.2 Calculation of birth and event rates

Throughout the paper, we estimate the:

1. Formation efficiency (equation B.1)

2. Birth rate density (equation B.8)

3. Merger rate density (equation B.15)

for each identified evolutionary channels. In this section, we discuss in detail how we determine these quantities.

(i) Formation efficiency: The formation efficiency expresses the number of ZAMS stellar systems formed that will evolve according to a specific evolutionary channel as a fraction of all ZAMS stellar systems formed. We calculate this quantity as:

$$\epsilon_{\text{formation}} = f_{\text{pm}} \cdot \frac{N_{\text{channel}}}{N_{\text{simulated}}}, \tag{B.1}$$

where N_{channel} is the number simulated systems that evolves according to the channel of interest, $N_{\text{simulated}}$ the total number of sampled systems, and f_{pm} is the portion of the simulated parameter space with respect to the complete parameter space, that is:

$$f_{\text{pm}} = f_{\text{triple}} \cdot f_{\text{M}_{1,\text{ZAMS}}} \cdot f_{\text{q,in}} \cdot f_{\text{q,out}} \cdot f_{\text{a,in}} \cdot f_{\text{a,out}}, \tag{B.2}$$

where f_{triple} is the assumed triple fraction, $f_{\text{M}_{1,\text{ZAMS}}}$ is the fraction of the simulated parameter space of primary masses:

$$f_{\text{M}_{1,\text{ZAMS}}} = \frac{\int_{20\,M_\odot}^{100\,M_\odot} M_{1,\text{ZAMS}}^{-2.3} dm}{\int_{0.08\,M_\odot}^{0.5\,M_\odot} M_{1,\text{ZAMS}}^{-1.3} dm + \int_{0.5\,M_\odot}^{100\,M_\odot} M_{1,\text{ZAMS}}^{-2.3} dm}, \tag{B.3}$$

225

where we assumed that the absolute minimum stellar mass is $M_{\mathrm{ZAMS,min}} = 0.08\,M_\odot$ and the absolute maximum stellar mass is $M_{\mathrm{ZAMS,max}} = 100\,M_\odot$, and as explained in section 3.3.6, we sample primary masses in the range of 20-100 $M_\odot$. The fraction of the simulated parameter space of inner mass ratios is:

$$f_{\mathrm{q,in}} = \frac{1.0 - 0.7}{1.0 - 0.0}, \tag{B.4}$$

since the distribution of (inner and outer) mass ratios is assumed to be uniform. In equation B.4, we assume that inner mass ratios of hierarchical triples have an interval of (0,1] and we sample from the interval of [0.7,1]. The fraction of the simulated parameter space of outer mass ratios is

$$f_{\mathrm{q,out}} = \frac{1.0 - 0.1}{1.0 - 0.0}, \tag{B.5}$$

where we assume that outer mass ratios triples have an interval of (0,1] and we sample from the interval of [0.1,1]. The fraction of the simulated parameter space of inner semimajor axis is:

$$f_{\mathrm{a,in}} = \frac{\log_{10}(40\,\mathrm{R_\odot}) - \log_{10}(14\,\mathrm{R_\odot})}{\log_{10}(10^5\,\mathrm{R_\odot}) - \log_{10}(14\,\mathrm{R_\odot})}, \tag{B.6}$$

since the distribution of (inner and outer) semimajor axis is assumed to be uniform in a logarithmic space. We assume that inner mass semimajor axes of all triples range from $14\,R_\odot$ to $10^5\,R_\odot$ and we sample from the interval of [14,40] $R_\odot$. Finally, the fraction of the simulated parameter space of outer semimajor axis is:

$$f_{\mathrm{a,out}} = \frac{\log_{10}(10^5\,\mathrm{R_\odot}) - \log_{10}(10^2\,\mathrm{R_\odot})}{\log_{10}(10^5\,\mathrm{R_\odot}) - \log_{10}(10^2\,\mathrm{R_\odot})}, \tag{B.7}$$

where we assume that inner mass semimajor axes of all triples range from $10^2\,R_\odot$ to $10^5\,R_\odot$ and we sample from the enitre interval. Equation B.2 for channels involving

isolated binaries reduces to $f_{\text{pm}} = f_{\text{binary}} \cdot f_{\text{M}_1,\text{ZAMS}} \cdot f_{\text{q,in}} \cdot f_{\text{a,in}}$.

ii) Birth rate density: The birth rate density gives the number density of ZAMS stellar systems in the local universe (that is at redshift $z \approx 0$), which will evolve according to a specific channel. We calculate the birth rate of systems in a certain channel as:

$$R_{\text{birth}} = \sum_{Z_i} \frac{\text{SFRd}^*(Z_i, z_{\text{ZAMS}} = 0)}{\tilde{M}} \cdot \epsilon_{\text{formation}}, \tag{B.8}$$

where we sum over the two metallicity values, at which we performed our simulations; $Z = 0.005$ and $Z = 0.0005$. SFRd*(Z, z) is defined as the metallicity-specific star formation rate density, and it gives the stellar mass formed within a metallicity range $Z_{\text{low}} \leq Z \leq Z_{\text{high}}$ at redshift z:

$$\text{SFRd}^*(Z, z) = \int_{Z_{\text{low}}}^{Z_{\text{high}}} f_{\text{met}}(Z, z) \text{SFRd}(z) dZ, \tag{B.9}$$

where Z_{low} and Z_{high} are 0.0015 (10^{-10}) and 0.01 (0.0015), respectively, for our model with $Z = 0.005$ ($Z = 0.0005$). Here, $Z = 0.0015$ is the midpoint between $Z = 0.005$ and $Z = 0.0005$ in logarithmic space, $Z = 0.01$ is the highest metallicity at which CHE binaries can still form GW sources at appreciable numbers and $Z = 10^{-10}$ is an arbitrarily chosen, extremely low metallicity value. In equation B.9, SFRd(z) is the star formation rate density, and we use the model from [205]:

$$\text{SFRd}(z) = \frac{0.01 \cdot (1+z)^{2.6}}{1 + ((1+z)/3.2)^{6.2}} \, M_\odot \text{yr}^{-1} \text{Mpc}^{-3}, \tag{B.10}$$

and $f_{\text{met}}(Z, z)$ is the metallicity distribution of the stellar mass formed. This quantity is also redshift dependent and assumed to follow a log-normal distribution [206]:

$$f_{\text{met}}(Z, z) = \frac{1}{\sigma\sqrt{2\pi}} \exp\left(\frac{(\log_{10}(Z) - \mu(z))^2}{2\sigma^2} \right), \tag{B.11}$$

B.2. Calculation of birth and event rates

with a standard deviation of $\sigma = 0.5$ and with a redshift-dependent mean metallicity $\mu(z) = \log_{10}(Z_\odot \cdot 10^{0.153-0.074z^{1.34}}) - 0.5\ln(10)\sigma^2$. Finally, the term $\tilde{M}$ in equation B.8 is the average mass of all stellar systems and we calculate this as:

$$
\begin{aligned}
\tilde{M} = {} & f_{\text{single}} \cdot \tilde{M}_{1,\text{ZAMS}} + \\
& f_{\text{binary}} \cdot \int_0^1 (1 + q_{\text{in}})\tilde{M}_{1,\text{ZAMS}} dq_{\text{in}} + \\
& f_{\text{triple}} \cdot \int_0^1 \int_0^1 (1 + q_{\text{in}})(1 + q_{\text{out}})\tilde{M}_{1,\text{ZAMS}} dq_{\text{in}} dq_{\text{out}},
\end{aligned}
\tag{B.12}
$$

where we have defined $\tilde{M}_{1,\text{ZAMS}}$, as the average mass of the primary, i.e.:

$$
\tilde{M}_{1,\text{ZAMS}} = \int_{0.08\,M_\odot}^{100\,M_\odot} M_{1,\text{ZAMS}} f_{\text{IMF}} dM_{1,\text{ZAMS}}
\tag{B.13}
$$

where f_{IMF} is the normalised, piecewise continuous initial mass function of [176], f_{single} and f_{binary} are the single and binary fractions, respectively. We neglect higher order systems, such that $f_{\text{triple}} = 1 - f_{\text{single}} - f_{\text{binary}}$.

We note that we also assume that the binary and triple fractions are independent on the primary mass of the system [which is clearly not consistent with observations, see e.g. 235, but commonly assumed in population synthesis studies as a simplification]. Assuming a flat mass ratio distributions for both the inner and outer binary, equation B.12 becomes:

$$
\tilde{M} = \left(f_{\text{single}} + \frac{3}{2} f_{\text{binary}} + \frac{9}{4} \cdot f_{\text{triple}} \right) \cdot \tilde{M}_{1,\text{ZAMS}},
\tag{B.14}
$$

The term $\text{SFRd}^*(Z_i, z_{\text{ZAMS}} = 0)/\tilde{M}$ in equation B.8 then gives the average number of stars formed at redshift $z = 0$ in a metallicity range of $Z_{\text{i,low}} \leq Z \leq Z_{\text{i,high}}$. Multiplying this term with $\epsilon_{\text{formation}}$ gives the number of systems formed in a given formation channel as a fraction of all systems formed in the above mentioned metallicity range for a given star formation history model. Summing these values over all

of our metallicity bins therefore yields the total birth rate of systems in a specific channel.

iii) Merger rate density: The merger rate density gives the rate density of a given astrophysical event (such as GW transients from coalescing double compact objects) in the local universe. The main difference between the birth and merger rate is due to the considerable delay time between the formation of the stellar system and the occurrence of the GW merger. For example, if the delay time for a GW source at $z = 0$ is $t_{\text{delay}} = 10.5$ Gyrs, then the redshift at ZAMS of its progenitor systems is $z_{\text{ZAMS}} \approx 2$, at which the star formation rate density is an order of magnitude higher with respect to its value at $z = 0$ [e.g. see models of 205]. We determine the merger rate density at $z = 0$ as:

$$R_{\text{event}} = \sum_{Z_i} \int_{0\,\text{Gyr}}^{13.5\,\text{Gyr}} \frac{\text{SFRd}^*(Z_i, z_{\text{ZAMS}}(t_{\text{delay}}))}{\tilde{M}} \cdot \tilde{\epsilon}(t_{\text{delay}}) dt_{\text{delay}}, \tag{B.15}$$

where z_{ZAMS} is the redshift at which the progenitor of a given astrophysical event is formed (and therefore it is a function of delay time), $\tilde{\epsilon}$ is the number of astrophysical events occurring at $z = 0$ with a delay time of t_{delay} as a fraction of all ZAMS stellar systems formed at $z = z_{\text{ZAMS}}$. We determine z_{ZAMS} for a given delay time via the standard relation for lookback time:

$$t_{\text{delay}} = \frac{1}{H_0} \int_{z=0}^{z_{\text{ZAMS}}} \frac{dz'}{(1 + z')E(z')} dz', \tag{B.16}$$

where $E(z) = \sqrt{\Omega_m(1 + z)^3 + \Omega_\lambda}$, with $\Omega_M = 0.3$, $\Omega_\lambda = 0.7$ and $H_0 = 70 \text{kms}^{-1}\text{Mpc}^{-1}$.

We note that our merger rate density should be only considered as an order of magnitude estimate at best. This imprecision is due to several uncertainties in stellar physics and, notably, the limited density of our metallicity grid. We performed simulations only at two metallicities to determine the merger rate density. How-

ever, the formation efficiency and delay times of GW sources originating from CHE systems is expected to be sensitively dependent on metallicity.

In particular, we overestimate the delay times for GW sources formed at $0.001 < Z \leq 0.005$, which in turn leads to an overestimation of the merger rate density at $z = 0$. This is because, we represent all systems formed in this metallicity range with our models at $Z = 0.005$, at which the stellar winds are stronger and therefore lead to wider BH-BH binaries. The longer time delays imply that GW sources merging at $z = 0$ are predicted to have formed at a larger redshift, at which the star formation rate is higher. In particular, [205] predicts that the cosmic star formation rate montonically increases up to $z \sim 2$. This could also explain why our merger rate is a factor of two higher than predicted by [292]. Similarly, we underestimate the delay times for GW sources formed at $0.0005 < Z \leq 0.001$, and therefore we might underestimate the merger rate densities for such systems. In particular, this could mean that the merger rate density of the TMT with a MS-MS accretor channel (discussed in section 3.6.5) could be significantly higher than predicted (shown in Table 3.3).

Bibliography

[1] Abbott D. C., Lucy L. B., 1985, Astrophysical Journal, 288, 679

[2] Abbott B. P., et al., 2016, Physical Review Letters, 116, 061102

[3] Abbott B. P., et al., 2019a, Physical Review X, 9, 031040

[4] Abbott B. P., et al., 2019b, The Astrophysical Journal, 882, L24

[5] Abbott B. P., et al., 2020, Living Reviews in Relativity, 23

[6] Abbott R., et al., 2021a, Physical Review X, 11

[7] Abbott R., et al., 2021b, Physical Review X, 11, 021053

[8] Abbott R., et al., 2021c, The Astrophysical Journal Letters, 913, L7

[9] Abbott R., et al., 2023, Physical Review X, 13, 011048

[10] Agrawal P., Hurley J., Stevenson S., Rodriguez C. L., Szecsi D., Kemp A., 2023, arXiv e-prints, p. arXiv:2303.10187

[11] Alexander M. E., 1973, Astrophysics and Space Science, 23, 459

[12] Amaro-Seoane P., et al., 2022, Astrophysics with the Laser Interferometer Space Antenna, doi:10.48550/ARXIV.2203.06016, https://arxiv.org/abs/2203.06016

[13] Anderson K. R., Lai D., Storch N. I., 2017, Monthly Notices of the Royal Astronomical Society, 467, 3066

[14] Andrews J. J., Cronin J., Kalogera V., Berry C. P. L., Zezas A., 2021, The Astrophysical Journal Letters, 914, L32

[15] Angulo C., et al., 1999, Nuclear Physics A, 656, 3

[16] Antognini J. M., Shappee B. J., Thompson T. A., Amaro-Seoane P., 2014, Monthly Notices of the Royal Astronomical Society, 439, 1079

[17] Antoni A., MacLeod M., Ramirez-Ruiz E., 2019, Astrophysical Journal, 884, 22

[18] Antonini F., Perets H. B., 2012, Astrophysical Journal, 757, 27

[19] Antonini F., Toonen S., Hamers A. S., 2017, Astrophysical Journal, 841, 77

[20] Barkat Z., Rakavy G., Sack N., 1967, Physical Review Letters, 18, 379

[21] Bartos I., Kocsis B., Haiman Z., Márka S., 2017, Astrophysical Journal, 835, 165

[22] Bavera S. S., et al., 2021, Astronomy and Astrophysics, 647, A153

[23] Belczynski K., Bulik T., Rudak B., 2004, The Astrophysical Journal, 608, L45–L48

[24] Belczynski K., Kalogera V., Rasio F. A., Taam R. E., Zezas A., Bulik T., Maccarone T. J., Ivanova N., 2008, Astrophysical Journals, 174, 223

[25] Belczynski K., Bulik T., Fryer C. L., Ruiter A., Valsecchi F., Vink J. S., Hurley J. R., 2010a, Astrophysical Journal, 714, 1217

[26] Belczynski K., Bulik T., Fryer C. L., Ruiter A., Valsecchi F., Vink J. S., Hurley J. R., 2010b, The Astrophysical Journal, 714, 1217–1226

[27] Belczynski K., Holz D. E., Bulik T., O'Shaughnessy R., 2016, Nature, 534, 512–515

[28] Belczynski K., et al., 2020a, Astronomy and Astrophysics, 636, A104

[29] Belczynski K., et al., 2020b, Astrophysical Journal, 890, 113

[30] Belczynski K., et al., 2022, Astrophysical Journal, 925, 69

[31] Bird S., Cholis I., Muñoz J. B., Ali-Haïmoud Y., Kamionkowski M., Kovetz E. D., Raccanelli A., Riess A. G., 2016, Phys. Rev. Lett., 116, 201301

[32] Björklund R., Sundqvist J. O., Puls J., Najarro F., 2020, New predictions for radiation-driven, steady-state mass-loss and wind-momentum from hot, massive stars II. A grid of O-type stars in the Galaxy and the Magellanic Clouds (`arXiv:2008.06066`)

[33] Björklund R., Sundqvist J. O., Singh S. M., Puls J., Najarro F., 2022, New predictions for radiation-driven, steady-state mass-loss and wind-momentum from hot, massive stars III. Updated mass-loss rates for stellar evolution, doi:10.48550/ARXIV.2203.08218, `https://arxiv.org/abs/2203.08218`

[34] Blaauw A., 1961, Bulletin Astronomical Institute of the Netherlands, 15, 265

[35] Blaes O., Lee M. H., Socrates A., 2002, Astrophysical Journal, 578, 775

[36] Blanchet L., 2014, Living Reviews in Relativity, 17, 2

[37] Bohm-Vitense E., 1958, Zeitschrift fuer Astrophysik, 46, 108

[38] Bond J. R., Arnett W. D., Carr B. J., 1982, in Rees M. J., Stoneham R. J., eds, NATO Advanced Study Institute (ASI) Series C Vol. 90, Supernovae: A Survey of Current Research. pp 303–311

[39] Bondi H., Hoyle F., 1944, Monthly Notices of the Royal Astronomical Society, 104, 273

[40] Braudo J., Bear E., Soker N., 2022, Monthly Notices of the Royal Astronomical Society, 510, 4242

[41] Briel M. M., Eldridge J. J., Stanway E. R., Stevance H. F., Chrimes A. A., 2022, Monthly Notices of the Royal Astronomical Society, 514, 1315

[42] Briel M. M., Stevance H. F., Eldridge J. J., 2023, Monthly Notices of the Royal Astronomical Society, 520, 5724

[43] Broekgaarden F. S., et al., 2021, Monthly Notices of the Royal Astronomical Society, 508, 5028

[44] Broekgaarden F. S., et al., 2022, Monthly Notices of the Royal Astronomical Society, 516, 5737

[45] Brookshaw L., Tavani M., 1993, Astrophysical Journal, 410, 719

[46] Brott I., et al., 2011, Astronomy and Astrophysics, 530, A115

[47] Camacho J., Torres S., García-Berro E., Zorotovic M., Schreiber M. R., Rebassa-Mansergas A., Nebot Gómez-Morán A., Gänsicke B. T., 2014, Astronomy and Astrophysics, 566, A86

[48] Cantiello M., Yoon S. C., Langer N., Livio M., 2007, Astronomy and Astrophysics, 465, L29

[49] Castor J. I., Abbott D. C., Klein R. I., 1975a, Astrophysical Journal, 195, 157

[50] Castor J., McCray R., Weaver R., 1975b, Astrophysical Journal Letters, 200, L107

[51] Caughlan G. R., Fowler W. A., 1988, Atomic Data and Nuclear Data Tables, 40, 283

[52] Cehula J., Pejcha O., 2023, Monthly Notices of RAS, 524, 471

[53] Chruślińska M., 2022, arXiv e-prints, p. arXiv:2206.10622

[54] Chruslinska M., Belczynski K., Klencki J., Benacquista M., 2018, Monthly Notices of the Royal Astronomical Society, 474, 2937

[55] Chruslinska M., Nelemans G., Belczynski K., 2019, Monthly Notices of the Royal Astronomical Society, 482, 5012

[56] Chruślińska M., Jeřábková T., Nelemans G., Yan Z., 2020, Astronomy and Astrophysics, 636, A10

[57] Claeys J. S. W., Pols O. R., Izzard R. G., Vink J., Verbunt F. W. M., 2014, Astronomy and Astrophysics, 563, A83

[58] Claret A., 2007, Astronomy and Astrophysics, 475, 1019

[59] Clayton M., Podsiadlowski P., Ivanova N., Justham S., 2017, Monthly Notices of RAS, 470, 1788

[60] Comerford T. A. F., Izzard R. G., 2020, Monthly Notices of the Royal Astronomical Society, 498, 2957

[61] Counselman Charles C. I., 1973, Astrophysical Journal, 180, 307

[62] Crowther P. A., et al., 2016, Monthly Notices of the RAS, 458, 624

[63] Darwin G. H., 1879, The Observatory, 3, 79

[64] Davies B., Beasor E. R., 2020, Monthly notices of RAS, 493, 468

[65] De Marco O., Passy J.-C., Moe M., Herwig F., Mac Low M.-M., Paxton B., 2011, Monthly Notices of RAS, 411, 2277

[66] Deloye C. J., Taam R. E., 2010, Astrophyiscal Journal, Letters, 719, L28

[67] Dewi J. D. M., Tauris T. M., 2000, Astronomy and Astrophysics, 360, 1043

[68] Di Carlo U. N., et al., 2020, Monthly Notices of the Royal Astronomical Society, 498, 495–506

[69] Dominik M., Belczynski K., Fryer C., Holz D. E., Berti E., Bulik T., Mandel I., O'Shaughnessy R., 2012, Astrophysical Journal, 759, 52

[70] Dominik M., et al., 2015, The Astrophysical Journal, 806, 263

[71] Dong S., Katz B., Socrates A., 2014, Astrophysical Journal, 781, L5

[72] Dorozsmai A., Toonen S., 2022, arXiv e-prints, p. arXiv:2207.08837

[73] Dorozsmai A., Toonen S., Vigna-Gómez A., de Mink S. E., Kummer F., 2024, Mon. Not. R. Astron. Soc., 527, 9782

[74] Duchêne G., Kraus A., 2013, Annual Review of Astron and Astrophysis, 51, 269

[75] Duffell P. C., D'Orazio D., Derdzinski A., Haiman Z., MacFadyen A., Rosen A. L., Zrake J., 2020, Astrophysical Journal, 901, 25

[76] Dunstall P. R., et al., 2015, Astronomy and Astrophysics, 580, A93

[77] Duquennoy A., Mayor M., 1991, Astronomy and Astrophysics, 248, 485

[78] Eggleton P. P., 1983, Astrophysical Journal, 268, 368

[79] Eggleton P., 2006, Evolutionary Processes in Binary and Multiple Stars

[80] Eggleton P. P., Kiseleva-Eggleton L., 2001, Astrophysical Journal, 562, 1012

[81] Ekström S., et al., 2012, Astronomy and Astrophysics, 537, A146

[82] Eldridge J. J., Stanway E. R., 2016, Monthly Notices of the Royal Astronomical Society, 462, 3302

[83] Eldridge J. J., Stanway E. R., Xiao L., McClelland L. A. S., Taylor G., Ng M., Greis S. M. L., Bray J. C., 2017, Publications of the Astron. Soc. of Australia, 34, e058

[84] Endal A. S., Sofia S., 1978, Astrophysical Journal, 220, 279

[85] Evans N. R., 2011, Bulletin de la Societe Royale des Sciences de Liege, 80, 663

[86] Evans C. J., et al., 2005, Astronomy and Astrophysics, 437, 467

[87] Fabrycky D., Tremaine S., 2007, Astrophysical Journal, 669, 1298

[88] Farmer R., Renzo M., de Mink S. E., Marchant P., Justham S., 2019, Astrophysical Journal, 887, 53

[89] Farr W. M., Sravan N., Cantrell A., Kreidberg L., Bailyn C. D., Mandel I., Kalogera V., 2011, Astrophysical Journal, 741, 103

[90] Flanagan E. E., Hughes S. A., 2005, New Journal of Physics, 7, 204

[91] Ford E. B., Kozinsky B., Rasio F. A., 2004, Astrophysical Journal, 605, 966

[92] Fowler W. A., Hoyle F., 1964, Astrophysical Journals, 9, 201

[93] Fragione G., Loeb A., 2019, Monthly Notices of the Royal Astronomical Society, 486, 4443

[94] Fragos T., Andrews J. J., Ramirez-Ruiz E., Meynet G., Kalogera V., Taam R. E., Zezas A., 2019, Astrophysical Journal, Letters, 883, L45

[95] Fragos T., et al., 2023, Astrophysical Journals, 264, 45

[96] Fraley G. S., 1968, Astrophysics and Space Science, 2, 96

[97] Fryer C. L., Belczynski K., Wiktorowicz G., Dominik M., Kalogera V., Holz D. E., 2012, The Astrophysical Journal, 749, 91

[98] Fullerton A. W., Massa D. L., Prinja R. K., 2006, Astrophysical Journal, 637, 1025

[99] Gallegos-Garcia M., Berry C. P. L., Marchant P., Kalogera V., 2021, Astrophysical Journal, 922, 110

[100] Gallegos-Garcia M., Fishbach M., Kalogera V., L Berry C. P., Doctor Z., 2022, Astrophysical Journal, 938, L19

[101] Ge H., Hjellming M. S., Webbink R. F., Chen X., Han Z., 2010, Astrophysical Journal, 717, 724

[102] Ge H., Webbink R. F., Chen X., Han Z., 2015, Astrophysical Journal, 812, 40

[103] Ge H., Webbink R. F., Chen X., Han Z., 2020, Astrophysical Journal, 899, 132

[104] Georgy C., Meynet G., Maeder A., 2011, Astronomy and Astrophysics, 527, A52

[105] Ghodla S., Eldridge J. J., Stanway E. R., Stevance H. F., 2022, Monthly Notices of the Royal Astronomical Society, 518, 860

[106] Giacobbo N., Mapelli M., 2018, Monthly Notices of the Royal Astronomical Society, 480, 2011

[107] Giacobbo N., Mapelli M., Spera M., 2017, Monthly Notices of the Royal Astronomical Society, 474, 2959–2974

[108] Gilkis A., Shenar T., Ramachandran V., Jermyn A. S., Mahy L., Oskinova L. M., Arcavi I., Sana H., 2021, Monthly Notices of the Royal Astronomical Society, 503, 1884

[109] Glanz H., Perets H. B., 2021a, Monthly Notices of the Royal Astronomical Society, 500, 1921

[110] Glanz H., Perets H. B., 2021b, Monthly Notices of the Royal Astronomical Society, 507, 2659

[111] Götberg Y., de Mink S. E., Groh J. H., 2017, Astronomy and Astrophysics, 608, A11

[112] Götberg Y., de Mink S. E., McQuinn M., Zapartas E., Groh J. H., Norman C., 2020, Astronomy and Astrophysics, 634, A134

[113] Groenewegen M. A. T., Lamers H. J. G. L. M., Pauldrach A. W. A., 1989, Astronomy and Astrophysics, 221, 78

[114] Haiman Z., Loeb A., 1997, Astrophysical Journal, 483, 21

[115] Hamann W. R., Koesterke L., 1998, Astronomy and Astrophysics, 335, 1003

[116] Hamann W. R., Koesterke L., Wessolowski U., 1995, Astronomy and Astrophysics, 299, 151

[117] Hamers A. S., Thompson T. A., 2019, Astrophysical Journal, 883, 23

[118] Hamers A. S., Pols O. R., Claeys J. S. W., Nelemans G., 2013, Monthly Notices of the Royal Astronomical Society, 430, 2262

[119] Hamers A. S., Rantala A., Neunteufel P., Preece H., Vynatheya P., 2021, Monthly Notices of the Royal Astronomical Society, 502, 4479

[120] Hamers A. S., Glanz H., Neunteufel P., 2022a, Astrophysical Journals, 259, 25

[121] Hamers A. S., Perets H. B., Thompson T. A., Neunteufel P., 2022b, Astrophysical Journal, 925, 178

[122] Han Z., Podsiadlowski P., Eggleton P. P., 1995, Monthly Notices of RAS, 272, 800

[123] Harrington R. S., 1968, Astronomical Journal, 73, 190

Bibliography

[124] Heger A., Woosley S. E., 2002, Astrophysical Journal, 567, 532

[125] Heger A., Langer N., Woosley S. E., 2000, Astrophysical Journal, 528, 368

[126] Heggie D. C., 1975, Monthly Notices of the Royal Astronomical Society, 173, 729

[127] Henyey L. G., Forbes J. E., Gould N. L., 1964, Astrophysical Journal, 139, 306

[128] Higgins E. R., Vink J. S., 2020, Astronomy and Astrophysics, 635, A175

[129] Hills J. G., 1983, Astrophysical Journal, 267, 322

[130] Hjellming M. S., Webbink R. F., 1987, Astrophysical Journal, 318, 794

[131] Hobbs G., Lorimer D. R., Lyne A. G., Kramer M., 2005, Monthly Notices of Ras, 360, 974

[132] Höfner S., 2015, in Kerschbaum F., Wing R. F., Hron J., eds, Astronomical Society of the Pacific Conference Series Vol. 497, Why Galaxies Care about AGB Stars III: A Closer Look in Space and Time. p. 333 (`arXiv:1505.07425`)

[133] Holman M., Touma J., Tremaine S., 1997, Nature, 386, 254

[134] Huang S. S., 1956, Astronomical Journal, 61, 49

[135] Huang S.-S., 1963, Astrophysical Journal, 138, 471

[136] Hughes S. A., 2014, Physics of the Dark Universe, 4, 86

[137] Humphreys R. M., Davidson K., 1994, Publications of the ASP, 106, 1025

[138] Hurley J. R., Pols O. R., Tout C. A., 2000, Mon. Not. R. Astron. Soc., 315, 543

[139] Hurley J. R., Tout C. A., Pols O. R., 2002, Monthly Notices of the Royal Astronomical Society, 329, 897

[140] Hut P., 1980, Astronomy and Astrophysics, 92, 167

[141] Hut P., 1981, Astronomy and Astrophysics, 99, 126

[142] Iben Icko J., Tutukov A. V., 1999, Astrophysical Journal, 511, 324

[143] Iglesias C. A., Rogers F. J., 1993, Astrophysical Journal, 412, 752

[144] Iglesias C. A., Rogers F. J., 1996, Astrophysical Journal, 464, 943

[145] Igoshev A. P., 2020, Monthly Notices of RAS, 494, 3663

[146] Inayoshi K., Hirai R., Kinugawa T., Hotokezaka K., 2017, Monthly Notices of the Royal Astronomical Society, 468, 5020

[147] Innanen K. A., Zheng J. Q., Mikkola S., Valtonen M. J., 1997, Astronomical Journal, 113, 1915

[148] Ivanova N., 2011, in Schmidtobreick L., Schreiber M. R., Tappert C., eds, Astronomical Society of the Pacific Conference Series Vol. 447, Evolution of Compact Binaries. p. 91 (`arXiv:1108.1226`), doi:10.48550/arXiv.1108.1226

[149] Ivanova N., Nandez J. L. A., 2016, Monthly Notices of RAS, 462, 362

[150] Ivanova N., Taam R. E., 2004, Astrophysical Journal, 601, 1058

[151] Ivanova N., Chaichenets S., Fregeau J., Heinke C. O., Lombardi J. C. J., Woods T. E., 2010, Astrophysical Journal, 717, 948

[152] Ivanova N., et al., 2013, Astronomy and Astrophysicsr, 21, 59

[153] Jackson B., Arras P., Penev K., Peacock S., Marchant P., 2017, Astrophysical Journal, 835, 145

[154] Janka H.-T., 2012, Annual Review of Nuclear and Particle Science, 62, 407

[155] Joyce M., Tayar J., 2023, Galaxies, 11, 75

[156] Kaaret P., Feng H., Roberts T. P., 2017, Annual Review of Astron and Astrophysics, 55, 303

[157] Kato S., 1966, Publications of the ASJ, 18, 374

[158] Katz B., Dong S., 2012, arXiv e-prints, p. arXiv:1211.4584

[159] King A. R., Taam R. E., Begelman M. C., 2000, Astrophysical Journal, 530, L25

[160] Kinoshita H., Nakai H., 1999, Celestial Mechanics and Dynamical Astronomy, 75, 125

[161] Kinugawa T., Inayoshi K., Hotokezaka K., Nakauchi D., Nakamura T., 2014, Monthly Notices of the Royal Astronomical Society, 442, 2963

[162] Kippenhahn R., Weigert A., Weiss A., 2013, Stellar Structure and Evolution, doi:10.1007/978-3-642-30304-3.

[163] Kiseleva L. G., Eggleton P. P., Orlov V. V., 1994, Monthly Notices of the Royal Astronomical Society, 270, 936

[164] Kiseleva L. G., Eggleton P. P., Mikkola S., 1998, Monthly Notices of RAS, 300, 292

[165] Klencki J., Nelemans G., 2018, Proceedings of the International Astronomical Union, 14, 417–425

[166] Klencki J., Moe M., Gladysz W., Chruslinska M., Holz D. E., Belczynski K., 2018, Astronomy and Astrophysics, 619, A77

[167] Klencki J., Nelemans G., Istrate A. G., Pols O., 2020, Astronomy and Astrophysics, 638, A55

[168] Klencki J., Nelemans G., Istrate A. G., Chruslinska M., 2021, Astronomy and Astrophysics, 645, A54

[169] Kobayashi C., Taylor P., 2023, arXiv e-prints, p. arXiv:2302.07255

[170] Kobulnicky H. A., Fryer C. L., 2007, Astrophysical Journal, 670, 747

[171] Kobulnicky H. A., et al., 2014, Astrophysical Journals, 213, 34

[172] Koch R. H., Hrivnak B. J., 1981, Astrophysical Journal, 248, 249

[173] Kochanek C. S., 2020, Monthly notices of RAS, 493, 4945

[174] Kolb U., Ritter H., 1990, Astronomy and Astrophysics, 236, 385

[175] Kozai Y., 1962, Astronomical Journal, 67, 591

[176] Kroupa P., 2001, Monthly Notices of the Royal Astronomical Society, 322, 231

[177] Krtička J., 2006, Monthly Notices of the Royal Astronomical Society, 367, 1282

[178] Krtička J., Kubát J., 2017, Astronomy and Astrophysics, 606, A31

[179] Kruckow M. U., Tauris T. M., Langer N., Szécsi D., Marchant P., Podsiadlowski P., 2016, Astronomy and Astrophysics, 596, A58

[180] Kruckow M. U., Tauris T. M., Langer N., Kramer M., Izzard R. G., 2018, Monthly Notices of the Royal Astronomical Society, 481, 1908–1949

[181] Kruckow M. U., Neunteufel P. G., Di Stefano R., Gao Y., Kobayashi C., 2021, Astrophysical Journal, 920, 86

[182] Kudritzki R. P., Pauldrach A., Puls J., 1987, Astronomy and Astrophysics, 173, 293

[183] Kulkarni S. R., Hut P., McMillan S., 1993, Nature, 364, 421

[184] Kummer F., Toonen S., de Koter A., 2023, The Main Evolutionary Pathways of Massive Hierarchical Triple Stars (arXiv:2306.09400)

[185] Lai D., Muñoz D. J., 2022, arXiv e-prints, p. arXiv:2211.00028

[186] Lamers H. J. G. L. M., Fitzpatrick E. L., 1988, Astrophysical Journal, 324, 279

[187] Langer N., 2012, Annual Review of Astronomy and Astrophysics, 50, 107–164

[188] Langer N., Maeder A., 1995, Astronomy and Astrophysics, 295, 685

[189] Langer N., Fricke K. J., Sugimoto D., 1983, Astronomy and Astrophysics, 126, 207

[190] Langer N., El Eid M. F., Fricke K. J., 1985, Astronomy and Astrophysics, 145, 179

[191] Langer N., et al., 2020, Astronomy and Astrophysics, 638, A39

[192] Laplace E., Götberg Y., de Mink S. E., Justham S., Farmer R., 2020, Astronomy and Astrophysics, 637, A6

[193] Leigh N. W. C., Toonen S., Portegies Zwart S. F., Perna R., 2020, Monthly Notices of the Royal Astronomical Society, 496, 1819

[194] Leitherer C., Robert C., Drissen L., 1992, Astrophysical Journal, 401, 596

[195] Lidov M. L., 1962, Planetary Space Science, 9, 719

[196] Lithwick Y., Naoz S., 2011, Astrophysical Journal, 742, 94

[197] Liu B., Muñoz D. J., Lai D., 2015, Monthly Notices of the Royal Astronomical Society, 447, 747

[198] Livio M., Soker N., 1988, Astrophysical Journal, 329, 764

[199] Loveridge A. J., van der Sluys M. V., Kalogera V., 2011, The Astrophysical Journal, 743, 49

[200] Lower M. E., Thrane E., Lasky P. D., Smith R., 2018, Physical Review D, 98, 083028

[201] Lubow S. H., Shu F. H., 1975a, Astrophysical Journal, 198, 383

[202] Lubow S. H., Shu F. H., 1975b, Astrophysical Journal, 198, 383

[203] Lurie J. C., et al., 2017, Astronomical Journal, 154, 250

[204] MacLeod M., Antoni A., Murguia-Berthier A., Macias P., Ramirez-Ruiz E., 2017, Astrophysical Journal, 838, 56

[205] Madau P., Dickinson M., 2014, Annual Review of Astron and Astrophysics, 52, 415

[206] Madau P., Fragos T., 2017, The Astrophysical Journal, 840, 39

[207] Maeder A., 1987, Astronomy and Astrophysics, 178, 159

[208] Maeder A., 2009, Physics, Formation and Evolution of Rotating Stars, doi:10.1007/978-3-540-76949-1.

[209] Maggiore M., 2007, Gravitational Waves. Vol. 1: Theory and Experiments. Oxford University Press, doi:10.1093/acprof:oso/9780198570745.001.0001

[210] Mandel I., Broekgaarden F. S., 2022, Living Reviews in Relativity, 25

[211] Mandel I., Farmer A., 2018, Merging stellar-mass binary black holes (arXiv:1806.05820)

[212] Mandel I., Müller B., 2020, Monthly notices of RAS, 499, 3214

[213] Mandel I., de Mink S. E., 2016, Monthly Notices of the Royal Astronomical Society, 458, 2634

[214] Mapelli M., 2016, Monthly Notices of the Royal Astronomical Society, 459, 3432–3446

[215] Mapelli M., 2020, Frontiers in Astronomy and Space Sciences, 7

[216] Marchal C., 1990, The three-body problem

[217] Marchant P., Langer N., Podsiadlowski P., Tauris T. M., Moriya T. J., 2016, Astronomy and Astrophysics, 588, A50

[218] Marchant P., Renzo M., Farmer R., Pappas K. M. W., Taam R. E., de Mink S. E., Kalogera V., 2019, Astrophysical Journal, 882, 36

[219] Marchant P., Pappas K. M. W., Gallegos-Garcia M., Berry C. P. L., Taam R. E., Kalogera V., Podsiadlowski P., 2021, Astronomy and Astrophysics, 650, A107

[220] Mardling R. A., Aarseth S. J., 2001, Monthly Notices of the Royal Astronomical Society, 321, 398

[221] Martinez M. A. S., Rodriguez C. L., Fragione G., 2021, On the Mass Ratio Distribution of Black Hole Mergers in Triple Systems, doi:10.48550/ARXIV.2105.01671, https://arxiv.org/abs/2105.01671

[222] Martinez M. A. S., Rodriguez C. L., Fragione G., 2022, Astrophysical Journal, 937, 78

[223] Mazeh T., 2008, in Goupil M. J., Zahn J. P., eds, EAS Publications Series Vol. 29, EAS Publications Series. pp 1–65 (arXiv:0801.0134), doi:10.1051/eas:0829001

[224] Mazeh T., Shaham J., 1979, Astronomy and Astrophysics, 77, 145

[225] McKernan B., et al., 2019, Astrophysical Journal, 884, L50

[226] McKernan B., Ford K. E. S., O'Shaugnessy R., Wysocki D., 2020, Monthly Notices of the Royal Astronomical Society, 494, 1203

[227] Meibom S., Mathieu R. D., 2005, Astrophysical Journal, 620, 970

[228] Meibom S., Mathieu R. D., Stassun K. G., 2006, Astrophysical Journal, 653, 621

[229] Mennekens N., Vanbeveren D., 2014, Astronomy and Astrophysics, 564, A134

[230] Mennekens N., Vanbeveren D., 2016, Astronomy and Astrophysics, 589, A64

[231] Menon A., et al., 2021, Monthly Notices of the Royal Astronomical Society, 507, 5013

[232] Michaely E., Perets H. B., 2014, Astrophysical Journal, 794, 122

[233] Miller M. C., Hamilton D. P., 2002, Astrophysical Journal, 576, 894

[234] Misner C. W., Thorne K. S., Wheeler J. A., 1973, Gravitation

[235] Moe M., Di Stefano R., 2017, Astrophysical Journals, 230, 15

[236] Mohamed S., Podsiadlowski P., 2011, in Kerschbaum F., Lebzelter T., Wing R. F., eds, Astronomical Society of the Pacific Conference Series Vol. 445, Why Galaxies Care about AGB Stars II: Shining Examples and Common Inhabitants. p. 355

[237] Mokiem M. R., et al., 2007, Astronomy and Astrophysics, 473, 603

[238] Moody M. S. L., Shi J.-M., Stone J. M., 2019, Astrophysical Journal, 875, 66

[239] Moreno Méndez E., De Colle F., López Cámara D., Vigna-Gómez A., 2022, arXiv e-prints, p. arXiv:2207.03514

[240] Muñoz D. J., Miranda R., Lai D., 2019, Astrophysical Journal, 871, 84

[241] Müller B., Heger A., Liptai D., Cameron J. B., 2016, Monthly Notices of Ras, 460, 742

[242] Nandez J. L. A., Ivanova N., Lombardi J. C. J., 2015, Monthly Notices of RAS, 450, L39

[243] Naoz S., 2016, Annual Review of Astron and Astrophysics, 54, 441

[244] Naoz S., Fabrycky D. C., 2014, Astrophysical Journal, 793, 137

[245] Naoz S., Farr W. M., Lithwick Y., Rasio F. A., Teyssandier J., 2011, Nature, 473, 187

[246] Naoz S., Farr W. M., Lithwick Y., Rasio F. A., Teyssandier J., 2013, Monthly Notices of RAS, 431, 2155

[247] Neijssel C. J., et al., 2019, Monthly Notices of the Royal Astronomical Society, 490, 3740–3759

[248] Nieuwenhuijzen H., de Jager C., 1990, Astronomy and Astrophysics, 231, 134

[249] O'Shaughnessy R., Kim C., Kalogera V., Belczynski K., 2008, Astrophysical Journal, 672, 479

[250] Olejak A., Fishbach M., Belczynski K., Holz D. E., Lasota J. P., Miller M. C., Bulik T., 2020, The Origin of inequality: isolated formation of a 30+10Msun binary black-hole merger (`arXiv:2004.11866`)

[251] Olejak A., Belczynski K., Ivanova N., 2021, Astronomy and Astrophysics, 651, A100

[252] Onno Pols F. V., 2011, Binary stars, lecture notes for MSC course at Utrecht University

[253] Öpik E., 1924, Publications of the Tartu Astrofizica Observatory, 25, 1

[254] Packet W., 1981, Astronomy and Astrophysics, 102, 17

[255] Paczynski B., 1976, Symposium - International Astronomical Union, 73, 75–80

[256] Paczynski B., Sienkiewicz R., 1972, Acta Astronomica, 22, 73

[257] Passy J.-C., et al., 2012, Astrophysical Journal, 744, 52

[258] Pauli D., Langer N., Aguilera-Dena D. R., Wang C., Marchant P., 2022, Astronomy and Astrophysics, 667, A58

[259] Pavlovskii K., Ivanova N., 2015, Monthly Notices of RAS, 449, 4415

[260] Pavlovskii K., Ivanova N., Belczynski K., Van K. X., 2017, Monthly Notices of the Royal Astronomical Society, 465, 2092

[261] Paxton B., Bildsten L., Dotter A., Herwig F., Lesaffre P., Timmes F., 2011, Astrophysical Journals, 192, 3

[262] Pejcha O., 2014, Astrophysical Journal, 788, 22

[263] Pejcha O., Metzger B. D., Tyles J. G., Tomida K., 2017, Astrophysical Journal, 850, 59

[264] Perets H. B., Fabrycky D. C., 2009, Astrophysical Journal, 697, 1048

[265] Perets H. B., Kratter K. M., 2012, Astrophysical Journal, 760, 99

[266] Peters P. C., 1964, Phys. Rev., 136, B1224

[267] Peters T., Banerjee R., Klessen R. S., Mac Low M.-M., Galván-Madrid R., Keto E. R., 2010, Astrophysical Journal, 711, 1017

[268] Petrovic J., Langer N., van der Hucht K. A., 2005, Astronomy and Astrophysics, 435, 1013

[269] Petrovich C., 2015, Astrophysical Journal, 799, 27

[270] Pijloo J. T., Caputo D. P., Portegies Zwart S. F., 2012, Monthly Notices of the Royal Astronomical Society, 424, 2914

[271] Pinsonneault M. H., Kawaler S. D., Sofia S., Demarque P., 1989, Astrophysical Journal, 338, 424

[272] Podsiadlowski P., Joss P. C., Hsu J. J. L., 1992, Astrophysical Journal, 391, 246

[273] Poelarends A. J. T., Herwig F., Langer N., Heger A., 2008, Astrophysical Journal, 675, 614

[274] Pols O. R., 1994, Astronomy and Astrophysics, 290, 119

[275] Pols O. R., Marinus M., 1994, Astronomy and Astrophysics, 288, 475

[276] Pols O. R., Schröder K.-P., Hurley J. R., Tout C. A., Eggleton P. P., 1998, Monthly Notices of the Royal Astronomical Society, 298, 525

[277] Popham R., Narayan R., 1991, Astrophysical Journal, 370, 604

[278] Portegies Zwart S. F., McMillan S. L. W., 2000, The Astrophysical Journal, 528, L17–L20

[279] Portegies Zwart S. F., Verbunt F., 1996, Astronomy and Astrophysics, 309, 179

[280] Postnov K. A., Yungelson L. R., 2014, Living Reviews in Relativity, 17

[281] Potekhin A. Y., Chabrier G., 2010, Contributions to Plasma Physics, 50, 82

[282] Prinja R. K., Barlow M. J., Howarth I. D., 1990, Astrophysical Journal, 361, 607

[283] Rakavy G., Shaviv G., 1967, Astrophysical Journal, 148, 803

[284] Ramirez-Agudelo O. H., et al., 2013, Astronomy and Astrophysics, 560, A29

[285] Reimers D., 1975, Memoires of the Societe Royale des Sciences de Liege, 8, 369

[286] Renzo M., Ott C. D., Shore S. N., de Mink S. E., 2017, Astronomy and Astrophysics, 603, A118

[287] Renzo M., Farmer R., Justham S., Götberg Y., de Mink S. E., Zapartas E., Marchant P., Smith N., 2020, Astronomy and Astrophysics, 640, A56

[288] Renzo M., et al., 2021, Astrophysical Journal, 919, 128

[289] Ribas I., Jordi C., Giménez Á., 2000, Monthly notices of RAS, 318, L55

[290] Richards S. M., Eldridge J. J., Briel M. M., Stevance H. F., Willcox R., 2023, Monthly Notices of the Royal Astronomical Society, 522, 3972

[291] Ricker P. M., Taam R. E., 2012, Astrophysical Journal, 746, 74

[292] Riley J., Mandel I., Marchant P., Butler E., Nathaniel K., Neijssel C., Shortt S., Vigna-Gómez A., 2021, Monthly Notices of the Royal Astronomical Society, 505, 663

[293] Riley J., et al., 2022, The Astrophysical Journal Supplement Series, 258, 34

[294] Ritter H., 1988, Astronomy and Astrophysics, 202, 93

[295] Rodriguez C. L., Antonini F., 2018, Astrophysical Journal, 863, 7

[296] Rodriguez C. L., Morscher M., Pattabiraman B., Chatterjee S., Haster C.-J., Rasio F. A., 2015, Physical Review Letters, 115

[297] Rodriguez C. L., Haster C.-J., Chatterjee S., Kalogera V., Rasio F. A., 2016, The Astrophysical Journal, 824, L8

[298] Rogers F. J., Nayfonov A., 2002, Astrophysical Journal, 576, 1064

[299] Román-Garza J., et al., 2021, Astrophysical Journal, 912, L23

[300] Romero-Shaw I., Lasky P. D., Thrane E., 2022, Astrophysical Journal, 940, 171

[301] Rozner M., Perets H. B., 2022, Astrophysical Journal, 931, 149

[302] Sabhahit G. N., Vink J. S., Higgins E. R., Sander A. A. C., 2021, Monthly Notices of the Royal Astronomical Society, 506, 4473

[303] Sana H., et al., 2012, Science, 337, 444

[304] Sana H., et al., 2013, Astronomy and Astrophysics, 550, A107

[305] Sana H., et al., 2014, Astrophysical Journals, 215, 15

[306] Sander A. A. C., 2022, arXiv e-prints, p. arXiv:2211.05424

[307] Sander A. A. C., Vink J. S., 2020, Monthly Notices of the RAS, 499, 873

[308] Sasaki M., Suyama T., Tanaka T., Yokoyama S., 2018, Classical and Quantum Gravity, 35, 063001

[309] Saumon D., Chabrier G., van Horn H. M., 1995, Astrophysical Journal, Supplement, 99, 713

[310] Schaerer D., Fragos T., Izotov Y. I., 2019, Astronomy and Astrophysics, 622, L10

[311] Schmidt P., 2020, Frontiers in Astronomy and Space Sciences, 7, 28

[312] Schootemeijer A., Götberg Y., de Mink S. E., Gies D., Zapartas E., 2018, Astronomy and Astrophysics, 615, A30

[313] Schootemeijer A., Langer N., Grin N. J., Wang C., 2019, Astronomy and Astrophysics, 625, A132

[314] Schrøder S. L., MacLeod M., Ramirez-Ruiz E., Mandel I., Fragos T., Loeb A., Everson R. W., 2021, arXiv e-prints, p. arXiv:2107.09675

[315] Schutz B. F., 1986, Nature, 323, 310

[316] Sen K., et al., 2022, Astronomy and Astrophysics, 659, A98

[317] Senchyna P., Stark D. P., Mirocha J., Reines A. E., Charlot S., Jones T., Mulchaey J. S., 2020, Monthly Notices of RAS, 494, 941

[318] Shao Y., Li X.-D., 2016, The Astrophysical Journal, 833, 108

[319] Shao Y., Li X.-D., 2021, Astrophysical Journal, 920, 81

[320] Shappee B. J., Thompson T. A., 2013, Astrophysical Journal, 766, 64

[321] Shu F. H., Lubow S. H., Anderson L., 1979, Astrophysical Journal, 229, 223

[322] Sigurdsson S., Hernquist L., 1993, Nature, 364, 423

[323] Silsbee K., Tremaine S., 2017, Astrophysical Journal, 836, 39

[324] Smeyers P., Willems B., 2001, Astronomy and Astrophysics, 373, 173

[325] Smith N., 2014, Annual Review of Astron and Astrophysics, 52, 487

[326] Soberman G. E., Phinney E. S., van den Heuvel E. P. J., 1997, Astronomy and Astrophysics, 327, 620

[327] Sobolev V. V., 1960, Moving Envelopes of Stars, doi:10.4159/harvard.9780674864658.

[328] Soker N., Bear E., 2021, Monthly Notices of the Royal Astronomical Society, 505, 4791

[329] Song H. F., Meynet G., Maeder A., Ekström S., Eggenberger P., 2016, Astronomy and Astrophysics, 585, A120

[330] Srinivasan R., Lamberts A., Bizouard M. A., Bruel T., Mastrogiovanni S., 2023, Monthly Notices of the Royal Astronomical Society, 524, 60

[331] Stanway E. R., Eldridge J. J., 2018, Monthyl Notices of RAS, 479, 75

[332] Stanway E. R., Eldridge J. J., Becker G. D., 2016, Monthly Notices of the RAS, 456, 485

[333] Stegmann J., Antonini F., Schneider F. R. N., Tiwari V., Chattopadhyay D., 2022a, Physical Review D, 106, 023014

[334] Stegmann J., Antonini F., Moe M., 2022b, Monthly Notices of the Royal Astronomical Society, 516, 1406

[335] Stevenson S., Ohme F., Fairhurst S., 2015, Astrophysical Journal, 810, 58

[336] Stevenson S., Vigna-Gómez A., Mandel I., Barrett J. W., Neijssel C. J., Perkins D., de Mink S. E., 2017, Nature Communications, 8

[337] Stevenson S., Sampson M., Powell J., Vigna-Gómez A., Neijssel C. J., Szécsi D., Mandel I., 2019, Astrophysical Journal, 882, 121

[338] Stone N. C., Metzger B. D., Haiman Z., 2017, Monthly Notices of the Royal Astronomical Society, 464, 946

[339] Sundqvist J. O., Björklund R., Puls J., Najarro F., 2019, Astronomy and Astrophysics, 632, A126

[340] Swaruba Rajamuthukumar A., Hamers A., Neunteufel P., Pakmor R., de mink S. E., 2022, arXiv e-prints, p. arXiv:2211.04463

[341] Szécsi D., Langer N., Yoon S.-C., Sanyal D., de Mink S., Evans C. J., Dermine T., 2015, Astronomy and Astrophysics, 581, A15

[342] Tang P. N., Eldridge J. J., Stanway E. R., Bray J. C., 2020, Monthly Notices of the Royal Astronomical Society, 493, L6

[343] Tassoul J.-L., 1978, Theory of rotating stars

[344] Tauris T. M., Dewi J. D. M., 2001, Astronomy and Astrophysics, 369, 170

[345] The LIGO Scientific Collaboration et al., 2021, arXiv e-prints, p. arXiv:2111.03606

[346] Thompson T. A., 2011, Astrophysical Journal, 741, 82

[347] Tiede C., Zrake J., MacFadyen A., Haiman Z., 2020, Astrophysical Journal, 900, 43

[348] Timmes F. X., Swesty F. D., 2000, Astrophysical Journal, Supplement, 126, 501

[349] Tokovinin A., 2010, VizieR Online Data Catalog, p. J/MNRAS/389/925

[350] Tokovinin A., 2014, Astronomical Journal, 147, 87

[351] Tokovinin A., Thomas S., Sterzik M., Udry S., 2006, Astronomy and Astrophysics, 450, 681

[352] Toonen S., Nelemans G., 2013, Astronomy and Astrophysics, 557, A87

[353] Toonen S., Nelemans G., Portegies Zwart S., 2012, Astronomy and Astrophysics, 546, A70

[354] Toonen S., Hamers A., Portegies Zwart S., 2016, Computational Astrophysics and Cosmology, 3, 6

[355] Toonen S., Perets H. B., Hamers A. S., 2018, Astronomy and Astrophysics, 610, A22

[356] Toonen S., Portegies Zwart S., Hamers A. S., Bandopadhyay D., 2020, Astronomy and Astrophysics, 640, A16

[357] Toonen S., Boekholt T. C. N., Portegies Zwart S., 2022, Astronomy and Astrophysics, 661, A61

[358] Tout C. A., Aarseth S. J., Pols O. R., Eggleton P. P., 1997, Monthly Notices of RAS, 291, 732

[359] Tremaine S., Yavetz T. D., 2014, American Journal of Physics, 82, 769

[360] Tutukov A., Yungelson L., 1979, Evolution of massive common envelope binaries and mass loss.. Vol. 83

[361] Tutukov A. V., Yungelson L. R., 1993, Monthly Notices of the Royal Astronomical Society, 260, 675

[362] Ulrich R. K., Burger H. L., 1976, Astrophysical Journal, 206, 509

[363] Vassiliadis E., Wood P. R., 1993, Astrophysical Journal, 413, 641

[364] Veras D., Ford E. B., 2010, Astrophysical Journal, 715, 803

[365] Verbunt F., Igoshev A., Cator E., 2017, Astronomy and Astrophysics, 608, A57

[366] Vigna-Gómez A., et al., 2018, Monthly Notices of the Royal Astronomical Society, 481, 4009

[367] Vigna-Gómez A., Toonen S., Ramirez-Ruiz E., Leigh N. W. C., Riley J., Haster C.-J., 2021, Astrophysical Journal, 907, L19

[368] Vigna-Gómez A., Liu B., Aguilera-Dena D. R., Grishin E., Ramirez-Ruiz E., Soares-Furtado M., 2022, Monthly Notices of the Royal Astronomical Society, 515, L50

[369] Vigna-Gómez A., Toonen S., Ramirez-Ruiz E., Leigh N. W. C., Riley J., Haster C.-J., 2021, The Astrophysical Journal, 907, L19

[370] Vinciguerra S., et al., 2020, Monthly Notices of the Royal Astronomical Society, 498, 4705–4720

[371] Vink J. S., 2012, in Davidson K., Humphreys R. M., eds, Astrophysics and Space Science Library Vol. 384, Eta Carinae and the Supernova Impostors. p. 221 (arXiv:0905.3338), doi:10.1007/978-1-4614-2275-4_10

[372] Vink J. S., 2020, Galaxies, 8, 43

[373] Vink J. S., Sander A. A. C., 2021, Monthly Notices of RAS, 504, 2051

[374] Vink J. S., de Koter A., 2005, Astronomy and Astrophysics, 442, 587

[375] Vink J. S., de Koter A., Lamers H. J. G. L. M., 2000, New theoretical Mass-loss rates of O and B Stars (`arXiv:astro-ph/0008183`)

[376] Vink J. S., de Koter A., Lamers H. J. G. L. M., 2001, Astronomy and Astrophysics, 369, 574

[377] Voss R., Tauris T. M., 2003, Monthly Notices of RAS, 342, 1169

[378] Weaver R., McCray R., Castor J., Shapiro P., Moore R., 1977, Astrophysical Journal, 218, 377

[379] Webbink R. F., 1984, Astrophysical Journal, 277, 355

[380] Wellstein S., Langer N., Braun H., 2001, Astronomy and Astrophysics, 369, 939

[381] Wen L., 2003, Astrophysical Journal, 598, 419

[382] Woltjer L., 1972, Annual Review of Astron and Astrophysis, 10, 129

[383] Woods T. E., Ivanova N., 2011, Astrophysical Journal, Letters, 739, L48

[384] Woosley S. E., 2017, Astrophysical Journal, 836, 244

[385] Woosley S. E., Weaver T. A., 1982, in Rees M. J., Stoneham R. J., eds, NATO Advanced Study Institute (ASI) Series C Vol. 90, Supernovae: A Survey of Current Research. p. 79

[386] Woosley S. E., Heger A., Weaver T. A., 2002, Reviews of Modern Physics, 74, 1015

[387] Wu Y., Murray N., 2003, Astrophysical Journal, 589, 605

[388] Xu X.-J., Li X.-D., 2010, The Astrophysical Journal, 716, 114–121

[389] Yoon S.-C., Langer N., 2005, Astronomy and Astrophysics, 443, 643

[390] Yoon S.-C., Langer N., Norman C., 2006, Astronomy and Astrophysics, 460, 199

[391] Yoshida T., Umeda H., Maeda K., Ishii T., 2016, Monthly Notices of the Royal Astronomical Society, 457, 351

[392] Zahn J. P., 1975, Astronomy and Astrophysics, 41, 329

[393] Zahn J. P., 1977, Astronomy and Astrophysics, 57, 383

[394] Zahn J. P., 2008, in Goupil M. J., Zahn J. P., eds, EAS Publications Series Vol. 29, EAS Publications Series. pp 67–90 (`arXiv:0807.4870`), doi:10.1051/eas:0829002

[395] Zevin M., Spera M., Berry C. P. L., Kalogera V., 2020, Astrophysical Journal Letters, 899, L1

[396] Zevin M., et al., 2021, Astrophysical Journal, 910, 152

[397] de Kool M., 1990, Astrophysical Journal, 358, 189

[398] de Kool M., van den Heuvel E. P. J., Pylyser E., 1987, Astronomy and Astrophysics, 183, 47

[399] de Mink S. E., Belczynski K., 2015, Merger rates of double neutron stars and stellar origin black holes: The Impact of Initial Conditions on Binary Evolution Predictions (`arXiv:1506.03573`)

[400] de Mink S. E., King A., 2017, Astrophysical Journal, 839, L7

[401] de Mink S. E., Mandel I., 2016, Monthly Notices of the Royal Astronomical Society, 460, 3545–3553

[402] de Mink S. E., Pols O. R., Hilditch R. W., 2007, Astronomy and Astrophysics, 467, 1181

[403] de Mink S. E., Cantiello M., Langer N., Pols O. R., Brott I., Yoon S. C., 2009, Astronomy and Astrophysics, 497, 243

[404] de Mink S. E., Langer N., Izzard R. G., Sana H., de Koter A., 2013, Astrophysical Journal, 764, 166

[405] de Vries N., Portegies Zwart S., Figueira J., 2014, Monthly Notices of the Royal Astronomical Society, 438, 1909

[406] du Buisson L., et al., 2020, Monthly Notices of the Royal Astronomical Society, 499, 5941

[407] van Son L. A. C., et al., 2022a, Astrophysical Journal, 931, 17

[408] van Son L. A. C., et al., 2022b, Astrophysical Journal, 940, 184

[409] van den Heuvel E. P. J., 1976, in Eggleton P., Mitton S., Whelan J., eds, Vol. 73, Structure and Evolution of Close Binary Systems. p. 35

[410] van den Heuvel E. P. J., Portegies Zwart S. F., de Mink S. E., 2017, Monthly Notices of the Royal Astronomical Society, 471, 4256

[411] von Zeipel H., 1910, Astronomische Nachrichten, 183, 345

[412] von Zeipel H., 1924, Monthly Notices of the Royal Astronomical Society, 84, 665